On the estimation of tissue optical parameters from diffuse reflectance spectroscopy

Walter C.P.M. Blondel[a,b], Prisca Rakotomanga[a,b], Maria Kholodtsova[a,b,c,d], Christian Daul[a,b],Viktor B. Loschenov[c,d], Marine Amouroux[a,b] and Charles Soussen[a,b]

[a]Université de Lorraine, CRAN, 2 avenue de la Forêt de Haye, 54516 Vandoeuvre-Lès-Nancy cedex, France
[b]CNRS, CRAN, 54516 Vandoeuvre-Lès-Nancy cedex, France
[c]General Physics institute, Russian Academy of Sciences, 38 Vavilova street, Moscow, Russia;
[d]National Research Nuclear University 'MEPhI' (Moscow Engineering Physics Institute), Kashirskoe avenue 31, 115409, Moscow, Russia
Author e-mail addresses: [a,b]{firstname.name}@univ-lorraine.fr, [c,d]m.kholodtsova@gmail.com, loschenov@mail.ru

Abstract: This contribution is a state of the art overview on inverse problem solving for spatially resolved diffuse reflectance spectroscopy challenging the precise estimation of multi-layer biological tissue optical parameters.

1. Introduction

Spatially resolved (also called steady-state) diffuse reflectance spectroscopy (SRDRS) is a fibered optical spectroscopy technique studied in many clinical applications for about two decades, especially in cancerology, to diagnose pathological modifications in epithelial tissues of skin and hollow organs (oral cavity, upper respiratory tract, lung, bladder, upper and lower digestive tracts, cervix). The system, sketched in Fig. 1, usually consist of a multiple fiber probe with several source-detector separations (SDSs), spectrophotometer(s) and a broadband non ionizing white light source (400-800 nm). SRDRS proved to be a valuable "optical biopsy" tool allowing clinicians to probe biological tissues non invasively, helping them to improve per-operative diagnostic and therapeutic guiding efficiency. The advantages of this approach are that: (i) rather simple and cost-effective instrumentation is needed which is favorable for clinical transfer, (ii) its resolution is not limited by the Abbe resolution and (iii) it is highly sensitive to changes in the concentration of chromophores such as melanin or oxy- and deoxy-hemoglobin, the size of the scattering centers (for instance cell nucleus) and the structural organization of the medium (cell orientation, multiple layers). It provides sets of spatially and spectrally resolved bulk reflectance data from which the local properties of the tissues are to be unmixed. Thus, the robust and precise estimation, at various tissue depths (see Fig. 1), of the absorption and scattering coefficients (μ_a and μ_s) as well as the anisotropy factor (g) remains a challenging problem in the development of SRDRS in order to provide new key features for characterizing pathological changes in tissues [1-8]. Therefore, the present contribution aims at providing a synthetic overview of the most recent contributions and latest advances on the estimation of the optical properties.

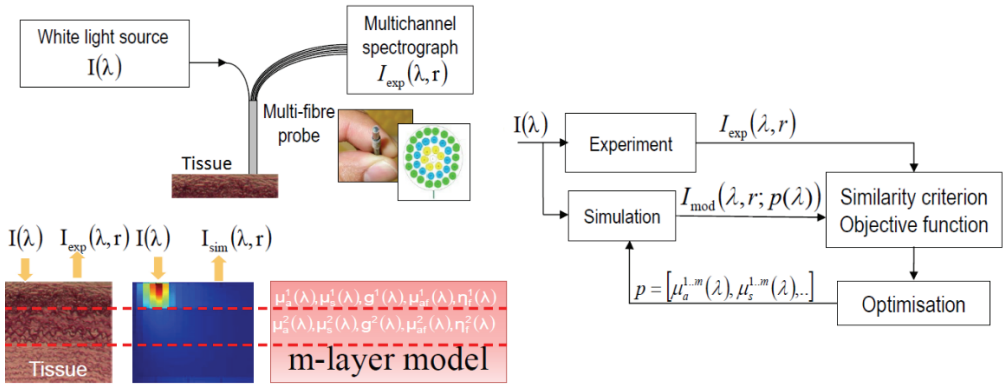

Fig. 1. Left top: Main constitutive parts of an SRDRS instrumentation set-up. Left bottom: schematic correspondence of the multi-layer configuration between tissue, mathematical and physical simulation and model. Right: General scheme of the inverse problem to be solved for estimating the optical properties of the tissue from SRDRS measurements (adapted from [9])

2. Description of the inverse problem to be solved

As sketched on Fig. 1, the inverse problem to be solved consists in finding the parameters of the mathematical and/or physical model, namely $p=\left[\mu_a^{1..m}(\lambda),\mu_s^{1..m}(\lambda),g^{1..m}(\lambda),t^{1..m}\right]$ (for a m-layer tissue model with thicknesses $t^{1..m}$), according to the data observed *i.e.* spatially resolved DR spectra. Because of the complexity of the interactions between light and biological tissues and the complexity of the tissue structure itself, this inverse problem is intrinsically ill-posed (close "similar" results may be obtained with different sets of parameter

values) and ill-conditioned (the solutions may suffer from numerical instability due to finite precision and errors in the experimental and forward problem simulated data). Firstly, mathematical and numerical modelling of the physical phenomena of light-tissue interaction, together with a physical model of the tissue, have to be chosen to describe the forward problem appropriately. The latter provides a set of spatially resolved (r) spectra $I_{\mathrm{mod}}(\lambda, r; p)$ simulated with the tissue parameter vector p. Secondly, an objective function (also called energy- or cost-function) is defined in order to quantify the difference (referred as a "distance") between the experimental and modelled data sets $I_{\mathrm{exp}}(\lambda, r)$ and $I_{\mathrm{mod}}(\lambda, r; p)$ respectively. Thirdly, an optimization procedure is applied with the aim of minimizing the latter distance by iteratively varying the values of the parameters in p. Thus, precise and robust convergence of the optimization procedure towards "true" (ground truth) values of the searched parameters is at stake throughout the choice of the cost-function and the optimization method.

3. Solutions proposed

Monte Carlo-based simulations are mainly used for modelling the forward problem as it is well appropriate to handle the complex geometry of the tissues, the complexity of the photophysical interactions and the geometrical features of the optical probe, especially for short SDSs. Solutions implementing fast GPU-based and/or look-up table based approaches are commonly employed [1,4-6,9-12] but also multi-layer diffusion models [3,13]. However, the inherent statistical noise in I_{mod}, which increases with SDS, has to be taken into account and its impact on local minima occurrence risk properly evaluated. The convergence of the optimization procedure highly depends also on the form of the cost function, which can include spectral and/or spatial normalization in the data-term and sometimes a regularization term. Non linear least squares curve fitting methods such as Levenberg-Marquardt are most popular although the latter belongs to local minimum search approaches. In order to improve the convergence towards a unique global minimum solution, strategies are developed around genetic algorithms [9,14]. The latter are also appropriate for handling the high dimension of the problem when taking into account the spectral resolution of the parameters to be estimated. Errors between ground truth known values of the parameters and their estimated values range from a few % up to several tens of % depending on the methods chosen among those mentioned above for every part of the problem.

4. Acknowledgments

The work was partly conducted in the frame of co-supervised PhD thesis between Université de Lorraine, CRAN-CNRS (France,Nancy) and GPI RAS (Russia, Moscow). The authors acknowledge the financial support for PhD grant of M. Kholodtsova from Conseil Régional de Lorraine and French Embassy in Moscow.

5. References

[1] R. Hennessy, M. Markey and J.W. Tunnell, "Impact of one-layer assumption on diffuse reflectance spectroscopy of skin," *Journal of Biomedical Optics*, 20(2):027001 (2015).

[2] A.J. Radosevich, A. Eshein, T.Q. Nguyen and V. Backman, "Subdiffusion reflectance spectroscopy to measure tissue ultrastructure and microvasculature: model and inverse algorithm," *Journal of Biomedical Optics*, 20(9):097002 (2015).

[3] Y.K. Liao and S.H. Tseng, "Reliable recovery of the optical properties of multi-layer turbid media by iteratively using a layered diffusion model at multiple source-detector separations," *Biomedical Optics Express*, 5(3):975-989 (2014).

[4] X. Zhong, X. Wen and D. Zhu, "Lookup-table-based inverse model for human skin reflectance spectroscopy: two-layered monte carlo simulations and experiments," *Optics Express*, 22(2):1852–1864 (2014).

[5] I. Fredriksson, M. Larsson and T. Strömberg, "Inverse monte carlo method in a multilayered tissue model for diffuse reflectance spectroscopy," *Journal of Biomedical Optics*, 17(4):047004 (2012).

[6] C. Liu, N. Rajaram, K. Vishwanath, T. Jiang, G.M. Palmer and N. Ramanujam, "Experimental validation of an inverse fluorescence monte carlo model to extract concentrations of metabolically relevant fluorophores from turbid phantoms and a murine tumor model," *Journal of Biomedical Optics*, 17(7):077012 (2012).

[7] R.H. Wilson and M.A. Mycek, "Models of light propagation in human tissue applied to cancer diagnostics," *Technology in Cancer Research & Treatment*, 10(2):121–134 (2011).

[8] Q. Liu and N. Ramanujam, "Sequential estimation of optical properties of a two-layered epithelial tissue model from depth-resolved ultraviolet-visible diffuse reflectance spectra," *Applied Optics*, 45(19):4776–4790 (2006).

[9] M.N. Kholodtsova, V. Loschenov, C. Daul and W. Blondel "Spatially and spectrally resolved particle swarm optimization approach to increase precision in optical properties estimation by means of tissular diffuse-reflectance spectroscopy", *Optics Express*, 24(12):12682-12700 (2016).

[10] X. Chen, F. Yuanming, L. Xiaohui, D. Jue, D. Yong and H. Xin-Hua, "Fast method for inverse determination of optical parameters from two measured signals," *Optics Letters*, 38(12):2095–7 (2013).

[11] M. Sharma, R. Hennessy, M.K. Markey and J.W. Tunnell, "Verification of a two-layer inverse monte carlo absorption model using multiple source-detector separation diffuse reflectance spectroscopy," *Biomedical Optics Express*, 5(1):40–53 (2013).

[12] E. Alerstam, W. Lo, T. Han, J. Rose, S. Andersson-Engels and L. Lilge, "Next-generation acceleration and code optimization for light transport in turbid media using gpus," *Biomedical Optics Express*, 1(2):658–675 (2010).

[13] R. Reif, O. A'Amar and I.J. Bigio, "Analytical model of light reflectance for extraction of the optical properties in small volumes of turbid media," *Applied Optics*, 46(29):7317–7328 (2007).

[14] M. Juger, F. Florian and K. Alwin, "Application of multiple artificial neural networks for the determination of the optical properties of turbid media," *Journal of Biomedical Optics*, 18(5):57005 (2013).

NEAR INFRARED IMAGING FOR ANGIOGRAPHY IN DIABETIC FOOT

Z. N. Abdulvapova[1], P.V. Grachev[2], O.N. Bondarenko[1], G.R. Galstyan[1]

[1] Endocrinology Research Centre, *Russia, Moscow*
[2]A.M. Prokhorov General Physics Institute RAS *Russia, Moscow*
E-mail address: zera1987@mail.ru

Abstract
Current Modern methods for lower limb ischemia (LLI) assessment have a number of limitations in the use in diabetic patients. Indocyanine green (ICG) fluorescence angiography (ICGA) is a new technique in assessing the perfusion disturbance in LLI.

Introduction
Noninvasive assessment of lower limb circulation is a cornerstone in the evaluation of the severity of PAD. In clinical settings, ankle pressure (AP), toe pressure (TP), and indices derived from their comparisons with arm pressure, as well as transcutaneous oxygen tension (tcpO2) and skin perfusion pressure (SPP), are currently available for measuring lower limb hemodynamics, the first two reflecting only the severity of arterial occlusive disease and the latter two local perfusion as well. In addition, tcpO2 and SPP may be measured at different, predetermined sites. Both of these methods, however, are limited in their applicability. Measurements can only be taken of the healthy area surrounding foot ulcers, and attachment of the probes is likely to be successful only on flat surfaces. Furthermore, the probes cannot be applied directly onto the ulcer [1]. Indocyanine green (ICG) fluorescence angiography (ICGA) is a new technique in assessing the perfusion disturbance in limb ischemia.

Materials and Methods: This study was performed in 4 diabetic patient with limb ischemia and foot ulcers. The principle of fluorescence imaging used in ICGA is simple: illuminate the tissue of interest with light at the excitation wavelength 785nm while observing it at longer emission wavelengths (810-850nm). The device is equipped with a 785-nm light-emitting diode (LED) as an excitation light source and a charge-coupled device (CCD) camera covered with a lens and filter set. Real-time fluorescence images were displayed on a monitor and recorded using the digital image processing method of the audio video interweave system. To evaluate the ICGA tests, multiple parameters were obtained and analyzed to assess the perfusion. These parameters included time of ICG intravenous injection (T_0), onset of basal intensity (T_{bas}), onset to maximum intensity from T_0 (Tmax0), onset to maximum intensity from T_{bas} ($Tmax_{bas}$), time from the onset to the end of intensity ($Tend_{bas}$) level of basal intensity (I_b), level of maximum intensity (Imax), the rate of intensity increase from baseline to peak intensity over time (IngR), the area under the curve of intensity over time (curve integral), the intensity at the end of the study (E_I), the magnitude of intensity decrease from peak intensity to the end of the study (En), the rate of intensity decrease from peak intensity to the end of the study (EnR) (Fig1). This parameters were assessed in several regions of interest (ROI): ROI 1, distal region of the first metatarsal bone, ROI 2; distal region of the forth metatarsal bone; ROI 3, the dorsum of the foot from the Chopart joint to the Lisfranc joint, ROI 4 - 5 cm below the medial epicondyle (Fig2.). Each region was 1,5x1,5 cm in size.

Results
There were not any adverse reactions during ICGA procedure. Data from all ROI with different ICGA parameters was collected. There were difference in Tmax0 and $Tmax_{bas}$ in different ROI more than 10 sec. Ongoing studies with patient recruitment database and ICGA parameters.

Conclusions
Foot wounds can be healed only with an appropriate level of blood supply and limb salvage efforts rely heavily on perfusion to lower limb. ICGA provides rapid qualitative visual and quantitative information about regional foot perfusion. Future study may include pre- and postdebridement and post closure site tissue viability, pre- and post-vascular intervention

levels of arterial flow, lower extremity flap viability and comparisons to the transcutaneous partial pressure of oxygen test as well as other noninvasive hemodynamic measurements.

Fig.1 ICGA test's parameters.

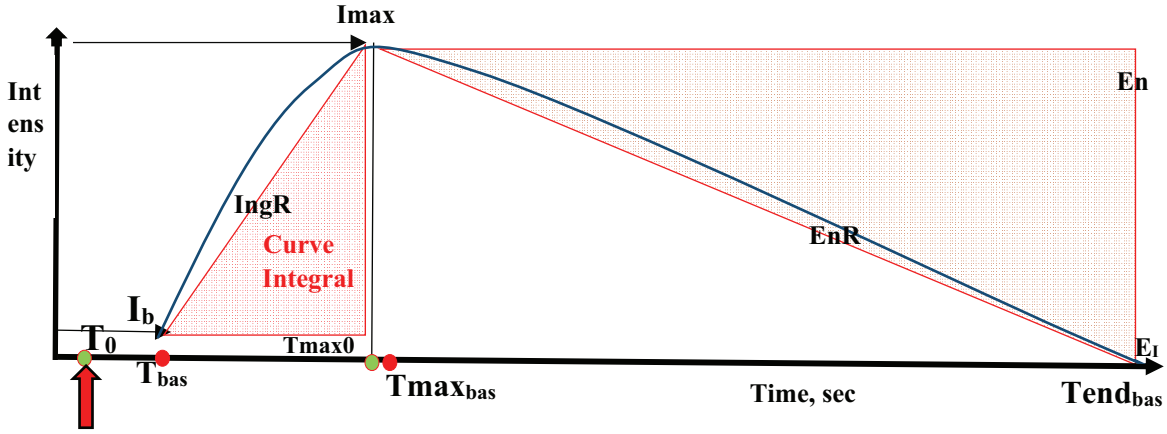

Fig 2. Regions of interest for ICGA test.

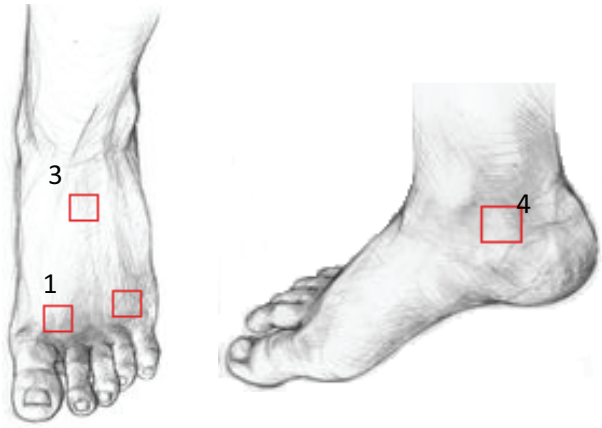

Fig 3. ROI of patient 1 and its parameters.

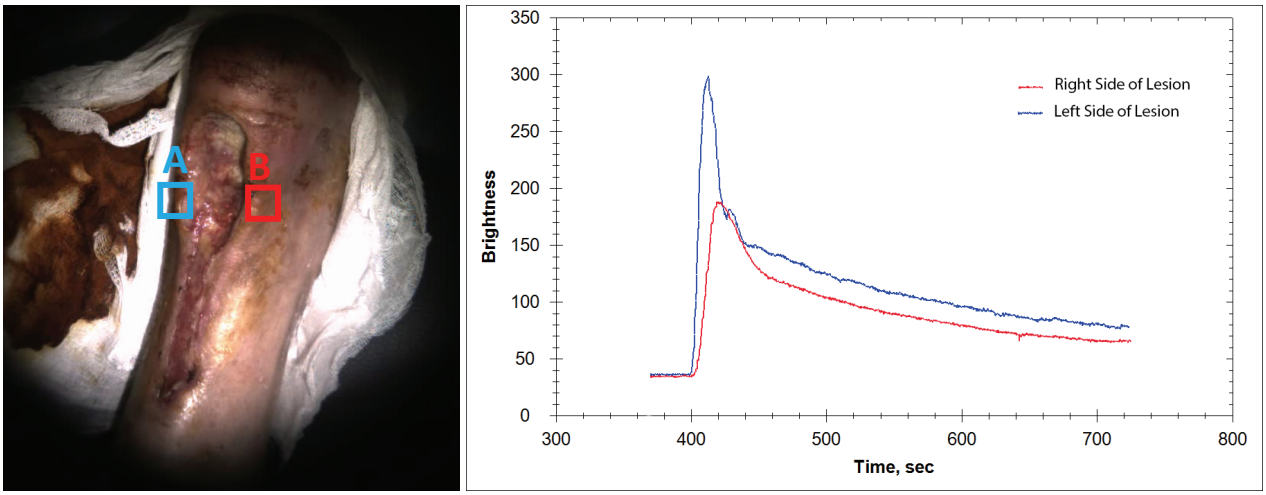

References

1. Terasaki H. et al. A quantitative method for evaluating local perfusion using indocyanine green fluorescence imaging //Annals of vascular surgery. – 2013. – Т. 27. – №. 8. – С. 1154-1161.

Photodynamic Therapy of Gonarthrosis with Fotoditazin

Zharova T.A.[1], Ivannikov S.V.[1], Tonenkov A.M. [1], Stranadko E.Ph.[2], Semenova L.A.[3], Smorchkov M.M.[4], Makarov V.I.[5], Romanishkin I.D.[5], Ryabova A.V.[5,6], Loschenov V.B.[5,6]

[1] I.M. Sechenov First Moscow State Medical University, Trubetskaya st., 8-2, Moscow 119991, Russia
[2] SSC Laser Medicine FMBA of Russia, Studencheskaya st, 40, Moscow, 121165, Russia
[3] V.A. Nasonova Scientific Research Institute of Rheumatology, Russian Academy of Medical Sciences, Kashirskoye Highway, 34A Moscow, 115522, Russia
[4] N.N. Priorov Central Research Institute of Traumatology and Orthopedics, Russian Federation Ministry of Health, Priorov st., 10, Moscow, 127299, Russia
[5] A.M. Prokhorov General Physics Institute, Russian Academy of Sciences. Vavilov Str., 38, Moscow, 119991, Russia
[6] National Research Nuclear University MEPhI (Moscow Engineering Physics Institute), Kashirskoe highway, 31, Moscow, 115409, Russia

Introduction

Degenerative-dystrophic changes of joints represent themselves as one of numerous and serious groups of locomotorium diseases. Osteoarthrosis is a group of diseases of different etiology that are based on causing harm to all of the joint components (cartilage, subchondral bone, synovial membrane, capsule, ligaments, periarticular tissue).

Materials and research methods

The experimental research is conducted with application of the model of posttraumatic gonarthritis on 35 rabbits-males (*Chinchilla* breed). Specific features of Chlorin e6 derivatives (Ce6) photosensitizer (PS) accumulation in tissues of a knee joint and efficiency of photodynamic therapy (PDT) at gonarthritis treatment are studied experimentally. By the method of fluorescent spectroscopy it is revealed that maximum amount of Ce6 is accumulated in a synovial membrane of a damaged knee joint of a rabbit 2.5 hour after its intravenous introduction (at Ce6 dose of 1.25 mg/kg). PDT was carried out with application of laser irradiation with wavelength of 662 nm. Intra-joint irradiation methods were applied. The area of the target was equal to 1.0 cm^2 at energy density in joint tissues of 240-300 J/cm^2.

Results

On the basis of the analysis of dynamics of Ce6 accumulation in the inflamed tissue of various compartments of a knee joint it is revealed that the maximum concentration of a Ce6 is registered 2.5 hour after introduction.

Fluorescent diagnostics in tissues of a knee joint with Ce6 can be used in clinical practice at gonarthritis before, during and after PDT for monitoring of Ce6 accumulation and treatment control.

Optimal radiation energy density was determined, which was 150 J/cm^2. In the studied time intervals (5-25 minutes) no dependency of PDT effect on irradiation time at the same energy density was observed.

Chlorin series PS is promising and can be used to treat gonarthritis in clinics.

Spectral-Temporal Pulse Construction for Optimal Nonlinear Raman Brain Imaging

E.A.Stepanov[1,2], A.A.Lanin[1,2], D.A.Sidorov-Biryukov[1,2], A.B.Fedotov[1,2], A.M.Zheltikov[1,2,3,4]

[1] *Physics Department, International Laser Center, M.V. Lomonosov Moscow State University, Moscow 119992, Russia*
[2] *Russian Quantum Center, ul. Novaya 100, Skolkovo, Moscow Region, 143025 Russia*
[3] *Department of Physics and Astronomy, Texas A&M University, College Station, TX 77843, USA*
[4] *Kurchatov Institute National Research Center, pl. akad. Kurchatova 1, Moscow 123182, Russia*
Author e-mail address: ea.stepanov@physics.msu.ru

Abstract: In the present work, we propose efficient strategies of pulse-width optimization applicable for nonlinear Raman brain imaging. Ultrashort laser pulses with the spectral bandwidth, accurately matched against the bandwidth of molecular vibrations, are shown to provide a higher power of the total signal without reducing the sensitivity of tumor detection in brain tissues.

1. Pulse-width considerations for nonlinear Raman brain imaging

The past few years have witnessed a breakthrough in the development of SRS microscopy as an innovative approach for microscopy and bioimaging [1, 2]. In neuroscience, nonlinear Raman scattering offers an attractive alternative to fluorescent-protein-based approaches to brain imaging. While CARS microscopy has been shown to hold much promise as a rapid, minimally invasive technique for molecular specific intraoperative optical diagnostics of brain lesions [3], SRS has been demonstrated to enable the fast label-free detection of brain tumors [4]. The Raman probing of molecular vibrations in some of the complex biological systems, such as the brain, may benefit, as we show below in this paper, from laser pulses with broader bandwidths, dictating the choice of femtosecond laser sources. With the spectral bandwidth of laser pulses accurately matched against the bandwidth of molecular vibrations, the coherent Raman signal will be shown to be radically enhanced, enabling higher sensitivities and higher frame rates in nonlinear Raman brain imaging [5].

In our scheme of SRS microscopy we detect the Raman-induced loss that the pump field experiences as a result of interaction with the Stokes field while passing through a sample. The relative SRS gain measured in this scheme, with the pump wave serving as a local oscillator, is given by

$$R \propto \int Re\left\{A_p(t)\left[A_s(t)\int_{-\infty}^{t} A_p(\theta)A_s^*(\theta)h(t-\theta)d\theta\right]^*\right\}dt$$

where A_p and A_s are the amplitudes of the input pump and Stokes fields, respectively, and h(θ) is the Raman function. In figure 1, we plot the SRS loss signal R calculated as a function of the driver pulse width $\tau \approx \tau_p \approx \tau_s$, τ_p and τ_s being the pump and Stokes pulse widths, with the Raman function calculated in such a way as to match the Raman spectra of the white matter, cortex, and xenografts human brain tumor in a mouse brain [4].

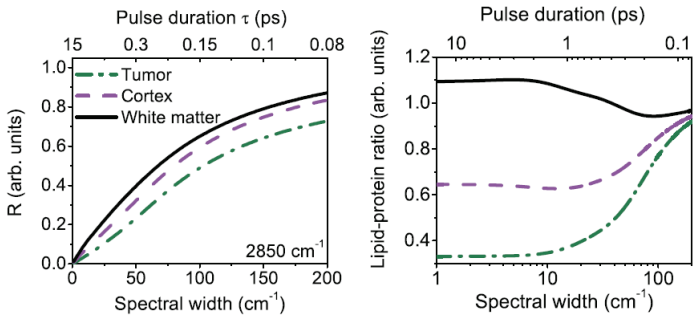

Figure 1. (Left) The SRS loss signal at the frequency of the lipid peak, $\Omega_l \approx 2850$ cm−1, calculated as a function of the pulse width and (right) The ratio R_l/R_p of the lipid SRS loss signal to the protein SRS loss signal calculated as a function of the pulse width for the white matter (solid line), cortex (dashed line), and xenografts human brain tumor (dashed–dotted line) in a mouse brain.

The total SRS loss signal is seen to increase with the pulse bandwidth (figure 2 (left)), τ^{-1}, as long as τ^{-1} remains smaller than the bandwidth Γ of a molecular vibration that dominates the Raman spectrum, saturating when τ^{-1} becomes larger than Γ. A high level of the total signal is, however, not sufficient for chemically specific imaging. The reliable detection of brain tumors requires not only a strong overall signal, but also a large difference between the signals from a tumor and a normal brain tissue. We suggest a method for the detection of this tumor by measuring the ratio R_l/R_p of the lipid SRS loss signal at $\Omega_l \approx 2850$ cm^{-1} to the protein SRS loss signal at $\Omega_p \approx 2930$ cm^{-1} and comparing the results of these measurements to the R_l/R_p ratio typical of a normal brain tissue. In figure 1 (right), we present the ratio R_l/R_p calculated as a function of the pulse width for the white matter (solid line), cortex (dashed line), and xenografts human brain tumor (dashed − dotted line) in a mouse brain. As long as the pulse width is longer than 500 fs, as our analysis shows, shorter pulses will give rise to a higher power of the total signal without reducing the R_l/R_p ratio, quantifying the sensitivity of tumor detection in brain tissues.

2. Spectroscopic analysis of complex multicomponent systems

In our SRS imaging experiments, we use transform-limited pump and Stokes pulses with pulse widths of 150 and 200 fs. Such ultrashort pulses inevitably impose limitations on the spectral resolution in nonlinear-optical microspectroscopy, making it difficult to resolve closely lying and overlapping lines in Raman spectra. However, the coherence of laser pulses suggests attractive solutions to this problem, allowing the spectral resolution of nonlinear microspectroscopy to be substantially improved by pulse chirping. A linear chirp defines a one-to-one map relating the frequency to the delay time τ between the laser pulses. With this map defined, the spectrum of a Raman-active mode can be found by measuring the intensity of the nonlinear Raman signal as a function of τ [6].

Linearly chirped pump and Stokes pulses used in our SRS spectroscopic experiments had pulse widths $T_{pu} \approx 3.7$ ps and $T_{st} \approx 3.2$ ps. The chirp parameter was adjusted by varying the distance between the diffraction gratings in the stretchers, providing a spectral resolution of about 6 cm^{-1}, which is 17 times higher than the spectral resolution (100cm^{-1}) attainable in the scheme with transform-limited pulses of the same pulse width. This offers a powerful tool for a reliable identification of molecular vibrations with close frequencies, enhancing the chemical selectivity of spectroscopic analysis of complex multicomponent systems [7].

3. Acknowledgments

This work was supported by the Russian State Targeted Program ‘Research and Development in Priority Areas of Development of the Russian Scientific and Technological Complex for 2014–2020’ (Contract 14.607.21.0092 of November 21, 2014; unique identifier of applied research: RFMEFI60714X0092).

4. References

[1] C. W.Freudiger et al, “Label-free biomedical imaging with high sensitivity by stimulated Raman scattering microscopy”, Science **322** 1857-1861 (2008)

[2] Y. Ozeki et al, “High-speed molecular spectral imaging of tissue with stimulated Raman scattering”, Nature Photonics **6**, 845–851 (2012)

[3] C.L. Evans et al, “Chemically-selective imaging of brain structures with CARS microscopy”, Optics Express **15**, 12076-12087 (2007)

[4] Ji Minbiao et al, “Rapid, Label-Free Detection of Brain Tumors with Stimulated Raman Scattering Microscopy”, Sci Transl Med **5**, 201ra119 (2013);

[5] A. A. Lanin, E. A. Stepanov, R. A. Tikhonov, D. A. Sidorov-Biryukov, A. B. Fedotov and A. M. Zheltikov, “Pulse-width considerations for nonlinear Raman brain imaging: whither the optimum?”, Laser Phys. Lett. **12** 115401 (2015)

[6] A. A. Lanin, E. A. Stepanov, R. A. Tikhonov, D. A. Sidorov-Biryukov, A. B. Fedotov and A. M. Zheltikov, “Multimodal nonlinear Raman microspectroscopy with ultrashort chirped laser pulses”, JETP Letters, **101**, 593–597 (2015)

[7] A. A. Lanin, E. A. Stepanov, R. A. Tikhonov, D. A. Sidorov-Biryukov, A. B. Fedotov and A. M. Zheltikov, “A compact laser platform for nonlinear Raman microspectroscopy: multimodality through broad chirp tunability”, J. Raman Spectrosc., doi: 10.1002/jrs.4860 (2016)

Near-IR Laser Heating of Rare-Earth Doped Composite Nanoparticle Colloids

I.R. Romanishkin[1], Y.V. Orlovskii[1,2], I.A. Burmistrov[3], D.V. Pominova[1], A.S. Vanetsev[1], E.O. Orlovskaya[1], A.V. Ryabova[1,4].

[1] A.M. Prokhorov General Physics Institute RAS, 38 Vavilov Str., 119991, Moscow, Russia

[2] Institute of Physics, University of Tartu, 14c Ravila Str., 50411, Tartu, Estonia

[3] M.V. Lomonosov Moscow State University, 1 Leninskie Gory, 119991, Moscow, Russia

[4] National Research Nuclear University MEPhI (Moscow Engineering Physics Institute), Kashirskoe Highway, 31, 115409, Moscow, Russia

Email: igor.romanishkin@gmail.com

Abstract: Hyperthermia is a potent method of cancer treatment. In this study we investigated the spatial heating effect of composite $DyPO_4$-covered nanogold and Nd^{3+}-doped LaF_3 nanoparticles under continuous-wave and repeating-pulse laser excitation. The results showed higher laser-to-temperature conversion effectiveness for nanoparticles with gold core.

Keywords

Hyperthermia treatment, thermal measurements, composite nanoparticles, plasmon nanoparticles, rare-earth ions

1. Introduction

The hyperthermia treatment is known as an auxiliary method for cancer treatment that increases the effectiveness of chemo- and radiotherapy. However, with the application of specific agents and the proper method of their excitation, it is possible to cause targeted thermal damage directly to cancer cells or even their organelles. Such precise effect requires releasing high amount of heat in the close vicinity of the hyperthermia agent for a very short time.

Rare-earth doped crystal nanoparticles present a novel approach for achieving hyperthermia viable temperatures [1]. Their narrow absorption bands allow for high selectivity of excitation. Wide phonon spectrum of the host lattice which is usually avoided in rare-earth utilization provides the means of multiphonon relaxation that heats the surrounding environment. Involved in this study $DyPO_4$ has been shown to provide temperatures suitable for hyperthermia in short time under laser excitation [2].

2. Materials and Methods

In this study we investigate the spatial heating capabilities of two types of composite colloids: $DyPO_4$-covered Au nanoparticles and LaF_3:Nd^{3+} (1%) nanoparticles. The studied gold nanoparticles were of two separate types – cylinder and star shaped. Gold star nanoparticles had absorption maximum at 535 nm, while gold cylinder nanoparticles had absorption maxima at 556, 705, 900 and 1030 nm. Absorption spectrum of $DyPO_4$ has distinct peaks at 760, 811 and 914 nm (Fig.1).

LaF_3:Nd^{3+} particles were also of two types and differed by the $DyPO_4$ covering layer thickness. During sample preparation the existing colloids were diluted 10 times with distilled water. Another set of samples was prepared with the addition of 1.6% Lipofundin® fatty emulsion to simulate scattering properties of biological tissue. A phantom of 1.6% Lipofundin® without the particles was also prepared.

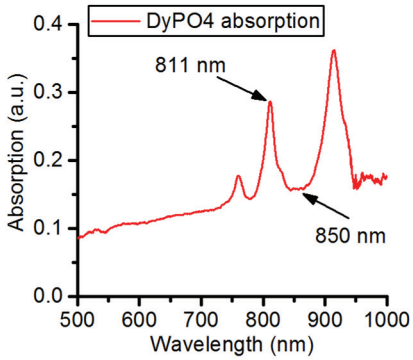

Fig.1. Absorption spectrum of the $DyPO_4$ sample at room temperature. Wavelength of 811 nm corresponds with $^6H_{15/2}$ - $^6F_{5/2}$ transition in Dy^{3+} whereas 850 nm was taken as reference.

The experiment was conducted in two parts: first to measure spatial temperature increase under continuous wave laser excitation, and last – to measure the wavelength selectivity of rare-earth excitation for the investigated composite particles.

The first stage consisted of excitation of 1 ml of the sample using 805 nm diode laser. The laser light was being delivered using an optical fiber. The illuminated sample was located in quartz cuvette with square base with 1 cm side. The depth of the sample was also 1 cm. The temperature measurements were taken from the side of the cuvette using CEDIP JADE MWIR SC7300M thermal camera. The sample was irradiated by laser for 3 minutes for every measurement.

For the second part the prepared samples were excited using the adjustable femtosecond laser Coherent Ultra II at 811 nm ($^6H_{15/2}$ - $^6F_{5/2}$ transition in Dy^{3+}) and 850 nm (for comparison), and with adjustable power. The 1 mm thick sample was pressed between two pieces of microscope cover glass and prevented from leaking out using a rubber liner. The excitation was conducted from underneath the sample with the laser spot equal to 10 um in diameter. The temperature increase was measured from the top of the sample using the thermal camera. The sample was illuminated during one minute for every measurement.

3. Results and Discussions

For spatial heating under 805 nm laser excitation the temperature rise was averaged per minute of laser irradiation due to the linear heating kinetics. The gold nanoparticles have shown to be 4 (for star shaped) and 18 (for cylindrical) times as effective as rare-earth composite particles in water solution. On the other hand, due to high scattering in 1.6% fatty emulsion the ratios have been 2 and 5 (for stars and cylinders respectively). In addition to that, the heating effectiveness for gold particles in the emulsion was 20% lower than in water.

On the other hand, in case of the femtosecond laser irradiation the kinetics was non-linear and the temperature reached steady-state within the experiment time, so the heating effectiveness was calculated from the total temperature change during the experiment. The heating effectiveness for gold particles was measured to be 1.4 higher when exciting the Dy^{3+} transition band for both particle types compared to illuminating with 850 nm laser. However, the temperature rise from cylindrical particles was 2.2 times higher than from the stars. The spatial temperature rise from rare-earth particles has been roughly the same for both wavelength and was 34 times less than for gold.

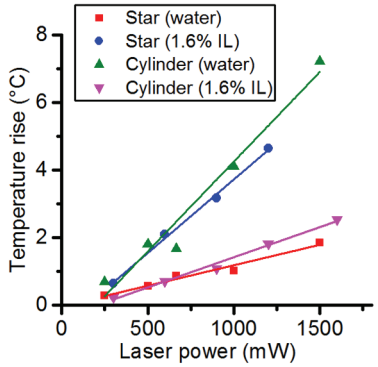

Fig.2. Temperature rise in composite nanoparticles with gold core after excitation using continuous wave laser at 805 nm. The types of nanoparticles studied had either cylinder or star core shape. The type of medium used is represented in parenthesis, with 1.6% IL being 1.6% fatty emulsion

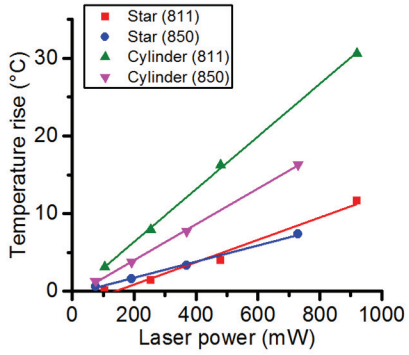

Fig.3. Temperature rise in colloid of composite nanoparticles with gold core after excitation using femtosecond laser pulses. The types of nanoparticles studied had either cylinder or star core shape and the excitation was conducted at 811 and 850 nm (denoted in parenthesis).

4. Conclusions

The experiment has shown the $DyPO_4$-covered gold nanoparticles to be several times more effective in laser-to-heat conversion with regards to spatial heating process compared to $DyPO_4$-covered Nd^{3+}-doped LaF_3 nanoparticles. At the same time, using gold core nanoparticles greatly reduces spectral selectivity of the studied excitation method compared to earlier results for rare-earth doped particles where the temperature difference between 811 nm and 850 nm laser excitation was more than 11 times higher.

5. Acknowledgement

This work is supported by MES RFMEFI61615X0064.

6. References

[1] EC Ximendes, U Rocha, KU Kumar, C Jacinto, D Jaque. “LaF3 core/shell nanoparticles for subcutaneous heating and thermal sensing in the second biological-window”, Applied Physics Letters 108 (25), 253103.

[2] Yu.V. Orlovskii, A.S. Vanetsev, I.D. Romanishkin, A.V. Ryabova, K.K. Pukhov, A.E. Baranchikov, E.V. Samsonova, K. Keevend, I. Sildos, V.B. Loschenov, "Laser heating of the $Y_{1-x}Dy_xPO_4$ nanocrystals," Opt. Mater. Express 5, 1230-1239 (2015)

Combined Spectroscopic Technique in Low-grade Glioma Neurosurgery Navigation

Savelieva T.A.[1, 2], Goryainov A.A.[3], Potapov A.A.[3]

[1] *A.M. Prokhorov General Physics Institute, Moscow, Russia*

[2] *National Research Nuclear University MEPhI (Moscow Engineering Physics Institute), Moscow, Russia*

[3] *N.N. Burdenko Neurosurgery Institute, Moscow, Russia*

e-mail: savelevat@gmail.com

Abstract: The method for the simultaneous *in vivo* analysis of fluorescence, scattering and absorption of brain tissues in adjacent spectral ranges from 500 to 800 nm is proposed. It helps to delineate low-grade glial tumors with low accumulation of fluorescent tumor marker by using other spectroscopic characteristics of tumor tissues.

Keywords:

Laser-tissue interaction, biophotonics, optical scattering, fluorescence, optical spectroscopy, LGG, glioma, neurosurgery

1. Background

Fluorescent navigation during resection of low-grade glioma (LGG) is not always a successful strategy. The reason for this lies in the low accumulation of the fluorescent marker (as a rule the 5-ALA induced protoporphyrin IX is used) in the tissues of benign gliomas. However, the optical navigation techniques are extremely convenient for microsurgery. These two factors motivate the high importance of developing a method of combined analysis of several optical characteristics of low-grade glial tumors.

2. Materials and methods

In this report we propose a method for the simultaneous in vivo analysis of fluorescence, scattering and absorption of brain tissues in adjacent spectral ranges from 500 to 800 nm. Detailed description of device is given in one of our previous article [1]. The specific features of its application to LGG, particularly the structure and biochemistry of the tumors that affect the spectral signal, are described. The method was used in the N.N. Burdenko Neurosurgery Institute on 13 patients with LGG. The results of spectroscopic analysis were confirmed by histological examination.

3. Results

Absence of fluorescence signal was observed in 6 patients, while the other spectroscopic features of tumor changes were present.

One of the interesting results was a negative correlation (-0.75) between the fluorescence level (the ratio of the fluorescence signal to the intensity of the backscattered laser signal was used as a fluorescence index) and tissues' light scattering (Fig.1 left). This means that the optical density of tumor tissues is lower than normal in case of low-grade glial tumors. Scattering signal from center of tumor was lower in average in two times than from normal white matter.

It was proposed a model of pathological changes, which explains this observation. The tumor is characterized by active growth, which leads to a high degree of vascularization of tissues and, consequently, improves blood supply to the tissues. We can observe it spectroscopically by increasing of the absorption coefficient. Thus there is a number of structural changes, namely, the displacement and the degradation of myelinated nerve fibers, growth of a size and number of nuclei, and mitochondria degradation. All these

changes have different effects on the optical scattering properties of tissue. Degradation of nerve fibers leads to a reduction of large scale scatterers in tissue as well as mitochondria degradation. At the same time the increasing of the size and number of nuclei has the opposite effect on the optical scattering coefficient. Thus, at various stages of tumor development its scattering coefficient varies non-monotonically. But it is always lower than the scattering coefficient of normal tissues.

In our study we also obtain a positive correlation (0.43) between the level of tissue oxygenation and the degree of light scattering (Fig.1 right). This is because the active growth of tumor causes hypoxia and switch cell metabolism to glycolysis.

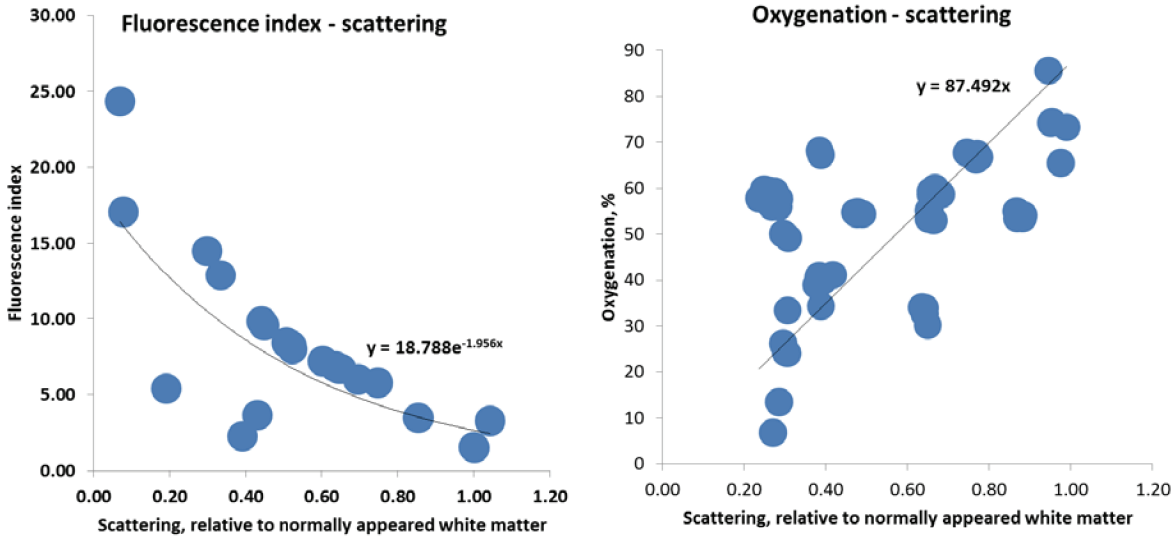

Fig.1. Fluorescence index – scattering diagram registered spectroscopically *in vivo* for one patient with gemistocytic astrocytoma (left); oxygenation – scattering diagram registered spectroscopically *in vivo* for one patient with oligoastrocytoma (right).

A mathematical model has been developed that takes into account all the changes described above. Modeling the interaction of light with individual scatterers of different shapes and sizes was carried out using a Mie solution for spheres and cylinders. Tissue absorption coefficients for modeling were based on published data on the optical properties of blood, as well as information on the blood oxygenation and blood filling obtained during the *in vivo* experiments. The Monte-Carlo simulation algorithm was developed to model the light propagation in media described by the mathematical models introduced above. Detailed description of this algorithm is given in one of our previous article [2]. The comparison of simulation results with experimental data showed the correctness of the mathematical model of combined spectroscopic signal formation and diagnostic value of combined spectroscopic technique.

4. References

[1] Savelieva T.A., Loshchenov V.B., Goryainov S.A., Shishkina L.V., Potapov A.A., "A spectroscopic method for simultaneous determination of protoporphyrin IX and hemoglobin in the nerve tissues at intraoperative diagnosis," Russian Journal of General Chemistry 85(6):1549-1557 (2015).

[2] Savelieva T.A., Kalyagina N.A., Kholodtsova M.N., Potapov A.A., Goryainov S.A., Loschenov V.B. "Numerical modelling and in vivo analysis of fluorescent and laser light backscattered from glial brain tumours" (SPIE Proceedings, Vol. 8230, 82300, 2012), L-1-L9.

This work was supported by the Competitiveness Programm of NRNU MEPhI.

The Development of methods for fluorescence imaging in theranostics oncological disease.

Filonenko EV*, Kaprin AD*, Urlova AN*, Loschenov MV**

* *National Medical Research Radiological Centre of the Ministry of Health of the Russian Federation*

** *Laboratory of laser biospectroscopy, Prokhorov General Physics Institute of the RAS, Moscow*

derkul23@uyandex.ru

Abstract.

In the presented work we have described main methods for fluorescence imaging in theranostics oncological disease, which are as follows: visually assessed fluorescence diagnosis, fluorescence spectroscopy and fluorescence navigation.

Keywords.

Fluorescence diagnosis, cancer, fluorescence spectroscopy, fluorescence navigation.

Introduction.

Detection of early cancer, intraoperative assessment of tumor boards and real-time control of efficacy of photodynamic therapy represent a very important medical problem. Methods of fluorescence diagnosis (FD) with photosensitizers have been used in detection of early cancer and assess tumor boards on the surface of skin and mucosa. There are two main methods for assessment of fluorescence imaging: visually and by values of diagnostic parameter from fluorescence spectroscopy. Visual assessment and fluorescence spectroscopy have their limitations such as the subjective nature of interpretating color density of the images and time-consuming calculation of diagnostic parameter. We studied FD with 5-aminolevulinic acid (5-ALA) in patients with skin, laryngeal, bladder cancer and lesions of central nervous system and female reproductive organs using these methods.

Materials and methods.

For FD we used 5-ALA given per os in the form of aqueous solution at a dose of 20–30 mg/kg body weight 3 h before procedure. Equipment produced by company “Karl Storz” (Tuttlingen, Germany), “Olympus” (Japan) was used for imaging under blue light excitation. Video-assisted fluorescent light-emitting diode device UFF-630/675-01 produced by company “BIOSPEK” (Moscow, Russia) was used during the endoscopy. Laser electron-spectrum analyzer for FD (LESA-01) by “BIOSPEK” (Moscow, Russia) with a wavelength of laser source at 632.8 nm and recoding spectrum of fluorescence in the range from 635 up to 800 nm was used to register local fluorescence spectrum. During local fluorescence spectroscopy 5–65 spectra were recorded in every patient. The values of diagnostic parameter (DP) were calculated and recorded in all cases. The values of DP were taken from several parts of the tumor under visual detection of fluorescence, after that the average value was calculated for each tumor. DP was calculated automatically by a special program as a ratio of the peak area of PpIX (690–720 nm) to the area of the reflected laser light (620–640 nm) and represented indirectly evidence of the Alasens-induced PpIX accumulation in the tissues. Fluorescence spectra of Alasens-induced PpIX in the intact tissue were recorded with the determination of the fluorescent contrast of neoplastic/normal tissue. Fluorescence imaging for navigation in photosesnsitized tissues during photodynamic therapy for malignant tumors in patients was performed with novel device which consisted of 2 light sources: one LED based white light source and another laser diode based source for fluorescence excitation at 635nm.

Results.

Thus, the study showed that sensitivity and specificity of fluorescence diagnosis with visual evaluation of fluorescence with 5-ALA were up to 97% and 78%, respectively. Complementation of this method by local fluorescence spectroscopy allows increasing the specificity. Fluorescence navigation of photosensitized tumors offers to detect malignant tumors and its borders by visual assessment of tumor and diagnostic parameter simultaneously and to perform treatment control on a real-time basis.

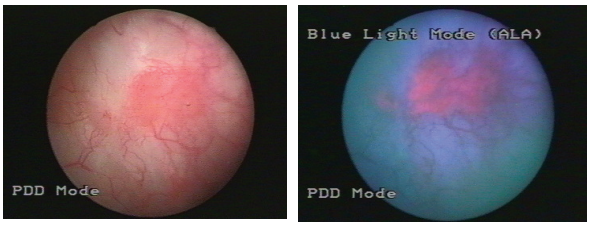

Fig. 1. Fluorescence diagnosis in patient with bladder cancer.

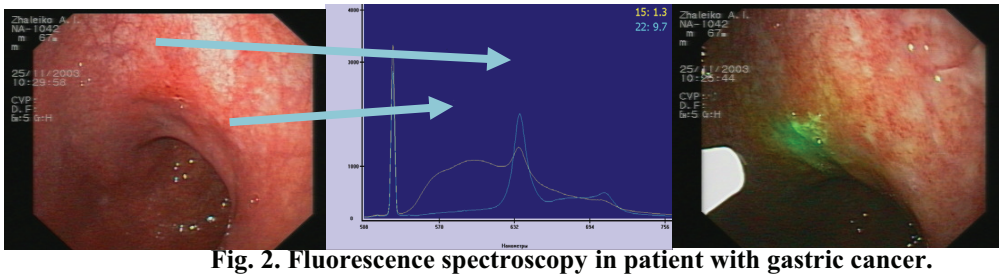

Fig. 2. Fluorescence spectroscopy in patient with gastric cancer.

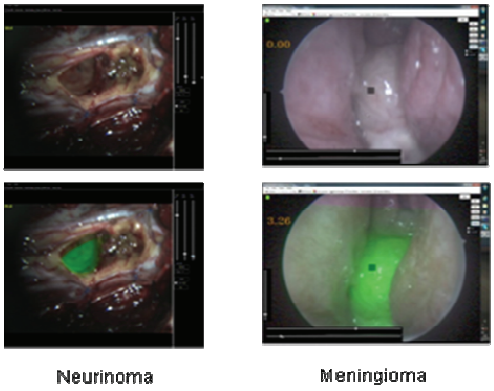

Fig. 3. Examples of fluorescence navigation in clinical conditions

References.

[1] Filonenko EV, Sokolov VV, Chissov VI, Lukyanets EA, Vorozhtsov GN. Photodynamic therapy of early esophageal cancer. Photodiagnosis and Photodynamic Therapy 2008 Sep;5(3): 187-91.

[2] Filonenko E.V. Flyuorestsentnaya diagnostika i fotodinamicheskaya terapiya – obosnovanie primeneniya i vozmozhnosti v onkologii (Fluorescence diagnostics and photodynamic therapy: justification of applications and opportunities in oncoligy). *Fotodinamicheskaya terapiya i fotodiagnostika.* 1, 3-7 (2014).

[3] Loshchenov, M., Zelenkov, P., Potapov, A., Goryajnov, S., & Borodkin, A. (2014). Endoscopic fluorescence visualization of 5-ALA photosensitized central nervous system tumors in the neural tissue transparency spectral range. Photonics & Lasers in Medicine, 3(2), 159-170.

DEVELOPING ALGORITHMS AND SOFTWARE FOR FLUORESCENCE IMAGING OF INTRACAVITARY ORGANS

Anam A. A., Loshchenov M. V.

National Research Nuclear University "MEPhI", Moscow, Russia

Laboratory of laser biospectroscopy, Prokhorov General Physics Institute of the RAS, Moscow.

ahmedanam@mail.ru, maxvl2000@gmail.com

Abstract: Fluorescence diagnosis is one of the most effective methods for detection of oncology diseases in early stages. That is why it is necessary to develop a software program which will provide all functionality for conducting this kind of experiments. Usually digital camera is used when this kind of experiments are being conducted. Under this circumstance a program primarily must interact with digital camera. The purpose of this research was making multifunction software for fluorescence diagnostics and imaging of fluorescent biotissues. This program should work under Windows OS and it should be made with using WPF (Windows Presentation Foundation). There are four main functions that the program must include: 1) displaying video stream; 2) saving video in a file; 3) registering single image in HDRI (high dynamic range imaging) mode; 4) calculating photosensitizer concentration by its image.

Introduction. Software development for biophisics use is in high demand in the novel science and R'n'D, especially in the area of fluorescence diagnostics where software has to work for both data acquisition from various devices and analytics implementing mathematic and image processing algorithms. So, we intended to create software for fluorescence imaging of photosensitized bio-tissues using modern technology for building applications. The main purpose of the software is to measure the fluorescence signal and convert it into the photosensitizer concentration with presence of: insufficient dynamic range of the registering device and ambient light. At the same time our program has to satisfy some conditions: 1) It should work quickly; 2) It should have simple and clear interface; 3) It is necessary to minimize user participations in all calculations (a user should click a button and get result).

Aim. Creating multifunction software for fluorescence imaging of intracavitary organs.

Materials and methods. WPF (Windows Presentation Foundation) is being used for building our application [1]. Programming language is C# [2]. Software is being developed in Microsoft Visual Studio.

Results. The result of this research is application that has been called "SFD" (Software for Fluorescence Diagnosis). SFD consists of four tabs: 1) Basic; 2) HDRI stack; 3) Stroboscope; 4) Calculations (Fig. 1).

Interface of basic tab can be divided into two parts: HDRI and recording video. HDRI part is need to receive an image with high dynamic range. It is necessary when digital camera is registering scene that has details with huge difference of intensity. In a resulting image all details can be distinguished. Recording video is also useful function.

The algorithm make up three stages: 1) Getting a certain number of images from camera; 2) Filtering these images; 3) Union filtered images. So, in HDRI stack tab you can see filtered image and a resulting image with high dynamic range (it is in the red frame).

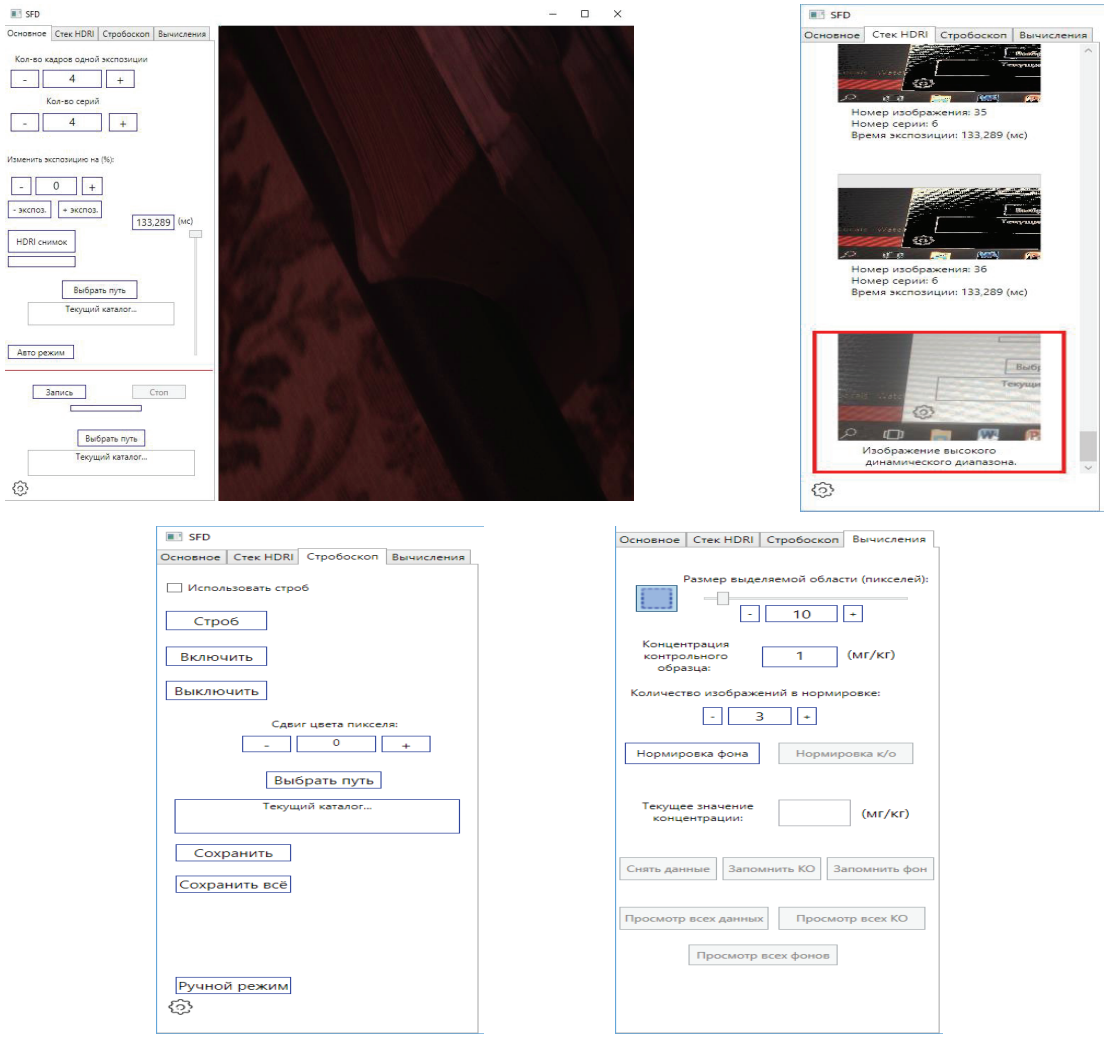

Figure 1 – SFD interface. Top left image – interface of basic tab; top right image – interface of HDRI stack tab; bottom left image – interface of stroboscope tab; bottom right – interface of calculations tab. Interfaces of all tabs beside basic tab has been illustrated without video stream control.

Stroboscope tab is necessary for fluorescence dermatoscopy. And calculations tab is necessary for conducting investigations on pharmacokinetics.

Conclusion. Nowadays we have software that can display video stream from digital camera, record video to a file, get an image with high dynamic range (HDRI mode), work in stroboscope mode and be used on pharmacokinetics studies. Program has not been tested on real tissue yet. We want to conduct these investigations in the nearest future.

References.

1. Adam Nathan, “WPF 4”, 2011.
2. Jeffrey Richter, “CLR via C#”, 4th edition, 2013.

The Spectral Fluorescence Method of the Bacteriochlorin Accumulation Dynamic Estimation in the Mice Skin with Superficial Wound Staphylococcus Infection

Akhlyustina E.V.[1],Maklygina Yu.S.[2], Borodkin A.V.[2], Ryabova A.V.[1,2], Kuneva A.A.[3], Rybakova P.A.[3], Yakovlev D.V.[3],Meerovich G.A.[2], Filonenko E.V.[4]

[1]National research nuclear university "MEPHI"

[2]Prokhorov General Physics Institute, Russian Academy of Sciences

[3]Pirogov Russian NationalResearch Medical University(RNRMU)

[4]P. Hertsen Moscow Oncology Research Institute – branch of the National Medical Research Radiological Centre of the Ministry of Health of the Russian Federation

e-mail:katya_ahlyustina@mail.ru

Abstract: Derivatives of bacteriochlorins (Bch) are promising for use as photosensitizers (PS) in near infrared spectral range (NIR, 750-850 nm) for photodynamic therapy (PDT) of tumors, local infectious in tissue damage (especially septic inflammation) and of the other pathological processes. The research results showed that the developed fluorescent spectroscopic approaches are promising in order to study pharmacokinetics and biodistribution of PS based on Bch on the mice experimental model of superficial wound Staphylococcus infection.

1. Introduction

The absorption of biological tissue in NIR spectral region is minimal, which provides possibility for effective PDT with Bch derivatives on sizable pathological locus [1]. Many photoactive substances are based on Bch which are hydrophobic and are used for PDT. Different nanostructured forms for intravenous injection such as liposomal, micellar, cremophor and cyclodextrin dispersions are created [2].The Bch derivatives have tumor affinity and effectively communicate with bacteria depending on their chemical composition, structure and dosage form model [3].The PS based on Bchderivatives have rapid pharmacokinetic. That's why the development of high-speed control methods for Bch biodistribution and pharmacokinetics measurement *in vivo* is important.

2. Materials and methods

The water cyclodextrin suspension of Bch in a concentration of 0.2 g/l was received from A.F. Mironov (Lomonosov Moscow State University of Fine Chemical Technologies).
The Bch biodistribution after intravenous injection was studied in experiments on superficial wound Staphylococcus infection. The linear Balb/c mice (males weighing 20-29g) were used. The skin of the mice backs was previously epilated. Under anesthesia the skin flap from the back was removed, and this place was seeded with the Staphylococcus culture. Two days later Bch was administered. The Bch dose amounted to 10 mg / kg, 20 mg / kg of animal body weight.
For the quantitative fluorescence measurements a fiber-optic spectrometer LESA-01-Biospec (BIOSPEC, Russia) was used [4]. The fluorescence was excited with a 532 nm laser. The fluorescence value was calculated as the area under the fluorescence peak (between 800 and 880 nm) divided by the area under the laser scattered peak (525-540 nm) – the so-called normalized fluorescence intensity (NFI): $NFI = S_{fl}/S_l$, where S_{fl} is the area under the fluorescence peak of the biological tissue and S_l is the area under the peak of the scattered laser component of the biological tissue. This technique allowed us to eliminate laser instability and partly take into account the fluorescence reabsorption when quantifying fluorescence intensity.Simultaneously with fluorescence spectral measurements the fluorescent video system (BIOSPEC) has been used. Fluorescent video system allows recording the fluorescence signal in a narrow wavelength range (820-870 nm) and obtaining the intensity in arbitrary units. The excitation wavelength was 532 nm in the experiments.

3. Results

The proposed approaches allowed studying the Bch distribution at different time after administration with high spatial, spectral and temporal resolution. It was demonstrated that the maximum concentration of Bch in the skin

is achieved in the time interval 60-130 minutes after PS administration. Thus, this time period is the most effective for PDT. The fluorescence intensity of Bch in the superficial wound Staphylococcus infection was higher than in normal skin (Fig.1). The average ratio of Bch fluorescence intensity in the wound to the skin surface was 11.8 for the Bch dose of 10 mg / kg and 21.8 for the Bch dose 20 mg / kg. Thus the contrast was improved with the increase of Bch dosages from 10 to 20 mg / kg. The distribution of fluorescence intensity of the mice skin was obtained by the fluorescent video system at various time points after Bch administration (Fig. 2a, b). Simultaneous 2D-control of the intensity distribution in the different mice bodyparts allowed evaluating the selectivity of the Bch accumulation dynamics (Fig.2c).

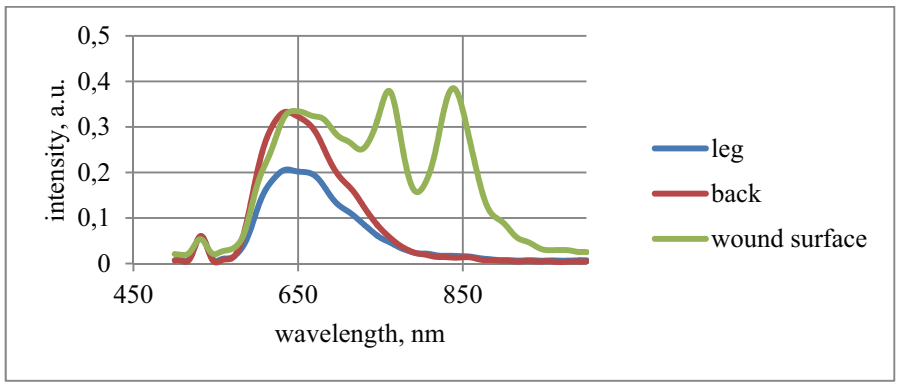

Fig.1.Fluorescence spectra of Bch in the superficial wound infection and normal skin (120 min after injection)

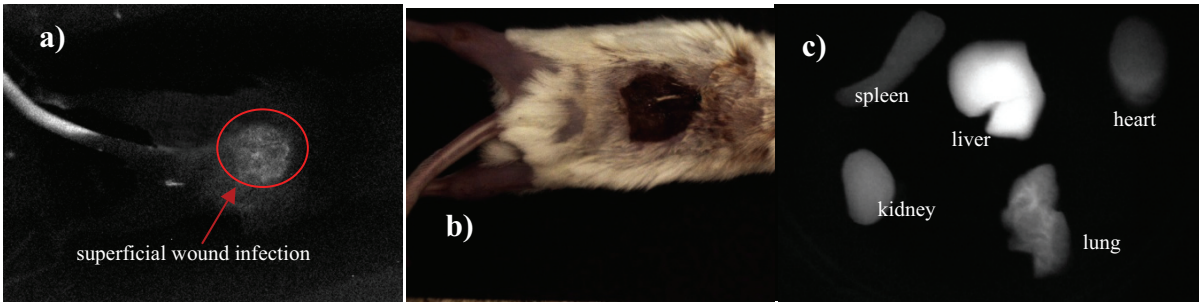

Fig.2.The fluorescence intensity of Bch a) in the superficial wound infection (black-and-white shot), b) in the superficial wound infection (color shot), c) in organs posthumously.

4. Conclusions

The spectral properties of studied Bch correspond to the maximum optical transparency region of biological tissues in the NIR that considers Bch to be the most promising.The research results showed that the developed fluorescent spectroscopic approaches are promising in order to study pharmacokinetics and biodistribution of PS based on Bch especially in the near infrared and infrared regions.

Acknowledgments

This work was supported by a grant RFBR # 15-29-04869-ofi-m.

1. T. Dai, Y.Huang, M.R. Hamblin."Photodynamic therapy for localized infections – state of the art".J. Photodiagnosis and Photodynamic Therapy. 2009; 6(3-4): 170–188.
2. Mironov A.F., Green M.A., Tsiprovsky A.G., et al. Patent RU2411943
3. Lukyanets E.A., Makarova E.A., Yakubovskaya R.I., et al. Patent RU2476218.
4. V. B. Loschenov, A. A. Stratonnikov, A. I. Volkova, and A. M. Prokhorov, Ross. Chem. Zh. XLII(5), 50-53 (1998).

Study of the Fluorescence Intensity Decay of Nanophotosensitizers Using Time-Resolved Spectroscopy Methods

F.G. Bystrov [1], V.I. Makarov [2], V.B. Loschenov [1, 2]
[1] Moscow, MEPHI, Department of Laser micro- and nanotechnology
[2] Moscow, A.M. Prokhorov General Physics Institute, RAS
augustbystrov@gmail.com

Abstract: The effect of the biological environment on the fluorescence properties of aluminum phthalocyanine nanoparticles (nan-AlPc) was studied. The measurements were carried out using registration system based on Hamamatsu streak camera C10627 with picosecond temporal resolution and picosecond laser with 637 nm wavelength and 65 ps pulse duration. The presence of two fluorescence lifetimes 5 ns and 10 ns was registered for nan-AlPc incubated with macrophages. The significant change in fluorescence kinetics of nan-AlPc, deposited under mice skin autografts, was observed after photodynamic treatment. Obtained information on nan-AlPc fluorescence kinetics is fundamental for building up a model of AlPc – biological environment interactions.

Molecular photosensitizers are widely use in the treatment of cancer and inflammatory diseases. Despite the achieved important, positive results there is a need to improve the selectivity of photosensitizer accumulation and a need to increase the selectivity of treatment impact. Taking into account these facts, the use of the nanophotosensitizers is considered to be promising. Aluminum phthalocyanine nanoparticles (nan-AlPc) are one of the representatives of this class of photosensitizers. It has been shown [1] that nan-AlPc can be used to assess the risks of skin autograft rejection and application of colloidal solution of nan-AlPc on autografts leads to the increase of fluorescence intensity in the case of inflammatory rejection. Furthermore, our studies have shown the decrease of fluorescence intensity after prolonged exposure to laser radiation - so-called photobleaching, that is absent for molecular form of aluminum phthalocyanine.

In this study we have examined the effect of the biological environment on the fluorescence properties of aluminum phthalocyanine nanoparticles. For this purpose, we have developed a registration system [2] based on Hamamatsu streak camera C10627 with picosecond temporal resolution, picosecond laser with 637 nm wavelength and 65 ps pulse duration and monochromator with fiber-optics input.

This work was made in three steps. Based on the fact that fluorescence of injected in biological tissue nan-AlPc appears mostly in pathologically changed areas we assumed that pH of environment can affects the fluorescence. Thus, the first step was to study the fluorescence kinetics of nan-AlPc water colloids at different pH. For this, five samples with pH 11, 10, 8, 3 and 2 were prepared and measured. It should be noted that aluminum phthalocyanine nanoparticles are insoluble in water and don't fluoresce under normal pH, which was confirmed by sample with pH 8.

The second step was to study the fluorescence kinetics of nan-AlPc incubated with immune cells. To simulate immune cells we used human monocytic cell line THP-1. Monocytes were differentiated into macrophages using ConA. Then, samples with monocytes and with macrophages were incubated with nan-AlPc colloid. Thus, two samples were prepared: one with monocytes containing nan-AlPc and one with macrophages containing nan-AlPc. In summary, the results obtained on the first and second step shown in Table 1.

Table 1: Fluorescence kinetics of nan-AlPc colloids with different pH and nan-AlPc in cells

Sample	Lifetimes of fluorescence	Photon Distribution	Quality of fit
Colloid with pH 11	$\tau_1 = 5$ ns $\tau_2 = 10$ ns	94% of photons 6% of photons	$\chi^2_R = 1{,}055$
Colloid with pH 10	$\tau = 5$ ns	-	$\chi^2_R = 1{,}018$
Colloid with pH 3	$\tau = 5$ ns	-	$\chi^2_R = 1{,}015$

Colloid with pH 2	τ_1 = 5 ns τ_2 = 2 ns	72% of photons 28% of photons	χ^2_R = 1,059
Monocytes with nan-AlPc	τ_1 = 6 ns τ_2 = 1,5 ns	93% of photons 7% of photons	χ^2_R = 1,024
Macrophages with nan-AlPc	τ_1 = 4,5 ns τ_2 = 9 ns	68% of photons 32% of photons	χ^2_R = 1,013

The third step was to evaluate the possibilities of time-resolved measurements on our experimental system for in-vivo application. For this, two mice with skin autografts were taken and nan-AlPc was added beneath one of the autografts. At first we analyzed the intensity decay of nan-AlPc deposited under autografts in order to identify the number of lifetime components and their distribution, and then we exposed experimental mice to the photodynamic effect and did the same analysis. The results are summarized in Table 2.

Table 2: Fluorescence kinetics of nan-AlPc in mice skin autografts before and after PDT

Sample	**Lifetimes of fluorescence**	**Photon Distribution**	**Quality of fit**
	Before PDT		
Mouse 1	τ_1 = 6 ns τ_2 = 1,1 ns	45% of photons 55% of photons	χ^2_R = 1,10
Mouse 2	τ_1 = 5,6 ns τ_2 = 540 ps	60% of photons 40% of photons	χ^2_R = 1,11
	After PDT		
Mouse 1	τ_1 = 4,2 ns τ_2 = 800 ps τ_3 = 150 ps	9% of photons 25% of photons 66% of photons	χ^2_R = 1,19
Mouse 2	τ_1 = 5,2 ns τ_2 = 460 ps	60% of photons 40% of photons	χ^2_R = 1,01

The difference in fluorescence kinetics for mouse 1 can be explained by taking into account the fact of formation of purulence under the skin autograft. For mouse 2 engraftment occurred normally.

Based on the fact that fluorescence of nan-AlPc is susceptible to the photobleaching effect that is absent for molecular form of aluminum phthalocyanine, it can be assumed that the appearance of nan-AlPc fluorescence in the diseased tissue is not only due to the normal dissolution, but also due to the transitions of surface molecules of the nanoparticle to the different orientation relative to the surface of nanoparticle caused by the peculiarities of the environment. The appearance of several fluorescence lifetime components, each of which corresponds to a particular state of the molecule on the surface, might be the evidence of these transitions.

References

[1] S.Yu. Vasilchenko, A.I. Volkova, A.V. Ryabova, V.B. Loschenov, V.I. Konov, A.A. Mamedov, S.G. Kuzmin and E.A. Lukyanets. “Application of aluminum phthalocyanine nanoparticles for fluorescent diagnostics in dentistry and skin autotransplantology”, J. Biophoton. 2010. T. 3, No. 5–6. P. 336–346.

[2] Bystrov F.G., Makarov V.I., Pominova D.V., Ryabova A.V., Loschenov V.B. “Analysis of photoluminescence decay kinetics of aluminum phthalocyanine nanoparticles interacting with immune cells”, Biomedical Photonics, 2016, T. 5, No. 4, pp. 3–8 (in Russian).

Broadband Terahertz in-line Phase Contrast Imaging

[1,2]A.A. Ushakov, [1]P.A. Chizhov, [1]V.V. Bukin, [2]A.B. Savel'ev, [1]S.V. Garnov.

[1]A.M. Prokhorov General Physics Institute Russian Academy of Science, 38 Vavilov Street, Moscow, Russia

[2]M.V. Lomonosov Moscow State University, 1 Leninskije goru, Moscow, Russia

e-mail: ushakov.aleksandr@physics.msu.ru

Abstract: We demonstrate a pulse broadband (from 0.1 to 1.5 THz) terahertz phase contrast imaging system by using the electro-optical crystal ZnTe. This system allows studying the depth information, refractive index and absorption of the objects.

1. Introduction

Due to the terahertz (THz) radiation source development the possibility of new devices for the tasks of spectroscopy, tomography and imaging has appeared [1]. Pulse sources of THz radiation allow to conduct measurements in the time-domain spectroscopy by using electro-optical detection technique [2]. Electro-optical crystal as a detector of THz radiation is used for the THz imaging [3]. Due to the point-by-point spatial scanning of the studying objects in such setups the sufficient decrease of the visualization rate is observed [3] that is a disadvantage of this method. In addition the visualization technique based on absorption does not allow studying the objects with low absorption of the THz radiation. For this research phase-contrast imaging principle [4] can be applied. However at this moment the studies with application of this technique were demonstrated only for the setups with a monochromatic radiation. In this paper the technique of in-line phase-contrast imaging by using the pulse broadband THz radiation and wide-aperture electro-optical crystal as a detector is demonstrated, that allows avoiding the point-by-point scanning and receiving the spectral information about studying object.

2. Experimental setup

The source of the optical radiation is a Ti:Sapphire laser (central wavelength 775nm, repetition rate 10 Hz, pulse duration 150 fs, pulse energy 2.8 mJ, Gaussian beam diameter 12 mm on the $1/e^2$ level, horizontal polarization). The main part of the radiation is used for the THz radiation generation in the THz source, based on the optical rectification of the femtosecond radiation with tilted front of amplitude in $LiNbO_3$ crystal [5]. THz radiation from the source is collimated by PTFE lens with focal length 10 cm. The studying object is introduced in the beam, thereafter this object is depicted onto the wide-aperture crystal surface ZnTe (10x10x0.5 mm^3) by PTFE lens with focal length 6 cm. The second part of laser radiation – probe pulse – is propagated through delay line, quarter wave plate, filters and expanding the beam lens. Thereafter the THz and optical beams are combined on the pellicle and directed to the ZnTe crystal. The surface of the detecting crystal is depicted by the telescope onto the digital camera. The polarizer is mounted before the telescope on the probe beam path. The presence of the THz field in the crystal causes the enlightenment or the shading of the crystal image on the digital camera due to linear electro-optical effect [6].

3. Image processing

From the obtained images of ZnTe crystal from the digital camera background (THz beam is passed through free space) and signal(THz beam goes through object under investigation) the spatio-temporal distributions of THz field has been received. Thereafter the discrete Fourier transformation of the time series for the obtained spatio-temporal distributions has been applied. Thus spatio-frequency distribution has been received. Thereafter for the different frequencies from the THz pulse spectrum distributions of the phase difference between the frames with studying object and without them have been created.

4. Results

The studying object is a 1mm thickness PTFE plate, which was introduced in the top half of the transmitting THz pulse. The pictures of spatio-temporal THz field distribution in the presence of PTFE plate and without it for experiment and numerical simulations are given on the figure 1.

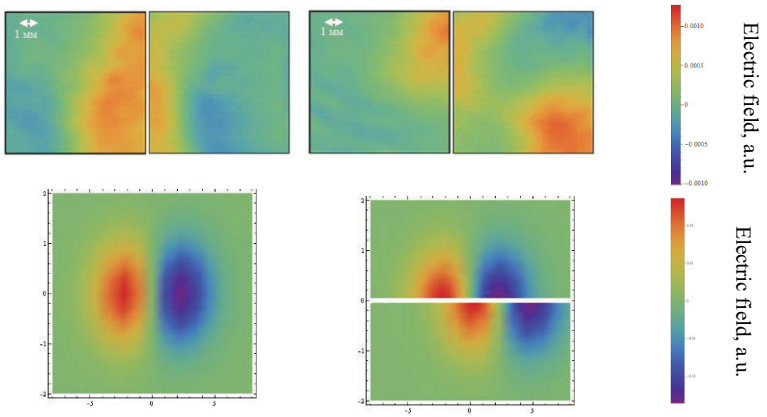

Fig. 1. Experimentally measured (top) and numerically calculated (bottom) spatio-temporal distribution of the THz field from $LiNbO_3$ crystal with the introduced PTFE plate (right) and without it (left)

The appropriate values of the phase difference for the frequency corresponding to the maximum of THz radiation are presented in figure 2. These results are good correlated with theoretical one, but the blur of the

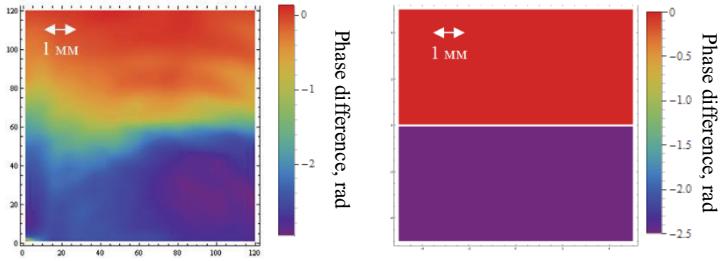

Fig. 2. Numerical calculations (right) and experimental measurements (left) of the phase-difference distribution for maximum frequency of spectrum of THz radiation partially passed through the PTFE plate

studying object border is caused by the diffraction of the THz pulse, which is not considered in the numerical simulations. Thus the phase-contrast imaging in the wide range of THz pulse frequencies have been realized.

5. References

[1] X.-C. Zhang, J. Xu, *Introduction to THz Wave Photonics* (New York: Springer, 2010).

[2] S. Wang, B. Ferguson, D. Abbott, X.-C. Zhang, "T-ray imaging and tomography", J. Biol. Phys., **29** (2 – 3), 247 (2003).

[3] Z. Jiang, X. Zhang, "Measurement of spatio-temporal terahertz field distribution by using chirped pulse technology", IEEE J. Quantum Electron., **36** (10), 1214 (2000).

[4] Y. Wang, Z. Zhao, Z. Chen, L. Zhang, K. Kang, J. Deng, "Continuous-wave terahertz phase imaging using a far-infrared laser interferometer", Applied Optics, **50** (35), 6453 (2011)

[5] J. Hebling, K.-L. Yeh, M.C. Hoffmann, B. Bartal, K.A. Nelson, "Generation of high-power terahertz pulses by tilted-pulse-front excitation and their application possibilities", JOSA B, **25** (7), B6 (2008).

[6] Zhiping Jiang and X.-C. Zhang, "2D measurement and spatio-temporal coupling of few-cycle THz pulses", Opt. Exp., **5** (11) 243 (1999).

The Study of Aluminum Phthalocyanine Nanoparticle Fluorescent Properties Changes in Tissue Engraftment for the Small Laboratory Animals Cross Skin Transplantation

Farrakhova D.S.[2], Akhlyustina E.V[2], Makarov V.I.[1], Pominova D.V.[2], Ryabova A.V.[1,2].
[1]A.M. Prokhorov General Physics Institute RAS, 38 Vavilov Str., 119991, Moscow, Russia
[2]National Research Nuclear University MEPhI (Moscow Engineering Physics Institute), Kashirskoe Highway, 31, 115409, Moscow, Russia
email: farrakhova.dina@mail.ru

Abstract: The possibility of aluminum phthalocyanine nanoparticles (nAlPc) application for evaluation of skin engraftment was studied. The analysis of fluorescent properties dynamic of tissue engraftment for cross skin transplantation of small laboratory animals was produced.

1. Introdution

One of the most important problems our day is a development of skin condition evaluation method based on the luminescence spectra analysis of biological tissues. The nAlPc colloidal solution was used as a photosensitizer in this study. The spectroscopic skin properties analysis in the monitoring mode is a foundation of inflammation stage evaluation method for skin transplantation. When nAlPc get into inflamed biological tissue, they start exhibiting fluorescent properties. The fluorescence intensity increases with the rise of macrophage concentration in the inflamed tissue [1]. This method gives an opportunity to determine the inflammation stage and gives accurate prediction of transplanted engraftment evaluation.

2. Materials and method

The study was conducted on laboratory mice. Cross skin transplantation was realized on two skin spaces of the mice's back. The nAlPc colloidal solution was added under the right autograft and the left autograft was used as a control one.

The skin autofluorescence and nAlPc fluorescence spectra analyzes were conducted for evaluation of nAlPc interaction with biological tissues. The spectra were obtained using the spectroscopy system LESA-01-Biospec. He-Ne laser (632.8 nm) was used for fluorescence excitation. Fluorescence spectra of autografts and normal skin were measured at 30 minutes, 1 hour, 2.5 hours, 3 hours, 4 hours, 1 day, 2 days, 4 days and 7 days after surgery.

3. Results and discussion

The fluorescence spectra of autograft with nAlPc are represented in figure 1a. Fluorescence intensity dynamic of autograft with nAlPc is presented in figure 1b.

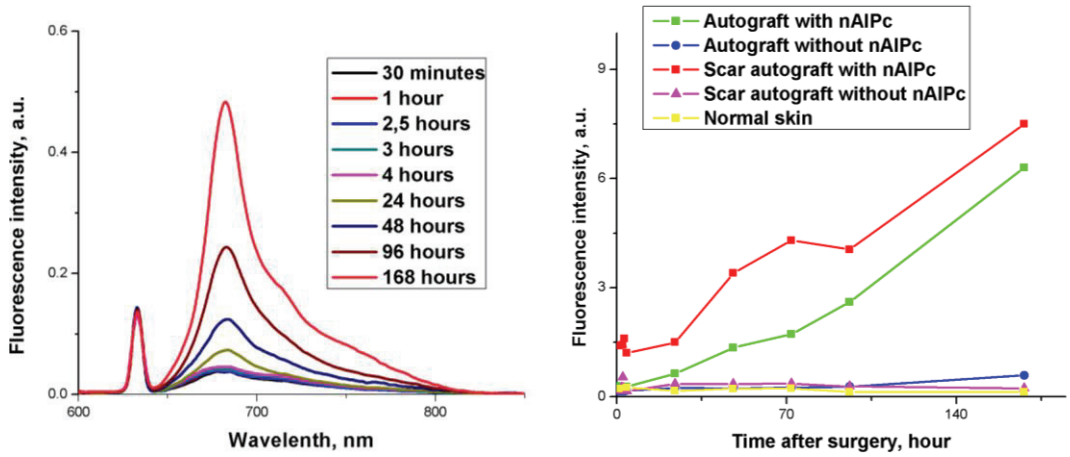

a) b)

Fig.1. a) The fluorescence spectra of autograft with nAlPc (mouse №1), b) The graph of fluorescence intensity dependence from time for autografts and normal skin after surgery (mouse №1).

Fluorescence intensity increased with time, which indicates the increase of the inflammatory reaction after cross skin transplantation. Consequently, the quality of tissue engraftment can be tracked with the help of nAlPc colloidal solution. This way allows taking action before the appearance of irreversible processes.

The nAlPc colloidal solution doesn't fluoresce which can be justified by fluorescence quenching in the molecular crystalline structure [2]. But nAlPc molecules begin fluoresce when they interact with inflamed tissue. This fact is connected with large concentration of macrophages in injured skin [1].

4. Conclusion

Evaluation of nAlPc fluorescent properties dynamic of nAlPc in the tissue engraftment for cross skin transplantation of small laboratory animals was conducted. The nAlPc fluorescence intensity increases over time with the rise of macrophages concentration in the injured skin. This method allows noninvasive determination of the skin surface physiological condition and evaluation of the stage and rate of engraftment or abruption of skin autografts. In addition, nAlPc colloidal solution may allow the acceleration of the healing process of autografts, because nAlPc can block an inflammatory response.

5. References

[1] Vasilchenko S.Y., Volkova A.I., Ryabova A.V., Loschenov V.B., Konov V.I., Mamedov A.A., Kuzmin S.G., Lukyanets E.A. Application of aluminum phthalocyanine nanoparticles for fluorescence diagnostics in dentistry and skin autotransplantology. // Journal of Biophotonics. Vol. 3 (5-6). 2010, p. 336-346.

[2] Steiner R., Breymayer J., Ruck A., Loshchenov V., Ryabova A. Crystalline organic nanoparticles for diagnosis and PDT. // Optical Methods for Tumor Treatment and Detection: Mechanisms and Techniques in Photodynamic Therapy XXIV. Vol. 9308. 2015. № 93080R.

Raman and FTIR spectroscopy in the THz frequency range in the study of protein structure

A. A. Mankova, N. N. Brandt, and A. Yu. Chikishev

Faculty of Physics and International Laser Center, Moscow State University, Moscow, 119991 Russia
mankova@physics.msu.ru

Abstract: Structural changes of proteins resulting from violation of optimal conditions for functioning are studied using low-frequency Raman and FTIR spectroscopy. Effects of thermal denaturation, cleavage of disulfide bonds, and inhibition on protein structure are analyzed

The structure-function relationship in protein molecules is a topical problem of modern science. Proteins are biological macromolecules that provide vital activity of living species, and it is known that even minor changes of the native protein structure may lead to malfunctioning or significant decrease in the functional activity. Theoretical works and computer simulations show that the characteristic frequencies of cooperative intramolecular vibrational modes of protein macromolecules belong to the THz frequency range. Such modes must be sensitive to the structural changes of a molecule and, hence, can be used to study variations in the functional activity of proteins. In this work, we employ low-frequency Raman and FTIR spectroscopy in the study of several proteins with different secondary structures and analyze spectral changes caused by modifications of native protein structure.

Maximum functional activity of a protein molecule is reached under optimal external conditions. Any variation in the environment and external effects (e.g., temperature variations and molecular interactions) may cause violation of optimal parameters of protein functioning. In particular, a significant decrease in the activity or even complete suppression of functioning result from denaturation or inhibition. Such variations in the activity are accompanied by structural changes. The denaturation affects higher levels of protein structure and, hence, the structure of active site can be altered whereas inhibition leads to a decrease in protein activity in the absence of crucial structural changes, since a chemical agent blocks only the active site.

Tris(2-carboxyethyl)phosphine (TCEP) and dithiothreitol (DTT) are used as chemical agents that cause protein denaturation due to the cleavage of disulfide bonds, and phenylmethanesulfonylfluoride (PMSF) serves as inhibitor. Spectroscopic data show that protein interaction with a relatively small PMSF molecule leads to noticeable structural changes of the protein molecule as a whole that, however, differ from the changes caused by interactions with denaturants. The effect of thermal denaturation is also studied using Raman and FTIR spectra. The spectroscopic data show that the effect of the thermal denaturation is stronger than the effect of cleavage of disulfide bonds. The spectra are approximated using Lorentzian curves with the band positions based on the published results. Spectral changes induced by external effects are interpreted using variations in the parameters of the fitting bands.

FTIR and Raman spectra of proteins with different secondary structures are compared. Correlations of the spectral changes in the low-frequency and fingerprint regions are observed. Application of the low-frequency vibrational spectra in the study of the secondary structure of protein molecules is discussed.

Aluminum phthalocyanine nanoparticles as a contrast agent for the detection of tooth enamel microcracks

Julia O. Kuznetsova[1], Dina S. Farrakhova[1], Maxim G. Yassin[2]
[1]*National Research Nuclear University MEPhI, Kashirskoe highway 31, 115409 Moscow, Russia*
[2] *Dental Clinic «Prodental», Str. The new boulevard 21, Dolgoprudny, 141707, Moscow region, Russia*
E-mail: JOKuznetsova@mail.ru

Abstract
This paper deals with a possibility of aluminum phthalocyanine nanoparticles (nAlPc) application for diagnosis, prevention and therapy of inflammatory diseases in dentistry. It was detected that nAlPc fluoresces in the nanoparticle form in the presence of pathologic microflora or inflammation process. It will make possible to detect the local accumulation of pathological microflora in the tooth enamel microcracks and peform diagnostics and treatment of inflammatory diseases. Experimental studies of interaction of nAlPc with tooth enamel and in the presence of different components of toothpaste. The nAlPc fluorescence is measured using fiber-optic spectrometer LESA-01BIOSPEC.

Introduction

Application of metal phthalocyanines nanoparticles in clinic practice opens new perspective to increase efficiency of fluorescence diagnostics (FD) and photodynamic therapy (PDT).
Early diagnosis of tooth-enamel microcracks has a great importance in modern dentistry for caries prevention. Diagnostic methods being used in clinical dentistry (visual inspection, probing, vital enamel staining [1]) can detect enamel damages of a rather large size. For diagnostics it is possible to use porphyrins autofluorescence when microflora is abundant in the microcracks [2]. Otherwise the microflora autofluorescence is relatively weak. The problem can be solved by using aluminum phthalocyanine nanoparticles (nAlPc) as exogenous fluorophore. nAlPc are convenient tool for fluorescence diagnostics because they do not fluoresce in the nanoparticle form but in the monomeric form it does. The fluorescence occurring when AlPc molecules arranged vertically are attached to the surface of the nanoparticles during the dissolution process or the interaction with pathological tissue, pathologic microflora and macrophages [3,4].
Besides it is possible to use nAlPc not only for fluorescent diagnostics but and in antimicrobial photodynamic therapy [5]. They are promising photosensitizer for clinical use because they have a good transportation in aqueous media and penetration into the tissue.
In dentistry the colloidal nAlPc solution can be used for detection of a local accumulation of pathological microflora on the enamel surface and in the microcracks area. Also the application possibility of nAlPc when adding them in different components of toothpaste is discussed in the present paper.

Materials and methods

Different human tooth which were extracted for reasons including periodontal problems, were used for investigation of application possibility of nAlPc for enamel microcracks diagnosis. After extracting all samples were placed into tubes with a sodium chloride solution 0.9%. Before the experiment teeth were mechanically cleaned and washed out in running water.
For the diagnosis of enamel microcracks by detecting nAlPc fluorescence in the areas of accumulation of pathogenic microflora it plans to create an unique toothpaste with nAlPc. For the creation of special composition with nanoparticles all paste components were separately examined. Experimental samples containing 100 mg of the test component and 500 μl of colloidal nAlPc solution in a concentration of 50 mg/l were prepared. Fluorescence spectra measurement was performed after 96 hours after their preparation to account for the possible increase in the interaction between the component and nAlPc.
Thereafter the base toothpaste composition was created. This composition was an almost an absolutely black body from the spectroscopic point of view.
For fluorescent measurements a fiber-optic spectrometer LESA-01BIOSPEC was used. He–Ne laser with the wavelength of 632.8 nm and the output power of 5 mW at the fiber end was used as an irradiation source for fluorescence excitation. A fiber-optic probe with one illuminating and six receiving fibers (each of 200 μm diameter) was attached to the spectrometer. Reference [6] contains the detailed information about experimental setup.

Results

Autofluorescent investigation of the hard tissues of the teeth has showed that the more demineralized enamel, the greater the intensity of the fluorescence of the enamel. Conversely, the higher mineralization degree of enamel corresponds the lower the enamel autofluorescence intensity. During experiment it was revealed that autofluorescence wavelength of carious enamel are shifted to in the red region of the spectrum.

Fluorescence spectra of nAlPc were obtained from the regions on the enamel surface with microcracks after applying nanoparticles on the whole enamel surface. It has also been found that over time there is the nAlPc fluorescence amplification in the areas of enamel microcracks. This indicates the presence of bacteria in this area.

For the prevention and early diagnosis of caries it was investigated basic toothpaste composition containing nAlPc in concentration of 10, 100 and 1000 mg/l. Researches the base toothpaste composition with the particles in concentrations of 10 and 100 showed that the fluorescence is absent or weak.

The base toothpaste composition in a concentration of 1000 mg/l was applied to the enamel surface microcracks, but also on the affected area of the enamel caries. The strong nAlPc fluorescence occurs only in the areas of carious lesions and is weak in the areas with a low content of bacteria.

Conclusion

The nAlPc included in toothpaste composition can be used as exogenous fluorophore for detection of a local accumulation of pathological microflora on the enamel surface and in microcracks in dentistry. In the future it is necessary to perform additional researches on selection of optimal toothpaste composition and nAlPc concentration to more accurately diagnose localization of microcracks on the tooth enamel surface.

Acknowledgments

This work was supported by the Competitiveness Programm of NRNU MEPhI. The research was carried out in Laser Biospectroscopy Laboratory at the A. M. Prokhorov General Physics Institute RAS together with the Laser Micro and Nanotechnology Department of NRNU MEPhI. We thank Professor Victor B. Loschenov for his scientific support.

References

[1] C. M. Cobb, “Lasers in periodontics: a review of the literature.,” *J. Periodontol.*, vol. 77, no. 4, pp. 545–564, 2006.

[2] J. Kuznetsova, M. Trottmann, G. Scheib, R. Leeb, R. Sroka, “OCT Imaging-characterization and medical applications,” in *16th International Conference “Laser Optics 2014”, St. Petersburg, Russia.*

[3] J. Breymayer, A. Ruck, A. V. Ryabova, V. B. Loschenov, and R. W. Steiner, “Fluorescence investigation of the detachment of aluminum phthalocyanine molecules from aluminum phthalocyanine nanoparticles in monocytes/macrophages and skin cells and their localization in monocytes/macrophages,” *Photodiagnosis Photodyn. Ther.*, vol. 11, no. 3, pp. 380–390, 2014.

[4] S. Yu. Vasilchenko, A. I. Volkova, S. B. Korovin, V. B. Loschenov, M. L. Sinyaeva, Ad. A. Mamedov, E. A. Luk`yanets, “Investigation ofaluminium phthalocyanine nanoparticles fluorescence properties in tooth enamel microdamages,” *Photodyn. Ther.*, vol. 5, no. 2, pp. 77–80, 2006.

[5] H. Asem, A. A. El-Fattah, N. Nafee, Y. Zhao, L. Khalil, M. Muhammed, M. Hassan, and S. Kandil, “Development and biodistribution of a theranostic aluminum phthalocyanine nanophotosensitizer,” *Photodiagnosis Photodyn. Ther.*, vol. 13, pp. 48–57, 2016.

[6] V. Loschenov, V. Konov, and A. Prokhorov, “Photodynamic therapy and fluorescence diagnostics,” *Laser Phys.*, vol. 10, no. 6, pp. 1188–1207, 2000.

Joint Application of Fluorescence Imaging and Local Fluorescence Spectroscopy for PD and PDT of Skin Cancer

Mukhin A.E.[1], Borodkin A.V.[2], Grachev P.V.[2], Stranadko E.F.[3]
[1]*National Research Nuclear University MEPhI, Moscow*
[2]*laser biospectroscopy laboratory, Prokhorov General Physics Institute of the RAS, Moscow*
[3]*State Science Center of Laser Medicine FMBA of Russia, Moscow*
mukhin.albert@gmail.com

Abstract. In this paper the results of PD of the patient with skin cancer of the ear is discussed. By "LESA-01-Biospec" and by fluorescent video system were held fluorescent spectra analysis and fluorescence imaging of the general dynamics of photosensitizer accumulation after 3 hours after drug injection before, during and after PDT.

Introduction. According to the data of Russian territories incidence of malignancies and mortality from them in 2014, the skin is a leading localization in the general structure of cancer incidence (12.6 %, with melanoma – 14.2%) [1]. Vast amount of current research is devoted to photodynamic therapy (PDT) of oncological diseases, including malignant skin tumors [2]. The undoubted advantage of PDT is the possibility of combining in a single procedure, the treatment and the fluorescent diagnostics, also known as photodiagnosis (PD). In case of skin cancer, PD is the most promising diagnostic method to clarify the borders of tumor proliferation, since the sensitivity of this method is much higher than other modern methods of diagnosis [3].

Materials and method. The patient with squamous skin cancer on the ear was admitted to the State Science Center of Laser Medicine department of oncology. To conduct therapy and diagnostics has been used a chlorine E6 photosensitizer permitted for use in Russia[4], "FOTODITAZIN" (LLC "VETA-GRAND", registration number № LS-001246 since 18.05.2012), that was injected intravenously in a dose 1 mg/kg of body weight.

PD was conducted before, during and after PDT via two equipments. By laser electron-spectral system "LESA-01-Biospec" was held fluorescent spectra analysis (fluorescence excitation on the wavelength 632.8 nm): the ear was visually divided on 5 sections (fig. 1a), in each of which were recorded fluorescent spectra throughout the therapy. By dual-channel laparoscopic fluorescent video system was performed visual evaluation of the photosensitizer accumulation in the normal and cancerous areas in on-line mode throughout the therapy (excitation on the 635 nm).

The irradiation was carried out on the laser system "LFT-02-Biospec" with the light wavelength 662 nm and the light dose 270 J/cm^2. The sapphire needle capillary was used at the end of therapy due to the necessity of the beam weakening for pain tolerance of the patient.

Results. PD after 3 hours after drug injection by fluorescent video system of tumor showed the border of proliferation and accumulation of the photosensitizer. By visualizing via black-white diagnostic and color navigation cameras that fluorescent video system used, tumors such as ear squamous skin cancer can be clearly imaged, the boundary between cancerous and normal areas can easily be identified (fig. 1b).

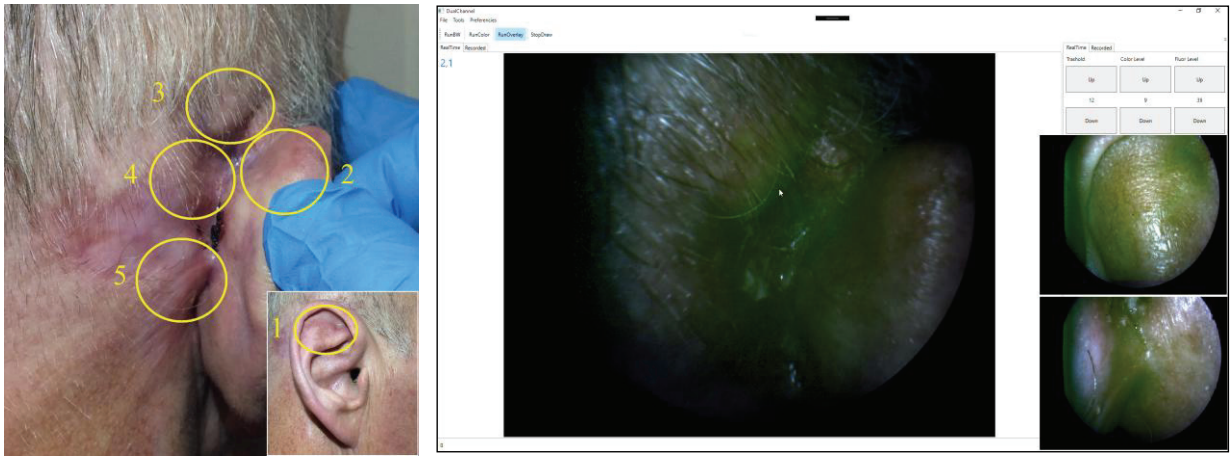

a) b)

Figure 1. a) The ear of the patient with highlighted areas; b) fluorescent video system images after PS administration. The cancerous area were imaged in green.

PD by laser electron-spectral system “LESA-01-Biospec” before therapy revealed a high level of photosensitizer accumulation in cancerous areas relative to normal skin (on the neck): average fluorescence index is equal to 1:2.2 (fig. 2a). During therapy after irradiations the dynamics of accumulation changed: in all area it is decreased due to photobleaching, particularly in section 2 the fluorescence index fell more than 2 times (fig. 2b). Then spectra after therapy (fig. 2c) showed a rise of photosensitizer accumulation in all area perhaps by reason of a blood flow. With continued therapy we would get more data.

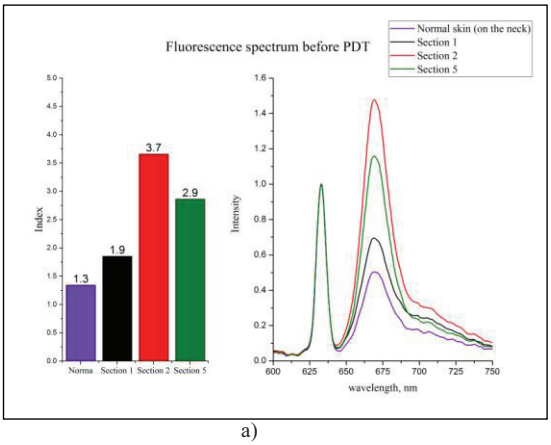

a)

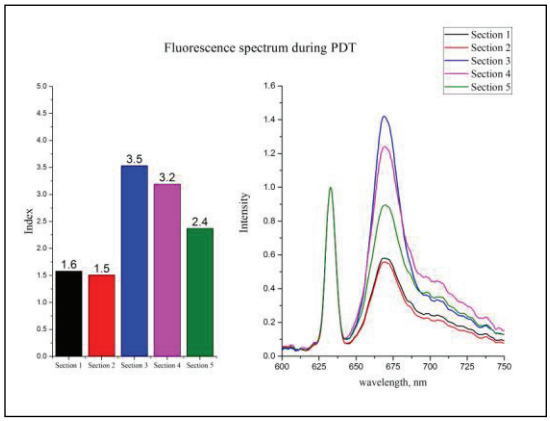

b)

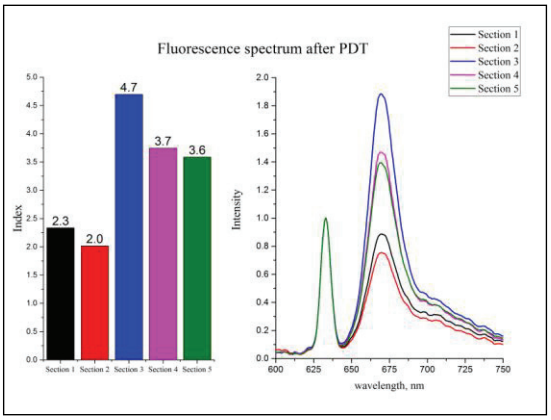

c)

Figure 2. The fluorescent spectra: a) before therapy in normal skin, section 1, section 2 and section 5; b) during and c) after therapy in section 1, section 2, section 3, section 4 and section 5.

- normal skin (on the neck)
- section 1 – upper part of auricle
- section 2 – the back of auricle
- section 3 – over the section 4
- section 4 – over the “recess” behind the auricle
- section 5 – under the “recess” behind the auricle

Conclusion. The data received by joint application of fluorescence imaging and local fluorescence spectroscopy point out to a high efficiency of fluorescent diagnostics method of skin cancer and show importance of photobleaching tracking of chlorine series photosensitizer during irradiation.

References.

[1] A.D.Kaprin, V.V.Starinsky, G.V.Petrova, “Malignancies in Russia in 2014 (morbidity and mortality)” (M.: Gertsen MSROI, 2016).
[2] V.K.Kapinus, Yu.S.Romanko, M.A.Kaplan et al, “The efficacy of fluorescence diagnostics and photodynamic therapy with photosensitizer photoditazin in patients with cancroid” (“Russian biotherapeutic journal”, 2005), №3, V.4, p. 71-77.
[3] V.N.Volgin, "Modern methods of diagnosis and treatment of basal-cell cancer" (M.: Burdenko MMCH, 2011).
[4] E.Ph.Stranadko, “Main stages of development of photodynamic therapy in Russia” (“Photodynamic therapy and photodiagnosis”, 2015), №1, V.4, p. 3-10.

ADAPTIVE OPTICS MULTISPECTRAL FUNDUS-CAMERA (AOMFC) FOR DETECTION OF RETINAL PATHOLOGY

Bolshunov A.V.[1], Katalevskaya E.A. [1],

Larichev A.V.[2], Iroshnikov N.G.[2]

[1]Research Institute for Eye Diseases,
Rossolimo str. 11A, Moscow, 119021,
tel. 8(499)248-78-98, 8(905)745-57-61,
bolshlas@mail.ru, ekatalevskay@mail.ru,
[2]Lomonosov Moscow State University, physics department,
Leninskie gory 1, bld.2, Moscow, 119991
tel. 8(495)939-16-82, larichev@optics.ru, nikita@optics.ru

Abstract

High-resolution adaptive optics multispectral fundus-camera imaging enables early detecting of dry age-related macular degeneration (AMD), nonproliferative and proliferative diabetic retinopathy, epiretinal membranes, idiopathic macular holes.

Introduction

The resolution ability of modern retinal imaging technologies, such as fundus-camera, fluorescent angiography (FA), optical coherence tomography (OCT), scanning laser ophthalmoscopy, is limited by aberrations of the human eye. To overcome this problem adaptive optics [1] has been successfully coupled with different retinal imaging techniques [3, 4, 5, 6]. We present the adaptive optics multispectral fundus-camera (AOMFC), that was developed by medical physics chair of Moscow State University. AOMFC enables measurement of wave aberrations of the human eye with the use of a Hartman-Shack wave-front sensor, correcting wavefront aberrations up to 4-th order with the use of bimorph deformable mirror and getting retinal images with the high spatial resolution.

The aim of this work is to compare the diagnostic features of AOMFC and a fundus-camera without adaptive optics.

Materials and methods: AOMFC optical performance was characterized by artificial eye with USAF resolution target and by measurement of residual aberrations of real eyes with the help of Hartmann-Shack sensor. 162 patients (227 eyes) were studied. The assessment included visometry, biomicroophthalmoscopy, fundus photography using AOMFC and the fundus-camera Topcon TRC-NW200 (Japan) without adaptive optics, FA, OCT.

Results

AOMFC demonstrates reduction of wavefront aberration beyond defocus in 5-10 times depending on the eye aberration's composition. The time required for correction is 0.1s.

In the eyes with dry form of AMD using of AOMFC enabled detecting of retinal drusen in 100% of cases, using fundus-camera TRC-NW200 - in 73,3% of cases. In the eyes with wet form of AMD FA was the most informative method [2].

In diabetic patients the detection frequency of microaneurysms and microhemorrhages, retinal venous abnormalities, primary retinal and optic disc neovascularization using AOMFC

was higher in comparison to fundus-camera without adaptive optics [2]. The results are presented in the table 1.

Table 1. The detection frequency of diabetic retinopathy using AOMFC and fundus–camera TRC-NW20.

	microaneurysms and microhemorrhages	retinal venous abnormalities	retinal and optic disc neovascularization
AOMFC	51,8%	26,8%	50%
fundus–camera TRC-NW20	28,6%	10,7%	18%
p	0,1	0,03	0,0003

By assessment of retinal hemodynamics FA was the most informative method. However the advantage of AOMFC of FA is the noninvasiveness of method.

In eyes with epiretinal tractional syndrome the detection frequency of pre-retinal membranes of macula using AOMFC was 80%, using fundus-camera without adaptive optics – 40%. Macular holes were diagnosed in 73,3% of cases using AOMFC, and in 40% of cases using fundus-camera without adaptive optics. OCT was used as a control method and proved pre-retinal membranes of macula and macular holes in all cases [2]. However OCT can't be used as a single diagnostic method because of limiting influence of human eye aberration on the transverse resolution of optical coherent tomographs.

Summary

High-resolution adaptive optics multispectral fundus-camera imaging enables early detecting of dry age-related macular degeneration, nonproliferative and proliferative diabetic retinopathy, epiretinal membranes, idiopathic macular holes.

References

1. Balashevich L.I. Optical aberrations of the eye: diagnostic and correction// Oculist. - 2001. – Vol.22, № 6. – P.12-15.
2. Bolshunov A.V., Iroshnikov N.G., Katalevskaya E.A., Larichev A.V. Clinical application of adaptive optics for detection of retinal pathology // Questions of laser ophthalmology edited by Bolshunov A.V. (Moscow, 2013.), P.66-82.
3. Cunefare D, Cooper RF, Higgins B et al. Automatic detection of cone photoreceptors in split detector adaptive optics scanning light ophthalmoscope images// Biomed Opt Express. – 2016. – Vol. 7, N5. – P.2036-50.
4. Meixner E, Michelson G. Measurement of retinal wall-to-lumen ratio by adaptive optics retinal camera: a clinical research// Graefes Arch. Clin. Exp. Ophthalmol. – 2015.- Vol.253, N 11. – P. 1985-95.
5. Salas M, Drexler W, Levecq X. et al. Multi-modal adaptive optics system including fundus photography and optical coherence tomography for the clinical setting//Biomed Opt Express. – 2016. – Vol.7, N5. – P.1783-96.
6. Wood EH, Leng T, Schachar IH et al. Multi-modal longitudinal evaluation of subthreshold laser lesions in human retina, including scanning laser ophthalmoscope-adaptive optics imaging// Ophthalmic Surg Lasers Imaging Retina. – 2016. – Vol.47, N3. – P.268-75.

AFTEREFFECT OF LOW-INTENSITY OF HE-NE LASER IRRADIATION ON THE ACTIVATION OF ATP SYNTHESIS AND REPROGRAMMING OF THE GENOME

T. I. Karu, V. M. Manteifel, L. V. Pyatibrat

Institute of Crystallography and Photonics of RAN, Moscow,
Institute of Photonic technology, Moscow, Troitsk, Pionerskaya2
Tel.:8(495)8510233
Fax:8(495)8510286
e-mail:tiinakaru47@gmail.com

Abstract. Aftereffect of low-intensity laser radiation (LILI) on the structure of mitochondria was revealed. Changes of mitochondria reflect activation of oxidative phosphorylation, which may be the result of genome reprogramming.

Summary. Aftereffect of low-intensity laser radiation (LILI) on the structure of mitochondria was revealed. Changes of mitochondria reflect activation of oxidative phosphorylation, which may be the result of genome reprogramming. Exposition of human peripheral blood lymphocytes in vitro by He-Ne laser (at 56 J/m^2) results in fusion of 80% of separate mitochondria (number of the small mitochondria in normal cell is about 40). One hour after irradiation the cells contain 2-4 elongated branched mitochondria and very few small mitochondria [1]. The total volume of mitochondria per cell does not change. Fusions of the bulk of mitochondria usually reflect the increased ATP synthesis via oxidative phosphorylation. It is known that such changes require the presence of specific proteins responsible for fusion of outer mitochondrial membranes [2]. The synthesis of these proteins is controlled by the expression of the corresponding genes – *Mfn1, Mfn2, Opa1*.

Laser irradiation has an aftereffect on mitochondria in successive generations of yeast Thorulopsis sphaerica. Exposition (at 460 J/m^2) results in changing giant mitochondrion in the cells cultivated for 18 hours [3]. First, the mitochondrial matrix is expanded. Secondly, relative proportion of cristae membranes is increased. It is known that cristae membranes contain all protein complexes of the mitochondrial electron transport chain (ETC). The detected changes of mitochondria may reflect the acceleration of ATP synthesis. The

increasing of the cristae per mitochondrion can be due to changed expression of genes regulating energy metabolism. For example, exposition of fibroblasts by LILI led to increased expression of genes, encoding subunits of protein complexes in the ETC [4, 5].

The hypothesis that the target of LILI is the cytochrome c-oxidase is now supported experimentally [6]. Absorption of photons by this enzyme results in accelerating electrons flow in the ETC; this causes increasing of $\Delta\Psi m$ and ATPm. Such functional changes have been identified in a few minutes after the irradiation. The presented data indicate the effect of LILI on prolonged activation of the oxidative phosphorylation in the cells-descendants. Light-sensitive reorganization of the mitochondria may be regulated on the gene level.

1. Bakeeva L. E., Manteifel, V. M., Karu, T. I. // Tsitologiya, 41 (11) 966-974 (1999)

2. Hoppins S., Lackner L., Nunnari // J. Annu. Rev. Biochem. 76: 751-780 (2007)

3. V. M. Manteifel, T. I. Karu // Trends in photochemistry and Photobiology Is, 12, 77-91 (2011)

4. R. T. Masha, N. N. Houreld, H. Abrahamse // Photomed Laser Surg., 31 (2) 47-53 (2013)

5. Zhang Y., Song S., Fong C. C., et al. // J. Investigative Dermatol., 120, 849-857 (2003)

6. Karu, T. I. // Photochem. Photobiol, 20 (84) 1091-1099 (2008)

Noninvasive blood glucose monitoring with THz reflection spectroscopy

O. P. Cherkasova[1], M.M.Nazarov[2, 4], A. P. Shkurinov[2, 3]

[1]*Institute of Laser Physics of SB RAS, pr. Lavrentyeva, 13/3, Novosibirsk, 630090, Russia*
E-mail: o.p.cherkasova@gmail.com
[2]*Crystallography and Photonics RAS, Moscow, Russia*
[3]*Lomonosov Moscow State University, Leninskie Gory, GSP-1, Moscow, 119991, Russia*
4- National Research Centre "Kurchatov Institute", Moscow, Russia

Abstract: Human skin optical properties were studied in vivo using terahertz time-domain spectroscopy with silicon Dowe prism in the attenuated total internal reflection (ATR) configuration. The measurements were carried out on volunteers with normal blood glucose concentration and after glucose intake. The variations of the reflection spectra of human skin were correlated with the changes in blood glucose level. Our results demonstrate the possibility of a non-invasive real-time measurement of blood glucose concentration.

1. Introduction

Monitoring of glycemic status is considered to be a cornerstone of diabetic patients care. Measurements of glucose concentration in blood are best determined by standardized laboratory techniques using blood plasma biochemistry analyzers. However, disadvantages are long measurement time, and a relatively large sample volume needed to obtain the results [1, 2]. During the last 20 years, many portable blood glucometers for humans have appeared on the market. They are readily available, inexpensive, and provide immediate results while utilizing small quantities of capillary blood [1, 3]. However, control of diabetes mellitus involves daily self-monitoring of blood glucose by finger puncture several times a day to obtain a blood sample for further analysis. This procedure is invasive, painful, non-safe and unpleasant for patients. In the past decades much attention had been paid to the development of spectroscopic methods for noninvasive glucose measuring. These approaches include polarimetry, near-infrared spectroscopy, Raman spectroscopy, photoascoustics and optical coherence tomography [4].

Terahertz time-domain spectroscopy (THz-TDS) has not yet found wide application in this field. A distinctive feature of this method is the possibility of measuring directly the refractive index, absorption coefficient, and hence complex permittivity spectrum of the sample in a single scan and in a broad frequency range. The application of THz spectroscopy for studies of both normal human skin and skin pathologies in vivo has been reported previously [5].We found no studies of the human skin optical characteristics when glucose concentration in blood is varied. However, it has previously been shown that the transmission coefficient of animal ear skin in subTHz (0.03-0.04) and THz (0.34) frequency ranges correlates with blood glucose concentration [6, 7]. In the present paper, we describe the studies of human skin using THz-TDS in vivo in 0.2-2 THz range. We measured the ATR spectra of human skin at normal blood glucose concentration and their variations during a standard oral glucose tolerance test.

2. Results

The THz time-domain spectrometer used in the study was described previously [8, 9]. The experiments were carried out using ATR optical scheme with a silicon right angle Dowe prism, with p-polarized radiation.

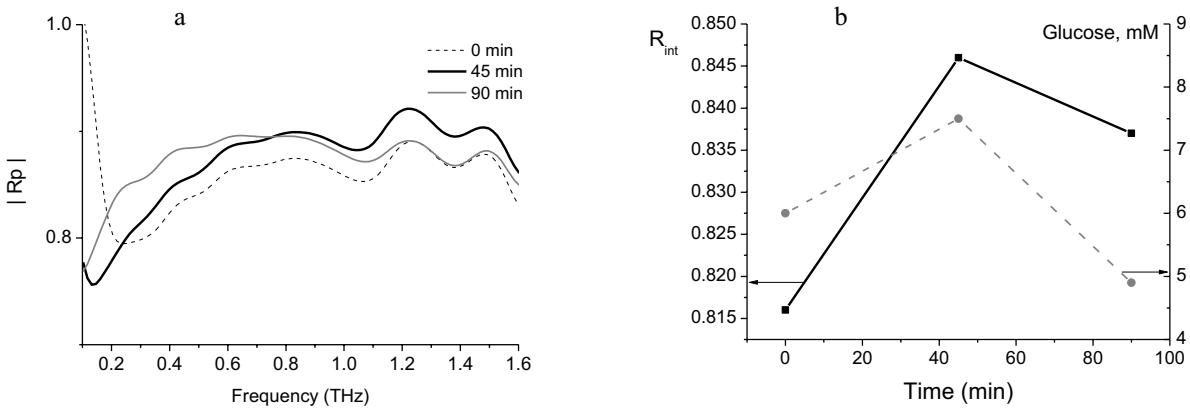

Fig. 1. (a) The ATR amplitude |Rp| of human skin at different times (0, 45, 90 min) after ingesting the glucose solution; (b) The ATR amplitude Rint (a) of human skin and glucose concentration in blood (mM) versus time (min) after glucose intake.

The ATR spectra of human palm skin after ingesting glucose solution are shown in Fig. 1. We used a 0.2 ml 84% glycerol solution in distilled water to improve optical contact and to increase the THz field penetration depth into the skin. The processing time of glycerol was 10 minutes. Since the temporal shape of reflected THz pulse E(t) is not changed considerably, we may use the pulse amplitude as the integrated characteristics of ATR amplitude R_{int}: $R_{int}=(E_{s,\,max}-E_{s,\,min})/(E_{r,\,max}-E_{r,\,min})$ (Fig. 1, b). Here E_s indicates signal, E_r – reference, E_{max} and E_{min} are corresponding maximal and minimal values in the time-domain. The largest variations ATR spectra are observed for the 0.1-0.5 THz frequency range. The amplitude of ATR signal of human palm skin is changed when blood glucose concentrations rise above the normal levels.

Analysis of the experimental reflection spectra was performed by comparing the experimental skin spectra with the dielectric function of skin model. The shape of THz spectra of the biological tissue is mainly determined by water present in it, having a strong dispersion at low frequencies. The dielectric permittivity of water can be described by Debye model.

3. Conclusions

We measured human skin spectra *in vivo* using THz-TDS in ATR optical scheme. The ATR spectra of palm skin were consecutively measured at 0-90 min after glucose intake at standard oral glucose tolerance test. We used glycerol to improve the optical contact between the palm skin and the surface of the prism and to increase the sensitivity of our method. The largest variations of the ATR spectra were observed within the 0.1-0.5 THz frequency range. These variations of the optical characteristics of human skin were correlated with the changes in blood glucose level. The ATR amplitude of human palm skin increased when the glucose concentrations in blood rose above the normal level. The changes observed in the spectra are described with good accuracy by the reduction in the ratio $\Delta\varepsilon_1/\tau_D$ in the Debye model of the glucose aqueous solution. This change in the response of bound water is the reason of the sensitivity of *in vivo* THz skin measurements to high glucose concentration in blood. Our results demonstrate the possibility of non-invasive real-time measurement of blood glucose concentration.

This work has been supported by RFBR (grant № 14-02-00846, № 14-02-00979 and № 16-52-00222).

References

[1] Rebel, A., Rice, M.A., Fahy, B.G., *"The Accuracy of Point-of-Care Glucose Measurements"*, Journal of Diabetes Science and Technology, **6**(2), 396-411 (2012).

[2] Summa, N.M., Eshar, D., Lee-Chow, B., Larrat, S., Brown, D.C., *"Comparison of a human portable glucometer and an automated chemistry analyzer for measurement of blood glucose concentration in pet ferrets (Mustela putorius furo)"*, Can. Vet. J., **55**, 865–869 (2014).

[3] Clarke, S. F., Foster, J. R., *"A history of blood glucose meters and their role in self-monitoring of diabetes mellitus"*, British Journal of Biomedical Science, **69** (2), 83-93 (2012).

[4] He, R., Wei, H., Gu, H., Zhu, Z., Zhang, Y., Guo, X., Cai, T.: Effects of optical clearing agents on noninvasive blood glucose monitoring with optical coherence tomography: a pilot study. J. Biomed. Opt., **17**(10), 101513-1 (2012).

[5] Zaytsev, K.I., Gavdush, A.A., Chernomyrdin, N.V., Yurchenko, S.O.: Highly Accurate in Vivo Terahertz Spectroscopy of Healthy Skin: Variation of Refractive Index and Absorption Coefficient Along the Human Body. IEEE Transactions on Terahertz Science and Technology, **5**(5), 817-827 (2015).

[6] Sigel, P.H., Lee, Y., Pikov, V.: Millimeter-Wave Non-Invasive Monitoring of Glucose in Anesthetized Rats. IEEE 39th International Conference on Infrared, Millimeter, and Terahertz Waves (IRMMW-THz 2014): proceedings, T2/D-8 (2014).

[7] Sun, C-K., Tsai, Y-F., Chen, H. United States Patent Application Publication. US 2013/0289370 A1 (2013) http://www.faqs.org/patents/app/20130289370#ixzz3HQzAOszh

[8] O. P. Cherkasova, M. M. Nazarov, A.A. Angeluts, A.P. Shkurinov, *"The Investigation of blood plasma in the terahertz frequency range"*, Optics and spectroscopy, **120**(1), 55-63(2016)

[9] O. P. Cherkasova, M. M. Nazarov, E. E. Berlovskaya, A. A. Angeluts, A. M. Makurenkov, A. P. Shkurinov, *"Studying human and animal skin optical properties by terahertz time-domain spectroscopy"*, Bulletin of the Russian Academy of Sciences Physics, **80**(4), 479-483 (2016).

High efficiency stimulated low-frequency Raman scattering in water/buffer suspension of potato viruses (PVX&PVA)

A F Bunkin[1], M Ya Grishin[2], O V Karpova[3], A D Kudryavtseva[4], V N Lednev[5], T V Mironova[4], S M Pershin[1], E K Petrova[3], M A Strokov[4], N V Tcherniega[4] and K I Zemskov[4]

[1]*Prokhorov General Physics Institute of the RAS, Vavilova, 38, Moscow, 119991, Russia*
[2]*Moscow Institute of Physics and Technology (State University), Dolgoprudny, Russia*
[3]*Lomonosov Moscow State University, Vorob'evy Gory, 1, Moscow, 119991, Russia*
[4]*Lebedev Physical Institute of the RAS, Leninskii pr, 53, Moscow, 119991, Russia*
[5]*National University of Science and Technology MISiS, Moscow, Russia*
akudr@sci.lebedev.ru

Abstract: Stimulated low-frequency Raman scattering (SLFRS), caused by Ruby laser pulses interaction with the vibration modes of potato viruses X (PVX) in Tris-HCl pH7,5 buffer and A (PVA) in water suspension was registered. Frequency shift (in GHz scale), efficiency conversion (up to 10%) and SLFRS threshold are measured.

1. Introduction

Viruses of any type are good examples of highly monodisperse systems. Most of viruses have cylindrical or spheroidal shape and have their own discrete set of acoustic eigenfrequencies. For their investigation low frequency Raman scattering (LFRS) [1, 2] can be used. LFRS is an inelastic light scattering by acoustic vibration modes of nano or submicron particles. Currently LFRS is realized for systems containing metal, dielectric, or semiconductor nanoparticles [3]. Systems consisting of viruses of different types are also the subject of intensive theoretical and experimental research [4-6]. Low frequency spectrum of the inelastically scattered light in rigid biological structures like in any nanoparticles system can not only give very important information about their shape and elastic properties but also and be used for size distribution in the system under consideration. Exact eigenfrequency value knowledge is very important as for virus identification so for realization resonant impact on virus. This very important application can be realized in the case of exact coincidence frequency of external influence with the virus eigenfrequency. As an external influence ultrasound or electromagnetic radiation of the proper frequency can be used. Another way for effective impact realization is biharmonic pumping – electromagnetic radiation containing two spectral components separated by the frequency corresponding to the eigenfrequency of the virus. For submicron and nanoscale structures typical eigenfrequncies are up to gigahertz and terahertz range respectively. For biharmonic pumping stimulated low frequency Raman scattering (SLFRS) can be used. SLFRS is a stimulated analogue of spontaneous LFRS [7, 8]. SLFRS can be excited in nano or submicron particles system under pulsed laser irradiation when its threshold is exceeded. SLFRS was observed in the system of the rod-like particles of tobacco mosaic virus (TMV) [9]. In this article we report on first experimental realization of SLFRS in potato viruses X and A in aqueous and Tris-HCl pH7,5 buffer suspensions. In order to take into consideration the elastic virus environment elastic properties we also measured the frequency shift of Stimulated Brilouin scattering (SBS) in Tris-HCl pH7,5 buffer and water.

2. Experimental

As samples potato viruses X and A in water and Tris-HCl pH7,5 buffer suspensions were used.

Potato virus X (PVX) is a type member of the Potexvirus genus (Alphaflexiviridae family). The genomic 5'-capped positive-strand RNA, 6435-nt long, is encapsulated in a flexuous filamentous particle about 515 nm long and 13.5 nm in diameter. Virion Mr is about 3.5×10^6 Da; S_{20w} is 115–130S, buoyant density in CsCl is 1.31 g/cm^3. A single linear positive sense RNA represents about 6% by weight of the virion. About 1300 identical coat protein (CP) subunits in PVX particle form a helical array (3.6-nm pitch) with the viral RNA packed between the turns of the helix. There are 8.9 CP subunits (each consisting of 236 amino acid residues) per turn of primary helix and five nucleotides are associated with each protein subunit. The RNA backbone is at a radial position of 3.3–3.5 nm.[10].

Potato virus A (PVA) is a single-stranded positive-sense RNA virus and a member of the family Potyviridae, the largest and one of the most economically important groups of plant viruses. The virions of potyviruses are flexuous and rod-shaped, 680-900 nm long and 11- 15 nm wide, made up of about 2000 units of a single structural protein (coat protein, CP) encapsidating a single molecule of positive single stranded (ss) RNA of approximately 10 kb. The particles of PVA are approximately 730 nm long and 15 nm wide. The genome is 9565 nucleotides long and contains a single open reading frame encoding a polyprotein of 3059 amino acids (aa). The

PVA coat protein comprises 269 amino acids and has a calculated Mr of 30,257. The potyviral RNA strand has a poly-A tail at the 3′end and a viral genome-linked protein VPg at the 5′end [11].

Tris or Tris(hydroxymethyl)aminomethane is an organic compound with the formula (HOCH2)3CNH2.. In biochemistry and molecular biology, Tris is widely used as a component of buffer solutions including, as a storage buffer for viral preparations. Tris has a pKa of 8.07 at 25 °C, which implies that the buffer has an effective pH range between 7.5 and 9.0. The useful buffer range for tris (7-9) coincides with the physiological pH typical of most living organisms. The pKa declines approximately 0.03 units per degree Celsius rise in temperature.

Ruby laser pulse (λ = 694.3 nm, τ = 20 ns, E_{max} = 0.3 J) has been used as a source of excitation. Exciting light has been focused into the quartz cell filled with suspension by lens with 50 mm focal length. The length of the cell was 1 cm. Energy of the laser pulse, radiation passing through and reflected from the cell were measured simultaneously by calibrated photodiodes. Fabri-Perot interferometers were used for spectral structure investigations: the range of dispersion was changed from 0.42 to 16.7 cm^{-1}. All measurements were realized both for forward and backward directions (for the light passing through the sample and for the light reflected from it).

SLFRS was experimentally registered for PVA in water suspension and for PVX) in Tris-HCl pH7,5 buffer. For PVA in water suspension two Stocks components in forward direction and one Stocks component in backward direction were registered. SLFRS frequency shift was found to be 0.28 cm^{-1} for the first Stocks component and 0.6 cm^{-1} for the second Stocks component. At the experimental conditions the threshold value of SLFRS excitation was 0.03 GW/cm^2. For PVX in Tris-HCl pH7,5 buffer two Stocks components in forward direction and one Stocks component in backward direction were registered. SLFRS frequency shift was found to be 0.21 cm^{-1} for the first Stocks component and 0.4 cm^{-1} for the second Stocks component. the threshold value of SLFRS excitation was 0.035 GW/cm^2. The threshold for backward and forward scattering was approximately the same. Line width and divergence of SLFRS were nearly the same as the corresponding values of the laser light. Maximum conversion efficiency for both cases was about 10 per cent. At the experimental conditions of excitation SBS in PVX in Tris-HCl pH7,5 buffer and PVA in water suspension was not registered but in Tris-HCl pH7,5 buffer and water it was excited and its frequency shifts were measured.

3. Conclusions

SLFRS was excited with high efficiency conversion in PVX in Tris-HCl pH7,5 buffer and PVA in water suspension was registered both for forward and backward directions. High efficiency conversion gives possibility to use SILFRS as the source of biharmonic pump for pulsed impact on virus system with the same eigenfrequencies. SLFRS also can be used for identification of different viruses.

4. References

[1] E. Duval, A. Boukenter, and B. Champagnon, , “Vibration Eigenmodes and Size of Microcrystallites in Glass: Observation by Very-Low-Frequency Raman Scattering” Phys. Rev. Lett. **56**, 2052-2055 (1986).

[2] M. Ivanda et al, “Low-wavenumber Raman scattering from CdSxSe1-x quantum dots embedded in a glass matrix”, Physical Review B **67**, 235329: 1-8 (2003).

[3] M. Montagna, "Brillouin and Raman scattering from the acoustic vibrations of spherical particles with a size comparable to the wavelength of the light", Physical Review B **77**, 045418-1 - 045418 – 9 (2008).

[4] M. Talati, P.K. Jha, “Acoustic phonon quantization and low-frequency Raman spectra of spherical viruses”, Physical Review E, **73**, 011901-1-6 (2006).

[5] Eric C. Dykeman, Otto F. Sankey, and Kong-Thon Tsen, “Raman intensity and spectra predictions for cylindrical viruses”, Physical Review E **76**, 011906 (2007).

[6] A. Balandin, V. Fonoberov, “Vibrational Modes of Nano-Template Viruses”, Journal of Biomedical Nanotechnology **1,** 90-95 (2005).

[7] N.V.Tcherniega et al, “Stimulated scattering caused by the interaction of light with morphology-dependent acoustic resonance”, Optics Letters **35**, 300-302 (2010).

[8] N.V. Tcherniega et al, “Experimental observation of stimulated low-frequency,Raman scattering in water suspensions of silver and gold nanoparticles”, Optics Letters **38**, 824-826 (2013).

[9] O V Karpova et al, “ Stimulated low-frequency Raman scattering in a suspension of tobacco mosaic virus” Laser Physics Letters 13, 085701 (2016)

[10] Atabekov J et al “ Potato virus X: structure, disassembly and reconstitution” Mol. Plant Pathol., 2007, **8**(5), 667-675

[11] J. L. Riechmann, S. Laín, J. A. García “Highlights and prospects of potyvirus molecular biology” J. Gen. Virol.,1992, **73**: 1-16, (1992)

Optimization of Spectral Range of Radiation to Enhance the Efficiency of Phototherapy for Neonatal Jaundice

V. Yu. Plavskii[1], A. V. Mikulich[1], I. A. Leusenko[1], A. I. Tretyakova[1], L. G. Plavskaya[1], N. S. Serdyuchenko[1], J. Gao[2], D. Xiong[2], X. Wu[2]

[1]*B.I. Stepanov Institute of Physics of NAS of Belarus, 68, Nezavisimosti Ave., 220072 Minsk, Republic of Belarus*

[2]*Suzhou Institute of Biomedical Engineering and Technology, 88 Keling Road, Suzhou New district, Jiangsu Province, 215163, P. R. China*

e-mail: a.mikulich@ifanbel.bas-net.by

Abstract: It is shown that efficiency of phototherapy for hyperbilirubinemia of newborns using LEDs depends not only on position of maximum in emission spectrum within the absorption band of bilirubin but also on width of spectrum of incident radiation.

1. Introduction

Phototherapy for hyperbilirubinemia of newborns is the most striking example of efficiency of application of optical technologies in medicine. The method is based on exposure of body surface of newborn to optical radiation of blue-green spectral region corresponding to the absorption band of bilirubin. Structural (lumirubin) and *cis-trans*-isomers of bilirubin (*Z,E*-bilirubin, *E,Z*-bilirubin) being more hydrophilic compounds are better excreted from organism than the native Z,Z-bilirubin. However, the problem of enhancement of efficiency of neonatal jaundice treatment is still actual despite a widespread usage of new LED sources in clinical practice to reduce bilirubin level in the blood of newborns.

The aim of the present work is to discuss from the point of view of photobiophysics the possible ways to enhance the efficiency for treatment of conjugated hyperbilirubinemia by optimization of spectral range of acting radiation and its intensity.

2. Materials and methods

The phototherapy procedure for newborns with syndrome of conjugated hyperbilirubinemia was carried out using phototherapeutic apparatus LEDlife developed by us on the basis of LEDs. The apparatus provided the possibility of exposure of body surface of newborn either to radiation of LED sources (Fig. 1) with fluence rate of 0,5 - 2,0 mW/cm^2 and emission maximum $\lambda \approx 462$ nm (blue spectral region) or simultaneously - to radiation of two types of LEDs - $\lambda \approx 462$ nm and 505 nm (blue-green spectral region).

3. Results and discussion

It is established in the experiments (Fig. 2) on study of regularities of newborns' blood photobleaching with increased level of bilirubin (obtained during the exchange transfusion) that due to the shielding effect of hemoglobin in the region of 400 - 450 nm it is the most prospective for phototherapy of hyperbilirubinemia of newborns to use the LEDs with emission maximum corresponding to the long-wavelength slope of the absorption band of bilirubin.

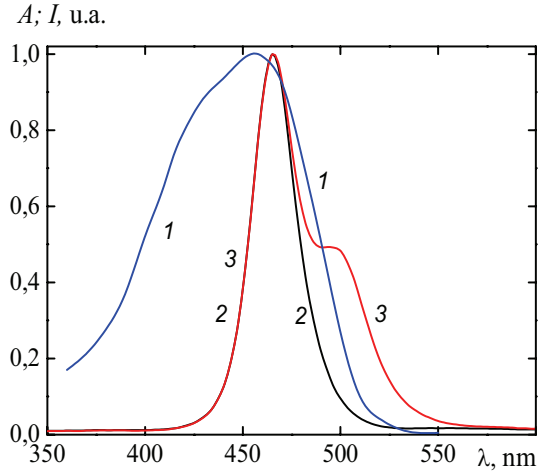

Fig. 1. Absorption spectra of bilirubin in a complex with human serum albumin (*1*) and emission spectra of LEDs of blue (*2*) and blue-green (*3*) spectral regions used for phototherapy of hyperbilirubinemia of newborns

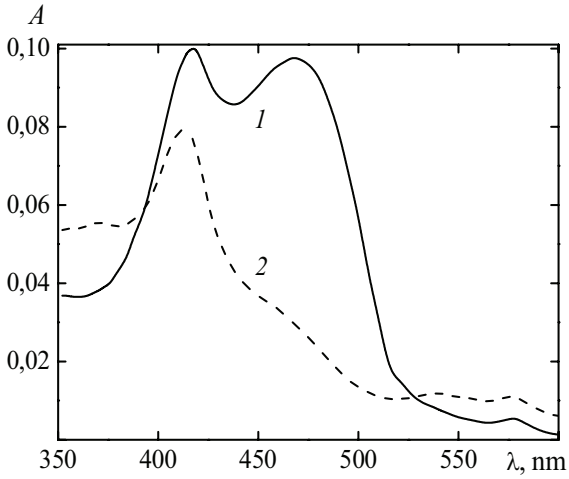

Fig. 2. Absorption spectra of partially hemolyzed blood of newborns with increased level of bilirubin before (*1*) and after (*2*) exposure to radiation of blue spectral region (dose - 21.6 J/cm^2)

At the same time, the efficiency of phototherapy depends not only on the position of maximum in emission spectrum of LEDs within the absorption band of bilirubin but also on the width of the spectrum of acting radiation. It has been for the first time shown in comparative studies that expansion of spectral range of radiation by adding the green component with $\lambda \approx 505$ nm to light of blue range with $\lambda \approx 462$ nm (under conditions with equal integrated fluence rate) increases the efficiency of reduction of total bilirubin level in the blood of newborns (Fig. 3). The efficiency of reduction of bilirubin level in the blood of newborns depending on the fluence rate of acting radiation in the range of 0.5 - 2.0 mW/cm^2 is approximated by a linear function.

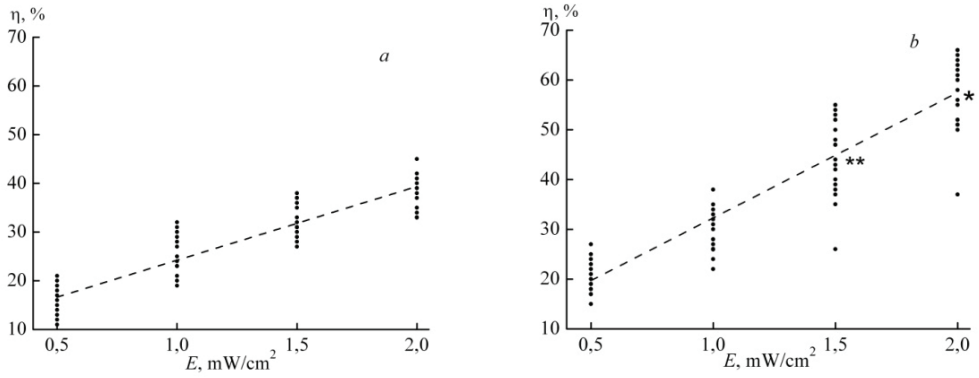

Fig. 3. Efficiency of reduction of bilirubin level in the blood of newborns after 24 h phototherapy using radiation of LEDs of blue (*a*) and blue-green (*b*) spectral regions in dependence on fluence rate of acting radiation (*$p < 0.01$; ** $p < 0.05$)

4. Conclusions

It is shown that the reasons of dependence of therapeutic effect on spectral composition of acting radiation within long-wavelength absorption band of bilirubin are following:

a) heterogeneity of absorption and isomerization characteristics of bilirubin in a complex with albumin due to localization of pigment in different binding sites on protein globule; influence of fatty acids and medicinal drugs on structure of pigment bound to albumin; structural heterogeneity of protein-carrier due to its ability to present in different aggregative states both in bloodstream and in extravascular area); b) dependence of optimal wavelength of radiation for photoisomerization of pigment on the depth of blood vessels which are the site for occurrence of photochemical reactions.

Furthermore, the expansion of the spectral range of acting radiation by addition of green component increases the yield of lumirubin due to displacement of equilibrium between *cis-trans*-isomers of bilirubin (*Z,E*-bilirubin, *E,Z*-bilirubin) towards the formation of *E,Z*-bilirubin (intermediate in the formation of lumirubin) as well as the volumes of blood being irradiated in which the reactions of photoisomerization are initiated underlying the therapeutic action of light when treating the hyperbilirubinemia of newborns. Thus, the efficient isomerization of bilirubin molecules in blood vessels (capillaries) which are localized at different depth from the skin surface (in range of 0 - 2 mm) is initiated by different wave lengths. For this reason, the usage of broadband radiation with spectrum corresponding to the long-wavelength slope of the absorption band of bilirubin has certain advantages over monochromatic (quasi-monochromatic) radiation.

Sensitizer-nanoparticles for tissue diagnostics and PDT

Rudolf Steiner[1,4], Claudia Scalfi-Happ[1], Rainer Wittig[1], Anastasia Ryabova[2,4], Susanna Gräfe[3] and Victor Loschenov[2,4]
[1]*Institute of Laser Technologies in Medicine and Metrology at the University of Ulm, Helmholtzstr. 12, 89081 Ulm, Germany*
[2]*A.M. Prokhorov General Physics Institute, RAS, 38 Vavilov Str., 119991 Moscow, Russia*
[3]*Biolitec Research GmbH, Otto-Schott-Str. 15, 07745 Jena, Germany*
[4]*National Research Nuclear University (MEPhI), Kashirskoe highway 31, Moscow 115409, Russia*
rudolf.steiner@ilm-ulm.de

Abstract: Nanoparticles of different kind of materials are used to enhance tissue diagnostics or the efficacy of photodynamic treatment. However, approved substances are mostly molecular solutions of porphyrins, phthalocyanines or chlorins. But it is also possible to use nanoparticles (NPs) of the raw material of such organic compounds, which are not soluble in water and not fluorescent. In-vitro experiments with mTHPC show that mainly macrophages will take up the NPs. Inside cells molecules are dissolved from the NPs, are fluorescent and photoactive. Therefore, NPs of mTHPC can specifically be used for fluorescence diagnostics of inflamed or cancerous tissue and for PDT.

Nanoparticles made from aluminum phthalocyanine (AlPc) raw material, or mTHPc, are non-fluorescent because of fluorescence quenching due to the molecular crystalline structure forming a stack of flat molecular layers. However, when AlPc molecules become detached from the particles, fluorescence occurs. First observations demonstrated the benefit of using aluminum phthalocyanine nanoparticles (nAlPc) for the assessment of the rejection risk of skin autografts in mice by measuring fluorescence intensities of detached AlPc molecules. Skin autografts showing a high fluorescence intensity of AlPc were finally rejected induced by an inflammatory process. In contrast, autografts with normal skin autofluorescence were accepted [4]. Therefore, nanoparticles or nano-emulsions from appropriate photosensitizers like porphyrins, chlorins or phthalocyanines, offer a new promising drug delivery system for hydrophobic sensitizers [1, 2]. They can be used for fluorescence diagnostics and treatment by photodynamic therapy (PDT) [3]. However, the reaction process has to be evaluated.

Nanoparticles made from large-dispersed aluminum phthalocyanine (nAlPc), or mTHPc, crystals are forming a stable colloid suspension. The nanoparticles are therefore suitable for clinical use by the possibility of good transportation in aqueous media and penetration into tissue. They are also suitable for fluorescence diagnostics because such nanoparticles do not fluoresce but when molecules dissolve from the nanoparticles, in the monomeric molecular form, fluorescence occur [3, 4]. This finding could be used to specifically detect inflammatory processes (figure 1) or tumors and will have the potential of using nAlPc, or mTHPc nanoparticles as a new treatment modality for PDT.

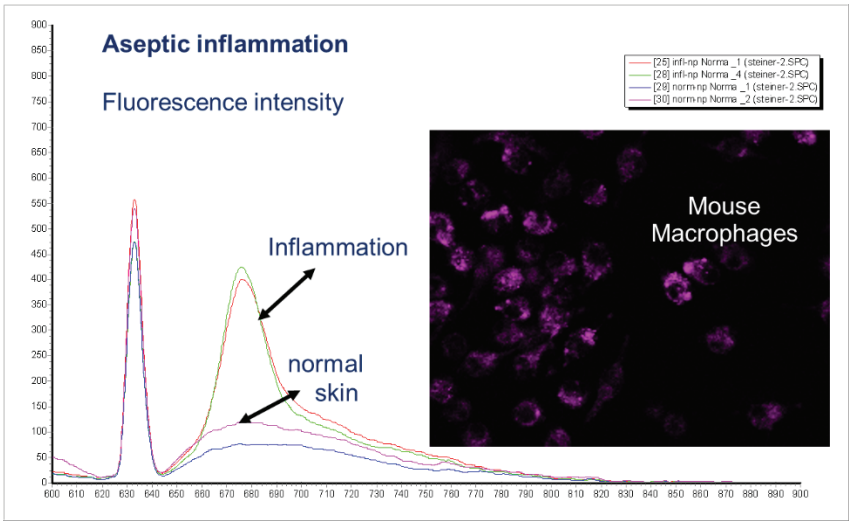

Figure 1: Fluorescence of tissue inflammation, after macrophages have taken up mTHPC nanoparticles and molecules have dissolved from the nanoparticles inside the cells.

Beside fluorescence, spectroscopic and microscopic techniques, confocal Raman micro-spectroscopy has become a powerful tool for the investigation of living cells and biological samples [5]. In a previous study we investigated the role of lipids in the discrimination between Caco-2 colon carcinoma cell line and the rat intestine epithelial cell line IEC-6 by confocal Raman microscopy [6] with the alpha300 R Raman microscope (WITec GmbH, Germany). To elucidate the fluorescence appearance of AlPc molecules after detachment from

the nanoparticles, also the Raman-micro-spectroscopic approach to follow the cellular uptake of photosensitizer nanoparticles in their crystalline, non-fluorescent form, might be helpful (figure 2). Crystalline nanoparticles of different size made from hydrophobic porphyrin-derived photosensitizer were applied to either L929 murine fibroblasts or to J774A.1 murine monocytes or macrophages and the results compared with the properties of the sensitizer Foslip®. In a further step, the dissolution process of the nanocrystals with increasing fluorescence signal was evaluated.

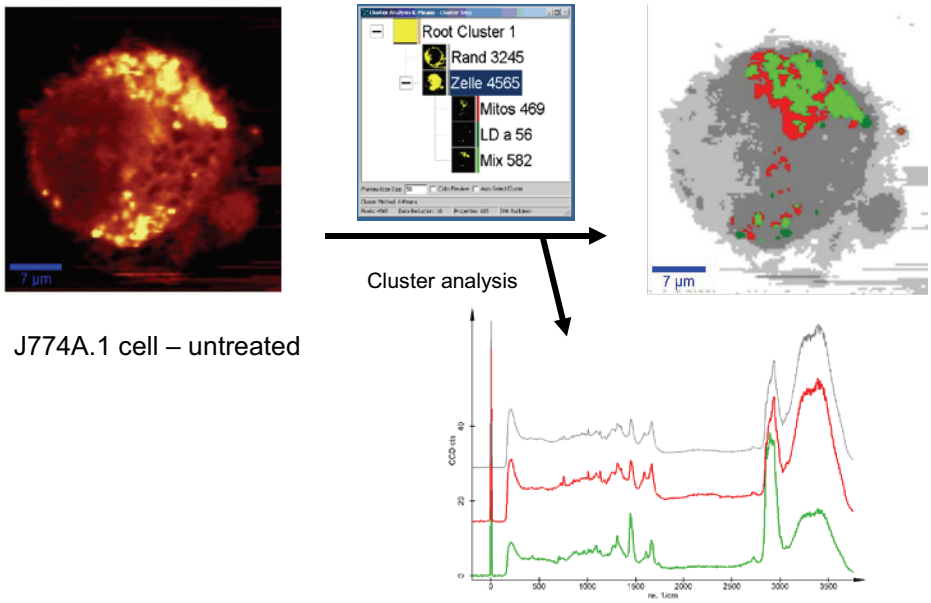

Figure 2: Raman microscopic imaging of the chemical content of macrophages after uptake of nanoparticles to see intracellular reaction mechanisms.

These investigations will help to understand the effect of photosensitizer particle size on cellular uptake and the differences in internalization mechanisms of the studied cell lines and the dissolution of photoactive molecules from the nanoparticles for diagnosis and PDT. The reactions of different types of macrophages will also be discussed.

[1] Lademann J, Richter H, Meinke MC, Lange-Asschenfeldt B, Antoniou C, Mak WC, et al.
Skin Pharmacol Physiol2013;26 (4—6):227—33.
[2] Dias Ribeiro AP, Carvalho Andrade M, de Fátima da Silva J, Habib Jorge J, Primo FL, Tedesco AC, et al.
Photochem Photobiol 2013; 89 (1):111—9.
[3] Zhang J, An F, Li Y, Zheng C, Yang Y, Zhang X, et al.
Chem Com-mun (Camb) 2013, http://dx.doi.org/10.1039/c3cc43413c.
[4] Vasilchenko SY, Volkova AI, Ryabova AV, Loschenov VB, Konov VI, Mamedov AA, et al. J Biophoton 2010;3(5—6):336—46.[5] Korbelik M. J Photochem Photobiol B: Biol 1993;20:173—81.
[5] Scalfi-Happ C., Rück A., Udart M., Hauser C., Dürr C. and Kriebel M., “Label-Free Detection of Tumor Markers in a Colon Carcinoma Tumor Progression Model by Confocal Raman Microspectroscopy”, Proc. of OSA-SPIE Vol. 8798 87980B-1, doi: 10.1117/12.2032459 (2013).
[6] Scalfi-Happ C, Jauss A, Hollricher O, Fulda S, Hauser C, Steiner R, Rueck A. “Confocal Raman microscopy for investigation of the level of differentiation in living neuroblastoma tumor cells”. Proc SPIE 2007, 6630:66300T. Doi:10.1117/12.729455, (2007).

Sapphire Shaped Crystals for Phototheranostics and Combined Anticancer Therapy

Shikunova I.A.[1], Volkov V.V.[2], Kurlov V.N.[1]
[1]Institute of Solid State Physics, Russian Academy of Sciences, Chernogolovka, Russia
[2]Center of Natural Research, General Physics Institute, Russian Academy of Sciences, Moscow Russia
E-mail: sh_irina@issp.ac.ru

Sapphire has a high refractive index and a broad transmission band spanning the UV, visible, and IR bands. Sapphire also has high hardness, very good thermal conductivity, tensile strength, and thermal shock resistance. The favorable combination of excellent optical and mechanical properties of sapphire, together with high chemical inertness and biocompatibility, high resistance to human blood and body fluids, makes it an attractive structural material for medicine. We have developed a new kind of medical instruments and devices for combined laser photodynamic therapy and thermal therapy, laser surgery, fluorescent diagnostics, and cryosurgery based on sapphire crystals of various shape with capillary channels in their volume.
Sapphire smart scalpels with simultaneous incision and fluorescent diagnostics of a resected tissue immediately during surgical operation have been developed. The principle of the new system is based on the use of isolated capillary channels in the volume of the sapphire scalpel for introducing of quartz waveguides, Fig. 1. One of the waveguides is used for delivering the laser radiation directly to the narrow region of the cutting edge and local excitation of photoluminescence. Another one is used for catching and transfer of photoluminescence to spectrometer. The scalpel employs rapid real-time feedback analysis for on-line diagnostics of tissues during surgery to remove a tumor. A laser optically coupled directly inside the edge allows obtain effective concentration of the laser energy in the area of the cutting edge of the scalpel for coagulation blood adjacent incision[1,2].

Fig.1. Sapphire ribbon with three capillary channels of 0.5 mm in diameter (at the left). Sapphire scalpel for diagnostic and coagulation on incised tissue during a surgical operation (at the right).

Sapphire needle capillaries were developed as new laser waveguide introducers for delivery radiation into a tumour during interstitial laser photodynamic therapy, thermotherapy, and ablation oh tumors, Fig. 2. These needles allow one to increase the irradiation volume substantially, to obtain an optimal temperature distribution, to simplify the design, and to eliminate a system for cooling the device. The high hardness of sapphire provides a stable point on the irradiator end for independent introduction of the irradiator into the tissue without using directors that lead to the increase in irradiator cross-section. The use of sapphire irradiators make it possible to improve the control over the dynamics of spatial photothermal distribution during the whole irradiation procedure, since the effective redistribution of released heat by the sapphire decreases the possibility of formation of overheating nuclei, leading to the appearance of thrombi, nontransparent to laser radiation[3].

Fig.2. At the left: sapphire needle capillaries (external diameter of 1.2 mm, internal diameter of 0.5 mm): (a) as grown closed capillary; (b) capillary with a point formed by mechanical operation of the butt; (c) capillary with a point and diffuser formed by mechanical operation. At the right: sapphire needle combined with quartz fiber (the geometry of light field).The geometry of light field in sapphire needle (OD 1.2 mm, ID 0.5 mm) combined with quartz fiber.

Also the system for removal of brain tumors based on a sapphire multi-channel probe with demarcation of borders of a tumor by fluorescent diagnostics with simultaneous coagulation and aspiration was developed, Fig. 3. It carries out simultaneous laser coagulation for a hemostasis, tumor aspiration via the through channel of a

sapphire probe, and also makes local optical measurements of properties of brain tissue for more exact and full removal of malignant tissue[4].

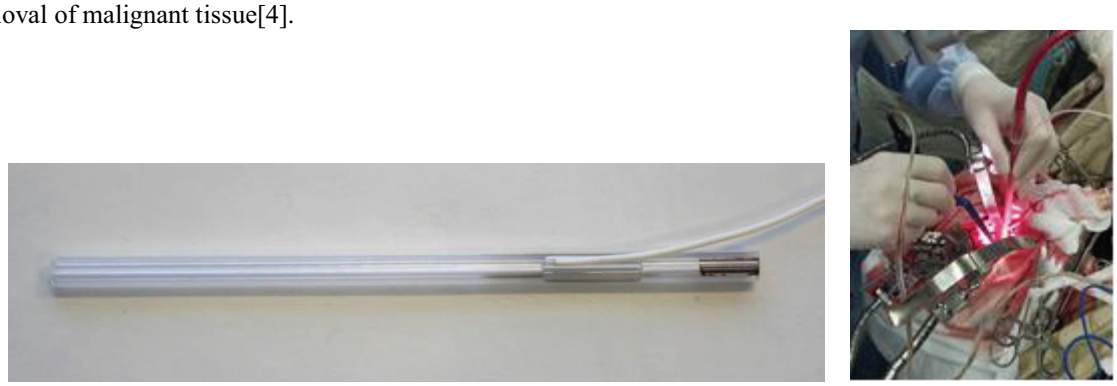

Fig.3. Sapphire multichannel probe for neurosurgery. Surgical operation on brain tumor removal using the sapphire probe for neurosurgery

The ability for broadband low-loss THz waveguiding in sapphire multichannel shaped crystals was demonstrated. The EFG/Stepanov technique of shaped crystal growth has been used to manufacture the THz photonic crystalline waveguide, Fig.5 The waveguide has been characterized via both numerical simulations and experiments: It allows guiding the THz-waves in multi-mode regime with the minimal power extinction coefficient of 2 dB/m at 1.45 THz [5]. These results demonstrate the capabilities of combining the EFG/Stepanov technology advantages with unique properties of sapphire (relatively low THz-wave absorption, high mechanical, thermal, chemical and radiation strength) for manufacturing the THz waveguides and endoscopic systems for medical applications of TPS.

Fig. 4. Sapphire terahertz photonic crystal waveguides

References

[1] Kurlov V N, Rossolenko S N, Abrosimov N V and Lebbou Kh 2010 Duffar Th. (Ed.) 2010 *John Wiley & Sons* 277

[2] Shikunova I A, Volkov V V, Kurlov V N, and Loshchenov V B, 2009 *Bull. Russ. Acad. Sci.: Phys.* 1345 73(10)

[3] Kurlov V N, Shikunova I A, Ryabova A V, Loschenov V B, 2009 *Bull. Russ. Acad. Sci.: Phys.* 1341 73(10)

[4] Kiselev A.M., Esin I.V., Shikunova I.A., Kurlov V.N., Tereshchenko S.G., Lapaeva L.G. Combined neuronavigation in surgery of cerebral malignant tumor// Almanac of clinical medicine, 2011, № 25, 58 - 63.

[5] K.I. Zaytsev, G.M. Katyba, V.N. Kurlov, I.A. Shikunova, V.E. Karasik, S.O. Yurchenko, "Terahertz Photonic Crystal Waveguides Based on Sapphire Shaped Crystals," IEEE Transactions on Terahertz Science and Technology 6(4), 576–582 (2016).

Spectral luminescent properties of bacteriochlorin and aluminum phthalocyanine nanoparticles as hydroxyapatite implant surface coating.

A.S. Sharova[1], Yu. S. Maklygina[2], B. Kundu[3], V.K. Balla[3], R. Steiner[4], V.B. Loschenov[1, 2]

[1]National Research Nuclear University MEPhI, Russia, Moscow

[2]A.M. Prokhorov General Physics Institute RAS, Russia, Moscow

[3]Bioceramics and Coating Division, CSIR-Central Glass and Ceramic Research Institute, India, Kolkata

[4] The Institute for Laser Technology in Medicine and Measurement Technique, Germany, Ulm

E-mail address:join93@rambler.ru

Abstract

The spectral luminescent properties of developed by us coating for the hydroxyapatite implants were experimentally investigated in this study. Crystalline bacteriochlorin and aluminum phthalocyanine nanoparticles with photobactericidal properties were used as an implant coating. This research opens the prospect of such technology application in order to provide the local inflammatory and autoimmune reactions prevention in the area of implantation.

Introduction

Surgical intervention with subsequent implantation is a difficult process in terms of post-operative recovery, preventing of inflammatory responses and the implant rejection processes. Currently, the most promising methods for the bactericidal effect achievement in the area of implantation are physical methods, particularly antimicrobial photodynamic therapy [1]. This method shows a pronounced photobactericidal activity and anti-inflammatory effect. Antimicrobial photodynamic therapy also prevents the dystrophic and sclerotic processes that can effectively reduce the risk of implant rejection and accelerate biointegration.

Materials and methods

The most perspective material, which is widely used in the field of clinical implantation our days, is hydroxyapatite. Hydroxyapatite is characterized by high stability, bioactivity and biocompatibility [2]. The photosensitizers in nanoform are used as effective photobactericidal substances for implant coating, which do not exhibit their photodynamic activity in the absence of inflammatory agents [3]. Meso-tetra(3-pyridyl)bacteriochlorin (Bch NPs) and non-sulfonated aluminum phthalocyanine (AlPhc NPs) were investigated as photosensitizers, that can provide the greatest penetration depth of photodynamic treatment. Test compounds have the absorption peak in the near infrared and red ranges, respectively. Such spectral medicines' features correspond to the maximum optical transparency region of biological tissues that considers Bch NPs and AlPhc NPs to be the most promising photosensitizers, especially in monitoring of pathological processes with deep localization [4, 5].

The luminescence spectra of Bch NPs and AlPhc NPs were examined with the use of a fiber spectrometer LESA-01-"BIOSPEC" [6] (in the range of 0.4 ÷ 1.1 μm) in various conditions including the interaction with surface hydroxyapatite molecules. The excitation of nanoparticles was realized by laser radiation sources with power density of ~100 mW/cm^2 and λ = 532 nm, 632.8 nm wavelengths, selected in accordance with photosensitizers absorption spectra peaks.

Results

The analysis of the luminescence spectra dynamics for the both types of crystalline nanoparticles have shown that initially inphotoactive photosensitizers' nanocrystals acquire the ability to luminescence in interaction conditions with hydroxyapatite surface molecules. However, the luminescence peaks intensity varies over time under the influence of the exciting laser radiation (Fig.1).

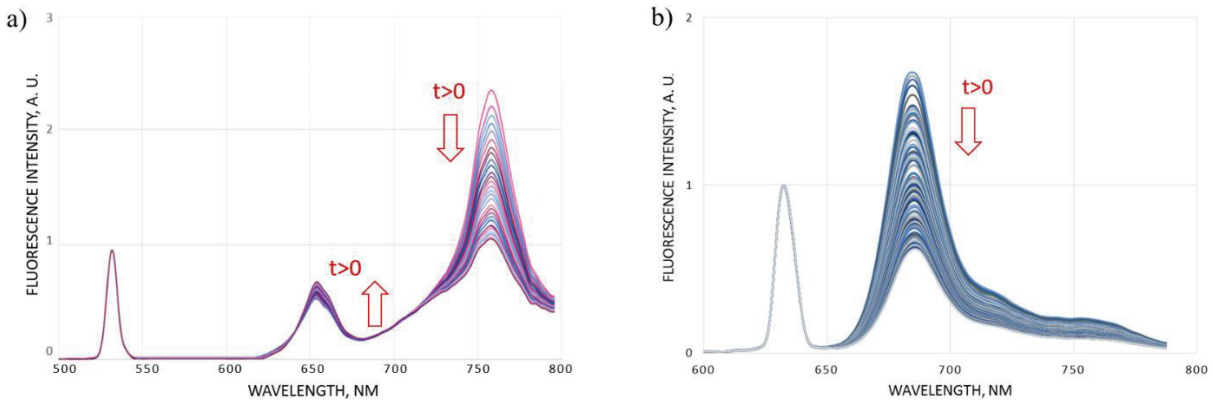

Fig.1. The dynamics of the luminescence spectra time transforming of the implant based on hydroxyapatite covered with a) Bch NPs (λ_{ex} = 532 nm); b) AlPhc NPs (λ_{ex} = 632.8 nm).

Conclusion

The possibility of the nanoparticles activation on the surface of covered implant was proved during the study. The activity level of nanoparticles was estimated by the control of photoluminescence intensity. Based on the research it was concluded that the photosensitizers' nanoparticles interact both among themselves and with a complex porous structure of the implant. The findings of the study suggest this technology promising in order to create implants with photobactericidal properties.

References

[1] Haag PA, Steiger-Ronay V, Schmidlin PR, «The in Vitro Antimicrobial Efficacy of PDT against eriodontopathogenic Bacteria», Int J Mol Sci., 16(11), 27327-38 (2015 Nov 13).

[2] Nandi SK, Kundu B, Mukherjee J, Mahato A, Datta S, Balla VK, «Converted marine coral hydroxyapatite implants with growth factors: in vivo bone regeneration», Mater Sci Eng C Mater Biol Appl., 49, 816-23 (2015 Apr).

[3] Ryabova A., Steiner R., Loschenov V, «The crystalline nanoparticles from photosensitizers capable to metamorphose in biotissue», (International Conference on Laser Applications in Life Sciences LALS, Ulm, Germany, 29 June-2 July 2014).

[4] Vasilchenko S.Yu., Volkova A.I., Ryabova A.V., Loschenov V.B., Konov V.I., Mamedov A.A., Kuzminand S.G., Lukyanets E.A., «Application of aluminum phthalocyanine nanoparticles for fluorescent diagnostics in dentistry and skin autotransplantology», J. Biophoton., 3, No. 5–6, 336–346 (2010).

[5] Oertel, M., Schastak, S. I., Tannapfel, A., Hermann, R., Sack, U., Mossner, J., Berr, F., «Novel bacteriochlorin for high tissue-penetration: photodynamic properties in human biliary tract cancer cells in vitro and in a mouse tumour model», J. Photochem. Photobiol. , 71, 1 –10 (2003).

[6] Loschenov V.B., Konov V.I., Prokhorov A.M., «Photodynamic therapy and fluorescence diagnostics», Laser Physics. , 10, No 6, 1188–1207 (2000).

Infrared (3-15 mkm) fiber skin *in vivo* spectroscopy and physiotherapy

L. N. Butvina[1*], A.L. Butvina[1], V. D. Bitsoev[2]
[1] FORC RAS, Moscow, Vavilov str. 38
[2]Moszdrav, Polyclinic 69, Moscow
**E-mail: butvina@fo.gpi.ru*

Abstract: Evanescent infrared spectroscopy by touch of the infrared fiber is a unique, non-traumatic method, does not require special preparation of the skin, is the method of optical biopsy. We have developed new fibers from silver halides with low optical losses in a wide spectral wavelength range of 3-15 μm, which allowed us to obtain spectra of skin in vivo from mild physiotherapy.

Evanescent infrared spectroscopy attenuated total reflection by touch of the infrared fiber is a unique, non-traumatic method, does not require special preparation of the skin by the method of optical biopsy. We have developed new non-toxic, non-hygroscopic fibers from silver halides with low optical losses in a wide spectral wavelength range of 3-15 μm which allowed us to obtain spectra of skin in vivo with good signal-to-noise, even at normal uncooled DTGS Fourier transform spectrometer Bruker. This allowed to reliably determine changes in the absorption spectra of skin in vivo from mild physiotherapy effects. Experiments were conducted to determine the impact of the exposure of the skin by yellow light by means of different devices (Zepter and BIC-1). From practice it is known that such illumination is used in physiotherapy.

Machine Zepter and apparatus BIK-1 are different by the presence of the fiber output radiation by the latter. In the experiment as part of the FTIR was used multimode nanostructured crystalline shell fiber with a diameter of 1 mm and a length of 2 m, connected to the Fourier spectrometer “Vector-22” through the lens of input-output. The spectrum was accumulated over 32 scans of the interferometer, with a spectral resolution of 4 cm-1. The fiber was bent plastically in the form of loop 180 degrees, with a bending radius of 4 mm. At the bend place the fiber cladding is removed by cutting, and that spot is pressed to the skin. The transmission spectrum of the obtained sensor is shown in Fig.1.

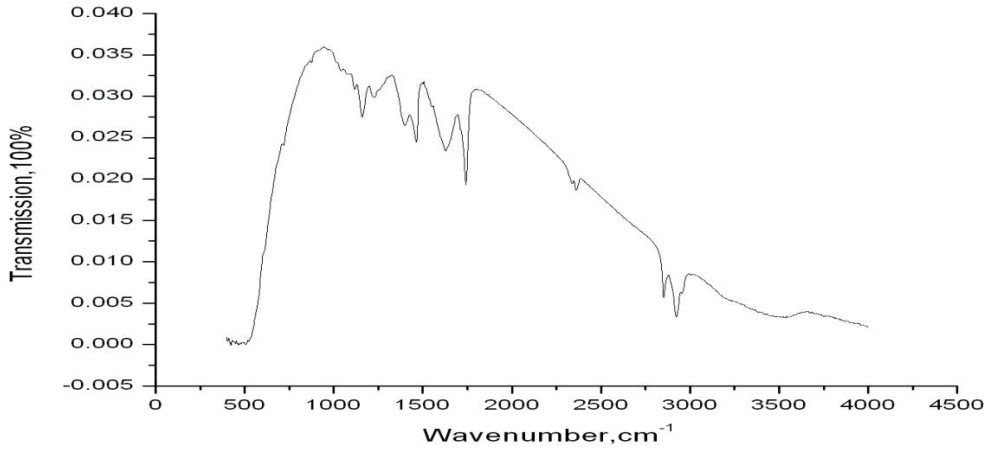

Fig.1

The initial spectrum os evanescent transmittance of the skin is shown inFig.2.

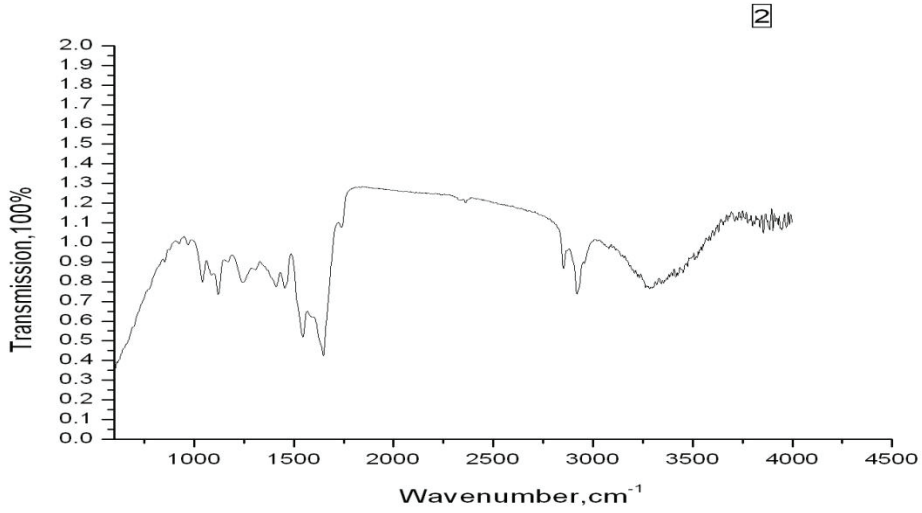

Fig.2

Spectrum after irradiation of this part of skin by apparatus Bic-1(4 min.)- Fig.3

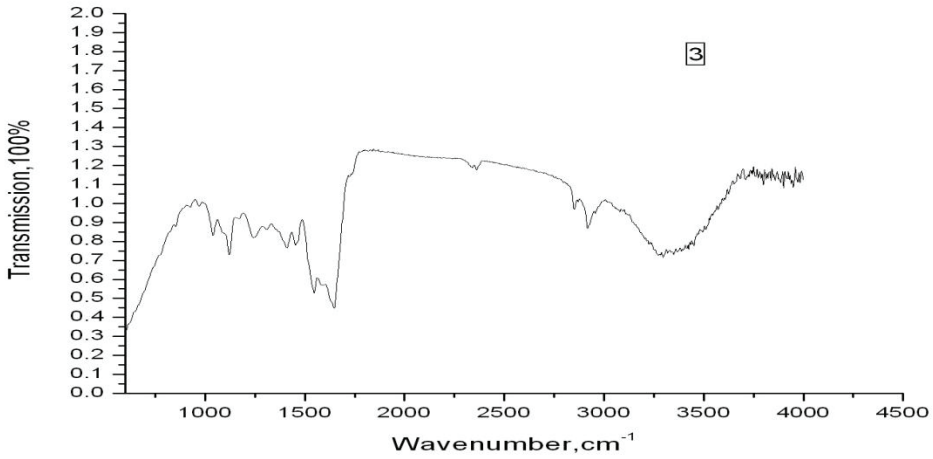

Fig.3

By change of spectra in the range of 900-600 cm-1 band and in the 3200-3500 cm-1 one can judge about changing the extent of hydration of the top layer of skin the stratum corneum.
It was discovered that the transmission on the slope of 600-900 cm-1 and in water lane 3200-3500 cm-1 was increased after exposure of Zepter, which shows the decrease of the degree of hydration of the top layer of the skin. Spectra of the skin after irradiation by apparatus BIK-1 indicate the preservation or even increase the extent of hydration of the stratum corneum of the skin. It is shown that spectra of skin are very informative and can be used to analyze through-dermal transport of any molecular substances and biopsy of skin changes.

Dissection of biological tissues under the influence of pulsed and quasi-continuous laser radiation

G.I. Zheltov[1], V.D. Burko[2], O.G. Romanov[3*]

1) B.I. Stepanov Institute of Physics of the National Academy of Sciences of Belarus; Minsk, 220072, Republic of Belarus
2) The Republican Clinical Medical Centre, Minsk, 220030, Republic of Belarus
3) Belarusian State University, Minsk, 220030, Republic of Belarus
**romanov@bsu.by*

Abstract: Physical basis of low-temperature laser ablation of biological tissues under pulsed and quasi-continuous laser radiation have been developed. The physical and mathematical models of thermo-mechanical effect of pulsed radiation on absorbing tissues are presented, and numerical modeling has been performed for typical laser systems used in laser surgery.

The irradiation of biological tissues with laser light sources is used in many medical procedures. Different mechanisms of interaction of laser radiation with biological tissues can be implemented depending on power, duration and repetition rate of the laser pulses, and depending on total time of irradiation [1]. In the case of laser pulses of pico- or nanosecond duration with an intensity of about 10^{10} W/cm^2, the most probable are the processes of photo ablation of tissue and the destruction of the structure due to optical breakdown of biological membranes in an intense light wave field. Thermal effects (hyperthermia, coagulation, etc.) play a major role under exposure time from milliseconds to minutes and the intensity of the radiation of about 1-10^3 W/cm^2 [2, 3].

Under the action of laser pulses with duration of less than 10^{-5} seconds the conditions for photo excitation of acoustic vibrations in non-uniformly heated tissues are usually fulfilled [4]. With increasing of intensity and decreasing of duration of exposure the probability of destruction (ablation) of tissue structure caused by cavitation [5] and optical (dielectric) breakdown [6] are increased.

Effect of cavitation is caused by the formation of the acoustic waves with a positive (compression) and negative (extension) phase in the irradiated area. Most of biological structures have a relatively high resistance to compressive stresses and significantly weaker resist the action of extension stresses. If the absolute value of extension stress in the negative phase of the pressure wave is greater than the extension threshold of the medium, there is a high probability of local tissue fragmentation followed by the formation of cavitation micro-bubbles [6]. This phenomenon can be the basis for the development of new principles of non-thermal, so called "cold" laser surgery, which provides increased selectivity of photo ablation of biological structures with different photo-physical properties and intactness of healthy tissue in the operating zone boundaries.

This work is devoted to the theoretical study of the thermo-mechanical effects under action of pulsed laser radiation on biological tissue. Methods for solving the problem is based on the numerical simulation of equations of motion of continuous media in the Lagrange form [7].

The continuity equation in the Lagrange coordinates is of the form:

$$V = V_0 \Delta \tag{1}$$

where $\Delta \equiv \partial(X,Y,Z)/\partial(x,y,z)$ is the Jacobian of the transformation from Euler coordinates (X,Y,Z) to Lagrangian coordinates (x,y,z); $V_0 = 1/\rho_0$, $V = 1/\rho$ are the initial and the current specific volumes, ρ_0 and ρ are the initial density.

The equations of motion in the Lagrangian form in the absence of external forces:

$$\frac{\partial^2 X}{\partial t^2}\frac{\partial X}{\partial x} + \frac{\partial^2 Y}{\partial t^2}\frac{\partial Y}{\partial x} + \frac{\partial^2 Z}{\partial t^2}\frac{\partial Z}{\partial x} = -\frac{1}{\rho}\frac{\partial P}{\partial x}; \tag{2}$$

$$\frac{\partial^2 X}{\partial t^2}\frac{\partial X}{\partial y} + \frac{\partial^2 Y}{\partial t^2}\frac{\partial Y}{\partial y} + \frac{\partial^2 Z}{\partial t^2}\frac{\partial Z}{\partial y} = -\frac{1}{\rho}\frac{\partial P}{\partial y}; \tag{3}$$

$$\frac{\partial^2 X}{\partial t^2}\frac{\partial X}{\partial z} + \frac{\partial^2 Y}{\partial t^2}\frac{\partial Y}{\partial z} + \frac{\partial^2 Z}{\partial t^2}\frac{\partial Z}{\partial z} = -\frac{1}{\rho}\frac{\partial P}{\partial z}. \tag{4}$$

Equations of change of Euler coordinates:

$$\frac{\partial X}{\partial t} = u_X, \ \frac{\partial Y}{\partial t} = u_Y, \ \frac{\partial Z}{\partial t} = u_Z \tag{5}$$

Equation of state in the form of Mie-Grueneisen:

$$P = P_C + P_H = \rho_0 u_0^2 (1 - V/V_0) + \Gamma C_V (T - T_0)/V, \tag{6}$$

where P_H and P_C are thermal and cold pressure components; $\Gamma = u_0^2 \beta / C_V$ is the Grueneisen coefficient; β is

the coefficient of volumetric expansion; C_V is the heat capacity of the medium, u_0 is velocity of sound.

The heat transfer equation is:

$$\rho C_V \frac{\partial T}{\partial t} = k_T \left(\frac{\partial^2 T}{\partial x^2} + \frac{\partial^2 T}{\partial y^2} + \frac{\partial^2 T}{\partial z^2} \right) + Q_S \,. \tag{7}$$

Here k_T is thermal conductivity of the medium; the value Q_S volume density of energy release: $Q_S = I(x,y,z,t)k_{abs}$, where $I(t,x,y,z)$ is the intensity of the laser beam, k_{abs} is the spectral absorption coefficient. The model allows us to calculate three-dimensional spatial-temporal distribution of pressure and predict the development of cavitation phenomena under laser irradiation on different biological structures.

Based on developed model a simulation of the kinetics of thermal stresses and strains arising from the pulsed and quasi-continuous laser radiation on biological tissue has been performed in a wide range of parameters of the exciting laser pulse and the absorbing medium. Particular attention is paid to the study of quasi-continuous exposure to radiation pulse having a relatively short leading front that provides isochoric heating of the tissue near the irradiated surface. It is shown that the bipolar acoustic wave, which arises in the medium, stimulates the formation of cavitation micro-bubbles, which cause a local optical enlightenment irradiated environment. Thus, the conditions for the isochoric heating of the tissue layer located deeper than zone of optical enlightenment becoming fulfilled. The front of heating are moving deep into biological tissue, and stimulates the generation of new acoustic pulse, which also can destroy the continuity of tissue due to formation of cavitation micro-bubbles. The process can continue when energy conditions for obtaining threshold values of the amplitude of acoustic pulse are fulfilled. The simulation results of this mode are shown in Figs.1, 2 in the form of space-time dependences of temperature and pressure in the medium. The analysis of spatial-temporal dynamics of the fields of temperature and pressure allows an assessment of the efficiency and speed of ablation of tissue from the radiation characteristics and physical properties of the medium. The results of modeling are in agreement with the experience of clinical use of surgical equipment based on Ho-laser with typical parameters: wavelength λ = 2100 *nm*, energy of pulse E = 1.5-2.5 *J*, beam size r = 400-600 μm, duration of leading front τ = 100 *ns* [8].

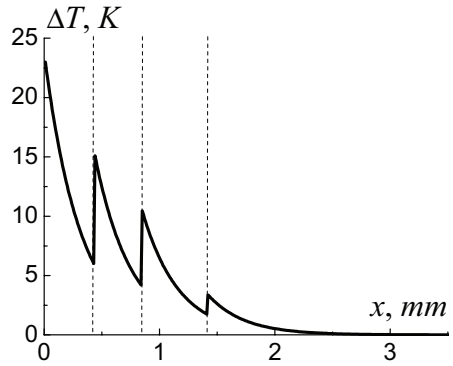

Fig.1. Distribution of temperature in the medium along the laser pulse propagation. The moving boundary of irradiated zone is depicted.

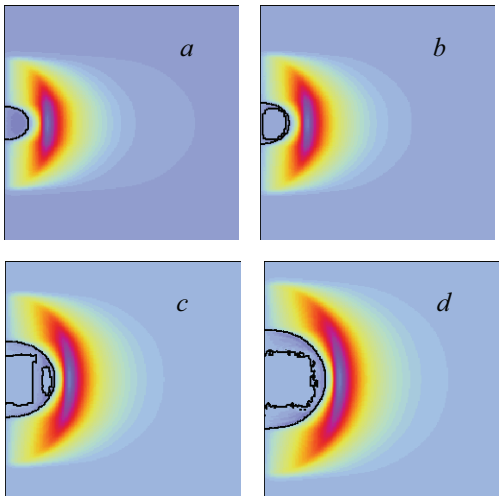

Fig.2. Spatial distribution of pressure in the medium (3.5x3.5 *mm*) in the following time steps: *t*=450 (*a*), 500 (*b*), 650 (*c*), 750 (*d*) *ns* from the start of laser pulse irradiation. The areas of formation of tissue discontinuity are noted.

References

[1] M. H. Niemz, *Laser-tissue Interactions: Fundamentals and Applications* (Springer-Verlag, Germany, 2003).

[2] T. Vo-Dinh, *Biomedical Photonics Handbook* (CRC Press, Boca Raton, 2003).

[3] J. Ashley and M. Welch, *Optical-thermal Response of Laser-irradiated Tissue* (Plenum Press, New York, 1995).

[4] L. M. Lyamishev *Laser Thermooptical Excitation of Sound*. Moscow: Nauka, 1989 (in Russian).

[5] G. I. Zheltov, V. A. Lisinetskii, A. S. Grabtchikov and V. A. Orlovich, "Low-threshold cavitation in water using IR laser pulse trains," Applied Optics **47**, 3549-3554 (2008).

[6] A. Vogel, N. Linz, S. Freidank and G. Paltauf, "Femtosecond-laser-induced nanocavitation in water: implications for optical breakdown threshold and cell surgery," Phys. Rev. Lett. **100**, 038102 (2008).

[7] O. G. Romanov, G. I. Zheltov and G. S. Romanov, "Numerical modeling of thermomechanical processes in absorption of laser radiation in spatially inhomogeneous media," J. of Eng. Phys. Thermophys. **84**, 772-780 (2011).

[8] V. D. Burko, P. Althaus, A. V. Strotsky, G. Zimmermann and U. Shmidt. Patent EA-B1-009381 (2007).

Laser Induced Relaxation of Triplet States for Sterically Distorted Metalloporphyrins

E. Zenkevich[1], A. Starukhin[2], V. Knyukshto[2], A. Gorski[3], M. Kijak[3], J. Solarski[3], A. Semeikin[4], T. Lyubimova[4], J. Waluk[3]

[1]*National Technical University of Belarus, Minsk 220013, Belarus*

[2]*B.I. Stepanov Institute of Physics, NAS of Belarus, 220072 Minsk, Belarus*

[3]*Institute of Physical Chemistry, PAN, Kasprzaka 44/52, Warsaw, Poland*

[4]*Ivanovo State University of Chemistry and Technology, 153000 Ivanovo, Russia*

E-mail: zenkev@tut.by

Within last decade, it was shown that for porphyrins, in which deformations from a planarity are induced by the interaction of bulky side substituents with tetrapyrrole macrocycle, various types of non-planar deformations are realized in ground and excited singlet states accompanied by the noticeable changes of optical, photophysical and redox properties of tetrapyrrole compounds. In this respect, time-resolved laser spectroscopy seems to be considered as a powerful tool for the studying such sterical hindrance effects in various solvents and in a wide temperature range.

We have shown for the first time that mono- and di-*meso*-phenyl substitution in octaethylporphyrins (OEP and Zn-OEP) leads to the drastic shortening of triplet lifetimes at 293 K (from ~1.5 ms down to 2-5 μs in degassed toluene solutions). In the case of Pd-octaethylporphyrin molecules (Pd-OEP) we have succeeded to compare spectral-kinetic results for pump-probe and phosphorescent measurements giving us the unique direct information concerning the influence of the non-planarity increase in a wide temperature range on all parameters of triplet states and their variation: i) T-state position in the energy scale, ii) direct phosphorescence lifetime in comparison with parallel T_1-T_n transient absorption decay, iii) phosphorescence quantum efficiency, iv) conformational and temperature change of the energy gap $\Delta E=E(S_1) - E(T_1)$, v) activation energy of temperature dependent phosphorescence rate constant for planar PdOEP and non-planar Pd-OEP-*meso*$(Ph)_n$ molecules. We have found also that the transition from planar Pd-OEP molecule to the sequential set of sterically hindered compounds Pd-5Ph-OEP → Pd-5,15Ph-OEP → Pd-5,10Ph-OEP → Pd-5,10,15Ph-OEP → Pd-5,10,15,20Ph-OEP manifests itself in the noticeable shortening of T-states (239.8 ns → 89.7 ns in toluene at 293 K) and drastic decrease of the efficiency of singlet oxygen generation (from 1.0 down to 0.05).

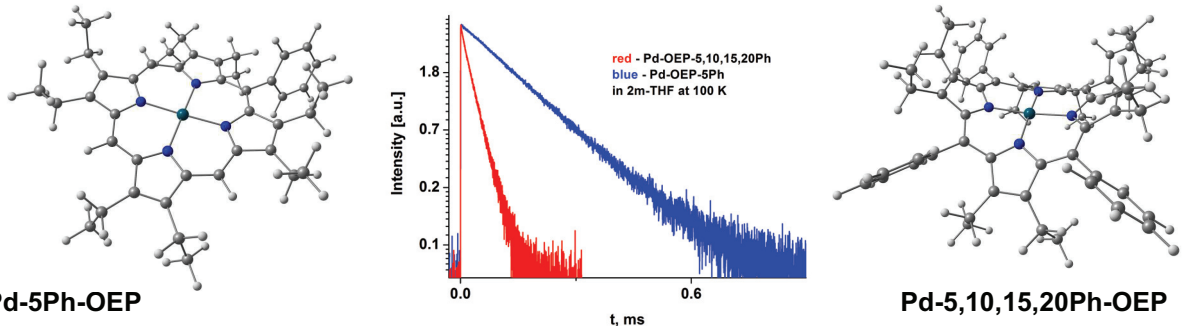

Pd-5Ph-OEP **Pd-5,10,15,20Ph-OEP**

Based on the whole set of steady-state and time-resolved results (absorption, fluorescence, phosphorescence, T_1-T_n transient absorption) together with the quantum chemical analysis (DFT, B3LYP functional with SVP basis set, Gaussian 09) the detailed picture of steric interactions between bulky meso-phenyl and side β-alkyl substituents of pyrrole ring as well as the reasons of T-state drastic shortening have been evaluated for compounds under study.

Spectroscopic Evaluation Method of Angiogenesis in the Healing of Skin Grafts Using Spectrally Sensitive to Inflammatory Reactions Aluminum Phthalocyanine Nanoparticles

Makarov V.I.[1], Pominova D.V. [1], Kholostsova M.N.[1], Ryabova A.V.[1,2], Loschenov V.B.[1,2]

Prokhorov General Physics Institute, Russian Academy of Sciences, 119991, Moscow, Vavilov Str., 38

National Research Nuclear University "MEPhI", 115409, Russia, Moscow, Kashirskoe highway, 31

Author e-mail adder: vi.makarov@physics.msu.ru

Abstract

The development of express method for assessing the state of skin graft by the spectroscopic properties of tissue components involved in the healing of the affected skin or healing of skin grafts was carried out in present work. To assess the extent of inflammation the spectrally sensitive to biological environment nanoparticles of aluminum phthalocyanine (NP-AlPc) were also used.

Keywords

Fluorescent diagnostics, backscattering spectroscopy, fluorescence video, skin grafts, oxygenation level of blood supply, the nanoparticles spectrally sensitive to inflammatory reactions.

1. Introduction

During transplantation of any tissue, acute rejection is a major cause of functional failure of the graft, and it is a major risk factor for the reduction of chronic graft rejection and to life. Nowadays, the only accurate method of determining the transplant rejection (which allows determining the fact of rejection, as well as its type) is biopsy. A search for new photosensitizers based on nanotechnology for this purpose is being carried out.

The proposed method for assessing the state of the skin by the spectroscopic properties of tissue components (using NP-AlPc applied locally) will evaluate the physiological condition of the skin and assess the degree and rate of engraftment or rejection while also controlling several biochemical and physiological parameters in the entire graft, or the whole area of the skin lesions. Such parameters include the oxygenation of hemoglobin in the tissue microvasculature; the blood supply level; blood flow and lymph flow; assessment of intracellular metabolism; assessment of the cellular respiration type (aerobic / anaerobic).

There is a principal opportunity to determine all of these settings in the monitor mode in real time.

2. Materials and methods

The experiment was performed in vivo in five outbred mice, on the back of each the cross-skin transplantation was carried out. We have added colloidal solution of aluminum phthalocyanine nanoparticles under the autograft located on the right and the other was left to monitor autograft engraftment without the nanoparticles.

The level of hemoglobin oxygenation and blood filling of tissue grafts were evaluated using diffuse backscattering spectroscopy [1], with a tungsten halogen lamp as a light source.

Assessment of the cellular respiration type of transplant during engraftment (aerobic / anaerobic) was carried out using fluorescence spectroscopy [2] by measuring the luminescence spectra of the oxidized and reduced NAD. The third harmonic of pulsed Nd: YAG laser was used as radiation source (λ=355 nm, τ_{pulse}=7 ns, ν=15 Hz).

Condition of blood and lymph flow in the autografts was assessed by analyzing the recorded fluorescent images using the exogenous photosensitizers and fluorescent dyes (Photosens and IcG) that absorb in the red and near-infrared spectral range for deeper penetration of light into the skin. Registration of fluorescent images was performed using video system that consists of a laser source, a broadband source diode, a beam splitter with a dichroic mirror and two digital cameras for recording color images and luminescence.

To evaluate the intensity of the immune response in the transplant engraftment we used a time-resolved fluorescence spectroscopy method in the pico- and nanosecond range using the aluminum phthalocyanine nanoparticles, spectrally sensitive to inflammatory reactions [3,4].

3. Results and discussion

Figure 1 shows the results of hemoglobin oxygenation measurements in the skin grafts from 2 mice on the seventh day after transplantation. All right transplants containing nanoparticles have the same degree of oxygenation that is three times lower than the norm which indicates the beginning of healing process. Left grafts differ from each other and, as can be seen from the figure, one of the grafts has critically low degree of oxygenation, which may indicate an unfavorable prognosis with respect to engraftment. Figure 2 shows the fluorescence spectra of NAD. The calculated concentration of NAD in the transplant without the nanoparticles is 2.5 times higher than transplants with NP-AlPc or the healthy tissue. Most probably this is due to the anaerobic cell respiration due to the limited access to the circulatory system, which can also indicate an unfavorable prognosis with respect to engraftment.

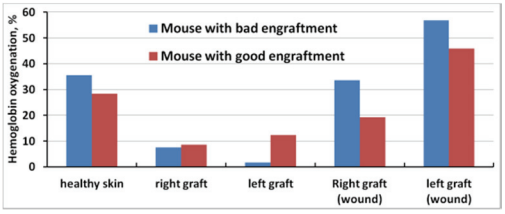

Fig.1. Oxygenation of hemoglobin in different parts of the skin.

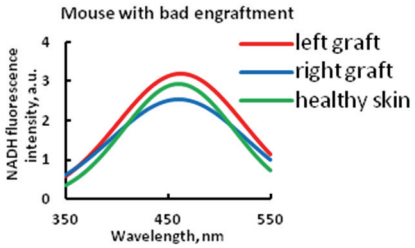

Fig.2. NADH fluorescence spectrum.

Figure 3 (left) shows the spread of indocyanine green in mouse skin tissue a few minutes after its administration 7 days after cross skin transplantation. It can be seen that the grafts fluoresce less than the healthy skin. This means that at this stage, new blood vessels have not yet developed in the graft tissue. Evaluation of lymph flow was made on the analysis of fluorescence images of skin grafts containing activated NP-AlPc (Figure 3, right). NP-AlPc interaction study with macrophages showed that NP-AlPc fluorescence intensity increases in the inflammation area.

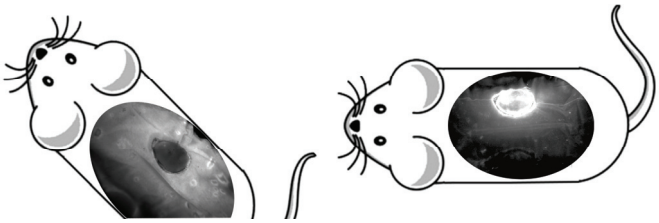

Fig.3. Fluorescent images of skin grafts with IcG (left) and NP-AlPc (right).

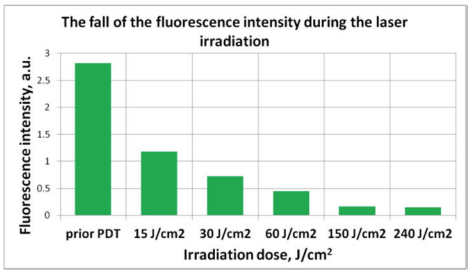

Fig.4. The fluorescence intensity at different PDT durations

Figure 4 shows the dependence of the right graft fluorescence intensity on the photodynamic treatment duration (at $\lambda = 670 \pm 5$ nm, power density of 0.5 W/cm^2). It can be seen that there is a distinct photobleaching, which is not observed while using molecular forms of AlPc. It was also found that NP-AlPc interaction with monocytes and macrophages leads to changes in their fluorescence lifetime.

4. Acknowledgement

This work was supported by a grant RFBR # 15-29-04869-ofi-m.

5. References

[1] Stratonnikov, A.A., Loschenov V.B. Evaluation of blood oxygen saturation in vivo from diffuse reflectance spectra // J.Biomed. Optics., v.6, p.457-467 (2001).

[2] Washington Y. Sanchez , Michael Pastore, Isha N. Haridass, Karsten König, Wolfgang Becker, Michael S. Roberts. Fluorescence Lifetime Imaging of the Skin // Advanced Time-Correlated Single Photon Counting Applications, volume 111 of the series Springer Series in Chemical Physics pp 457-508, 14 April 2015.

[3] Bystrov F.G., Makarov V.I., Pominova D.V., Ryabova A.V., Loschenov V.B. Analysis of photoluminescence decay kinetics of aluminum phthalocyanine nanoparticles interacting with immune cells // Biomedical Photonics. 2016. T. 5. № 1. C. 3-8.

[4] Makarov V.I., Vasil'Chenko S.Yu., Ryabova A.V., Loschenov V.B. Use of optical-spectral methods for in vivo noninvasive assessment of nanoparticles accumulation in biological tissues // Russian Journal of General Chemistry. 2015. T. 85. № 1. C. 341-345.

Terahertz Irradiation of Parent Drosophila Accelerates an Achieving the Adult State in Offspring of the First Generation

Viacheslav I. Fedorov, Natalya Ya. Weisman[1], Eugenia F. Nemova

Institute of Laser Physics SB RAS, Prospekt Lavrentyeva 13/3, Novosibirsk, Russia, 630090

[1]Institute of Cytology and Genetics SB RAS, Prospekt Lavrentyeva 10, Novosibirsk, Russia, 630090

vif41@mail.ru

Abstract: An adulthood achievement of offspring obtained from irradiated females mating with irradiated or non-irradiated males is shortened by a few days. Maximal maturation of individuals occurs for one day earlier than the control. In the offspring of irradiated males and nonirradiated females a development to the adult stage differs significantly on a number of parameters.

1. Introduction

It was demonstrated that terahertz radiation influences genetic system of plants and animals. A maturation of organism is the process of sequential switching of more and increasingly complex gene systems. In present study we investigated terahertz radiation influence on development dynamics of offspring obtained from irradiated or non-irradiated females mating with irradiated or non-irradiated males.

2. Methods

Fruit flies of both sexes subjected to 30-minute exposure of broadband terahertz radiation (0.1 - 2.2 THz) with a pulse power of 8.5 mW, a pulse duration of 1 ps and a repetition rate of 76 MHz. After the irradiation was carried out mating of irradiated and intact individuals in various combinations. As a control used flies that were near terahertz source during irradiation, but do not fall into the irradiation zone. We used clutch of eggs in the first two days after irradiation, which corresponds to mature eggs at the time of irradiation. the adult stage of offspring individuals. , It was recorded the number of reaching the adult stage of offspring individuals and their gender (daily from the first case of reaching). To determine the significance of differences between the curves of the maturation dynamics the $\chi 2$ test was used.

3. Results

The progenies derived from mating of unexposed females with non-irradiated or intact males. The first case of reaching of adult state in individuals of both sexes is registered on the 11^{th} day from the beginning of mating. The number of individuals is small. The following day, the maturing of males and females is increased significantly and reaches a maximum value on the 13^{th} day from the beginning of mating. Then, the number of ripe specimens of both sexes is decreased consistently.

The progeny derived from mating of intact females and unexposed males. The first case of reaching of adult state in individuals of both sexes is registered on the 12^{th} day from the start of mating. The following day, the maximum number of ripe individuals of both sexes is recorded. After that, it is indicated a consistent decrease in the number of ripe individuals. The total duration of the ripening period varies from 8 to 10 days at different variants of mating. The curves of development dynamics of males and females do not differ significantly. Sex ratio was 1: 1.

The progenies derived from mating of irradiated females with irradiated or intact males. The first case of reaching of adult state in individuals of both sexes is registered on the 11^{th} day from the beginning of mating.

The number of individuals is small. The following day, the maximum number of ripe individuals of both sexes is recorded compared to other days. Third day of maturing is characterized by a decrease in the number of individuals, reaching the adult stage. Then, the relative number of ripe individuals sharply decreased. The total duration of the ripening period was within 5 - 6 days. The curves of development dynamics of males and females do not differ significantly. Sex ratio was 1: 1.

The progenies derived from mating of intact females and irradiated males. The first case of reaching of adult state in individuals of both sexes is registered on the 11^{th} day from the start of mating, but the maximum number of ripe individuals of both sexes is registered on the 13^{th} day from the beginning of the mating. The total duration of the ripening period was 7 days in males and females. Total number of ripe males was higher than females. Sex ratio was 1: 0.83. The curves of development dynamics of males and females are different significantly ($\chi 2$ = 4,86). Another difference was the dynamics of subsequent reduction in the relative abundance of mature flies. In males, it was almost as good as in the control group. Females have been a sharp decrease in the relative number of ripe individuals. This curve of development dynamics significantly different from the control ($\chi 2$ = 8.41).

Thus, terahertz radiation causes a shortening of development period to adulthood in offspring obtained by mating irradiated females with both irradiated and non-irradiated males. In the case of progeny derived from mating of irradiated males and intact females, the effect of THz radiation depends on the sex of offspring.

The effect of THz radiation on parental drosophila, manifested in changing the dynamics of offspring development to adulthood, may be relevant to the question of a possible biohazard of terahertz radiation.

The study of chromatin organization in germinal mammalian oocyte by optical tweezers.

M.S. Syrchina[1], A.V. Aybush[1], A.A. Ocychenko[1], A.D. Zalesskiy[1], G.A. Serobyan[1], A.N.Kostrov[1], A.A. Titov[1], V. A.Nadtochenko[1,2,3]*

N[1] *Semenov Institute of Chemical Physics, RAS, Russia, Moscow*
[2] *Institute of Problems of Chemical Physics, RAS, Russia, Chernogolovka*
[3] *MSU, Faculty of Chemistry, Russia, Moscow*
e-mail: nadtochenko@gmail

Abstract: laser tweezers was applied to examine viscoelastic properties of chromatin in germinal vesicles of mammalian oocyte.

Introduction. Fully-grown mammalian oocytes (or germinal vesicle, GV), rather than typical nucleoli, contain prominent but structurally homogenous in optical image bodies called "nucleolus-like bodies" (NLBs). Figure 1 shows main components in GV oocyte: a) zona pellucida (ZP) shows the strong glycoprotein membrane surrounding the plasma membrane of mammalian oocytes, the layer that cover oocyte; b) cytoplasm (CYT) containing the cytosol, organelles, cytoskeleton, and various particles; c) germinal vesicle (GV) shows the enlarged nucleus of an oocyte before it develops into an ovum and d) NLB immersed in germinal vesicle. NLBs accumulate a vast amount of material, but their biochemical composition and functions remain uncertain [1].We suggest a new method, based on applying of optical tweezers for investigation of «NLB» surrounded by chromatin in GV-oocytes. Movement dynamics analysis (speed measurement and path definition) of «nucleolus-like bodies» within karyoplasm will allow us to evaluate elastic properties of chromatin and reveal the traits of its connection with «nucleolus-like bodies».

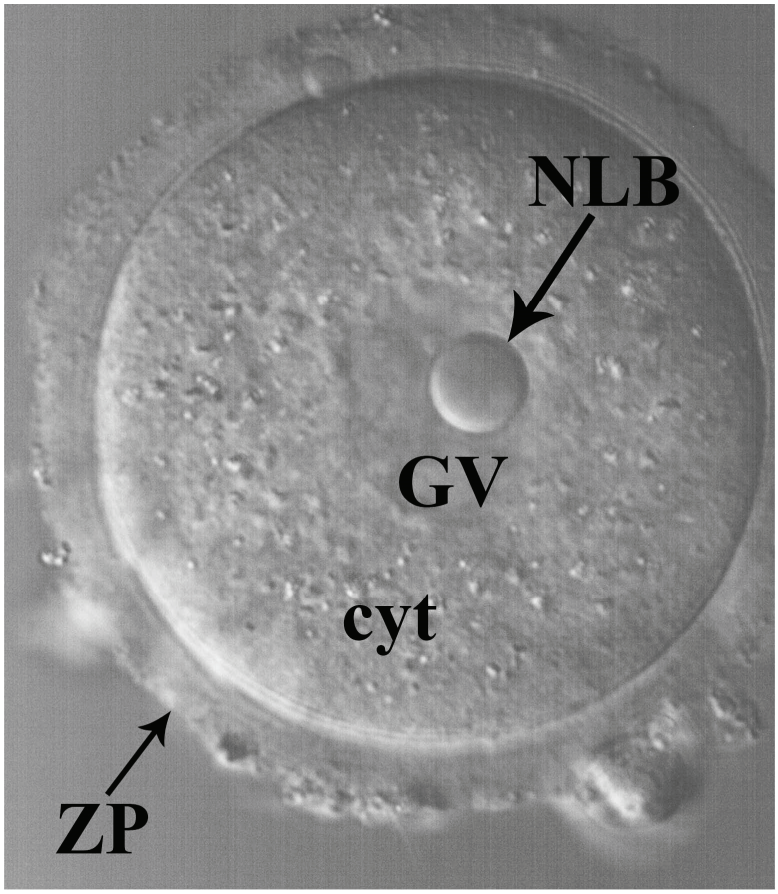

Figure 1. Differential Interference contrast (DIC) image of GV oocyte in the phosphate buffer droplet. NLB – nucleolus-like body; GV – nucleoplasm in the germinal vesicle; CYT – cytoplasm; ZP - zona pellucida.

Experimental. Laser tweezers were realized with tightly focused laser from Ti:sapphire oscillator (wavelength 780 nm, mean power at the sample plane 260 mWt). Laser was focused in the oocyte nucleolus with microscope objective (magnification 60x,N.A. 0,7). Fluorescent staining of oocytes with Hoehst 33342 was performed. It was revealed that after fluorescent light illumination (wavelength 385 nm) initial elastic bounding of nucleolus was broken. GV-oocytes were collected from C57Bl/CBA 8-9 week old mice.

Results and discussion.. Figure 2 demonstrates the motion of NLB trapped by optical tweezers. Figure 3 depicts the tracking of NLB motion. It was shown that native oocyte nucleolus exhibit viscoelastic bounding to the initial

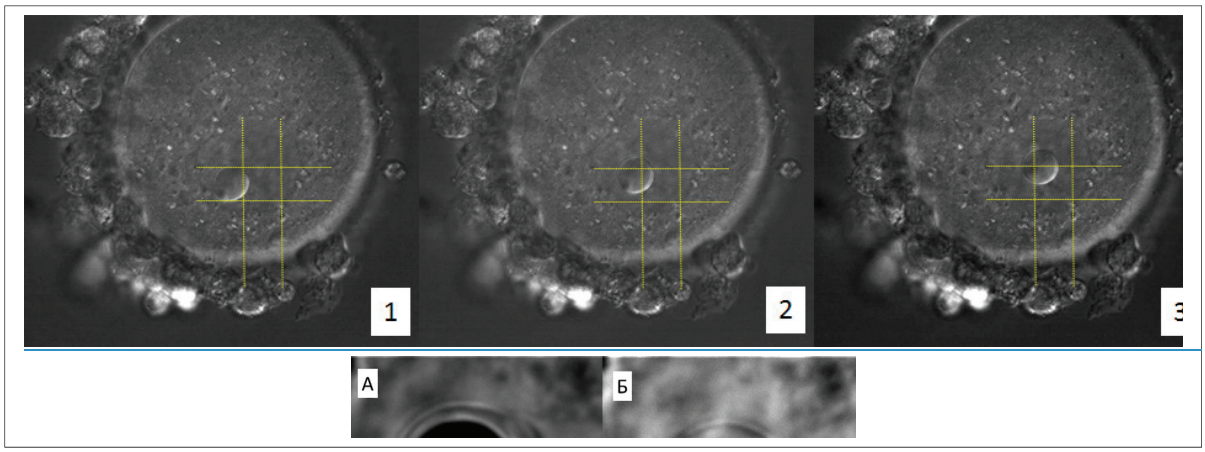

position. Mean trapping force of laser tweezers acting on nucleolus was determined as 7 pN and elastic deformation of nucleolus was investigated. During mouse antral follicle development GV-oocyte performs structural and morphological changes. These changes lead to the modification of the viscoelastic properties of chromatin surrounding NLB. Oocyte growth and its next transition to preovulatory phase associated with chromatin reorganization and «nucleolus-like bodies» formation that ignificantly differ from typical somatic cells nucleoli. Understanding the mechanisms of interaction between «nucleolus-like bodies» of GV-oocytes and chromatin linked with these structures can be useful in characterizing the GV-oocyte potential for meiosis resumption, fertilization and subsequent embryonic development.

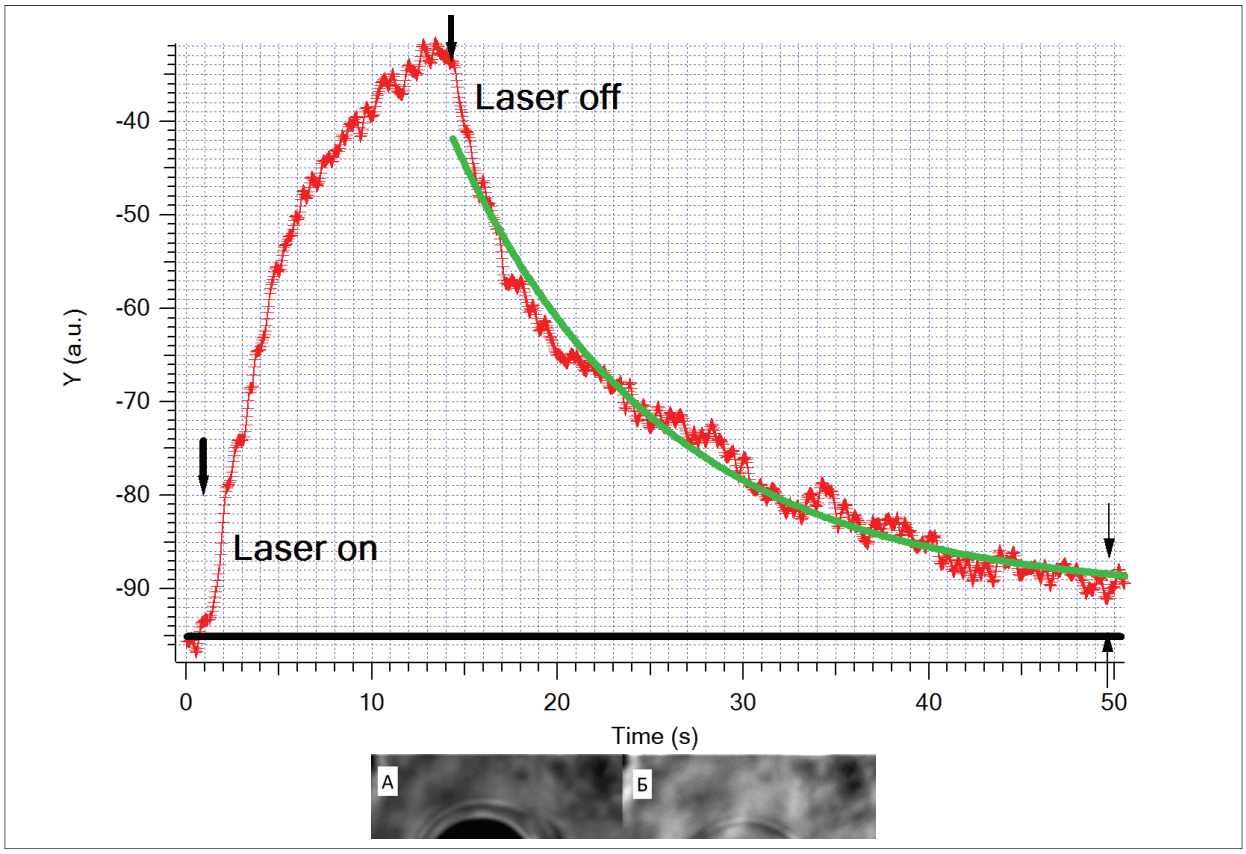

This work was supported by the Russian Science Foundation grant 14-14-00856.

References

[1] Alexander Gulin, Victor Nadtochenko, Artyom Astafiev,Valentina Pogorelova, Sami Rtimi, Alexander Pogorelov “Correlating microscopy techniques and ToF-SIMS analysis of fully grown mammalian oocytes” Analyst, **141**, 4121–4129, (2016)

Fiber-optic cell-resolved online thermometry in laser-assisted thermogenetics

A.A. Lanin,[1,2] I.V. Fedotov,[1,2] Y.G. Ermakova,[3] D.A. Sidorov-Biryukov[1,2], A.B. Fedotov[1,2], V.V.Belousov,[3] and A.M. Zheltikov[1,2,4,5]

[1] Physics Department, International Laser Center, M.V. Lomonosov Moscow State University, Moscow 119992, Russia
[2] Russian Quantum Center, ul. Novaya 100, Skolkovo, Moscow Region, 143025 Russia
[3] Shemyakin and Ovchinnikov Institute of Bioorganic Chemistry, Russian Academy of Sciences, Moscow 117997, Russia
[4] Department of Physics and Astronomy, Texas A&M University, College Station, TX 77843, USA
[5] Kurchatov Institute National Research Center, pl. akad. Kurchatova 1, Moscow 123182, Russia
Author e-mail address: zheltikov@physics.msu.ru

Abstract: Nitrogen–vacancy centers of diamond coupled with an optical fiber are shown to enable online fiber-format cell-resolved thermometry of thermogenetically activated neurons, facilitating a quantitative analysis of thermogenetic effects, characterization of thermosensitive ion channels, and optimization of laser neurostimulation.

Technologies allowing the electrical activity of specific cells in a living organism to be controlled with a high resolution both in space and time offer new, unprecedented opportunities for the functional analysis of complex biological systems. Optogenetic methods [1 – 4] employ genetically encoded light-sensitive ion channels for a spatially precise selective modulation of specific cells within complex distributed networks of neurons, thus offering unique tools for studying the mechanisms whereby the dynamics of these networks controls cognitive responses, memory, learning, and behavior. As a promising alternative to optogenetic strategies, thermogenetics uses thermosensitive ion channels [4 – 8] to drive the cell activity by temperature variations. However, since temperature changes affect many physiological processes in a living organism, cell activation by temperature variations requires special precautions in order to avoid heating that would be incompatible with the general physiology of the organism and to make sure that temperature variations are small enough to prevent increased background activity of cells, such as a spontaneous firing of neurons. These difficulties limit neuroscience applications of thermogenetics primarily to experiments with fruit flies [9, 10], despite the availability of a broad variety of thermosensitive members within the vast family of TRP channels, covering broad ranges of working temperatures and activation thresholds, possessing an exceptional thermal sensitivity, and allowing neurons expressing these channels to be switched from silent to robustly active mode by a slight change in temperature.

Here, we show that nitrogen–vacancy centers of diamond [11 – 13] coupled with an optical fiber [14, 15] enable online fiber-format cell-resolved thermometry of thermogenetically activated neurons, facilitating a quantitative analysis of thermogenetic effects, characterization of thermosensitive ion channels, and optimization of laser neurostimulation.

Our laser-based system combining IR excitation with fluorescent microscopy and ultrahigh-resolution quantum thermometry of activated cells is sketched in Fig. 1a. In this experimental scheme, the frequency-tunable output of the Ti: sapphire-laser-pumped femtosecond optical parametric oscillator (OPO) is loosely focused with a long-focal-length lens into a spot 670 μm in diameter, providing a uniform irradiation of a large number of TRPA-expressing cells within the sample. The transverse profile of the laser beam measured within the sample plane is shown in Fig. 1b. For the highest efficiency and minimum phototoxicity of laser heating, the central wavelength of the OPO output is tuned to the local maximum of water absorption at around 1440 nm.

A fiber-optic probe with a 300-mm-diameter nitrogen–vacancy (NV) diamond crystal attached to the tip of the fiber (Fig. 1a) adds a unique modality to our experiments, enabling accurate *in situ* temperature measurements with a single-cell resolution by means of optically detected magnetic resonance (see the Methods section for a detailed description of fiber-based thermometry implemented as a part of our experimental approach). In Fig. 1d, we present the difference $\Delta T = T - T_0$ between the temperatures T and T_0 measured with and without laser irradiation of the sample as a function of the laser wavelength λ. The $\Delta T(\lambda)$ dependence (the solid line in Fig. 1d) strongly correlates with the spectrum of water absorption (the dashed line in Fig. 1d), showing that absorption of IR light by water dominates laser-induced heating in our experiments, with the

heating rate per unit laser power within the studied range of laser intensities estimated as 0.25 ± 0.01 K/mW for $\lambda \approx 1440$ nm (Fig. 1e).

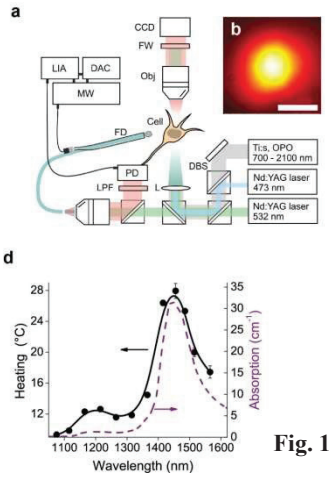

Fig. 1

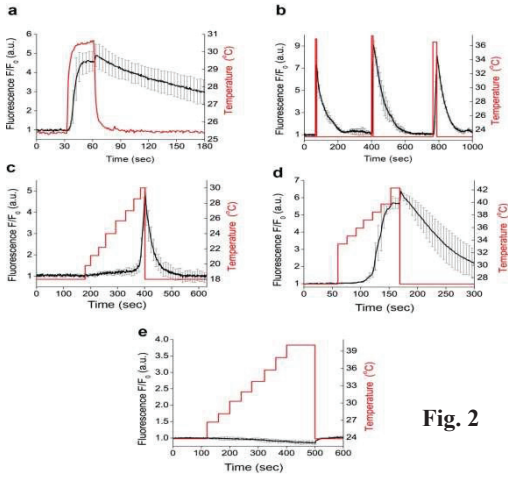

Fig. 2

Fig. 1. Local heating, fluorescent imaging, and quantum thermometry of living cells. (**a**) Laser thermogenetics and fluorescent imaging of single cells: Ti:s, mode-locked Ti: sapphire laser; OPO, femtosecond optical parametric oscillator; Obj, microscope objective; FW, filter wheels; DBS, dichroic beam-splitting cube; LPF, long-pass filter; FD, fiber probe with a nitrogen–vacancy diamond quantum temperature sensor; MW, microwave source; LIA, lock-in amplifier; DAC, data acquisition circuit; CCD, CCD camera. (**b**) Transverse profile of the IR laser beam. The scale bar is 500 mm. (**c**) The spatial profile of the temperature within an area irradiated by a 100-mW, 1440-nm laser beam measured using diamond positioned on the tip of the optical fiber (details in the Methods section). (**d**) Absorption spectrum of water (dashed line) versus the temperature change $\Delta T = T - T_0$ induced in the sample by 100-mW laser radiation measured as a function of the laser wavelength λ (solid line), where T and T_0 are the temperatures of the sample with and without laser radiation. (**e**) Temperature change ΔT as a function of the IR laser power with $\lambda = 1440$ nm.

Fig. 2. Activation of caTRPA1 in cells using femtosecond IR laser pulses delivered by the OPO operating in the quasi-cw mode. (**a**) R-GECO1.1 fluorescence (black line) reflects Ca^{2+} dynamics in the cytoplasm with the laser beam turned on at $t \approx 30$ s and off at $t \approx 60$ s. (**b**) Repeated caTRPA1 activation cycles. (**c, d**) With the temperature of HEK293 cells expressing snake TRPA1 increased in a stepwise fashion using properly adjusted IR laser radiation, the activation thresholds of caTRPA1 (**c**) and eolTRPA1 (**d**) were determined. (**e**) A similar heating of control cells does not induce Ca^{2+} elevation. The fluorescence signal is averaged over 11 (**a**) and 5 (**b** – **e**) cells. The black line is the fluorescence response. The red line is the temperature in the medium.

References

[1] K. Deisseroth, "Optogenetics," Nature Methods **8**, 26–29 (2011).

[2] G. Miesenböck, "The optogenetic catechism," Science **326**, 395–399 (2009).

[3] I. Diester, et al. "An optogenetic toolbox designed for primates," Nature Neuroscience **14**, 387–397 (2011).

[4] F. Zhang, et al. "Multimodal fast optical interrogation of neural circuitry," Nature **446**, 633-39 (2007).

[5] D.D. McKemy, W.M. Neuhausser, and D. Julius, "Identification of a cold receptor reveals a general role for TRP channels in thermosensation," Nature **416**, 52–58 (2002).

[6] H. Xu, et al. "TRPV3 is a calcium-permeable temperature-sensitive cation channel," Nature **418**, 181–186 (2002).

[7] A. Moqrich, et al. "Impaired thermosensation in mice lacking TRPV3, a heat and camphor sensor in the skin," Science **307**, 1468–1472 (2005).

[8] A. Patapoutian, A.M. Peier, G.M. Story, and V. Viswanath,"ThermoTRP channels and beyond: mechanisms of temperature sensation," Nat. Rev. Neurosci. **4**, 529–539 (2003).

[9] J.G. Bernstein, P.A. Garrity, and E.S. Boyden, "Optogenetics and thermogenetics: technologies for controlling the activity of targeted cells within intact neural circuits," Curr. Opin. Neurobiol. **22**, 61 – 71 (2012).

[10] D.E. Bath, et al. "FlyMAD: rapid thermogenetic control of neuronal activity in freely walking Drosophila," Nature Methods **11**, 756 – 762 (2014).

[11] J.R. Maze,et al. "Nanoscale magnetic sensing with an individual electronic spin in diamond," Nature **455**, 644–647 (2008).

[12] J.M. Taylor, et al. "High-sensitivity diamond magnetometer with nanoscale resolution," Nature Phys. **4**, 810–816 (2008).

[13] G. Kucsko, et al. "Nanometre-scale thermometry in a living cell," Nature **500**, 54–58 (2013).

[14] I.V.Fedotov, L.V.Doronina-Amitonova, A.A.Voronin, A.O.Levchenko, S.A.Zibrov, D.A.Sidorov-Biryukov, A.B.Fedotov, V.L.Velichansky, A.M.Zheltikov "Electron spin manipulation and readout through an optical fiber," Scientific Reports **4**, 5362(6) (2014).

[15] I.V. Fedotov, L. V. Doronina-Amitonova, D. A. Sidorov-Biryukov, N. A. Safronov, S. Blakley, A. O. Levchenko, S. A. Zibrov, A. B. Fedotov, S. Ya. Kilin, M. O. Scully, V. L. Velichansky, and A. M. Zheltikov, "Fiber-optic magnetic-field imaging," Opt. Lett. **39**, 6954-6957 (2014).

Optical Tweezer on the Base of 4-channel LC Modulator for Trapping of Biological Objects

A.V. Korobtsov[1], S.P. Kotova[1,2], N.N. Losevsky[1], A.M. Mayorova[1,2], S.A. Samagin[1]

[1]Lebedev Physical Institute, 221, Novo-Sadovaya Str., Samara, 443011, Russia;

[2] Samara National Research University 34, Moskovskoye shosse, Samara, 443086, Russia.

e-mail: mayorovaal@gmail.com

Laser tweezers proved to be of great importance for various applications in biology and medicine as a noninvasive sterile tool. They are extensively used in many biotechnical laboratories. The minimization of negative laser radiation effect on trapped objects is one of most critical problems during optical manipulation of micro-objects of biological origin. One way of solution of this problem is the choice of right radiation wavelength [1]. On the other hand during trapping of eukaryotic cells with sizes significantly exceeding the size of point optical trap, the maximum of radiation typically gets to the nucleus as the most optically dense structure of the cell [2]. Thus the stable trapping of cells by their peripheral part with the traps in the forms of rings, ellipses and their arcs is the relevant problem.

For the formation of contour traps we propose to use a 4-channel liquid crystal modulator (LC focusator). Its use in the scheme of optical tweezers allows generating optical traps in the form of rings and ellipses and also to control their size and shape in real-time by changing potentials of the control contacts. Sufficient energy efficiency, wider spectral range compared to one for commercial multipixel spatial modulator, the simplicity and compactness of the device and the control system, and as a result lower cost of the system are the advantages of LC focusator.

The scheme of LC focusator is presented in fig.1. Two cylindrical modal LC lens are jointed into one device. The nematic LC-layer is sandwiched between two glass substrates covered with the transparent high-resistance coatings and low-resistance non-transparent strip-shaped contacts.

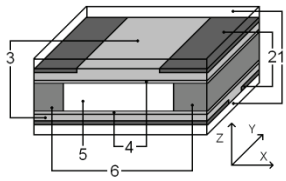

Fig.1. The scheme of LC focusator. 1 – glass substrates, 2 – contact electrodes, 3 – high resistive conductive layer, 4 – orienting coating, 5 – LC layer, 6 - spacers.

It is possible to change the voltage distribution on the aperture by controlling the electrical parameters of the device. The LC molecules become reoriented under the voltage applied (S-effect). This results in the change of the spatial distribution of the phase delay introduced by the LC layer into the transmitted light. Two operation regimes of LC focusator can be selected: with a small and with high modal parameters. The physical meaning of this value is that the square of modal parameter is the ratio of the resistance of the high resistive conductive layer and the LC layer impedance and its magnitude determines the nature of the voltage distribution over the aperture.

To achieve the operation regime with a small modal parameter it is necessary to decrease the frequency and/or resistance of the transparent conductive coatings. In this regime the type of voltage distribution and accordingly the shape of the profile of the phase delays are determined by the amplitudes and relative phases of the potentials. The equipotential lines of elliptic type can be realized. These potential distributions are transformed to corresponding phase profiles in the form of elliptical or circular truncated cones. In the region of Fresnel diffraction at a small distance from the LC focusator the points with maximum intensity in a transverse plane will be located on the contour curve, replicated the shape of the equipotential lines of the voltage profile. Thus you can generate the light fields with intensity distributions in the shape of rings, ellipses (with different relation of its major axes and their arbitrary orientation to aperture boundaries) and their arcs. And due to the embedding of LC focusator into the optical tweezer scheme (fig. 2) you can form the optical traps of such shapes.

Trapping experiments were carried out using the radiation wavelength 532 nm. The *Saccharomy cescerevisiae* yeast cells suspended in water were used as the objects of biological origin for micromanipulation. The yeast cells are weakly absorbing objects at the used radiation wavelength. The optical traps had the forms of rings or ellipses with the capability of change of their shapes and sizes. The trapping efficiency was estimated by so called escape velocities – the maximal velocities of the object stage motion for which the micro-object remained to be captured by the optical trap. This value depends on both trap parameters and type and size of micro-objects.

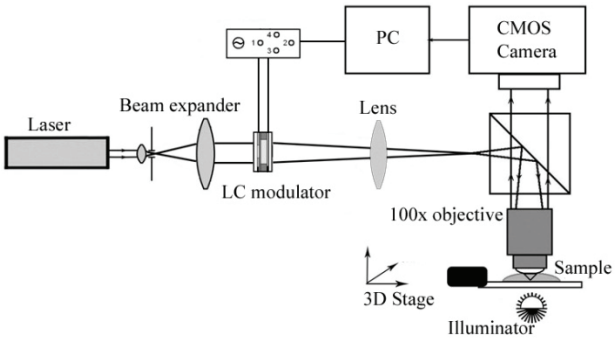

Fig. 2 The scheme of optical tweezer with LC focusator.

It was demonstrated that the contour optical trap generated with the use of LC focusator effectively captured micro-objects which sizes were comparable with the optical trap sizes. Thus the observed escape velocities of yeast cells (of the size about 5x6 mkm) were about 15 mkm/sec at 5.6 mW radiation power in the optical trap. The fragments of the video record, illustrating the capture and confinement of an individual yeast cell by the ring optical trap are presented in fig. 3.

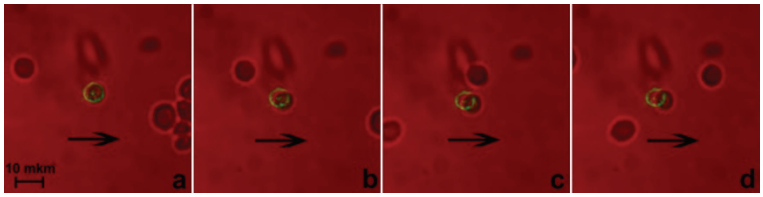

Fig.3. Capture and confinement of a single *Saccharomy cescerevisiae* cell. The arrow shows the direction of the microscope stage movement.

It was also shown that such optical traps can be used for the trapping of large (about 20 mkm) micro particles. The yeast cells, aggregated into a single particle were used as a large microobject. The selected frames of the video of the experiment are presented in Fig.4.

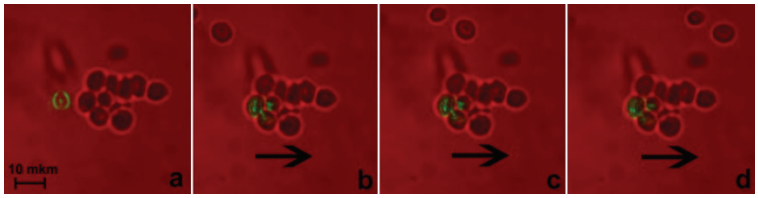

Fig.4. Trapping and confinement of a large microparticle. The arrow shows the direction of the microscope stage movement..

Besides, the dependence of trapping efficiency on the optical trap shape was also demonstrated. And also the size of the trap has influence on the escape velocity value. The possibility of control of trapping efficiency by changing the trap diameter was demonstrated in the experiments with the ring traps. The decrease of traps' diameters resulted in the increase of the escape velocity at first but then the velocity became constant. Due to this fact it is possible to effectively trap micro-object without affecting its central part.

It was shown by means of numerical simulation that light fields with a transverse intensity distribution not only in the shape of rings or ellipses, but in the shape of squares, diamonds, parallelograms and octagons can be generated using an LC focusator operation regime with high modal parameter. And contour optical traps of such shapes can be formed. Taking into account the diversity of shapes and sizes of biological objects, as well as experimentally demonstrated dependence of capture efficiency on optical trap shape we believe that contour traps of such forms can also be useful in biomedical applications.

The work was supported by the Russian Foundation for Basic Research (grant No.16-29-14012).

References

[1] A. Ashkin J. M. Dziedzic and T. Yamane, *Optical trapping and manipulation of single cells using infrared laser beams*, Nature, **330**, 769-771, (1987).

[2] S. Fore, J. Chan, D. Taylor and T. Huser *Raman spectroscopy of individual monocytes reveals that single-beam optical trapping of mononuclear cells occurs by their nucleus,* Journal of Optics **13**(4): 044021 (2011).

QUANTUM MEDICINE: MOLECULAR APPEARANCE

Zalesskaya G. A., Astafieva L.G.
Stepanov Institite of Physics National Academy of Sciences of Belarus, pr. Nezavisimosti 68, Minsk, 220072 Belarus
zalesskaya@imaph.bas-net.by

Abstract: The effect of phototherapy on blood oxygenation and metabolic processes were studied. It was shown that blood irradiation exerts influence on oxygen exchange and formation of reactive oxygen species regulating many processes in living organism.

The purpose of this work is the study of molecular mechanisms of low-intensity optical radiation (OR) action on the patient blood which was irradiated *in vivo* by OR of different wavelengths (254, 632.8, 670, 780 nm). About the two hundreds of blood samples were analyzed after extracorporeal, intravenous or over-vein blood irradiation. The objects of research were the spectral characteristics of the samples of venous blood, degree of hemoglobin oxygenation in venous (S_VO_2) and arterial blood, blood gas composition, especially the partial pressure of oxygen (p_VO_2), acid-base balance indices, the hemoglobin concentration as well as the content of some metabolic products. The dynamic of blood oxygenation during phototherapy (PT) course was determined. Taking account of optical properties of human tissues, the depth penetration of OR in blood and skin tissue were evaluated in the range 405-950 nm, efficiency of action was compared for OR of different λ .

It was established that quantitative differences in photooxygenation of the blood in different patients depended primarily on the original content of hemoglobin fractions and optical characteristics of blood at the wavelengths studied. We showed that the irradiation of blood by therapeutic doses of OR for wavelengths used initiated the similar molecular changes in blood and its components and that monochromatic incoherent light acts equally as efficiently as laser radiation.

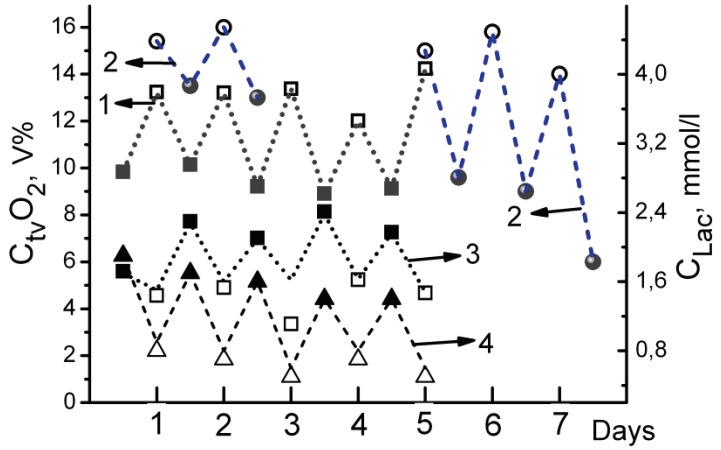

Fig.1.Oscillation of the oxygen content in venous blood (Ct_VO_2): 1- before (■) and during (□) the procedure of intravenous blood irradiation (λ=670 nm); 2- before (●) and during (○) the procedure of UV blood irradiation (λ=254 nm). Oscillation of the lactate concentration ($C_{lac.}$): 3- before (▲) and during (Δ) the procedure of intravenous blood irradiation ; 4- before (●) and during (○) the procedure of UV blood irradiation.

The difference in short- and long-term changes in characteristics of blood oxygenation was observed. An increase of oxygen partial pressure and decrease of carbon dioxide partial pressure in venous blood were obtained during and immediately after blood irradiation. Reversibility of the photoinduced changes in the characteristics of blood oxygenation was reveled. They increased during blood irradiation and decreased to the beginning of the next procedure up to the level which was close up the initial level or even less it. It was established that during the PT treatment there were positive changes in the blood oxygenation. As a rule, p_VO_2 and S_VO_2 increased up to normal values under the influence of PT and then decreased after the irradiation finishing to initial or even lower values during time interval not exceeding 15 minutes. So in the patients with low values of S_VO_2 in venous blood, their normalization was obtained during blood irradiation. Periodic oscillation of not only the p_VO_2, S_VO_2, and Ct_VO_2 values but also the lactate, glucose, Ca^{2+} concentration and viscosity of blood occurred during PT, which indicated the immediate reaction of the body during irradiation. Analysis of the metabolic products (lactate, glucose) showed that during the course of treatment, the periodic oscillation in their concentration was observed with positive changes during course.

By the end of blood irradiation course, changes of gas composition in venous blood as well as degree of hemoglobin saturation by oxygen prove to be varying strongly among various persons, depending ob both the photoinduced changes in the S_VO_2 values and the initial values of blood oxygenation. Changes in the metabolic product concentration obtained after completion of the course depended on two quantities: their initial concentration, which decrease for high initial levels and conversely increase for low initial levels, and photoinduced changes in the level of oxygen hemoglobin saturation.

In the following discussion, hemoglobin was considered as a primary photoacceptor at blood irradiation with OR of different wavelengths which was absorbed by blood. The next primary action mechanism was reviewed: oxyhemoglobin photodissociation following photoexcitation of hemoglobin electronic states; altering the oxygenation characteristics and oxygen exchange in the body; improvement in oxygen utilization by tissues and oxygen consumption in cells; correction of the process for oxygen reactive species (ROS) production. The biochemical effects are generated by the activation of molecular oxygen to ROS which initiate a cascade of molecular reaction, resulting in the observed therapeutic effects.

In conclusion, it was established that absorption of OR by blood irradiated by its therapeutic doses has an effect on oxygen exchange in the body, altering the oxygenation characteristics. Consequently, the balance changes between production of ROS and their inhibition by antioxidant systems, resulting in intensification of metabolic processes.

Simulation of Thermographic IR Images of a Localized Heat Source Hidden in Biological Tissue

A. P. Ivanov and V. V. Barun
B.I. Stepanov Institute of Physics, Belarus National Academy of Sciences, Nezavisimosti Pr. 68, Minsk 220072, Belarus
ivanovap@dragon.bas-net.by, barun@dragon.bas-net.by

Abstract: Thermal imager data are simulated at varying power, depth, and dimensions of an internal heat source. The main idea of the paper is to get insight into tissue depth by using observations of tissue surface. The observed quantities are discussed as applied to various inverse problems of source parameters retrieval.

1. Introduction

Currently thermographic methods on the base of infrared (IR) images are actively incorporated into medical practice. The essence of these methods is non-invasive recording of thermal images of open biotissue surfaces to make a conclusion, for example, on inflammatory pathology of internal regions having an enhanced temperature of a studied organ or on dystrophic pathology with a reduced temperature. In spite of obvious benefits of these methods, they are not widely applied in medicine. One of the main limiting factors is the thermal image recording from a tissue surface only to indirectly bear information on the temperature regime of an internal region that is shadowed by intermediate tissue layers. The effects of biotissues on the results cannot, naturally, be excluded. In other words, the thermal action of a tissue slab between the investigated tissue region and the thermal imager creates noisy images. Because of this, the techniques to correct the IR images for their refinement and for the extraction of the information on the temperature of the interested tissue area are very urgent. Such techniques would enable one to make conclusions on parameters of the thermal regime of internal organs and to derive their temperatures by a non-invasive way without temperature sensors implanted into the tissue. The design of the correction method will enable one to qualitatively improve the information content and the validity of diagnostic techniques for practical physicians and provide a powerful toll for studying a person organism by scientists. This paper discusses the IR imaging of biotissue surfaces, gives relations between tissue parameters and characteristics of an internal heat source, and outlines means to solve the inverse problem on retrieving the source characteristics from image data of a thermal imager.

2. Simulation method

As a basis for the investigations, we will use the known stationary solutions [1, 2] for spatial temperature distributions created in a semi-infinite medium by elementary heat sources, namely by point spherical and line cylindrical ones, under Newtonian heat exchange at the surface. By integration over spatial coordinates, these solutions can be obviously generalized for a spherical or cylindrical source of an arbitrary radius. So one can compute the temperature in any point of a medium. A thermal imager records usually IR radiation from an object, not its temperature directly. Each volume element of biotissues radiates according to the Plank's formula and Kirchhoff's law. Owing to the non-uniform spatial temperature distribution, one needs to integrate over tissue depth to get an optical signal (or radiance) exiting surface at any its point. While integrating, the extinction of light should be accounted for. We will consider below wavelength range λ of about 2 to 10 μm. Due to the strong water absorption, let the extinction be provided by radiation absorption only with scattering neglecting. By doing so, the temperature and IR radiation images are computed.

3. Errors in temperature measurements owing to volumetric glowing of biotissue

It is well known that skin temperature is usually lower than that of tissue volume. Therefore, a thermal imager observes not the tissue surface temperature, but some higher value due to the volumetric glowing. Fig. 1 illustrates the effect of systematic error δT_0 in measured surface temperature on the estimate of source temperature excess ΔT_s. Here solid lines are theoretically calculated and dashed ones are re-calculated on the base of tissue temperature with accounting for the volumetric tissue glowing. Consider the effect of the glowing due to a heat source on the error in retrieving the temperature excess ΔT_s of the latter. Let the experimentally measured value of ΔT correspond to point A of Fig. 1. Then, according to line *4*, temperature ΔT_s corresponding to point A* will be determined. The ΔT value should be really decreased by δT_0, i.e. to go to point B, which corresponds to ΔT_s of point B*. In this case, the error δT_s in ΔT_s will be about 1 K. In other words, the

volumetric tissue glowing provides for an enhanced source temperature, which can be important for solving the respective inverse problems.

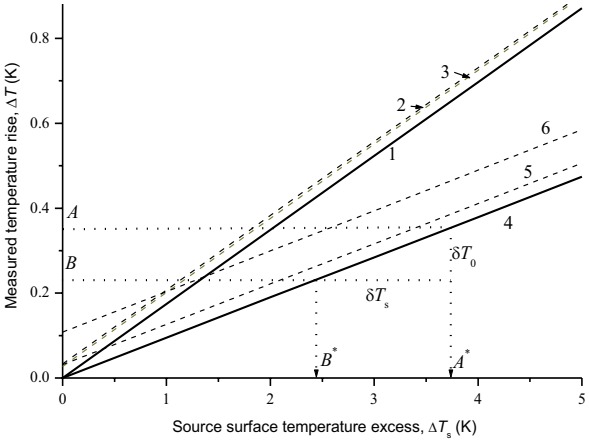

Fig. 1. ΔT *vs* ΔT_s. Curves 1, 2, and 3 – h = 0.2 cm^{-1}; 4, 5, and 6 - h = 0.8 cm^{-1}; 1 and 4 – monochrome detector; 2 and 5 – spectral PtSi/$Si_{1-x}Ge_x$ detector; 3 and 6 – spectral PtSi/Si detector

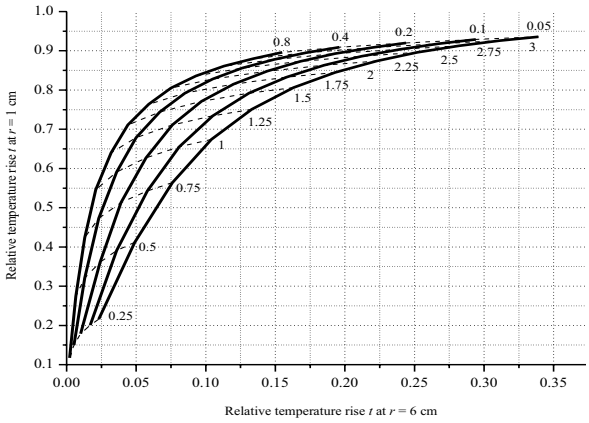

Fig. 2. Nomograms for retrieving simultaneously source depth a and heat exchange parameter h. Numbers near thin and bold curves give a, cm and h, cm^{-1} values, respectively

4. On the solution to inverse problems

Illustrate some opportunities of retrieving various characteristics of tissue and of internal heat source by using thermographic IR images. Let one observe the surface temperature rise created by a spherical heat source at several radial coordinates r from the source center. Then the theoretical nomograms of relative temperature rise shown in Fig. 2 opens an opportunity to retrieve simultaneously source depth a and heat exchange parameter h. The relative rise means here the temperature increase at point r with respect to that at r = 0. When thermophysical characteristics of tissue and source depth are known, one can determine Q/κ value, where Q is the heat power, W/cm^3 and κ, W/(cm.K) is the biotissue thermal conductivity, by using theoretical equations for measured surface temperature rise dependence $\Delta T(r,0)$. Note the appreciable effect of parameter h on the temperature.

5. Conclusion

Recording a thermal image of a person body finds currently wide applications in medical practice, e.g. for diagnosing organism conditions, exposing pathological body regions, etc. Usually, the gathered image data are transformed into surface temperature maps. But there obviously arise a number of questions. For example, what a value we have measured, if temperature distribution over the body depth is non-uniform? This paper gives a quantitative answer to it. Namely, the estimates are provided here to relate data of a thermal imager with thermophysical, optical and geometrical parameters of a system under consideration. Note that this system includes both the depth-varying temperatures of biotissue under the action of a human organism and spatially varying ones under the action of a heat source. The latter can simulate a pathological tissue region. The second question occurs from the following physically transparent fact. Really, one observes a tissue surface, but desires to retrieve a temperature of an internal heated region. How are the observations related with a quantity of interest? Here are provided analytical tools to solve the inverse biooptical problem on deriving not only the source temperature, but also the heat source depth, its thermal power and dimensions, thermophysical parameters of tissue itself, etc. The presented data can be used for designing dedicated algorithms and program codes of IR biomedical image processing for various medical and biophysical applications.

6. References

[1] H.S. Carslaw and J.C. Jaeger, *Conduction of Heat in Solids,* 2nd ed., (Oxford: Clarendon Press, 1959).

[2] J.W. Draper and J.W. Boag, "The calculation of skin temperature distribution in thermography," Phys. Med. Biol., **16**, 201 — 211 (1971).

The development of fiber-optic scaffold for the glioblastoma diagnosis and prevention.

Yu. S. Maklygina[1], A.V. Borodkin[1], G.M. Yusubalieva[2], V.B. Loschenov[1,3]

[1]*A.M. Prokhorov General Physics Institute RAS, Russia, Moscow*

[2]*V. P. Serbskij State Research Center of Forensic and Social Psychiatry, RUSA Ministry of Health, Moscow, Russia*

[3]*National Research Nuclear University MEPhI, Russia, Moscow*

E-mail address:us.samsonova@physics.msu.ru

Abstract

The main goal of the research is creation of the unique fiber-optical multipurpose system created on the basis of porous optical fibers. The fiber-optical scaffolds would perform the role of the structure which is promoting and setting the of glial cells growth. Also this system acts as a port for delivery of photosensitizers and laser radiation for the purpose of cellular processes monitoring. So developed system allows to implement a regular fluorescent diagnostics and timely photodynamic therapy of the probed area.

Keywords

Optical technologies, spectroscopy, fluorescence diagnostics, photodynamic therapy, fiber-optic scaffolds, optically generated conduits, neuroscience, neurophotonics, glioblastoma, manipulation of brain cancer growth along optically generated conduits.

Introduction

Brain gliomas are known for invading and spreading along the white matter channels and along the blood vessels [1]. Based on this observation this research aims at creating the guide rails for tumors that consist of porous optical fibers, structurally imitating white matter channels and blood vessels in order to direct the growth of localized tumor cells outwards: from the place of primary localization to a more easily accessible place outside the cerebral cortex for subsequent introduction of external effects aimed at the tumor cells destruction [1]. The monitoring of the process of cell growth consists of detection using the methods of fluorescent spectroscopy of the areas with high fluorescence caused by high accumulating molecules concentration of photosensitizer in glioblastoma cells. This approach of monitoring process gives the observer close to complete understanding of the processes happening within the probed area. In case of gliomas, the directional growth of cancer cells from intracranial area of the primary tumor into the outer part of the brain is necessary to reduce the size of the primary tumor, and to conduct the timely directed therapeutic effect on cancer cells.

Materials and methods

In vitro studies were performed on the cell culture of glioma C6 using confocal laser scanning microscopy. The in vivo studies were performed on experimental animals with induced malignant glioma in the intracranial region. During the study scaffolds of different materials, shapes and sizes were developed and tested in experimental animals. The developed scaffolds were fixed subcutaneously on the skull of the experimental animals and served as a port for the local delivery of the photosensitizer and laser radiation. The evaluation of abscesses and rejection processes was made after implantation by magnetic resonance imaging (MRI). The fluorescence monitoring of the tumor area were examined with the use of a fiber spectrometer LESA-01-"BIOSPEC" [2] (in the range of 0.4 ÷ 1.1 μm). The fluorescence monitoring was realized by laser radiation sources with power density of ~100 mW/cm^2 and λ = 632.8 nm wavelengths and the photodynamic therapy was realized by laser radiation sources with and λ = 675 nm, selected in accordance with phthalocyanine series photosensitizers absorption spectra maximums.

Results

In this study glioma C6 cell growth processes along the optical fibers were visualized using confocal laser scanning microscopy. These in vitro studies showed that malignant glioma cells formed agglomerates and fastening around the optical fibers proliferating directionally along the fiber structures. The in vivo studies showed that the malignant glioma cell growth from intracranial region up to the extracranial part by the internal fiber-optic structure of scaffold reducing the intracranial tumor volume. During the study scaffolds of different shapes and sizes were developed and tested in experimental animals. Successful testing by MRI (no abscesses and rejection scaffolds) allowed to determine the optimal properties and the external dimensions of the brain scaffolds. The developed scaffolds were fixed subcutaneously on the skull of the experimental animals and served as a port for the local delivery of the photosensitizer and laser radiation followed by photodynamic therapy, leading to malignant cell death. So as final result of the photodynamic therapy (phthalocyanine series photosensitizer, excitation radiation $\lambda = 675$ nm) was observed high therapeutic effect and was ensured access to the tumor for monitoring processes (Fig. 1).

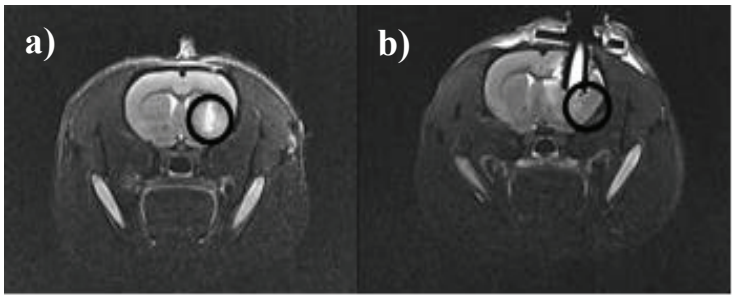

Fig.1. a) MRI of rat's brain. Before therapy. b) MRI of rat's brain with scaffold. After PDT, $\lambda = 675$ nm.

Conclusion

Thus the developed fiber-optic system allows continuous monitoring of the processes taking place in the primary tumor, reducing the volume of the primary tumor. This fiber-optic scaffold allows to implement a prevention by the timely photodynamic therapy. Also it is planned to use infrared photosensitizers in order to achieve a high therapeutic effect on the pathological effects of deep brain tissue localization. Such a combined approach can provide lasting effect the treatment and prevention of glioblastomas.

References

[1] Guiding intracortical brain tumour cells to an extracortical cytotoxic hydrogel using aligned polymeric nanofibers Jain A, Betancur M, etc.Nat Mater. 2014 Mar; 13(3):308-16

[2] Loschenov V.B., Konov V.I., Prokhorov A.M., «Photodynamic therapy and fluorescence diagnostics», Laser Physics. , 10, No 6, 1188–1207 (2000).

The temperature and thermal stresses fields at cornea shape alterations under the ring-shaped laser source.

Baum O.I. [1], Omelchenko A.I. [1], Kasianenko E.M. [1], Bolshunov A.V. [2], Sipliviy V.I. [2], Sobol E.N. [1].

[1] Institute Photonic Technologies of Federal Scientific Research Centre "Crystallography and Photonics" of RAS, 142190, Moscow(Troitsk), Pionerskaya 2, Troitsk, Russia.
[2] Federal State Scientific Institute "Research Institute of Eye Diseases", Moscow, Russia

Contact Email: baumolga@gmail.com

The new laser method for non-ablative correction of cornea shape and eye refraction is presented.
For correction of the eye refraction the special ring-shaped laser beam with various ring diameters allows obtaining controllable alterations of the eye refraction. The alteration in the cornea shape in vitro on minipig eyes and in vivo on rabbit eyes have been obtained with the help of ring-shaped source of laser radiation with wave length 1,56 μm. These alterations have axial symmetry without any pathological changes in central part of cornea.
At ring-shaped distribution of intensity of laser radiation, the tension and temperature of cornea surface has also ring-shaped distribution that results in deformation of cornea in central part and heating only on periphery. This leads to the absence of any pathological changes in central part of cornea.
Theoretical model for calculation of eye refraction has developed to estimate laser settings for desirable changes in the eye refraction.

Thermo mechanical processes at laser normalization of intraocular pressure.

Baum O.I. [1], Bolshunov A.V. [2], Khomchik O.V. [2], Zheltov G.I. [3], Romanov O.G. [4], Sobol E.N.[1].

[1] Institute Photonic Technologies of Federal Scientific Research Centre "Crystallography and Photonics" of RAS, 142190, MoscowfTroitsk), Pionerskaya 2, Troitsk, Russia.
[2] State Research Institute of Eye Diseases of Russian Academy of Medical Sciences, Moscow, Russia
[3] B.I. Stepanov Institute of Physics, NAS RB, Minsk, Belarus.
[4] Belarusian State University; 220030, Minsk, Belarus

Contact Email: baumolga@gmail.com

The theoretical calculations of thermo mechanical stress at novel and innovative technique for IOP normalization based on enhancing role of sclera outflow is presented. This technique creates permeable pathways for water transport as a result of pore system formation under nondestructive thermo mechanical effect of pulsed laser irradiation.
The theoretical calculations of thermo mechanical stress showed the area of maximum stress concentration. Space-distribution of stress have confirmed by atomic force microscopy.
The experimental results of in vivo experiments in rabbit eye sclera have shown twenty times increase of water permeability. The results of numerical modeling with this newly developed theoretical model are in satisfactory agreement with the experimental data.
Clinical trials performed for 36 eyes of 36 patients with primary open angle glaucoma (resistant form) have demonstrated stable normalization of the IOP with one year follow-up observations.
The prospects of novel non-invasive technique for glaucoma treatment have been demonstrated.

Dual channel video fluorescence diagnostic system for intraoperational navigation during protoporphyrin IX photosensitized malignant tumor resection in central neural system.

Loshchenov MV*, Borodkin AV*, Golbin DA, Gorjainov SA**, Zelenkov PV**, Potapov AA****

** Laboratory of laser biospectroscopy, Prokhorov General Physics Institute of the RAS, Moscow*

***Burdenko Neurosurgery Institute, Moscow*

maxvl@mail.ru

Abstract.

In the presented work we have developed a novel neurosurgery fluorescence diagnostic system for navigation in photosesnsitized neural tissues during neurosurgery operations on neural malignant tumors in patients. This system contains a beamsplitter adapter based on a dichroic mirror where white light image goes to a high sensitivity monochrome camera and color image goes to a color camera. Both images are spectrally resolved. Then both images go to processor unit and then displayed on the monitor. In the clinical conditions the presented system indicated all the residual tumors including meningioma, neurinoma, and glioblastoma.

Keywords.

Fluorescence diagnostics, neurosurgery, meningioma, glioblastoma, GBM, fluorescence navigation, neurinoma, operation microscope.

Introduction.

Fluorescence navigation in the modern neurosurgery of malignant tumors is one of the most sensitive and specific methods of diagnostics to improve the quality of operations and thus to increase the survival time of the patient. Fluorescence diagnostic in presence of specific photosensitizers brings even better results in terms of sensitivity and specificity. Here we present a novel device for the fluorescence navigation of photosensitized tumors and results of its clinical applications with different kinds of malignant tumors of central nervous system. To do that we have developed fluorescence diagnostic upgrade system for operation microscope and endoscope. In our fluorescence system we implemented a number of innovative features including fluorescence excitation in 635nm and two registration cameras.

Materials and methods.

All patients were administered with photosensitizer Alasens 3 hours prior to the surgery per oz. The transnosal operations were carried out with Karl Storz endoscope, spinal tumors were operated with Carl Zeiss OPMI microscope, head brain tumor tumor were operated with Carl Zeiss OPMI Pentero operation microscope. For the fluorescence diagnostics we developed a system which consists of 2 light sources one LED based white light source and another laser diode based source for fluorescence excitation at 635nm. To register the white light image and fluorescence image we developed a dichroic mirror based beam splitter with two digital cameras. One color camera for registering reflected back white light image and one monochrome camera for fluorescence signal. Both images in real time are processed in computer with special software involving use of the GPU NVIDIA GeForce video card

and displayed to the monitor. To deliver the illumination light we have developed a Y-shaped fiber optic light guide which collects light from both the light sources, mixes them together and exposes them to the operation field.

Results.

We carried out experiments with meningioma infiltrated in the cavity of nose, neurinoma in the cord of the spinal brain and glioblastoma in the head brain. As for the clinical result we got strong fluorescence signal on top of the video signal in natural colors for all three nosologies. As the technical result we developed the system which meets the following innovative properties:

1. Because of the fluorescence excitation in the red range of optical spectrum we are scanning the tissue 3 – 5 times deeper than all the market available devices. More, we can make fluorescence diagnostics in the presence of blood.
2. We can output the fluorescence navigation information on top of the real time video signal from the tissue in natural colors.
3. Using 2 cameras we can assess photosensitizer concentration in the photosensitized tissue.

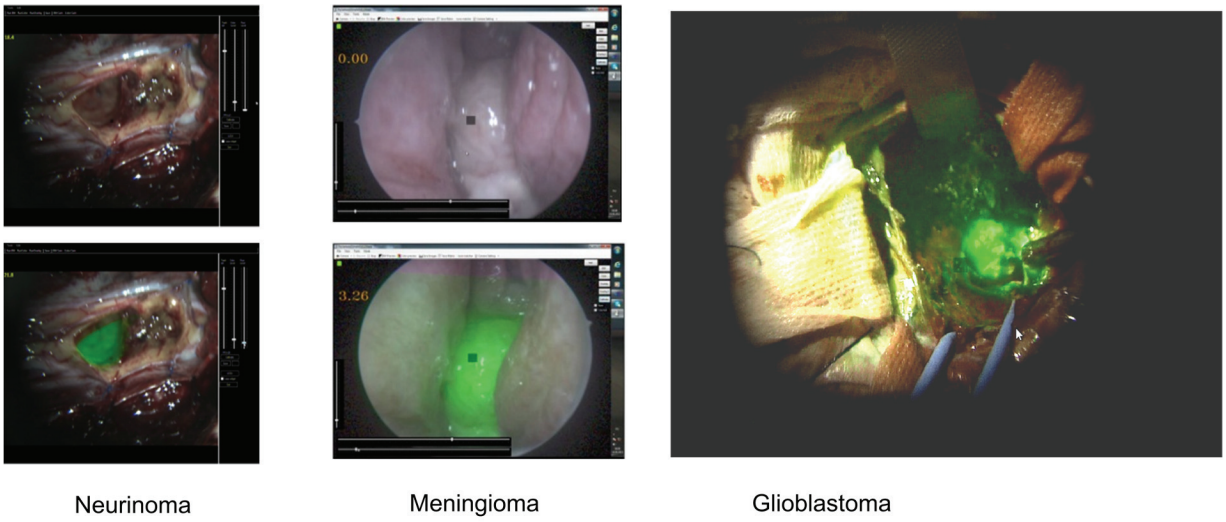

Fig. 1. Examples of method application in clinical conditions.

References.

[1] Loshchenov, M., Zelenkov, P., Potapov, A., Goryajnov, S., & Borodkin, A. (2014). Endoscopic fluorescence visualization of 5-ALA photosensitized central nervous system tumors in the neural tissue transparency spectral range. Photonics & Lasers in Medicine, 3(2), 159-170.

[2] Markwardt, N. A., Haj-Hosseini, N., Hollnburger, B., Stepp, H., Zelenkov, P., & Rühm, A. (2015). 405 nm versus 633 nm for protoporphyrin IX excitation in fluorescence-guided stereotactic biopsy of brain tumors. *Journal of biophotonics*.

Light Fields in Skin Tissue with Rough Surface

A. P. Ivanov and V. V. Barun
B.I. Stepanov Institute of Physics, Belarus National Academy of Sciences, Nezavisimosti Pr. 68, Minsk 220072, Belarus
ivanovap@dragon.bas-net.by, barun@dragon.bas-net.by

Abstract: Fluence rate inside skin tissue and its diffuse reflectance are analytically simulated. The roughness of skin surface and light refraction at the epidermis and stratum corneum interface are accounted for. Light penetration depth is shown to be independent of the skin relief, whereas the reflectance to increase with roughness variance.

1. Introduction

Light characteristics inside and outside biotissues provide a basis for solving various problems of biomedical optics, such as the optimization of light therapy, laser hypothermia, optical diagnostics methods. Irradiating and scattered light interacts with rough skin surface to somewhat change its power and angular parameters. This can effect on spatial distribution on absorbed and scattered power, light penetration depth, and action spectra for tissue chromophores. Besides, variations of refractive indices at tissue layer interfaces result in changes of angular patterns near the surface and in the depth. Therefore, it is interesting to evaluate the influence of these factors on light fields in skin tissue and on the retrieval of its parameters.

2. Tissue model and simulation method

The investigations are based on the optical and structural tissue model [1] and on the evaluations [2] of skin roughness parameters. Tissue is treated as a three-layer medium comprising optically thin stratum corneum and epidermis and optically thick dermis. The model includes the set of thicknesses d_{sc} and d_e of the thin layers, volume fractions f_m and C_V of melanin and capillaries, and blood oxygen saturation S. We assume below constant d_{sc} = 20 μm, d_e = 100 μm, C_V = 0.02, and S = 0.75. The skin surface relief is simulated by the Gaussian probability density of micro area tilts with variance D_γ ranging from 0 (plane Fresnel surface) to 0.44.

We use analytic approaches [3, 4] to solving the radiative transfer equation in a multi-layered absorbing and scattering medium for the simulations. Multiple scattering and multiple light re-reflections between the skin layers and the surface are treated. Light angular patterns near the surface are set as $I(\theta) = I_{sc}(\theta)I_e(\eta)I_d(\eta)$, where θ is the polar angle, $\eta(\theta) = \mathrm{asin}(n\sin\theta/n_i)$, n = 1.55 and n_i = 1.33 are the refractive indices of stratum corneum and epidermis (the same for dermis), respectively. These three angular functions describe light propagation in the corresponding tissue layers. Angle η treats the refraction of light propagating from dermis (n_i) to surface (n). Then, as a first step, the diffuse reflectance as a function of η and D_γ [5] and the angularly integrated surface albedo R^* are calculated for surface irradiation by light scattered in tissue volume. So the problem on light characteristics inside and outside the tissue reduces to the calculation of light fields for a medium with surface albedo depending on skin roughness. This can be done by the method of [4].

3. Results

The said first calculation step has showed that surface albedo R^* as a function variance D_γ behaves differently at varying wavelengths λ. In the red, R^* decreases with D_γ increasing. On the other hand, albedo R^* has a maximum in the blue at small variances $D_\gamma \approx 0.07 - 0.08$, where R^* of rough surface increases by approximately 1.3 – 1.5 times as compared with plane interface. The reasons are discussed in detail elsewhere [5]. Naturally, one can observe the corresponding opposite features in light transmission (equal to $1 - R^*$) of rough skin surface. These features lead to spectral dependences of tissue diffuse reflectance R_{sk} shown in Fig. 1. In the blue, one can see that the albedo values to slightly depend on skin roughness. The opposite situation occurs in the red and near IR, where R_{sk} increases absolutely by 0.05 to 0.1 and the respective relative values do the same by 25 to 50 %. This is due to the higher transmission of diffuse multiply scattered light by rough skin surface as compared to the plane one. Fig. 1 illustrates also the calculations made for the plane surface without accounting for the refraction. This factor is seen to essentially affect the spectral albedos R_{sk}.

Another important parameter of light fields in a turbid medium is light propagation depth. It determines, for example, light action on tissue chromophores, tissue heating by light, etc. The definite conclusion on this parameter can be done from the data of Fig. 2. It illustrates the depth structure of scattered fluence rate W at 800 nm inside skin tissue. At the upper dermis region, W values reduce by the influence of skin roughness and angular pattern $I(\theta)$. We can also note here the essential effect of light refraction on W. However, in deeper tissue regions at larger z, neither the roughness nor the refraction affect the fluence rate. It follows from these data, in particular, that light penetration depth is essentially independent of the two factors studied in the paper.

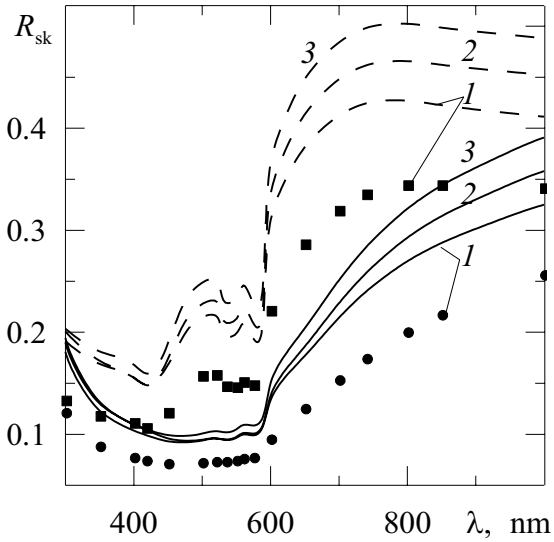

Fig. 1. Skin albedo spectra at $f_m = 0.16$ (solid lines, ●) and 0.04 (dashed, ■), symbols ● and ■ show calculations without accounting for the refraction, $D_\gamma = 0$ (curves *1*, ●, ■), 0.2 (*2*), and 0.44 (*3*)

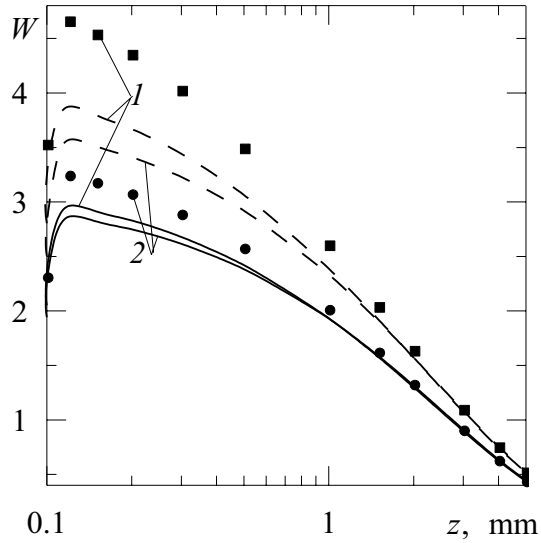

Fig. 2. Fluence rate as a function of tissue depth z at $f_m = 0.16$ (solid lines, ●) and 0.04 (dashed, ■), ● and ■ shows calculations without refraction, $D_\gamma = 0$ (*1*, ●, ■) and 0.44 (*2*), λ = 800 nm

4. Conclusion

The above results enable answering to the question, when one should account for the roughness of skin surface and light refraction while solving direct and inverse problems of biomedical optics. As pointed out, neither the roughness nor the refraction affect the fluence rate at large z. Another situation occurs for studies of tissue heating by red or near IR radiation. For example, it is shown in [6] that the main heating mechanism here is heat transfer from epidermis to dermis. One can see from Fig. 2 that the roughness and the refraction result in the reduction of fluence rate in epidermis. So this layer would have lower temperature, which reduces dermis heating too.

There are known various techniques to retrieve structural and biophysical parameters of soft tissues by using backscattered light. For example, the method to non-invasively determine f_m, d_e, C_V, and S by measured spectral albedo R_{sk} is proposed in [7]. It follows unambiguously from the above results that the solution to the inverse problem requires accounting for the skin roughness and angular pattern $I(\theta)$. However, the solution is complicated by the dependence of reflectance R^* on the parameters desired. It is favorable in this respect that our simulations show the slight effect of C_V and S on R_{sk}, so that one can set $I_d(\eta) \equiv 1$. Function $I(\theta)$ will only depend on product $f_m d_e$ that can be retrieved [7] by measuring R_{sk} at two wavelengths λ = 500 and 570 nm. Besides, the proposed calculation model enables one to determine variance D_γ, which can be useful for evaluations of the efficiency of various dermatology and cosmetology procedures. The similar remarks can be applied to other methods of retrieving tissue parameters such as spatially resolved spectroscopic ones.

5. References

[1] V.V. Barun and A.P. Ivanov, "Thermal Effects of a Short Light Pulse on Biological Tissues. I. An Optical-Thermophysical Model," Biofizika **49**, 1004 – 1012 (2004).

[2] V.V. Barun and A.P. Ivanov, "Light Scattering by Rough Surface of Human Skin. I. Luminance Factors of Reflected Light," Quantum Electron. **43**, 768 ─ 776 (2012).

[3] E.P. Zege, A.P. Ivanov, and I.L. Katsev, *Image Transfer though a Scattering Medium* (Springer-Verlag, 1986).

[4] V.V. Barun and A.P. Ivanov, "Light absorption in blood during low-intensity laser irradiation of skin," Quantum Electron. **40**, 371 ─ 376 (2010).

[5] V.V. Barun and A.P. Ivanov, "Light Scattering by Rough Surface of Human Skin. II. Diffuse Reflectance," Quantum Electron. **43**, 979 – 987 (2013).

[6] V.V. Barun and A.P. Ivanov, "Role of Epidermis in the Optics and Thermal Physics of Human Skin," Optics Spectrosc. **107**, 909 – 916 (2009).

[7] A.P. Ivanov and V.V. Barun, "Light Reflection Spectra as a Diagnostic Tool for the Structural and Biophysical Parameters of Skin," Optics Spectrosc. **104**, 300 – 307 (2008).

Multicomponent diode laser gas analyzer for medical screening diagnostics: Qualitative and quantitative feature of biomarkers of human exhaled air at different functional states

A. Karabinenko[1], A. Bogomolova[1], S. Shastun[2] , A. Nadezhdenskii[3], Ya. Ponurovskii[3], M. Spiridonov[3], V. Zaslavskii[3]

[1] Pirogov Russian National Research Medical University (RNRMU), Ostrovitianov str. 1, 117997 Moscow, Russia. E-mail: karabinenkoa@mail.ru
[2] Peoples Friendship University of Russia., 117198 Moscow, Russia
[3] A.M. Prokhorov General Physics Institute, 38 Vavilov str.,119991 Moscow, Russia E-mail: ponur1960@yandex.ru

Screening tests are effective methods of assessing the functional state of the organism. The screening study in medicine is understood as a set of measures aimed at identifying the diseases in a large group of patients in the absence of pronounced symptoms. The main requirements for a screening test is its simplicity, noninvasiveness, and safety of the testing procedures, as well as high processing speed and the ability to detect diseases at an early stage.

An experimental prototype of multi-channel analyzer for non-invasive screening and biomedical research was developed on the basis of fiber coupled the near-IR range diode lasers. Device enables to measure $^{12}CO_2$, $^{13}CO_2$, CH_4, NH_3 and H_2S biomarkers of the exhaled air. Detection of CH4 was carried out in the wavelength range of 1.65 μm, ammonium NH_3 in the 1.51 μm and the $^{12}CO_2$, $^{13}CO_2$ and H_2S in the range 1.60 μm. Measuring the concentrations of the five molecules simultaneously were carried out in Herriot type multipass cell with full optical path length of 26 m and a volume of 2.5 liters. All measurements were made in real time. Fig. 1 presents photo multi-channel diode laser analyzer for non-invasive screening and biomedical research.

Clinical tests of the diode laser spectrometer were performed in the Moscow City Clinical Hospital No 12. The measurements were performed in 162 patients with various diseases in phase and remission at rest, during exercise, recovery and after meals. Identified biomarkers of exhaled air, allowing to assess the state of the cardiorespiratory function, gaseous Ingredients, reflecting the intensity of the digestive system and the degree of infestation B. Helicobacter pylori, the nature of the food regime. Identified deviations biomarkers of exhaled air levels have diagnostic and prognostic value during mass screening.

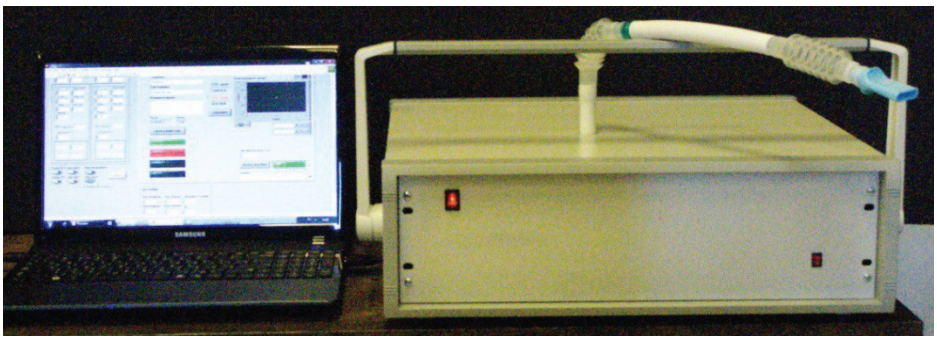

Fig.1 Photo multi-channel diode laser analyzer for non-invasive screening and biomedical research

References

1. *А. Какрабиненко и др., Тезисы I Всероссийской конференции с международным участием ««Химический анализ и медицина», Москва 2015, стр. 10.*

Fluorescence meter for diagnostic purpose with reference channel

V.N. Grishanov, D.V. Kornilin, D.S. Burkov
Samara University, 34, Moskovskoye shosse, Samara, 443086, Russia
vladgrishanov@yandex.ru

Abstract: Proposed fluorescence meter estimates skin autofluorescence made *in vivo* for advanced glycation endproduct evaluation. This instrument is helpful for prognosis of chronic diseases. Light emitting diode with a peak wavelength of 365 nm was utilized.

Fluorescence diagnosis of skin in vivo rapidly introduced into medical practice. Skin accumulates products, reflecting the processes occurring in the body. The most attractive use by screening autofluorescence (AF), as AF intensity measurement does not require any additional material and time costs and traumatic patient procedures. The level of development of modern optoelectronics able to provide the diagnostic sensitivity of the fluorometer, sufficient for reliable registration of a relatively low intensity AF. It is proved that fluorescent assessment of the content of glycation end products (AGE) predicts mortality in diabetes and quality of operations in renal transplant patients [1]. Increased production of advanced glycation end products in the skin is observed during its aging [2], and acute ischemic heart disease [3]. Therefore, the development of a portable, easy-to-use and easily replicable equipment for measuring in vivo skin fluorescence intensity very relevant.

The diagnostic criterion of AF level acts ratio [1, 3]:

$$AU = \frac{\int_{420}^{600} I_{\Phi}(\lambda)d\lambda}{600-420} \times \frac{420-300}{\int_{300}^{420} I_{B}(\lambda)d\lambda}, \quad (1)$$

Where $I_{\Phi}(\lambda)$ – skin fluorescence intensity spectrum of the radiation in the wavelength range (420 - 600) nm; $I_B(\lambda)$ – is the spectrum of the reflected intensity elastically skin fluorescence excitation radiation in the wavelength range (300 - 420) nm. The experimental spectra $I_{\Phi}(\lambda)$ and $I_B(\lambda)$ recorded by spectrometer, which is part of the device for measuring the level of AF. The integration procedure of the spectra in analog form is carried out quite simply by photodetector with spectral parameters adjusted by filters.

Diagnostic fluorometer with a reference channel has been implemented in accordance with the block diagram shown in Fig. 1. The exciting fluorescence radiation 9 from ultraviolet (UV) LED EOLD-365-525 1 passes through the cleaning filter 2 made from colored optical glass UFS6 3 mm thick and a protective glass 3 (microscope slide 1 mm thick) to which is applied from the outside inner side of the forearm - the fluorescent object of study 4. Some scattered forearm skin excitation and fluorescence radiation 10 goes through the cutting filter FGL435 made by firms Thorlabs from the glass GG435 Schott glass with thickness 2 mm 5 and falls on a silicon photodiode BPW21R 6. Then photodiode current will be directly the first factor is proportional to the expression (1). Items 5 and 6 are the main components channel AF measurement. Apart from the protection against ingress of dust into the opto-electronic unit fluorometer glass 3 stabilizes the distance from the emitter and photo detector to the object and allows you to disinfect the surface fluorometer in contact with the patient's skin.

The reference channel is used photodetectors photodiode SFH 229 without the cutting filter, ie, its light-sensitive area falls as a light AF, and not how it is weakened by the elastically scattered radiation skin 10. Since the radiation intensity of the AF of at least 4 orders of magnitude weaker than the intensity of the exciting radiation, it is natural to assume that the current SFH 229 photo-diode is proportional to the intensity of elastically scattered radiation. Thus, the photodiode current gives an assessment of the second factor expression (1). All elements of the optical circuit placed inside a light-tight metal housing 8. Inside the housing is available an electronics board 7.

The circuit board is divided into blocks: in receiving unit, a control unit and communication, power supply, transmitter unit [4]. The receiving unit is converting the optical signal coming from on-sample, in electric and amplification. The photoelectric converter is based on the photodiode circuit and current-to-voltage converter. communications and control unit is designed to digitize the signal received from the receiving unit and transmitting the digitized data to the personal computer 12. The power supply source is a stabilized voltage.

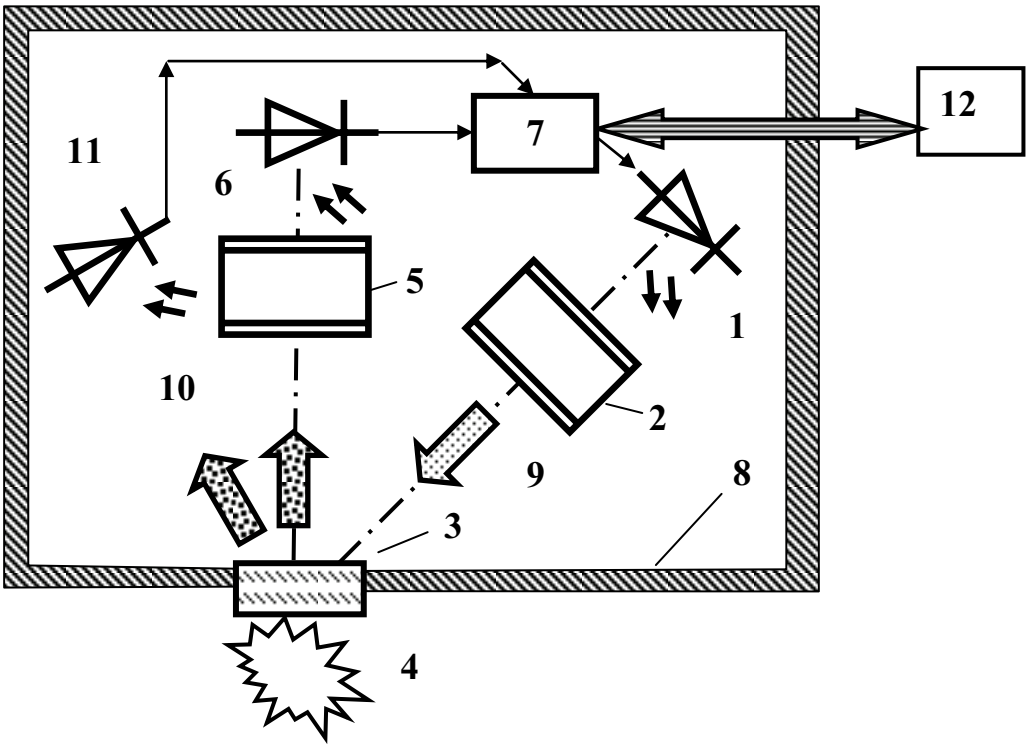

Fig. 1. Block diagram of the fluorometer: 1 - LED EOLD-365-525; 2 - cleaning filter of colored optical glass UFS6; 3 - safety glass; 4 - the object of study; 5 - Trim filter FGL435; 6 - photodiode BPW21R; 7 - electronics board; 8 - metal casing; 9 - flow of excitation radiation; 10 - scattered toward photodetectors flux; 11 - photodiode SFH 229; 12 - PC

The software generates a fluorometer in the computer table digitized readout AF and the reference measurement channels. These reference averaged and AU (1) is calculated according to the criterion of the average values. In addition, the software fluorometer via a USB port and an internal microcontroller electronics board controls the duration of the diagnostic procedures and the transfer of digitized signals AF intensity in the computer. It implements creation, replenishment and storage of diagnostic results database and patients and moments of fixing those values. On the computer screen displays the waveforms of the AF and the reference channel, allows the physician to monitor the dynamics of the signal during a diagnostic procedure. The time interval during which the fixed pairs of ~ 1000 counts, is only 20 seconds. For operational information at the end of the procedure issued the arithmetic mean value of the intensity of the AF and elastic scattering, their coefficients of variation, as well as the AU value.

With the device held more than 100 diagnostic tests on volunteers both at the university and in the clinic. He demonstrated the full functionality and operability. Medical aspects of the tests carried out are analyzed.

[1] Meerwaldt R., Graaff R., Oomen P. H. N. et al. «Simple non-invasive assessment of advanced glycation endproduct accumulation», Diabetologia 47, 1324 – 1330 (2004).

[2] Papayan G. V., Petrishchev N. N., Krylova E. V. et al. «Method of estimating the biological age of skin by means of a fluorescence multispectral video dermatoscope», Journal of Optical Technology 77(2), 60 – 67 (2010).

[3] Mulder D. J., van Haelst P. L., Graaff R. et al. «Skin autofluorescence is elevated in acute myocardial infarction and is associated with the one-year incidence of major adverse cardiac events», Netherlands Heart Journal 17(4), 162 – 168 (2009).

[4] Kornilin D.V., Grishanov V.N. «Portable fluorescence meter for medical applications», Proc. of SPIE Vol. 9887 98871N-1. - CCC code: 0277-786X/16/$18 doi: 10.1117/12.2227392. – 7 p. (2016).

Development of intraoperative videosystem for fluorescence diagnostics and photodynamic therapy monitoring of malignant tumors

Borodkin A.V.[1], Linkov K.G.[1], Grachev P.V[1] Loshchenov M.V.[1]

[1]*Prokhorov General Physics Institute, Russian Academy of Sciences*

e-mail: borodkin.aleksandr@gmail.com

Abstract: The primary goal of this development is to increase the efficacy of the intraoperative visualization of malignant tumors with development of fluorescence diagnostics methods. Fluorescence diagnostics allows precise determining of tumor boundaries. Also we developed a technique for assessment of photosensitizer(PS) concentration and dosimetry and control of photodynamic therapy (PDT) efficacy. The developed system uses 635nm laser light for the fluorescence excitation to achieve deeper penetration depth.

1. Introduction

The uniqueness of PDT is that the same drug can serve as both the therapeutic agent and the imaging contrast agent. PS have a propensity for preferential accumulation in neoplastic tissues. Upon excitation with the appropriate wavelength PS fluoresces in the visible spectral range. In order to achieve either optimal staging or complete or optimal cytoreduction, visualization of tumor lesions is important.

2. Materials and methods

A schematic diagram of the fluorescence diagnostic video-system in Fig. 1. White light diode light source and the color camera are used for visual navigation. Fluorescence excitation is performed with 635nm diode laser. The monochrome digital CCD camera registers fluorescence signal. Images that recorded by the cameras are transmitted to the personal computer with specially developed software. After the affine transformation both images are combined and displayed. Optical filters provide spectral resolution of the light-sensitive camera sensors from high-intensity radiation from the laser. After the system was pre-calibrated on phantoms we evaluated the ratio between the fluorescence intensities in the peritumoral area and in the tumor itself. We have an opportunity to estimate qualitatively and quantitatively concentration of a photosensitizer in the area of interest with the subsequent indication of concentration value on the screen. The system was tested on phantoms and brain tumors with 5-ALA induced protoporphyrin IX (PpIX) [1]. In the current work we carried out the tests on tumors of female reproduction organs with use of chlorine-based photosensitizers.

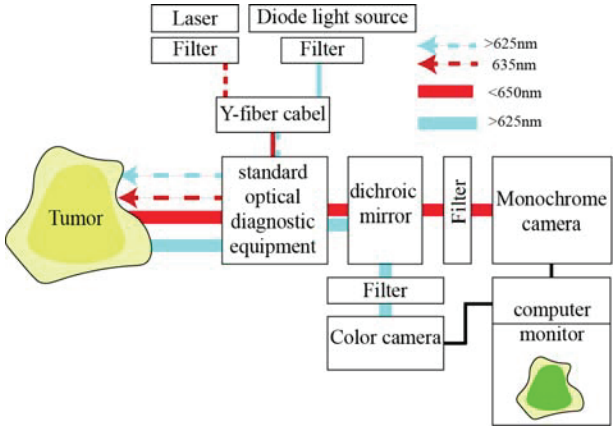

Fig. 1. Schematic diagram of fluorescence diagnostic video-systems.

3. Results

System complies standard optical diagnostic imaging equipment such as laparoscopes, endoscopes, cystoscopes, and neurosurgical microscopes. Constructive feature of the device allows to create the full color image of biological tissues jointly with fluorescent sections from new growths where have been selectively collected molecules of PS on one

screen, and, the pathological centers can be highlighted by any color to the discretion of the operator. In Fig. 2 we can see natural color image combined with fluorescence image of dysplasia of vulva in overlay mode. Area colored with green color corresponds to the maximum luminescence intensity. According to the PS concentration assessment (top left corner of the screen) fluorescence intensity in dysplasia is 6,4 times higher than in normal tissue.

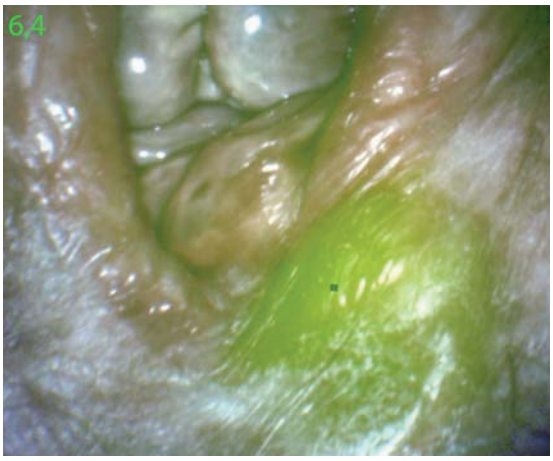

Fig. 2. Real-time image during the fluorescence diagnostics. Tumor fluorescence is marked with green color. Dysplasia of vulva. Chlorine based photosensitizer Fotolon.

4. Conclusions

Optical methods and digital imaging provide more opportunity for cancer surgery by real-time fluorescence guidance by discriminating between healthy tissues and malignant tumors. Considering less light absorption in tissue in the red spectral range the system presented in this work has higher sensitivity and better ability of tumor detection.

[1] Loshchenov, M., Zelenkov, P., Potapov, A., Goryajnov, S., Borodkin, A. Endoscopic fluorescence visualization of 5-ALA photosensitized central nervous system tumors in the neural tissue transparency spectral range Photonics and Lasers in Medicine. 2014, 3 (2), pp. 159-170

Biological Activity of Low-Intensity Continuous, Quasi-Continuous and Pulsed Laser Radiation of Nano- and Picosecond Ranges

V. Yu. Plavskii, N. V. Barulin, A. V. Mikulich, A. I. Vodchits, I. A. Khadasevich, L. E. Batay, A. S. Grabchikov, A. I. Tretyakova, L. G. Plavskaya, V. A. Orlovich

B.I. Stepanov Institute of Physics of NAS of Belarus, 68, Nezavisimosti Ave., 220072 Minsk, Republic of Belarus

e-mail: v.plavskii@ifanbel.bas-net.by

Abstract: It is established that biological effect of laser radiation controlled on functional activity of zooplankton and sturgeon sperm is strongly dependent on the mode of acting radiation under conditions with equal average power density.

1. Introduction

Recent achievements in the field of physics and technology of the lasers have made available for widespread clinical use the laser sources generating the radiation in continuous, modulated, quasi-continuous and pulsed modes in different regions of the optical range. However, the advantages and disadvantages of these regimes of regulatory action are not obvious. As we have shown earlier, a convenient model for studying the regulatory action of low-intensity laser radiation are fish embryos and sperm as well as zooplankton.

The purpose of this work - a comparative study of the biological activity of continuous, quasi-continuous and pulsed low-intensity laser radiation of nano- and picosecond time ranges with equal average power density.

2. Materials and methods

Zooplankton (branchiopod crustaceans) *Artemia salina L.* and sturgeon sperm were used as objects. As a test, to check the action of laser radiation, percentage of nauplii hatched from cysts (protective shells) after activation of eggs in salt water in a stable thermal regime was chosen. The indicators of biological action on fish sperm were the data on duration of sperm motility as well as their curvilinear velocity after activation with water. The value of photobiological effect (dose curve) was evaluated in comparison with control intact objects. The exposure was realized using the second-harmonic radiation (wavelength – 532 nm, average output power ~30 mW) of Nd:YAG-lasers working in continuous and quasi-continuous (pulse repetition rate – F = 1 kHz, pulse duration – τ = 100 ns) modes, as well as in pulsed mode with generation of nanosecond (τ = 15 ns, F = 10 Hz) and picosecond (τ = 60 ps, F = 20 Hz) pulses. Comparative studies upon exposure to radiation of red (632.8 nm, He-Ne laser) and near IR (808 and 976 nm – diode lasers; 1064 and 1342 nm – diode pumped Nd:YVO_4 laser; 1176 nm – diode pumped Nd:YVO_4 laser (1064 nm) with intracavity Raman self-frequency conversion) spectral region were also carried out. Power density – 3 mW/cm^2.

3. Results and discussion

It is shown for the first time, that, despite the significant differences in peak values of intensity of acting factor, both continuous and quasi-continuous radiation and radiation of nano- and picosecond ranges are able to have both stimulating and inhibiting effects on all investigated parameters of functional activity of biological systems in a certain range of dose rates. As an example, Fig. 1 shows the effect of continuous, quasi-continuous and pulsed laser radiation of nano- and picosecond time ranges with λ = 532 nm under equal average power density of 3 mW/cm^2 on the duration of the motility of sturgeon sperm after activation with water in percentage to control (η, %). Data show that the optimal dose of optical radiation which initiates the stimulation of functional characteristics of biosystems is strongly dependent on the mode of acting radiation. For example, using the aforementioned parameters of acting factors, the optimal stimulating dose when controlling the sperm motility is 135 mJ/cm^2 for continuous radiation; 90 mJ/cm^2 – for quasi-continuous and nanosecond and 60 mJ/cm^2 – for picosecond radiation. At the same time, maximal stimulating effect (compared to the control) is (140±6) % for continuous; (163±9) % – for quasi-continuous; (122±6) % – for nanosecond and (115±7) % – for picosecond modes. Even more pronounced stimulating effect (180±9) % has a continuous radiation of red spectral region. It is typical that stimulating effect in the case of nano- and picosecond modes is observed in a very narrow dose interval: 30–60 mJ/cm^2. The rapid suppression of functional characteristics of biological systems is observed upon increasing the dose: at a dose of 1.8 J/cm^2 duration of sperm motility reduced more than two times compared to the control. Similar bell-shaped dose curves are registered when controlling the curvilinear sperm velocity and percentage of nauplii hatched from cysts after activation of eggs in salt. This type of dose curves testifies to “soft” regulatory nature of biological action of laser radiation. On the other hand, similar nature of

dose curves upon control of functional characteristics differing in their structural organization of biological systems (zooplankton and fish sperm) is evidence of biological significance of the results obtained.

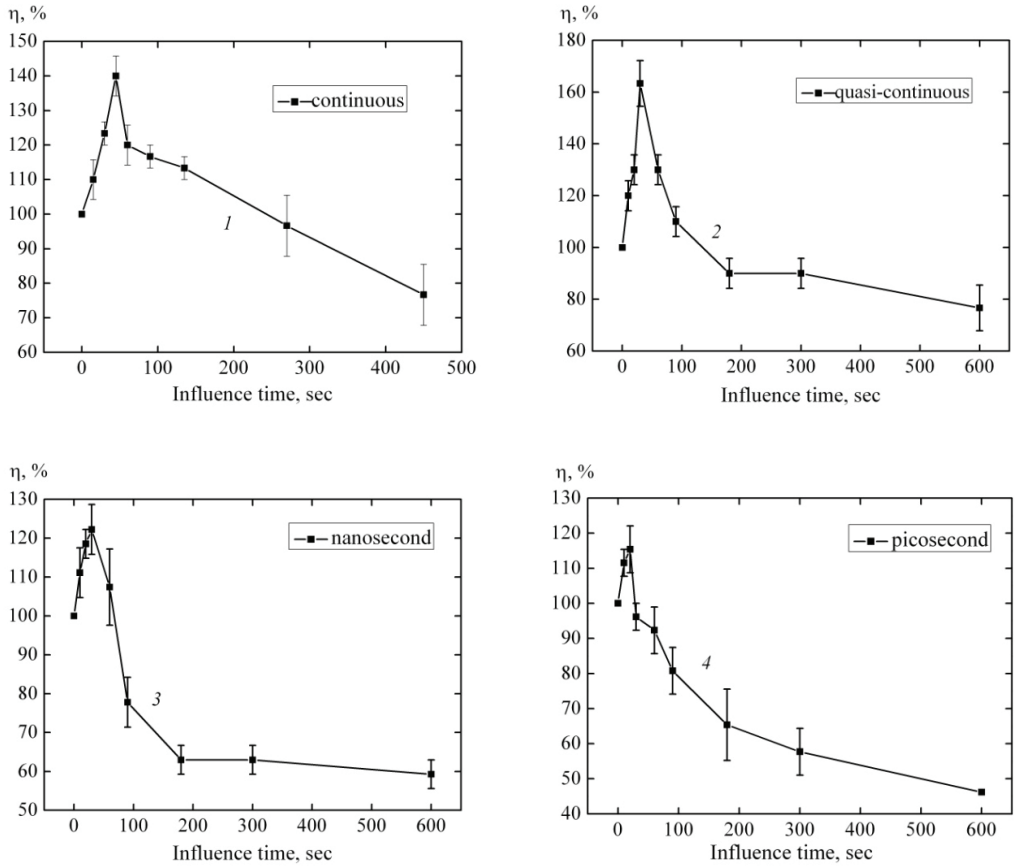

Fig. 1. Effect of continuous (1), quasi-continuous (2), pulsed laser radiation of nano- (3) and picosecond (4) time ranges (P = 3,0 mW/cm^2) with λ = 532 nm on the sperm motility

Studies have shown that photobiological effects initiated by laser radiation are strongly dependent on the wavelength of incident radiation. It is noteworthy that, under optimal conditions, if radiation exposure λ = 632,8 nm, λ = 976 and λ = 1064 nm has an inhibitory effect on the hatching of the nauplii, then the radiation with λ = 808 nm, λ = 1176 nm and λ =1342 nm has stimulating effect. The results obtained by the action of laser radiation on the hatching of the nauplii *Artemia salina L.* allow to make some conclusions about bioactivity of optical radiation of the near IR spectral range. Since the laser light with λ = 808, 976, 1064, 1176, 1342 nm is outside the absorption band of the porphyrins, the possible role of photosensitized reactions involving them should be excluded. Severe photobiological effect when exposed to radiation λ = 1176, 1342 nm can also questioned the role of the direct photochemical reactions of oxyhemoglobin (and other macromolecules containing the prosthetic groups), as the impact of a powerful pulsed laser radiation with a wavelength λ = 1060 nm for its solutions does not cause any reversible or irreversible spectral changes. Note also that the presence of extreme points in the absorption spectrum of aqueous solutions of macromolecules in λ = 1100-2500 nm is almost completely determined by the solvent.

In our opinion, most likely, that dissolved molecular oxygen and water can act as acceptors of laser radiation of near infrared spectral region, determining its biological effects. Despite small molar extinction coefficient there is the data confirming the possibility of direct triplet-singlet excitation of molecular oxygen being photobiological importance. Accounting low value of molar extinction coefficient of such transition and relatively low power density of exciting radiation (3 mW/cm^2) the concentration of singlet oxygen in biological system is sufficiently small to generate noticeable destructive action. Most likely, that its formation in biological system can play signal (trigger) function that influences running the bio-chemical and physiological processes in organism, for example, such as starting the apoptosis.

However, the presence of biological effects when exposed to radiation cysts nauplii out of the corresponding bands of direct excitation of singlet oxygen suggests that, in addition to molecular oxygen, a water - an universal biological environment, which plays a leading role in the maintenance and regulation of homeostasis in living systems - can be an acceptor of laser radiation of near-infrared region of the spectrum.

The Use of Semiconductor Lasers and LEDs as Fungicidal Factor

A. V. Mikulich, A. I. Tretyakova, L. G. Plavskaya, I. A. Leusenko, V. S. Ulashchik, V. Yu. Plavskii
B.I. Stepanov Institute of Physics of NAS of Belarus, 68, Nezavisimosti Ave., 220072 Minsk, Republic of Belarus
e-mail: a.mikulich@ifanbel.bas-net.by

Abstract: The ability of polyene antibiotic amphotericin B to act as photosensitizer and to enhance its fungicidal action upon exposure to radiation (semiconductor lasers and LEDs) corresponding to absorption band of amphotericin B has been shown.

1. Introduction

At present time, fungal infections are one of the major healthcare problems due to development of resistance of pathogens to fungicides used. Generally, antimicrobial agents bind in sufficient concentrations in infected area for effective bactericidal (fungicidal) action. However, due to acquired resistance microbial strains become not sensitive to them. In our opinion, one of the most realistic, feasible and low-cost ways to improve the treatment of fungal infections can be antimicrobial photodynamic therapy using antifungal drugs that have been approved for use in clinical practice and exhibit the photodynamic activity as photosensitizers. Unfortunately, the possibility of implementing the fungicidal technologies by using the photosensitizing properties of antifungal drugs has not been studied.

In this paper, we have for the first time shown that one of the most widely used for treating the fungal infections polyene antibiotic amphotericin B is an effective photosensitizer and upon exposure to radiation of laser and LED sources in its absorption band is able to provide light-induced fungicidal effect.

2. Materials and methods

A formulation of polyene antifungal antibiotic amphotericin B Fungizone (lyophilized powder for injection) was used as photosensitizer. The objects sensitive to the light in the presence of amphotericin B were enzymes molecules (lactate dehydrogenase, LDH) in solution, BGM cells from African green monkey kidney, the experimental animals (rats) when modelling the contact dermatitis on depilated areas of the skin.

3. Results and discussion

Influence on biological systems in absence and in presence of photosensitizer was realized using radiation of semiconductor laser with emission maximum $\lambda = 405$ nm as well as LED sources with $\lambda = 395$ nm that is practically corresponds to the long-wavelength absorption spectrum of antibiotics (Fig. 1). Detailed studies of the structure of amphotericin B showed that this compound in aqueous solution in the neutral pH values exists as mixture of monomeric, dimeric and oligomeric forms. At the same time, photosensitizing activity of the drug is due to the monomeric forms. A distinctive feature of photonics of amphotericin B- forbidden by the rules of symmetry transition $S_0 \rightarrow S_1$; absorption in the UV and visible region of the spectrum is due to the transition $S_0 \rightarrow S_2$.

It is shown that the fluorescence of aqueous solutions of amphotericin B is explained mainly by emission of monomers both in the emission channel $S_1 \rightarrow S_0$ and $S_2 \rightarrow S_0$. Contrary to popular opinion, contribution of dimeric forms to fluorescence is negligible. Dissociation of aggregated forms of amphotericin B under excitation by UV radiation to the monomers and their subsequent fluorescence both in emission channel $S_1 \rightarrow S_0$ and $S_2 \rightarrow S_0$ was registered.

It is established using spectral-luminescent methods that one of targets for photodynamic action of amphotericin B is enzymes of glycolysis system as it is supported by light-induced inhibition of their activity upon exposure to laser radiation with $\lambda = 405$ nm. Apparently, the radical processes rather than reactions involving singlet oxygen are dominant in the mechanism of photodynamic damage of enzyme. This is supported by a pronounced decrease in the effect of photoinactivation of enzyme when adding the electron donors and electron acceptors (cystine, NAD^+) to mixture under irradiation, as well as during replacement of aqueous solutions with heavy water solutions. As is known, in the case of the predominant participation of singlet oxygen in photochemical reactions one would expect a sharp increase in LDH photoinactivation upon replacement of H_2O with D_2O due to an increase of the lifetime of singlet oxygen. In this respect, the observed decrease in the effect of amphotericin B sensitized photoinactivation of LDH upon irradiation of solutions in the presence of sodium azide may also be due to the quenching of excited states of antibiotic by sodium azide.

It is shown that, depending on the type of biosubstrate, its damage sensitized by amphotericin B can involve singlet oxygen. Sensitized by amphotericin generation of singlet oxygen in aqueous media was confirmed using a fluorescent probe Singlet Oxygen Sensor Green - specific fluorescence sensor of $^1O_2$.

Fig. 2 shows that the exposure of cells preincubated with photosensitizer to laser radiation of blue spectral region (corresponding to the absorption band of amphotericin B) causes their dose-response photodestruction (decrease in cellular survival).

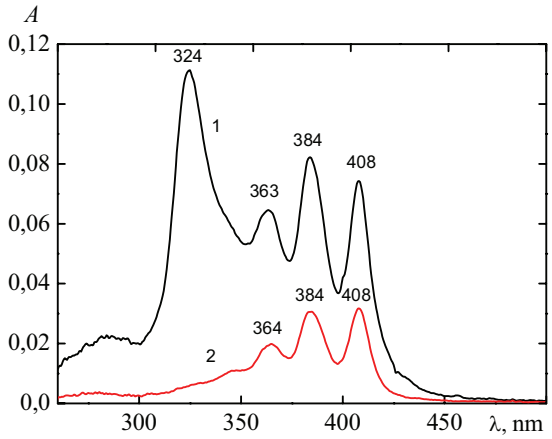

Fig. 1. Absorption spectra of concentrated (C_1 = 2 μM) (1) and diluted (C_2 = 0,06 μM) (2) aqueous solutions (pH 6,0) of amphotericin B: 1 – cuvette, l = 10 mm; 2 – cuvette, l = 50 mm

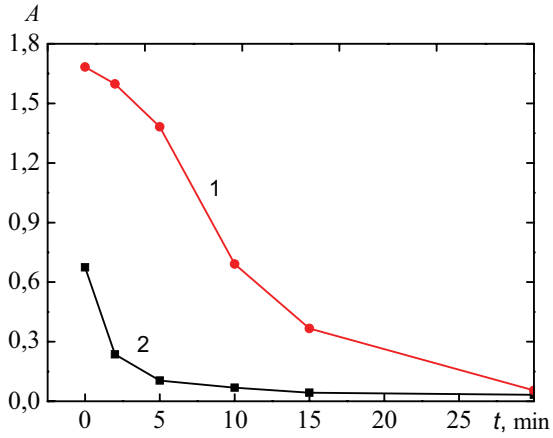

Fig. 2. Index of cellular survival assessed by MTT-test upon irradiation of cellular monolayer in absence (1) and presence (2) of amphotericin B (λ = 395 nm, P = 20 mW/cm^2)

It is also shown in experiments on modelling the contact dermatitis on depilated areas of the skin of rats (Fig. 3) that the exposure to radiation corresponding to the absorption band of amphotericin B causes a twofold increase in its fungicidal action.

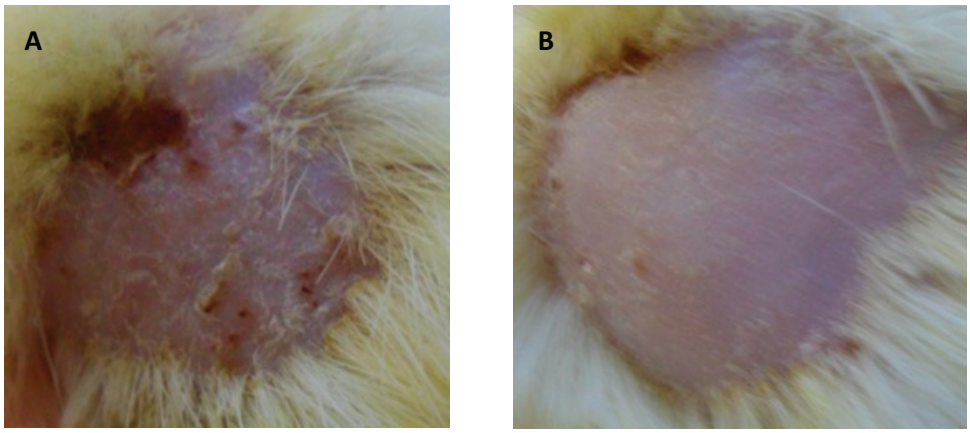

Fig. 3. Area of skin inflammation of experimental model of dermatitis before (A) and after (B) photodynamic therapy with amphotericin B as photosensitizer

The results obtained can be used in medical practice to treat the fungal infections of the skin, mouth, female genital area, etc. The availability of photosensitizer (amphotericin B) approved for use in medical practice and phototherapeutic equipment corresponding to its absorption spectrum allow to develop the necessary medical technology.

Photostability of bilirubin and the mechanism of its photosensitizing effect on animal cells in culture

O. A. Kozlenkova[1], L. G. Plavskaya[1], O. N. Dydinova[1], A. V. Mikulich[1], I. A. Leusenko[1], A. I. Tretyakova[1], V. Yu. Plavskii[1], J. Gao[2], D. Xiong[2], X. Wu[2]

[1] *Laboratory of organic heterogeneous media, B.I. Stepanov Institute of Physics of NAS of Belarus, 68, Nezavisimosti prospect, 220072 Minsk, Republic of Belarus*

[2] *Suzhou Institute of Biomedical Engineering and Technology, Chinese Academy of Sciences, 88 Keling Road, Suzhou New district, Jiangsu Province, 215163, P. R. China*

e-mail: olga.kozlenkova@gmail.com

Abstract. The exposure to radiation of LED sources with λ_{em} = 465 and 520 nm causes identical damaging effects on animal cells that may be due to significant change in the spectral characteristics of bilirubin upon entering into the cells.

1. Introduction.

The ability of bilirubin to act as sensitizer in biological systems at various levels of structural organization is the subject of numerous studies in light of widespread use of phototherapy for treating hyperbilirubinemia of the newborns. The question of the possible side effects of such phototherapy is still the subject of heated debate. In recent years, the urgency of this problem became even more acute in connection with the application for the treatment of neonatal hyperbilirubinemia of new light sources based on high-brightness LEDs, allowing vary over a wide range both the intensity and the wavelength of incident radiation within the absorption band of the pigment (λ=400-530 nm).

The aim of the present work – the study of mechanism of sensitized by pigment damage of the cells in culture upon irradiation with LED sources of blue and green spectral range as well as comparable studies of photostability of bilirubin in cells and in a complex with albumin.

2. Materials and methods

The object of the study was African green monkey kidney cells BGM in the logarithmic growth phase. The cells were grown in disposable Petri dishes in a nutrient medium MEM (minimal essential medium) with 10% bovine serum at 37 °C and a 5% CO_2 incubator. The cellular monolayers were preincubated with bilirubin in a concentration of 40 mM for 2 hours, and then exposed to radiation of LED sources with emission band maximum at about 465 nm or 520 nm. Photostability of bilirubin was investigated in cell growth medium, in which bilirubin is mainly bound to albumin, as well as in BGM cells. Photochemical stability of bilirubin was evaluated spectrophotometrically by comparing the absorbance of the bilirubin solution extracted from the cells using DMSO immediately after irradiation by LED source and unirradiated cells. We use an MTT-test as a criterion for the metabolic cells activity assessment.

3. Results and discussion

Studies have shown that bilirubin can have a sensitizing effect on the cells (as supported by the data on reduction of viability) when excited by optical radiation with wavelength λ = 465 nm and λ = 520 nm. It is found that the photobiological effect depends on the physiological state of the cells, the dose of incident radiation and the concentration of the photosensitizer. Dependence of cell survival on energy dose upon irradiation of cells in the presence of bilirubin by LED sources with an emission band maximum at about 465 and 520 nm is mono-exponential function (Fig.1). This indicates that it is bilirubin that acts as a sensitizer but not its photoproducts. Another unique feature of these curves - practically identical photobiological effect for radiation with λ = 465 nm, corresponding to the maximum of the absorption spectrum of bilirubin-albumin complex, and for radiation with λ = 520 nm corresponding to the long-wavelength slope of the specified spectrum. Therefore, the inclusion of bilirubin in the cells is accompanied by significant changes in its absorption characteristics. It is shown in experiments with a quencher of $^1O_2$ sodium azide that the decisive role in the mechanism of photodegradation of cells belongs to singlet oxygen (Fig. 2). Indeed, the fraction of viable cells (relative to control) in the absence of other additives upon irradiation of the cells (P = 20 mW / cm^2, t = 5 min) sensitized with bilirubin is γ = (45,5 ± 1,6)%. Under the same conditions of irradiation for cells in the presence of 5 mM of sodium azide the fraction of viable cells is significantly increased and γ = (97,9 ± 5,7)%. Thus, sodium azide actually blocks the damage of the cells sensitized with bilirubin.

It was determined, that changing the power density of light in 3-4 times with appropriate compensation of dose due to the irradiation time has practically no influence on the photobiological effect (Fig. 2). Therefore, the contribution of photothermal processes in decrease of cellular viability sensitized with bilirubin in the selected

power density range (not more than 20 mW/cm^2) is not significant. In the absence of bilirubin, as well as in case of incubation of the cells with bilirubin (C_{BR} = 40 μM) without light exposure, the effect is extremely low.

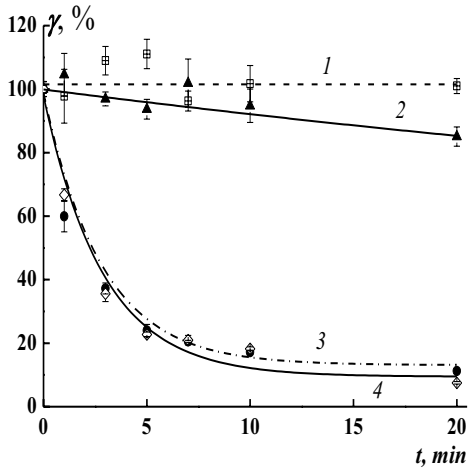

Fig. 1. The dependence of percentage of viable cells sensitized with bilirubin on the irradiation time by LED sources with emission band maximum at λ_{em} = 465 nm (curve 2,3) and λ_{em} = 520 nm (curve 1, 4): 1,2 – without bilirubin; 3,4 – cells, sensitized with bilirubin (C_b = 40μM), power density P = 20 mW/cm^2

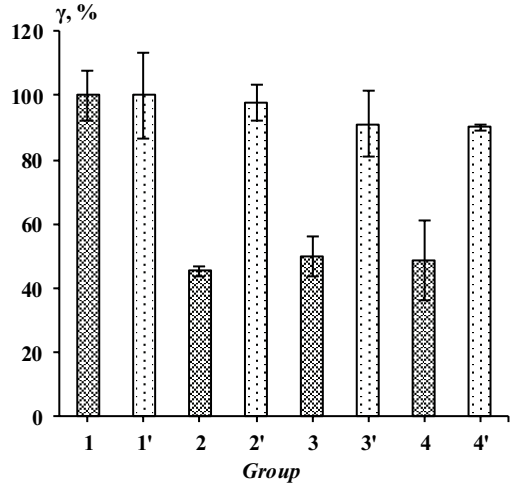

Fig. 2. The percentage of surviving cells upon irradiation with LED sources with emission band maximum at λ_{em} = 465 nm without sodium azide (1,2,3,4) and with addition of sodium azide (1 ', 2', 3 ', 4') under the conditions of constancy of light energy exposure dose: 1,1 '- no irradiation; 2,2' t_{irr} = 5 min, P = 20mW/cm^2; 3,3 '- t_{irr} = 10 min, P = 10 mW/cm^2; 4,4 '- t_{irr} = 20 min, P = 5 mW/cm^2.

It has been for the first time shown that the inclusion of bilirubin in the cells, where it is predominantly localized in the mitochondria, is accompanied by increased photochemical stability compared to pigment molecules bound to albumin (Fig. 3). The findings suggest that bilirubin has a high photochemical stability in the lipid environment. Among the possible causes of increased bilirubin photostability at its intracellular localization are considered: a) the formation, along with the monomers, of tetrapyrrole dimeric forms; b) the presence of closely located antioxidants; c) slow diffusion of oxygen involved in the reaction self-sensitized discoloration of the pigment; g) quenching of the triplet state of bilirubin by other biomolecules.

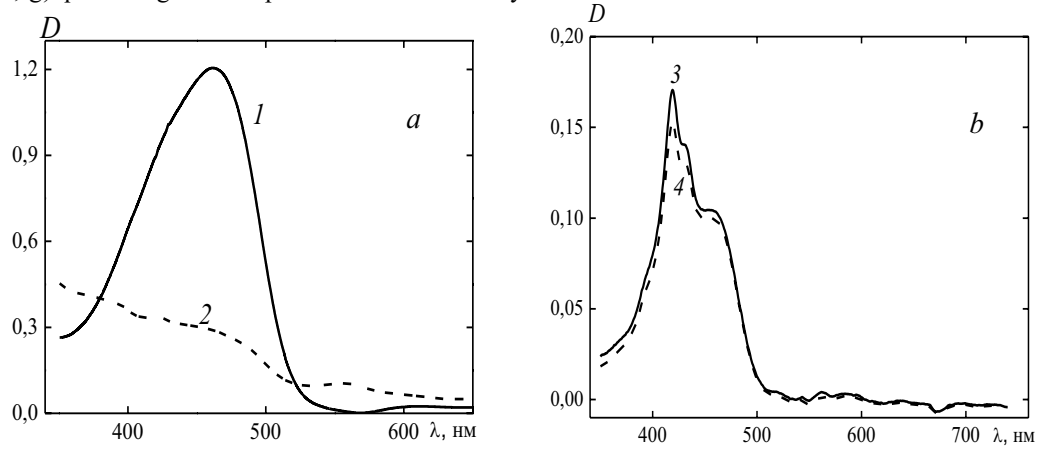

Fig. 3. Absorption spectra of bilirubin in medium (a) and a DMSO solution (b) after extraction from the cells without prior exposure (curves 1 and 3) and after exposure to radiation λ = 465 nm, power density P = 20 mW / cm2 for t = 5 min (curves 2 and 4).

4. Conclusions.

It is shown that bilirubin located within cells is characterized by high photochemical stability and can act as a photosensitizer, causing photodamaging lethal effect on animal cells in culture. The addition of sodium azide to the system being irradiated, the quencher of singlet oxygen, reduces the biological effect that points to the decisive role of singlet oxygen in the mechanism of photodynamic action. The exposure to radiation of LED sources with an emission band maximum at about 465 and 520 nm causes identical damaging effects on animal cells in culture that may be due to significant change in the spectral characteristics of bilirubin upon entering into the cells. Bilirubin localized in the animal cells can perform the function of the selective filter, shielding radiation which is potentially capable of causing the photoisomerization of bilirubin bound to albumin molecules.

Time-Resolved Laser-Induced Fluorescence Spectroscopy for Identification of Pituitary Adenoma

A. N. Sobchuk[1*], N. A. Nemkovich[1], Yu.V Kruchenok[1], Yu. G. Shanko[2], A. I. Chuhonsky[2]
[1]*B.I.Stepanov Institute of Physics, National Academy of Sciences of Belarus,*
68 Nezavisimosti Avenue, Minsk, 220072,Belarus
[2]*Republican Research and Clinical Center of Neurology and Neurosurgery, Ministry of Health of the Republic of Belarus,*
24 F. Skoriny Street, 220114, Minsk, Belarus
**E-mail: sobchuk@ifanbel.bas-net.by*

Abstract: Rapid and high-sensitivity identification of pituitary adenoma can be carried out by measuring the autofluorescence decays. It is found that a significant difference is observed in the autofluorescence mean lifetime of tumorous and healthy tissues in the 380–600-nm spectral range.

It is well known that human tissues contain biomolecules that fluoresce well in the UV, visible, and near-IR regions because they incorporate endogenous chromophores. The latter include tryptophan, tyrosine, dinucleotides, collagen, flavins, lipofuscins, porphyrins, etc. The characteristics of the intrinsic fluorescence of the chromophores depend on their distribution in the tissues, the concentration of ions, the properties of the microenvironment, and other factors. The appearance of a pathological process affects the physicochemical microcharacteristics of the tissues and therefore changes the autofluorescence parameters of the tumors.

Steady-state and time-resolved measurement methods are used for the fluorescence analysis of tissues. Steady-state measurements, as a rule, involve recording the luminescence intensity at a definite wavelength, the emission and excitation spectra, and the emission anisotropy. The main drawbacks of steady-state measurements are that the fluorescence intensity depends on the optical excitation and emission layout, the surface inhomogeneity of the tissues, different concentrations of the chromophores, and the presence of endogenous absorbers in the tissues, especially hemoglobin and oxyhemoglobin. Time-resolved diagnostic methods are largely free of the drawbacks inherent to steady-state spectroscopy, because endogenous absorbers only attenuate the intensity of the intrinsic fluorescence of the tissues; i.e., they act as an internal filter but do not change the character and duration of the luminescence decay, as well as weakly affecting the kinetics of the autofluorescence spectra. It should be pointed out that it is convenient to analyze and to statistically process the values of the preexponential factors and fluorescence lifetimes of the separate components of the luminescence decay when it is resolved into exponentials.

The measurements were made on samples of healthy and tumorous tissues of the pituitary taken after an operation carried out at the Republican Research and Clinical Center of Neurology and Neurosurgery, Ministry of Health of the Republic of Belarus. The tissue samples were fixed in 0.9% physiological solution and were investigated a few hours after being taken. The presence of a tumor was estimated macroscopically immediately after taking the sample and microscopically from the results of a histological study. Nineteen tissue samples were investigated, from which there were eight samples of pituitary adenoma and eleven samples of healthy pituitary tissue.

The system for exciting and registration the autofluorescence decays includes HORIBA PicoBrite pulsed semiconductor LED (emission wavelengths 342 nm, pulse width at half–height 700 ps, pulse-repetition rate 10 MHz), a SOLAR ML-44 monochromator (inverse linear dispersion 18.7 nm/mm), a Hamamatsu H5773 photomultiplier (recording range 185–820 nm, time resolution 180 ps) and a Becker& Hickl SPC-130 time-correlated photon-counting module. The mean emission power of the semiconductor LED during experiments at a pulse repetition rate of 10 MHz was 1 μW, while the time to record each autofluorescence decay is 3 minutes. The fluorescence is excited and recorded via a Avantes optical fiber probe FCR-7UV400-2-ME, which consists of one central optical-fiber 400 μm in diameter for transporting the excitation light from the LED to the tissue and six optical fibers of the same diameter located around the central optical fiber for recording the emission signal. The probe was 1–2 mm away from the tissue surface during the measurements, and the light spot was 2 mm in diameter.

Our studies showed that the autofluorescence kinetics of the tissues in the spectral range 380–600 nm does not have an exponential character. It follows from representing the kinetics as a superposition of exponentials that the contribution to the autofluorescence includes two subnanosecond components with lifetimes, respectively, of 0.39–0.53 and 1.9–2.5 ns and a slower nanosecond component with a fluorescence lifetime of 6.9–8.2 ns. The mean lifetimes of the short-lived components are less in tumorous tissue than in healthy tissue, and the mean lifetimes of the slower nanosecond component is about the same in the various objects of investigation.

Figure 1 illustrates how the autofluorescence mean lifetime of the tissues depends on the emission wavelength. It can be seen that the autofluorescence mean lifetime of healthy and tumorous tissues initially increases with increasing wavelength to about 500 nm and then begins to decrease. The difference between the autofluorescence mean lifetime of tumorous and healthy tissues monotonically increases with increasing wavelength and, when recorded at 600 nm, reaches the highest value of 1.6 ns.

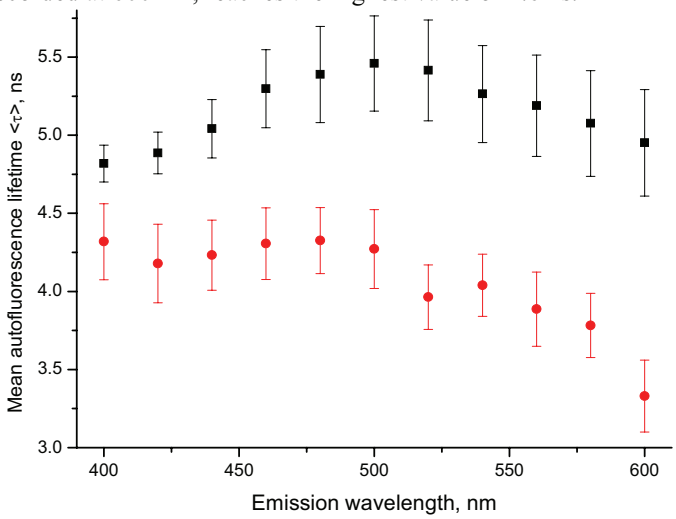

Fig. 1. Autofluorescence mean lifetime of healthy pituitary tissue (●) and tissue of a pituitary adenoma (■).

Discriminant analysis is used to analyze the data obtained here. Autofluorescence mean lifetime at emission wavelengths 380, 400, 420, 440, 460, 480, 500, 520, 540, 560, 580 and 600 nm were selected as discriminant variables. The calculated values of the discriminant functions are shown in Fig. 2. The sensitivity and specificity of the identification of pituitary adenoma, determined by means of discriminant analysis, are 100%.

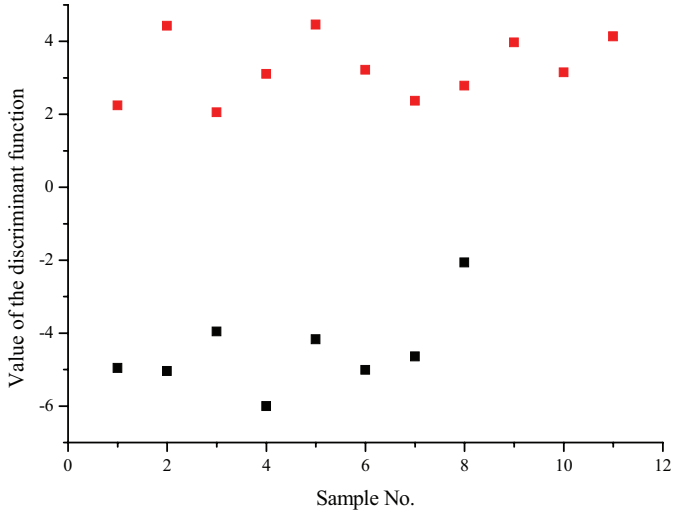

Fig. 2. Values of the discriminant function of healthy (■) and tumorous (■) tissues.

Rapid and high-sensitivity identification of pituitary adenoma can be carried out by measuring the autofluorescence decays at emission wavelengths 380-600 nm. The method can be improved further by using excitation wavelengths of about 260 nm, which makes it possible to additionally record the UV autofluorescence of tyrosine and tryptophan.

The Investigation of Tubulins Intracellular Distribution in Healthy and Cancerous Colon Tissue

S. B. Bushuk[1], A. S. Portyanko[2], Ju. A. Kalvinkovskaya[1], B. A. Bushuk[1]

[1]*B. I. Stepanov Institute of Physics, National Academy of Science of Belarus, The Republic of Belarus, Minsk, Nezalezhnasty Ave. 68, e-mail:bushuk@dragon.bas-net.by*

[2]*Belarusian State Medical University, The Republic of Belarus, Minsk, Dzerzhynsky Ave. 83, e-mail:aportyanko@yahoo.com*

Abstract: The distribution of βI-tubulins, acetyl-tubulins and tyrosin-tubulins in microtubules of healthy and cancerous cells has been investigated by FRET-FLIM method. It has been shown that in healthy tissue unlike the cancerous one the microtubules structure contains colocalized tubulins.

Laser scanning microscopy, fluorescence microspectroscopy and fluorescence lifetime imaging (FLIM) methods have been applied for the investigation of colon cancer tissue slices containing mitotic cells labeled by antibodies specified to α- and β-tubulins.

The main attention was paid to the investigation of the distribution of βI-tubulins and acetyl-tubulins in microtubules around DNA of dividing cells using FRET (Forster Resonance Energy Transfer) method. To solve this problem the following activities have been carried out.

At the first stage of experiments thin slices of colon cancer tissues (~10μm thickness) treated by specified to βI-tubulin antibodies containing Alexa Fluor 488 labels (donor molecules), acetyl-tubulin antibodies containing Alexa Fluor 546 labels (acceptor molecules) and DAPI stained DNA have been investigated by fluorescence microspectroscopy and laser scanning confocal microscopy methods. CW He-Ne laser operated at 543 nm was used to measure acetyl-tubulin containing microtubules distribution. Argon-ion laser operated at 488 nm was used to measure βI-tubulin containing microtubules distribution. Analysis of 3D confocal images of mitotic cancer cells have shown that both tubulins are colocalized in microtubules. At the second stage of experiments FLIM-FRET method was used to register tubulins distribution at very short (<10 nm) distance. Femtosecond Ti:Sapphire laser yielding 100 fs pulses operated at 930 nm wavelength in order to minimize tissue photodamage and to provide the excitation only for Alexa Fluor 488 donor labels by two-photon mechanism. Fluorescence lifetime images of the area including several mitotic cells have been registered by time-correlated single photon counting method using Becker&Hickl SPC-830 board. First, the mitotic cells were treated only by specified to βI-tubulin antibodies containing Alexa Fluor 488 labels (donor molecules). It has been established that Alexa Fluor 488 fluorescence decay is well described by single-exponential law with fluorescence lifetimes of 2.5 ns. Then the slices were treated by two types of antibodies simultaneously with optimal concentration. It was established that Alexa Fluor 488 fluorescence lifetime does not alter in vicinity of both mitotic poles but in regions outlying from the poles the shorter fluorescence lifetime is registered. Reduction of Alexa Fluor 488 fluorescence lifetime (energy donor) in these regions can be accounted for by nonradiative excitation energy transfer to acceptor molecules (Alexa Fluor 546). Thus it has been established using FLIM-FRET method that the microtubule structure around DNA of dividing cells in regions outlying from the poles contains βI-tubulins and acetyl-tubulins in very close proximity.

In the second part of the investigation laser scanning microscopy, fluorescent microspectroscopy and fluorescence lifetime imaging methods (FLIM) were applied to the investigation of healthy and cancerous colon tissue slices containing interphasic and mitotic cells labeled by antibodies specified to various tubulins (βI tubulins, acetyl-tubulins and tyrosin-tubulins).

The main attention was paid to the investigation of the distribution of βI-tubulins, acetyl-tubulins and tyrosin-tubulins in microtubules of healthy and cancerous cells using FRET-FLIM method.

Complex investigation of tubulins distribution has been performed in several stages. At first stage of experiments thin slices (~10μm thickness) of healthy and cancerous colon tissue treated by specified to tyrosin-tubulin antibodies containing Alexa Fluor 488 labels (donor molecules), βI-tubulin antibodies containing Alexa Fluor 555 labels (acceptor molecules) and DAPI stained DNA were investigated. It has been established that in healthy tissue slices containing only specified to tyrosin-tubulin antibodies measured Alexa Fluor 488 fluorescence lifetime is about 2.35 ns in interphasic cells and somewhat higher in mitotic cells (2.51 ns). In healthy tissue slices treated by two types of antibodies simultaneously the following values of Alexa Fluor 488 fluorescence lifetime were registered – 2.12 ns in interphasic cells and 2.27 ns in mitotic cells. In cancerous tissue slice containing only specified to tyrosin-tubulin antibodies measured Alexa Fluor 488 fluorescence lifetime was 2.28 ns in interphasic cells and 2.35 ns in mitotic cells. In cancerous tissue slices treated by two

types of antibodies simultaneously with optimal concentration the following values of Alexa Fluor 488 fluorescence lifetime were registered – 2.00 ns in interphasic cells and 2.22 ns in mitotic cells.

Essential reduction of Alexa Fluor 488 fluorescence lifetime as energy donor both in healthy and cancerous cells is determined by nonradiative excitation energy transfer to acceptor molecules (Alexa Fluor 555). Thus it has been established using FLIM-FRET method that the microtubules structure contains βI-tubulins and tyrosin-tubulins in very close proximity.

At the second stage of the experiment thin slices of healthy and cancerous colon tissues (~10μm) treated by specified to βI-tubulin antibodies containing Alexa Fluor 488 labels (donor molecules), acetyl-tubulin antibodies containing Alexa Fluor 546 labels (acceptor molecules) and DAPI stained DNA have been investigated. It has been established that in healthy tissue slices containing only βI-tubulin specified antibodies Alexa Fluor 488 fluorescence lifetime is measured to be 2.38 ns in interphasic cells and somewhat higher in mitotic cells (2.48 ns). In the slices treated by two types of antibodies simultaneously with optimal concentration the following values of Alexa Fluor 488 fluorescence lifetime were registered: 2.28 ns in interphasic cells and 2.35 ns in mitotic cells. In cancerous tissue slice containing only specified to βI-tubulin antibodies Alexa Fluor 488 fluorescence lifetime was measured to be 2.47 ns in interphasic cells and in 2.49 ns mitotic cells. In the slice treated by two types of antibodies simultaneously with optimal concentration the following values of Alexa Fluor 488 fluorescence lifetime were registered: 2.40 ns in interphasic cells and 2.42 ns in mitotic cells. Thus it has been established using FLIM-FRET method that in healthy tissue unlike the cancerous one the microtubules structure contains βI-tubulins and acetyl-tubulins in close proximity.

Depth independent Cerenkov radiation mediated therapy with 5-ALA photosensitizer

Yu. S. Maklygina [1], A.V. Ryabova [1, 2], V. B. Loschenov [1, 2] , E. N. Sokolov [3], D. I. Nevzorov [3], E. Yu. Grigoreva [3], M. B. Dolgushin [3], B. I. Dolgushin [3]

[1]A.M. Prokhorov General Physics Institute RAS, Russia, Moscow

[2]National Research Nuclear University MEPhI, Russia, Moscow

[3]Blokhin Russian Cancer Research Center, Russia, Moscow

E-mail address:us.samsonova@physics.msu.ru

Abstract

The combination of light and photosensitizers for phototherapy is so promising. But the shallow penetration of the laser radiation into tissue limits the method of photodynamic therapy. The main goal of the research is overcoming these limitations by using Cerenkov radiation from radionuclides to activate the photosensitizer. Histological analysis of tumor sections showed the selective destruction of cancerous cells (glioma C6). These results offer a way to achieve depth independent Cerenkov radiation mediated therapy using different types of photosensitizers.

Keywords

Positron emission tomography, Cerenkov radiation, depth independent photodynamic therapy, photosensitizers, the inside cancer therapy.

Introduction

Light-based methods suffer from the rapid attenuation of the light in tissue. That is why current assumption is that the Cerenkov radiation (CR) could serve as a depth independent light source for photoinduced inside cancer therapy [1]. Radionuclides are an ideal source for Cerenkov radiation because of their positron emission, which travel faster than the speed of light in the medium emitting from in the main ultraviolet light to visible spectrum (250-600 nm). Radionuclides such as Fludeoxyglucose (^{18}F-FDG) are widely used in positron emission tomography (PET) that allows observing metabolic processes in the body especially in clinical oncology. FDG is widely used to detect diverse tumors with exceptionally high sensitivity because it accumulates in highly proliferating tumor cells undergoing an enhanced glucose metabolism. 5-Aminolevulinic acid (5-ALA) has become an integral part in the treatment of malignant glioma that is why in this research this photosensitizer (PS) used for CR-induced therapy.

Materials and methods

The in vivo studies were performed on experimental animals with induced malignant glioma C6 in the groin. During the study intravenous injections of 5-ALA and tracer amounts of FDG were made successively at intervals of 2 hours respectively. Observation of metabolic processes and the FDG concentrations in tissues was imaging by the PET. 5-ALA acts as PS whereas the FDG induce the CR that in combination resulted in CR-induced therapy. The evaluation of photodynamic effect of CR-induced therapy was made using confocal laser scanning microscopy.

Results

Histological analysis of tumor sections were visualized using confocal laser scanning microscopy posthumously. Analysis of tumor sections of 5-ALA-treated mice revealed efficiently proliferating of glioma C6 cells formed agglomerates (fig.1a). Analysis of tumor sections of FDG+5-ALA-treated mice revealed selective destruction of proliferating cells in the tumor region as well as pronounced necrotic zones that occupied

approximately 20-30% of the tumor mass (fig.1b). Large areas of FDG+5-ALA-treated tumors exhibited a loss of cellular architecture and significantly high distribution of apoptotic foci (fig.1b). These findings suggest that the damage to cells probably was mediated by the CR-induced free radicals. Thus a comparison of the FDG-untreated (fig.1a) and FDG-treated (fig.1b) tumor sections using confocal microscopy shows predominantly apoptotic cells in the latter that confirms the selectivity of the method.

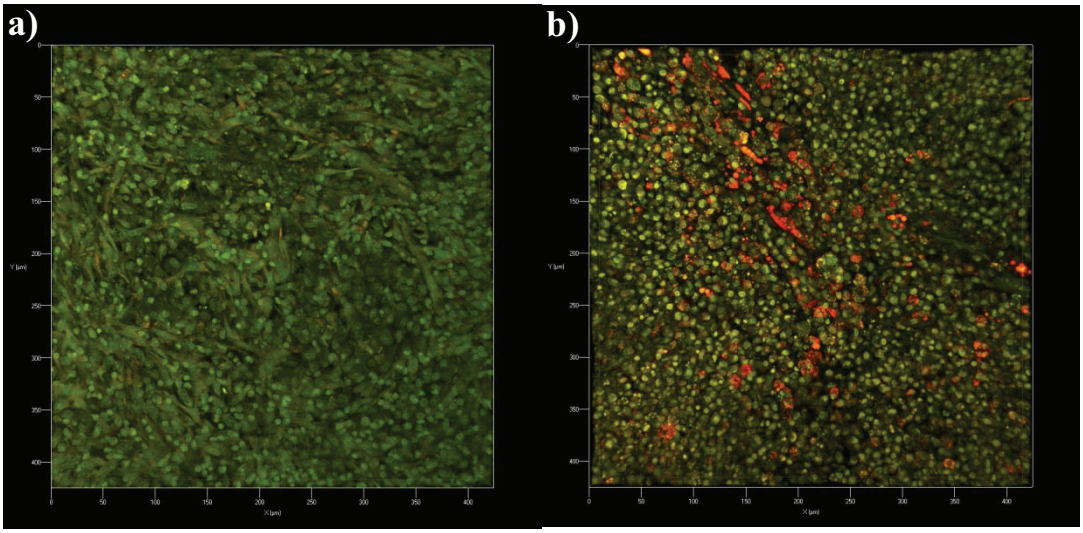

Fig.1. Histological analysis of tumor sections of a) 5-ALA-treated and FDG-untreated
b) FDG+5-ALA-treated by means of confocal microscopy

Conclusion

In this study, we have demonstrated a new approach using CR from PET radionuclides to activate 5-ALA for phototherapy. The effect of the complimentary radical-generation mechanisms enabled an effective CR-induced therapy using tumor-targeted PS. Although FDG equally accumulates in non-tumor-associated pathologies, such as inflammation, CR- induced therapy is only effective when both the CR source and the PS are in the same cell, which minimizes off-target toxicity. The established biocompatibility of all the components used in the study means our work creates a path to human translation. Thus the approach opens up the possibility of treating a variety of lesions by the depth-inside therapy.

References

[1] Breaking the depth dependency of phototherapy with Cerenkov radiation and low-radiance-responsivenanophotosensitizers. Kotagiri N, Sudlow GP, Akers WJ, Achilefu S. Nature Nanotechnology 2015 Apr; 10(4):370-9, doi: 10.1038/nnano.2015.17.

Spectroscopic diagnostics of laser-induced change of structure of ascorbic acid solution

Danyaeva Y.S., Kutsenko S.A.
Volgograd State University
University Ave., 100, Volgograd, 400062, Russia
lf@volsu.ru

Abstract. The results of research of effect of powerful laser radiation on the structure of the electronic spectra of ascorbic acid are presented. Changes in the molecule's structures are defined by comparing the results of experiments and quantum chemical calculations.

Spectroscopy in conjunction with a numerical modelling successfully used for qualitative and quantitative analysis of chemical and biological objects. We investigated the effect of powerful laser radiation on the structure of the electronic spectra of ascorbic acid in this paper.

The measurements were performed on an automated multi-channel spectral complex on the basis of monochromator MDR-23 in the ultraviolet range. Solutions with concentrations from 0.00025% to 0.4% have been investigated. Change in the fundamental absorption band of ascorbic acid in 260 nm was recorded. The solutions were exposed to continuous light semiconductor laser with a wavelength of 400 - 650 nm, pulsed - periodic YAG: Nd^{3+} laser in the Q-switched mode with wavelength of 1.06 microns, a pulse duration of 20 ns and a nitrogen laser with wavelength 337 nm, a pulse duration of 10 ns.

Absorption coefficient solutions decreases monotonically. As a result of irradiation of solutions by powerful pulsed radiation with increasing laser power, the band shifted into the visible region, its width increases. At the same time there is a band at 450 nm, which was absent in the spectra of solutions before irradiation. Similar changes take place at higher temperatures solutions and associated with the conversion of ascorbic acid to dehydroascorbic.

The results of our experimental data are confirmed by our numerical quantum calculations . They showed that the conversion of ascorbic acid to dehydroascorbic changes the electron spectrum. Not observed bands in the 192 - 175nm corresponding to $\pi \rightarrow \pi^*$ transitions between atoms linked by a double bond C = C. Changed the band corresponding to $\pi \rightarrow \pi^*$ transitions in atoms of the C = O double bond: in comparison with the spectrum of ascorbic acid increased their intensity, as new formed C = O bond in the molecule dehydroascorbic acid. The weak dehydroascorbic acid line in the ultraviolet region with a wavelength of 283 nm appeared in the spectrum. It appeared in results from the $n \rightarrow \pi^*$ transition in atoms are not linked by a double bond. It is the band at 260 nm is shifted into the visible region and is reduced in intensity, which could be observed in the spectrum of the ascorbic acid solution. In addition, there is a band at 500 nm in the electronic spectrum of dehydroascorbic acid.

Substances used to stabilize ascorbic acid solutions do molecule more stable to increase of temperature and light exposure.

Thus, the absorbed light energy causes a redistribution of the valence electrons and has a significant impact on the structure and stability of the molecule. Also thanks to the enol group ascorbic acid has strong reducing properties, so it is easily oxidized in solution under the influence of oxygen, turning into dehydroascorbic acid. Thermal energy and laser light are used as catalysts for this transformation.

Laser Systems and Fiber Optic Tools for Photodynamic Therapy

Kirill G. Linkov, Vladimir V. Volkov

Prokhorov General Physics Institute, Russian Academy of Sciences, 38 Vavilov Str., Moscow, 119991, Russia
Author e-mail address: rkir@mail.ru

Abstract: New therapeutic laser systems and fiber-optic light delivery tools were designed for further development of fluorescence diagnosis and photodynamic therapy methods. Features and advantages of the developed laser equipment and possible applications of the fiber-optic instruments are considered.

1. Introduction

Fluorescence diagnosis and photodynamic therapy are promising new directions in a wide spectrum of medical disciplines such as urology, dermatology, gynecology, gastroenterology, ophthalmology, and neurosurgery [1-4]. Laser equipment for fluorescence diagnosis and photodynamic therapy developed in Laser Biospectroscopy Laboratory in A.M.Prokhorov General Physics Institute, Russian academy of Sciences since the 1990s. Designed equipment have proved itself. Many devices are in the clinics from 1996-1998 and still working flawlessly. In total, clinics and academic institutions of Russia and some foreign countries obtained more than 300 units developed by our team. About a quarter of them are laser therapeutic devices.

An important part of equipment are fiber-optic systems. They are used for diagnosis. An optical probe combined with a laser electronic spectrum analyzer LESA-01-BIOSPEC is widely used as a common device for fluorescence diagnosis and for absorption spectroscopy [5]. Additionally, fiber-optic tools are required for therapy. At present, polymeric and quartz optical fibers are the most acceptable fibers in medicine for light delivery systems. Ordinary light scattering fiber tips, such as frontal or cylindrical ones have undoubtedly found a wide spread medical application for PDT in routine clinical practice. To date, there are a number of light scattering fiber tips using different manufacturing methods. They are intended for clinical use, for example, for illumination of skin diseases, subcutaneous tumors of hollow organs and for the treatment of brain tumors or prostate.

2. Laser therapeutic systems

We have developed advanced laser therapeutic systems. Development was carried out with the maximum addition of modern electronic components, taking into account the current requirements for optimizing costs and import substitution. List of modifications of the system is repeatedly expanded, including versions with different emission wavelengths and output optical power. It is possible to manufacture laser devices for use with photosensitizers registered in Russian Federation and promising photosensitizers being developed or tested currently. Regulatory requirements for medical devices, published at the time of development, were taken into account. The focus, as ever, has been on improving the reliability of the equipment and ensure its long-term trouble-free operation.

New medical laser therapeutic systems was registered, have passed all necessary tests and are delivered in the clinic in 2016 under the model designation "Laser System LPhT-02-BIOSPEC".

3. Fiber-optic tools for therapy

Regarding the therapeutic light delivery systems, we have designed different applicator types, which look like a thin capillary coupled with a quartz fiber. An experimental ex-vivo and in-vivo studies revealed an ability of such applicators to provide different types of therapy, namely: PDT, hyperthermia, interstitial laser coagulation and laser-induced interstitial thermotherapy. All these kinds of laser interstitial minimal invasive therapy permit selective photothermal tumor destruction with a protection of the surrounding organ structure. The expansion of the tissue-destroying effect is highly dependent on the laser parameters and applicator type involved.

The method of photo or thermal impact by laser radiation on the lesions needs a subsequent preclinical trial both as alternative method of a tumor therapy for primary or recurrent cases, and combined with surgery.

4. References

[1] Belyaeva L.A., Adamyan L.V., Stepanyan A.A., Linkov K.G., Loshchenov V.B., LASER FLUORESCENCE SPECTROSCOPY WITH 5-AMINOLEVULINIC ACID IN OPERATIVE GYNECOLOGY, Laser Physics. 2004. V. 14. No 9. P. 1207-1213.

[2] Zavodnov V.Y., Kuzin M.I., Kharnas S.S., Linkov Kirill G., Loschenov Victor B., Stratonnikov A.A., Posypanova A.M., PALLIATIVE TREATMENT OF PATIENTS WITH MALIGNANT STRUCTURES OF ESOPHAGUS, Proceedings of SPIE - The International Society for Optical Engineering Photochemotherapy: Photodynamic Therapy and Other Modalities. sponsors: SPIE - Int Soc for Opt Engineering, Bellingham, WA USA, EOS-The European Optical Society, ELA-The European Laser Association; editors: Ehrenberg Benjamin, Jori Giulio, Moan Johan, Bar-Ilan University, Ramat-Gan, Israel. Barcelona, Spain, 1996. C. 482-483.
[3] Model S.S., Savelieva T.A., Linkov K.G., SYSTEM FOR DETERMINING THE CONCENTRATION AND VISUALIZATION OF THE SPATIAL DISTRIBUTION OF PHOTOSENSITIZERS BASED ON TETRAPYRROLE COMPOUNDS IN THE TISSUES OF THE HUMAN OCULAR FUNDUS, Progress in Biomedical Optics and Imaging Proceedings of SPIE. Russian Foundation for Basic Research, Russian Academy of Sciences, U.S. Civ. Res. Dev. Found. Indep., States Former Soviet Union (CRDF), SPIE Student Chapter. 2013. P. 86990E.
[4] Savelieva T.A., Loshchenov V.B., Volkov V.V., Linkov K.G., Goryainov S.A., Potapov A.A., THE METHOD OF INTRAOPERATIVE ANALYSIS OF STRUCTURAL AND METABOLIC CHANGES IN THE AREA OF TUMOR RESECTION, Proceedings of SPIE - The International Society for Optical Engineering Cep. "Biophotonics: Photonic Solutions for Better Health Care IV" 2014. P. 91290V.
[5] Stratonnikov A.A., Edinac N.E., Klimov D.V., Linkov K.G., Loschenov V.B., Luk'yanets E.A., Meerovich G.A., Vakoulovskaia E.G., CONTROL OF PHOTOSENSITIZER IN TISSUE DURING PHOTODYNAMIC THERAPY BY MEANS OF ABSORPTION SPECTROSCOPY, Progress in Biomedical Optics and Imaging. 1996. V. 2924. P. 49-60.

Singlet Oxygen Generation by Zeolite-Porphyrin Complexes

M.V. Parkhats[1], S.V. Lepeshkevich[1], A.S. Stasheuski[1], B.M. Dzhagarov[1]
H.H. Sargsyan[2], R.K. Ghazaryan[3], A.G. Gyulkhandanyan[2], G.V. Gyulkhandanyan[2]

[1]Institute of Physics NAS of Belarus, 68 Nezavisimosti Ave., Minsk, 220072, Belarus
e-mail: m.parkhots@ifanbel.bas-net.by
[2]Institute of Biochemistry, NAS of Armenia, 5/1, P. Sevak str.,Yerevan, 0014, Armenia
e-mail: gvg536898@yahoo.com
[3]Yerevan State Medical University, 2 , Koryun str., Yerevan, 0025, Armenia

Abstract: The investigated zeolite-porphyrin complexes generate singlet oxygen with low quantum yields and can not be used as photosensitizes for photodynamic therapy.

Many strategies are developed to improve efficiency of photodynamic therapy (PDT), a form of phototherapy involving light and photosensitizers (PS) to treat tumors. PS incorporation into different types of nanoparticles is one of such strategies allowing to increase tumor targeting and to minimize side effects of photosensitizers. However, PS incorporation can reduce photodynamic activity of PS by changing its photophysical properties and singlet oxygen generation.

In the present work, we try to use nanozeolites as carriers for PS. Zeolites are crystalline aluminosilicates consisting of enclosed regular cavities and channels of well-defined size and shape, that are widely used in ion exchange technology, catalysis, filtering and gas adsorption. It is also known that natural zeolite clinoptilolite possesses antitumor activity based on a stimulation of immune system [1].

Nanoparticles of natural zeolite clinoptilolite (Noyemberyan region, Republic of Armenia) of nanometric sizes (80-150 nm) and cationic porphyrins such as Zn-meso-tetra(4-N-hydroxyethyl-pyridyl) porphyrin (ZnTOEt4PyP) and meso-tetra(4-N-hydroxyethyl-pyridyl) porphyrin (TOEt4PyP) (Fig. 1) were used as carrier and photosensitizers, respectively. Zeolite-porphyrin complexes were obtained by adding of small amount of porphyrin to nanozeolite solution. Centrifugation was used to remove unbound porphyrin molecules. Absorption spectra were recorded on a spectrophotometer Cary-500 Scan. Kinetics of the triplet-triplet absorption were measured on a nanosecond laser spectrometer (excitation wavelength 532 nm, Nd:YAG laser (LS-2132U, LOTIS TII, Belarus), pulse width 8 ns, repetition rate 13 Hz). Time resolved singlet oxygen luminescence in the near-infrared region was recorded on a nanosecond laser NIR spectrometer (excitation wavelength 532 nm, Nd:YAG laser (DTL-314QT, Laser-export Co. Ltd.), pulse width 10 ns, the pulse energy 1 μJ, repetition rate 2.5 kHz). To determine quantum yields of photosensitized singlet oxygen generation (γ_Δ) TOEt4PyP in an aqueous solution (γ_Δ = 0.77) was used as a standard [2]. All experiments were carried out in distilled water at room temperature.

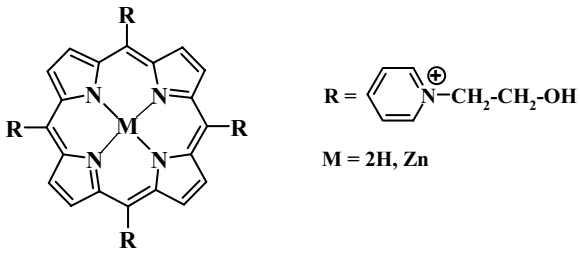

Fig. 1. Structural formulas of ZnTOEt4PyP and TOEt4PyP.

The aim of the work is to investigate photosensitized singlet oxygen generation by nanozeolite-porphyrin complexes and their photophysical properties.

It was shown that complexation of porphyrins ZnTOEt4PyP and TOEt4PyP leads to transformations and red shifts of the absorption and fluorescence spectra. Significant broadening and changes in the relative intensity of the Soret band are observed. The interaction of both porphyrins with nanozeolite causes also the fluorescence quenching. Kinetic absorption studies show that the kinetics of triplet-triplet absorption of nanozeolite-porphyrin complexes have two-exponential character. The obtained photophysical properties of nanozeolite-porphyrin complexes indicate the presence of an inhomogenity in porphyrin interaction with nanozeolite. Moreover, conformational changes and aggregation effects upon adsorption of cationic porphyrins on anionic $[AlSi]O_4^-$ framework of nanozeolite can not be excluded.

The kinetics of singlet oxygen luminescence photosensitized by porphyrins, nanozeolite-porphyrin complexes as well as signal of nanozeolite in an aqueous solution were investigated. It was obtained that the kinetic of singlet oxygen luminescence photosensitized by nanozeolite-porphyrin complexes have no the rise component that always observed for PS in solutions (Fig. 2). The kinetics of singlet oxygen luminescence photosensitized by nanozeolite-porphyrin complexes are well fitted by a biexponential decay function with $\tau_1 \sim$ 300 ns (fast component) for both nanozeolite-porphyrin complexes and $\tau_2 = 6.6 \pm 0.5$ mks and 9.8 ± 0.8 mks (low component) for nanozeolite-TOEt4PyP and nanozeolite-ZnTOEt4PyP, respectively (Fig. 2). Based on the control measurements of nanozeolite without porphyrins, it was concluded that the fast component τ_1 characterizes luminescence of nanozeolite. On the other hand, based on the spectral properties of the detected signal, the slow component τ_2 can be unambiguously attributed to the luminescence of singlet oxygen.

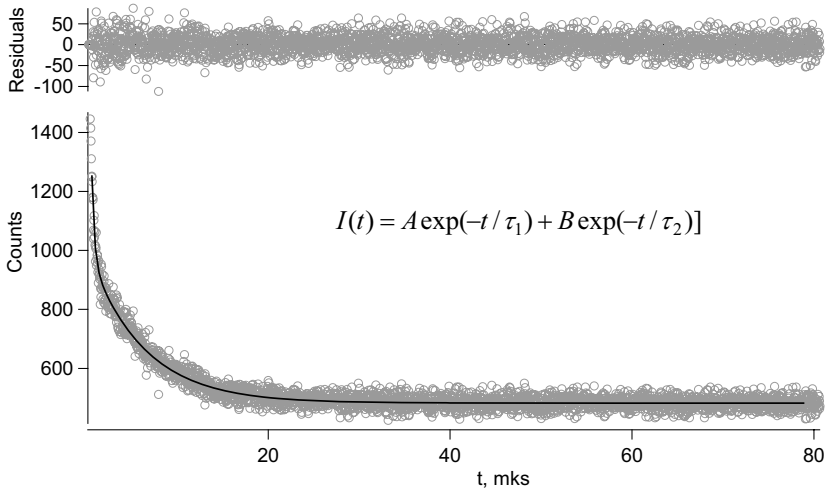

Fig. 2. Kinetics of singlet oxygen luminescence photosensitized by nanozeolite-TOEt4PyP complex in aqueous solution. Concentrations of TOEt4PyP and nanozeolite, 10 μM and 0.6 mg/ml, respectively. Excitation wavelength, $\lambda_{exc} = 532$ nm, detection wavelength, $\lambda_{det} = 1270$ nm.

Quantum yields of photosensitized singlet oxygen generation by nanozeolite-porphyrin complexes were found to not exceed 0.04 and 0.01 for nanozeolite-TOEt4PyP and nanozeolite-ZnTOEt4PyP, respectively. Such low quantum yields of singlet oxygen generation can be explained by (i) the porphyrin aggregation upon interaction with nanozeolite and by (ii) the quenching of singlet oxygen by aluminia anions from $[AlSi]O_4^-$ framework of nanozeolites [3]. It should be noted that the refractive index of zeolite (n = 1.47-1.48) is larger than that of water (n=1.33). Taking into account the dependence of radiative rate constant of singlet oxygen deactivation (k_r) on the refractive index (n) [4], it is expected that k_r in zeolite is 3 times greater than the one in water. Therefore, the above mention values of the quantum yields of singlet oxygen generation in nanozeolite can be considered as the upper limits of γ_Δ.

Thus, it is demonstrated that the complexes of nanozeolite-TOEt4PyP and nanozeolite-ZnTOEt4PyP generate singlet oxygen with very low quantum yields and can not be used as photosensitizes for photodynamic therapy.

This work was supported by the Foundation of Basic Research of the Republic of Belarus (Grants No. Ph14Arm-015 and Ph15SO-036).

[1] K. Pavelic, M. Hadžija, L. Bedrica et. al., **"**Natural zeolite clinoptilolite: new adjuvant in anticancer therapy", J. Mol. Med. **78**, 708 – 720 (2001).

[2] A. S. Stasheuski, V. A. Galievsky, V. N. Knyukshto et al. "Water-soluble pyridyl porphyrins with amphiphilic *n*-substituents: fluorescent properties and photosensitized formation of singlet oxygen", J. App. Spectr. **80**, 813 – 823 (2014).

[3] S. Jockusch, J. Sivaguru, N. J. Turro, V. Ramamurthy, "Direct measurement of the singlet oxygen lifetime in zeolites by near-IR phosphorescence", Photochem. Photobiol. Sci. **4**, 403 – 405 (2005).

[4] B. M. Dzhagarov, E. S. Jarnikova, M. V. Parkhats, A. S. Stasheuski, "Dependence of the spontaneous emission of singlet oxygen on the refractive index and molecular polarizability of the surrounding dielectric media", Opt. Spectrosc. **116**, 1003 – 1008 (2014).

Molecular Oxygen Migration Through the Xenon Docking Sites of Human Hemoglobin and Its Isolated Chains

Sergei V. Lepeshkevich
B.I. Stepanov Institute of Physics, National Academy of Sciences of Belarus, 68 Nezavisimosti Ave, Minsk 220072, Belarus
s.lepeshkevich@ifanbel.bas-net.by

Abstract: In the α subunits of human hemoglobin, in addition to the direct His(E7) channel, there is at least one alternative ligand escape route leading to the exterior via the xenon docking sites.

Human hemoglobin is an allosteric protein that carries molecular oxygen (O_2). Human hemoglobin is a tetramer consisting of two α and two β subunits. Each subunit carries one identical heme group, which can reversibly bind one diatomic ligand such as O_2 or CO. The deoxygenated hemoglobin has a low-affinity structure (T-state) and the oxygenated one has a high-affinity structure (R-state). As tetrameric hemoglobin is oxygenated, its quaternary structure is changed and the O_2 affinity is increased. Since the pioneering work of Gibson [1], flash photolysis techniques have been extensively used for kinetic studies of O_2 rebinding to ferrous hemoglobin [2−5]. It is commonly accepted that, after photodissociation, the ligand remains temporarily trapped in the distal heme pocket of the hemoglobin subunits. Subsequently, the ligand can rebind to the heme iron or migrate through the protein matrix into the solvent, from where it can return into the protein. Both ligand migration and rebinding, and, consequently, protein reactivity are modulated by structural determinants such as internal cavities, hydrogen-bonding residues in the distal heme pocket, and the intrinsic heme reactivity. Small internal cavities with volume up to 100 $Å^3$ are generally hydrophobic and have an ability to bind Xe atoms by non-covalent specific interactions. Recently [6], X-ray diffraction studies of deoxygenated human hemoglobin and its quadruple mutant (Leu(B10)Tyr and His(E7)Gln in the α and β subunits), filled with Xe atoms under pressure, have revealed the presence of up to six Xe docking sites in the α subunits, and two sites in the β subunits. Both cavities in the β subunits are close to the heme, and do not appear to serve as ports of ligand entry into or escape from the protein matrix. In the α subunits, the found Xe docking sites have been proposed [4,6] to define potential routes within the protein matrix for ligand migration between the distal heme pocket and solvent. In the present work, to experimentally verify if the ligand migration occurs via the Xe docking sites in human hemoglobin, laser flash photolysis techniques were used to study the O_2 rebinding to the α and β subunits within tetrameric hemoglobin and its isolated chains under Xe pressure. In the case when the photodissociated ligand visits Xe docking sites, filling these sites with Xe atoms under pressure is expected to change the ligand rebinding. In the present work, it was investigated the influence of Xe atoms on the nanosecond geminate O_2 rebinding and on the efficiency of O_2 escape from the α and β subunits within tetrameric human hemoglobin and its isolated chains as well as on the bimolecular O_2 rebinding to each subunit within tetrameric hemoglobin. To simultaneously measure the individual parameters of the O_2 rebinding to each subunit within tetrameric hemoglobin, the approach [7] was applied.

Kinetics for the O_2 rebinding to hemoglobin and its isolated chains were measured on a nanosecond laser spectrometer [5]. The second harmonic (532 nm) of a 8 ns Nd:YAG laser (LS-2132U, LOTIS TII, Belarus) was used for photoexcitation. The bimolecular and nanosecond geminate O_2 recombination to tetrameric human hemoglobin and its isolated chains was examined using a previously described methodology [5]. The O_2 rebinding was measured in the presence and absence of Xe using a high-pressure cell. Kinetic measurements were conducted in 1 atm of air with up to 25 atm of Xe. The O_2 rebinding to tetrameric hemoglobin was studied when the primary photodissociation level does not exceed 10% and no more than 1% of O_2 was released from fully saturated hemoglobin [2]. Such photoexcitation level was used to ensure the experimental conditions when photo-irradiated tetrameric hemoglobin loses statistically only one molecule of oxygen and the tetramer remains in the R state.

In the present work, it was shown that filling internal cavities in the isolated α and β chains as well as in the β subunits within tetrameric hemoglobin with Xe atoms results in the decrease of the time constant of the slowest nanosecond component of the geminate O_2 rebinding. The observed decrease in the time constant is explained by a reduction of the free internal volume accessible for O_2 diffusion within the protein matrix after Xe insertion. These results demonstrate that, after photodissociation, O_2 molecule does visit the Xe docking sites. Unfortunately, changes in the geminate O_2 rebinding to the α subunits within tetrameric hemoglobin caused by Xe insertion cannot be detected by our technique since this O_2 rebinding process is considered to occur on subnanosecond time scale [2]. Moreover, Xe insertion into the isolated α chains and into the α subunits within tetrameric hemoglobin was found to cause the decrease in the efficiency of O_2 escape by a factor of ~1.30 and 3.3, respectively. On the contrary, for the β subunits both in the isolated state and within tetrameric hemoglobin,

the efficiency of O_2 escape does not change. Within the experimental accuracy, the rate constants of the bimolecular O_2 rebinding to the α and β subunits in the isolated state and within tetrameric hemoglobin do not change as well.

In the isolated β chains and β subunits within tetrameric hemoglobin, the lack of Xe effects on the rate constant for the bimolecular O_2 recombination suggests that the Xe docking sites in the β subunits do not serve as ports of O_2 entry. Our results directly support the conclusions made by Olson *et al*. [8,9] that the direct channel between the heme pocket and solvent is the major route for ligand entry into and escape from the β subunits of human hemoglobin. Moreover, based on the results of Adachi *et al*. [10], the observed decrease in the time constant of the slowest nanosecond component of the geminate O_2 rebinding upon Xe insertion into the isolated β chains and into the β subunits within tetrameric hemoglobin in the R state suggests that, after photodissociation, O_2 molecule visits at least Xe2 cavity in the β subunits. In our experiments, the absence of observed effects of Xe on the rate constant for the bimolecular O_2 rebinding to the isolated α chains and α subunits within tetrameric hemoglobin also supports the idea that the E7 channel is the major route for ligand entry.

To adequately explain the observed changes in the empirical parameters describing the O_2 rebinding, it was proposed a kinetic model for O_2 dissociation, migration through two alternative pathways, and rebinding in the α and β subunits in the isolated state and within tetrameric hemoglobin. It was shown that, in the α subunits, the significant fraction of O_2 molecules escapes through the Xe docking sites. In particular, in the isolated α chains and α subunits within tetrameric hemoglobin, nearly one- and two-third escaping molecules of O_2 leave the protein via the Xe docking sites, respectively. The observed increase in the fraction of O_2 molecules escaping via the Xe cavities at incorporation of the isolated α chains into the tetrameric hemoglobin can be explained by damping of protein motions by the adjacent subunits. On the contrary, the present experimental data indicate that molecular oxygen does not escape from the β subunits through the Xe cavities and support the idea that O_2 molecule escapes from the β subunits mainly through the His(E7) gate.

The present data indicate that ligand migration pathways in the α subunits differ from those in the β subunits. In the α subunits, in addition to the direct E7 channel, there is at least one alternative ligand migration route leading from the distal heme pocket to the solvent via the Xe docking sites. Since all Xe cavities are saturated with Xe atoms equally well [6], it is not possible at present to determine those Xe cavities whose occupation by Xe atoms leads to the observed changes in the O_2 rebinding. However, it can be hypothesized that the alternative pathway for O_2 escape from the α subunits involves the Xe3 cavity. This site is the closest to the heme iron, the primary docking site, and the exterior, being separated from the solvent only by His^{58}(E7) and Phe^{46}(CD4).

[1] Q.H. Gibson, "The photochemical formation of a quickly reacting form of haemoglobin," Biochem. J. **71**, 293-303 (1959).

[2] S.V. Lepeshkevich, J. Karpiuk, I.V. Sazanovich, B.M. Dzhagarov, "A kinetic description of dioxygen motion within alpha- and beta-subunits of human hemoglobin in the R-state: geminate and bimolecular stages of the oxygenation reaction," Biochemistry **43**, 1675-1684, (2004).

[3] S.V. Lepeshkevich, M.V. Parkhats, I.I. Stepuro, B.M. Dzhagarov, "Molecular oxygen binding with α and β subunits within the R quaternary state of human hemoglobin in solutions and porous sol–gel matrices," Biochim. Biophys. Acta **1794**, 1823-1830 (2009).

[4] S.V. Lepeshkevich, S.A. Biziuk, A.M. Lemeza, B.M. Dzhagarov, "The kinetics of molecular oxygen migration in the isolated α chains of human hemoglobin as revealed by molecular dynamics simulations and laser kinetic spectroscopy," Biochim. Biophys. Acta **1814**, 1279-1288 (2011).

[5] S.V. Lepeshkevich, S.N. Gilevich, M.V. Parkhats, B.M. Dzhagarov, "Molecular oxygen migration through the xenon docking sites of human hemoglobin in the R-state," Biochim. Biophys. Acta. **1864**, 1110-1121 (2016).

[6] C. Savino, A.E. Miele, F. Draghi, K.A. Johnson, G. Sciara, M. Brunori, B. Vallone, "Pattern of cavities in globins: the case of human hemoglobin," Biopolymers **91**, 1097-1107 (2009).

[7] B.M. Dzhagarov, S.V. Lepeshkevich, "Kinetic studies of differences between α- and β-chains of human hemoglobin: an approach for determination of the chain affinity to oxygen," Chem. Phys. Lett. **390**, 59–64 (2004).

[8] I. Birukou, R.L. Schweers, J.S. Olson, "Distal histidine stabilizes bound O_2 and acts as a gate for ligand entry in both subunits of adult human hemoglobin," J. Biol. Chem. **285**, 8840-8854 (2010).

[9] I. Birukou, J. Soman, J.S. Olson, "Blocking the gate to ligand entry in human hemoglobin," J. Biol. Chem. **286**, 10515-10529 (2011).

[10] S.-I. Adachi, S.-Y. Park, J.R.H. Tame, Y. Shiro, N. Shibayama, "Direct observation of photolysis-induced tertiary structural changes in hemoglobin," Proc. Natl. Acad. Sci. U.S.A. **100**, 7039-7044 (2003).

Highly Stable and Widely Tunable Ultrashort Pulse Distributed Feedback Dye Laser for Biomedical Applications

T.Sh.Efendiev, V.M.Katarkevich, Yu.V.Kruchenok, V.Yu.Plavskii, A.N.Sobchuk
B.I.Stepanov Institute of Physics, National Academy of Sciences of Belarus
68 Nezavisimosti Ave., 220072, Minsk, Belarus
E-mail: katarkevich@dragon.bas-net.by

Abstract: Highly stable and widely tunable ultrashort pulse distributed feedback dye laser excited by a diode-pumped solid-state Nd:YLF micro laser is reported. The realized laser source is especially suitable for the time-resolved spectroscopic studies of biomedical objects.

1. Introduction

For the time-resolved spectroscopic measurements in biology, medicine, photochemistry, etc. simple and convenient to use laser sources delivering tunable ultrashort pulses (USPs) with high repetition rates and good reproducibility of the parameters are required. Distributed feedback (DFB) dye lasers are especially suitable for this purpose because they allow us in the simplest way to obtain the wavelength tunable USPs both under picosecond and nanosecond excitation [1, 2]. Until recently, the USP DFB dye laser systems used in spectroscopy, biology, ecology etc. were based on the rather expensive and large-frame pump sources, such as N_2-lasers, excimer lasers, flashlamp-pumped Nd:YAG-lasers, etc. [3–13]. For this reason, in spite of the relative simplicity of the DFB dye lasers themselves, the resultant USP laser systems appeared to be too complicated, expensive, and, hence, hardly accessible. Recent progress in the development of the sufficiently high peak power diode-pumped solid-state (DPSS) microchip lasers with their compact design and rather unique output characteristics makes them particularly attractive as pumping sources for the DFB dye lasers. This opens way for creating compact, easy to use and reliable USP DFB dye laser systems with performance characteristics especially suitable for biomedical applications.

Earlier, we have demonstrated that a DFB dye laser pumped with the second harmonic (λ_p = 532 nm) from a subnanosecond ($\tau_{0.5}$ ~ 0.5 ns) DPSS Nd:LSB microlaser provides highly stable and efficient generation of subnanosecond and picosecond pulses continuously tunable in the visible and near infrared (IR) spectral ranges [14–16]. At the same time, for the time-resolved spectroscopic studies of different biological and chemical species the USP emission tunable in the near ultraviolet (UV) spectral region is in high demand. In this work, we report on a compact, efficient and highly stable USP laser source continuously tunable from the near UV to the near IR, which is based on a DFB dye laser pumped by a subnanosecond DPSS Nd:YLF microlaser.

2. Experimental details

An improved model of the earlier developed DFB dye laser providing high performance operation with an easy possibility of wavelength tuning from the near UV to the near IR is employed in the present work. A compact STA-01-08-1047-SH/TH Nd:YLF microlaser (Standa Ltd., Lithuania) delivering subnanosecond pulses ($\tau_{0.5}$ ~ 0.3 ns) both at the second (λ_P = 523.5 nm) and third (λ_P = 349 nm) harmonics upon a spectral linewidth of $\Delta\lambda_{0.5} \le 0.003$ nm and a pulse repetition rate f up to 100 Hz is used as a pump source for a DFB dye laser. The microlaser output pulse energy reaches E_P ~160 and ~80 μJ at the second and third harmonics, respectively, at a pulse-to-pulse energy stability of $\sigma_P \le 0.4\%$ (RMS) and a beam quality factor of $M^2 \le 1.5$. Depending on the pump light wavelength employed (λ_P = 349 or 523.5 nm), either a quartz or K-8 glass right-angle isosceles prism-cell filled with a laser dye serves as the DFB laser oscillator. To initiate the DFB lasing in a dye solution, the two s-polarized microlaser beams formed in a view of narrow horizontal stripes are symmetrically coupled into the active medium through the side faces of the prism. This results in the first-order DFB laser operation with a wavelength λ_L given by

$$\lambda_L = \frac{n_s \lambda_P}{2 n_{pr} \sin\theta}, \qquad (1)$$

where n_s is the refractive index of the dye solution at the lasing wavelength λ_L, λ_P is the pump wavelength, n_{pr} is the refractive index of the prism material at the pump wavelength λ_P, and θ is the incident angle of the pump beams at the prism - dye solution interface. The DFB lasing represents the two identical light beams symmetrically outcoupled from the excited dye volume through the end windows of the cell. The smooth tuning

of the lasing wavelength λ_L is readily realized by varying the intersection angle 2θ of the pump beams. The latter is accomplished through synchronous rotating the two turning mirrors of a DFB laser.

3. Experimental results

The output characteristics of a DFB dye laser excited by the third and second harmonics of a Nd:YLF microlaser were investigated in detail. It was established that, when pumped with full power of a microlaser (i.e. at high pumping levels $\gamma = E_P/E_{Thr}$, where E_{Thr} is the threshold pump energy, which is typically of a few μJ near the maximum of the dye gain profile), a DFB dye laser provides generation of subnanosecond pulses ($\tau_{0.5}$ ~ 0.2 – 0.25 ns) tunable from ~400 to ~760 nm. In this operational mode, the optical-to-optical energy conversion efficiency is as high as η_{max} ~60% upon a spectral linewidth of the DFB laser emission of $\Delta\lambda_{0.5} \leq$ 0.01 nm and a pulse-to-pulse energy stability of σ_L ~ 1% (RMS). At pumping intensities not very high above the threshold ($\gamma \leq 2$) generation of single transform-limited picosecond pulses ($\tau_{0.5}$ ~15 – 65 ps) with a time-bandwidth product of $\Delta\nu_{0.5} \times \tau_{0.5} \sim 0.3$ is ensured by a DFB dye laser. In this regime, A DFB dye laser exhibits a pulse-to-pulse energy stability of σ_L ~ 3% (RMS) at typical values of lasing efficiency η of a few percents.

In order to continuously cover the whole (~360 nm wide) spectral range, a set of liquid laser dye solutions of the appropriate concentration were used as active medium of a DFB dye laser. For the majority of the employed compounds ethanol was established to be the most suitable solvent both in terms of the dye solubility and its lasing efficiency. To increase lasing efficiency and extend tuning range for the dyes with rather weak absorption at the pump wavelength, the excitation energy transfer from the auxiliary (donor) dye was employed through the use of the properly selected binary dye mixtures. It should be noted that a DFB dye laser successfully operated at all frequencies provided by a Nd:YLF microlaser (i.e. $f \leq 100$ Hz) without dye solution flow through the cell.

The developed DFB dye laser is currently employed as a tunable USP light source in a home-made picosecond laser spectrofluorimeter intended for the studies of a wide range of objects being of interest for biology and medicine [15]. We believe that it can also be used in a number of other scientific and applied research, where tunable USPs of moderate peak power and wide spectral coverage are required.

4. References

[1] V. A. Zaporozhchenko, A. N. Rubinov, and T. Sh. Efendiev, "Generation of ultrashort pulses in distributed feedback dye laser," Pis'ma Zh. Tekh. Fiz. **3**, 114-116 (1977) (in Russian).

[2] Zs. Bor, "A novel pumping arrangement for tunable single picosecond pulse generation with a N_2 laser pumped distributed feedback dye laser," Opt. Commun. **29**, 103–108 (1979).

[3] A.N.Rubinov, and T.Sh.Efendiev, "Holographic DFB dye lasers," Opt. Acta, **32**, 1291-1301 (1985).

[4] T.Sh.Efendiev, V.M.Katarkevich, and A.N.Rubinov, "Generation of tunable picosecond pulses in a simple distributed feedback dye laser under N_2 -laser pumping," Optics Communs, **55**, 347-352 (1985).

[5] P.L. Kukk, D.S. Feklistov, and R.P. Tamkivi, "Excimer-laser-pumped picosecond laser source for time-resolved measurements," Sov. J. Quantum Electron. , 993–995 (1986).

[6] G. M. Gale, B. Pedersen, and P. Schanne, "Kilohertz picosecond distributed feedback dye laser system," Opt. Communs. **76**, 138–142 (1990).

[7] P.P.Yaney, D.A.V.Kliner, P.E.Schrader, and R.L.Farrow, "Distributed-feedback dye laser for picosecond ultraviolet and visible spectroscopy," Rev. Sci. Instrum., **71**, 1296-1305 (2000).

[8] N.Khan, and A.Idrees, "Overexposure analysis of pulsed distributed feedback laser source," J. of Biomed. Opt., **6**, 86-89 (2001).

[9] N.Takeyasu, T.Deguchi, M.Tsutsumikawa, J.Matsumoto, and T.Imasaka, "A tunable picosecond dye laser for use in dioxin analysis," Anal. Sci., **18**, 243-246 (2002).

[10] T. Dreier, and J. Tobai, "Rotational State Resolved Measurement of Relaxation Times and Ground State Recovery Rates in Small Radicals in Atmospheric Pressure Flames Using Picosecond Pump-Probe Degenerate Four-Wave Mixing," Laser Physics **13**, 286–292 (2003).

[11] T. Uchimura, T. Deguchi, and T. Imasaka "Development of a narrow-band tunable picosecond dye laser and its application to excited-state lifetime measurement of a chlorinated aromatic hydrocarbon," Anal. Sci. **21**, 693–695 (2005).

[12] T. Ushimura, S. Kawanabe, Y. Maeda, and T. Imasaka, "Fluorescence lifetime imaging microscope consisting of a compact picosecond dye laser and a gate charge-coupled device camera for application to living cells," Anal. Sci. **22**, 1291–1295 (2006).

[13] D. Q. Hoa, T. Uchimura, T. Imasaka, and N. D. Hung, "Fluorescence lifetime measurement of dibenzofuran and monochlorodibenzofuran," Science and Technology of Advanced Materials **7**, 714–717 (2006).

[14] T.Sh. Efendiev, V. M. Katarkevich, Ch. O. Qajar, and R. A. Karamaliyev, "Picosecond distributed feedback dye laser excited with diode-pumped solid-state micro laser," Azerb. J. of Physics. Fizika **17**, 7–10 (2011).

[15] T.Sh. Efendiev, V.M. Katarkevich, Yu.V. Kruchenok, V.Yu. Plavskii, A.N. Rubinov, and A.N. Sobchuk, "Ultrashort pulse distributed feedback dye laser for biomedical applications," in Technical Digest of the International Conference on Lasers, Applications, and Technologies (LAT'2013) (June 18-22, Moskow, Russia), paper #LFL32.

[16] V.M. Katarkevich, A.N. Rubinov, T.Sh. Efendiev, S.S. Anufrik, and M.F. Koldunov, "Highly efficient solid-state distributed feedback dye laser based on polymer-filled nanoporous glass composite excited by a diode-pumped solid-state Nd:LSB microlaser," Appl. Opt. **54**, 7962-7972 (2015).

The nanostructure formation via laser ablation of porous silicon for biomedical applications

F.V. Kashaev[1], T.P. Kaminskaya[1], S.V. Zabotnov[1], D.A. Loginova[2], P.D. Agrba[2], M.Yu. Kirillin[3], L.A. Golovan[1]

[1]- Lomonosov Moscow State University, Faculty of Physics, 1/2 Leninskie Gory, Moscow, 119991, Russia
[2]-Lobachevsky State University of Nizhny Novgorod, 23 Gagarin ave, Nizhny Novgorod, 603950, Russia
[3]-Institute of Applied Physics RAS, 46 Uljanov str.,Nizhny Novgorod, 603950, Russia
e-mail: kashaev.fedor@gmail.com

Abstracts: In this paper we report on the formation of por-Si nanostructures, fabricated by means of laser ablation in helium and water. The investigation of structural and optical properties of the formed particles confirms a possibility of their application in optical coherence tomography and photodynamic therapy.

The great interest of scientists in researching of nanodimensional structures is caused by their variety of possible applications in optoelectronics, photonics and biomedicine. These materials possess electronic and optical properties different from properties of the bulk materials due to the quantum confinement effect. There are many various ways of producing nanoparticles, among which it is possible to distinguish a method of a laser ablation. The advantages of this method include chemical purity of the fabrication process and possibility of changing the structural, optical and electronic properties of the nanoparticles produced by ablation of varying conditions (such as the type of buffer medium or medium pressure) [1].

Due to biocompatibility and biodegradability of silicon [2], the nanoparticles of this material formed by laser ablation may be used in nanobiophotonics [3]. Due to the efficient light scattering of porous silicon the nanoparticles formed by ablation of por-Si could be used as contrasting agents for visualization of model biosimilar environments by methods of optical diagnostics [4]. In addition the electronic properties of silicon nanoparticles with small size (less than 5 nm) allow using them as photoluminescent labels for photodynamic therapy and diagnosis [5].

This work presents results of experiments of the nanoparticle formation as a result of ultrafast laser ablation of porous silicon in water and helium. During the experiment the target was irradiated with Cr:forsterite femtosecond (1250 nm, 180 fs, 10 Hz, 10 J/cm^2) and Nd:YAG picosecond (1064 nm, 30 ps, 10 Hz, 7 J/cm^2) laser pulses at room temperature. The choice of porous silicon as a material for experiments is caused by a lower threshold of ablation in comparison with crystalline silicon. During the ablation of the crystalline silicon ablation threshold is equal to1 J/cm^2, whereas for porous materials threshold equals 0,1 J/cm^2. This feature leads to a greater exit of substance at lower energy costs at a case of ablation of porous silicon.

Determination of the structural properties of the formed samples is important due its influence on optical and electrical properties of the particles. The size of nanoparticles fabricated via laser ablation was determined by atomic-force microscopy (AFM) and ranges from 10 to 60 nm. Then the histograms of particle size distribution were constructed by these results and monotonic dependence of nanoparticle size variation on the buffer gas pressure was found: the nanoparticle size decreased with increasing pressure. The samples with minimum size of nanostructures was obtained at a case of ablation in helium at pressure 500 mbar (Fig.1)

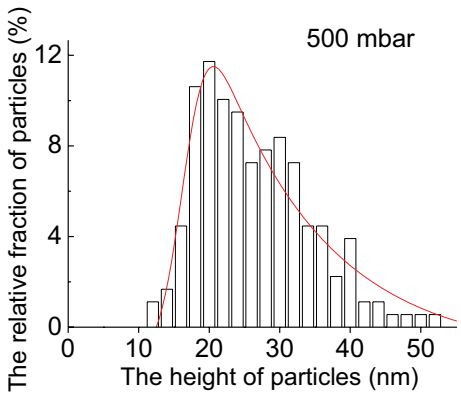

Fig.1 Particle size distribution of silicon nanoparticles, formed by means of the fs laser ablation of por-Si in helium at pressure 700mbar.

By means of a Raman scattering spectroscopy the phase structure of the created nanoparticles was defined. The measurements indicated the presence of crystalline phase of silicon (peak near 520 cm^{-1}) in the formed

nanoparticles and the broadening and shifting (to 518,5 cm^{-1}) of the peak evidenced about the quantum-size effect. Besides structural properties, optical properties were also investigated. Fig 1 demonstrates the photoluminescence spectrum of the nanostructures, formed by femtosecond laser ablation in helium at pressure 100mbar.

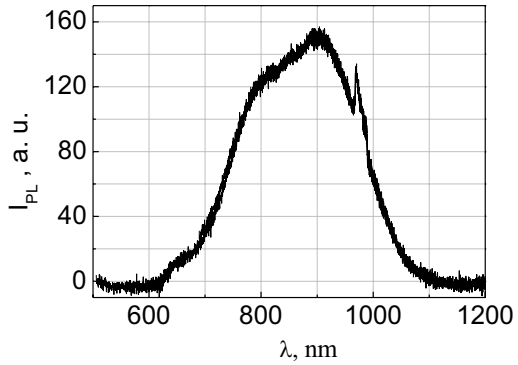

Fig.1 Photoluminescence spectrum of the nanoparticles formed by femtosecond laser ablation of porous silicon p-type in helium (100 mbar)

This work was financially supported by the Russian Foundation for Basic Research (project 15-32-20227).

[1] G.N. Makarov, "Laser application in nanotechnology: receiving nanoparticles and nanostructures by methods of laser ablation and laser nanolithography", Physics-Uspekhi **183**, 673-718 (2013).
[2] R. Henstock, L.T. Canham, S.I. Anderson, "Silicon: the evolution of its use in biomaterials", Acta Biomaterialia **11**, 17-26 (2015).
[3] P. Blandin, K.A. Maximova, M.B. Gongalsky, et al., "Femtosecond laser fragmentation from water-dispersed microcolloids: toward fast controllable growth of ultrapure Si-based nanomaterials for biological applications", J. Mater. Chem. B. **1**, 2489–2495 (2013).
[4] M.Yu Kirillin, E.A. Sergeeva, P.D Agrba et al., "Laser-ablated silicon nanoparticles: optical properties and perspectives in optical coherence tomography", Laser Physics **25**, 075604 (2015).
[5] P. Jusenas, W. Chen., YP. Sun, et al., "Quantim dots and nanoparticles for photodynamic and radiation therapies of cancer", Adv. Drug Delivery Rev. **60**, 1600-1614 (2008).

Laser Scanning Microscope Usage for Investigation of the Dynamics of a Chemical Agent Penetration into the Skin

T. A. Zheleznyakova[1, 2], A. A. Ryzhevich[1], S. V. Solonevich[1], S. B. Bushuk[1]
[1] *Institute of Physics of NAS of Belarus, 68 pr. Nezalezhnastsi, 220072, Minsk, Belarus;*
e-mail: tol@dragon.bas-net.by
[2] *Belarusian State University, Radiophysics and Computer Technologies Dept., 4 pr. Nezalezhnastsi, 220030, Minsk, Belarus;*
e-mail: zhelez@bsu.by

Abstract: We investigated the preparation concentration dependence on the depth by luminescence microscopy after locating preparation on skin. We found out a temporary depot of the preparation between the horny layer and the underlying epidermis layer.

1. Introduction

The aim of this work was to determine using a laser scanning microscope temporal regularities of penetration into the skin of a chemical preparation, which is a luminescent mark too, without the effects of radiation in order to subsequently determine the additional influence of laser radiation on this process. Earlier in [1] we determined the concentration of the introduced preparation on the surfaces of the side sections of defrosted samples of biological tissue *ex vivo*. In this work a study of the preparation concentration in the deep has been done through the outside surface of the biological tissue sample. Used samples didn't undergo the extreme physical and chemical actions. It means that we can use this method in configuration described to biological tissue *in vivo* in the future.

2. Experiment

We used samples of chicken skin which was not exposed to freezing and defrosting, in the form of squares with dimensions of the sides ~ 1 cm. As the introduced preparation and luminescent mark, we used a water solution of rhodamine 6G with a concentration of $5 \cdot 10^{-5}$ mol/l, which was applied by dosing unit to the skin surface at zero-time. The wavelength of the luminescence of an water solution of rhodamine 6G is λ_{lum} = 550-570 nm, the absorption maxima are at the wavelength of 346 and 530 nm. The radiation absorption coefficients of rhodamine 6G, alcohol and water almost do not change in the range of 650-900 nm and are negligible [1, p. 124]. The study of the preparation concentration distribution in tissue depth was carried out using laser scanning microscope LSM 510 (hereinafter LSM) manufactured by Zeiss (Germany). We used two-photon excitation of the preparation luminescence which is usually less damaging for biological samples than single-photon excitation [2, p. 607]. Based on the series of images produced by LSM we constructed diagrams of the average pixel brightness depending on the distance from the sample surface to the studied layer for different time intervals after application of the preparation to the sample – 1, 3, 5 and 10 min. Average brightness of the pixels was obtained by using the ImageJ tools. The distance between adjacent layers was 2 μm. The background luminescence of the sample has been taken into account. We assumed that the initial luminescence intensity of the preparation is directly proportional to the concentration of the luminophor in biological tissue because of the smallness of the preparation concentration in tissue the luminescence quenching and reabsorbtion do not occur. The process scheme of radiation propagation in biotissue with a luminophor is presented in figure 1.
The brightness of the pixel in digital photography is directly proportional to the radiation intensity $I_3(\lambda_{lum})$ with the luminescence wavelength λ_{lum} incidenting on the corresponding pixel of the CCD-camera sensor.

We used a lens with a large numerical aperture (NA = 0.75), so within the investigated depth in the sample it is possible to speak about the independence of the efficiency of light collection from the x coordinate. Generally, the absorption and scattering coefficients depend not only on wavelength but also on the coordinate x of the investigated layer. However, the penetration depth of the luminophor in this case is not more than 100 μm, so we assume that the optical properties of the investigated region do not depend on x and correspond to the optical properties of the epidermis of human skin. Subject to some assumptions, the concentration of the luminophor is described with restored intensity value $I_3'(\lambda_{lum})) = I_3(\lambda_{lum}) \exp[(2\alpha(\lambda_0) + \alpha(\lambda_{lum}))x]$, where the wavelength of the laser radiation is λ_0 = 790 nm, the wavelength of the rhodamine 6G luminescence is λ_{lum} = 550-570 nm, where $\alpha(\lambda_0)$ and $\alpha(\lambda_{lum})$ are skin attenuation coefficients for radiation with the wavelength λ_0 and λ_{lum} respectively. The effective attenuation coefficient is calculated by the formula $\alpha = (3\alpha^a(\alpha^a+\alpha^{s'}))^{1/2}$, where α^a is the absorption coefficient, $\alpha^{s'}$ is the reduced (transport) scattering coefficient. On the basis of data available in [3, p. 40] we can assume that for λ_0 $\alpha^a(\lambda_0) \approx 40$ cm^{-1}, $\alpha^s(\lambda_0) \approx 420$ cm^{-1}, $\alpha^{s'}(\lambda_0) \approx 62$ cm^{-1}, and for λ_{lum} $\alpha^a(\lambda_{lum}) \approx 40$ cm^{-1}, $\alpha^s(\lambda_{lum}) \approx 500$ cm^{-1}, $\alpha^{s'}(\lambda_{lum}) \approx 110$ cm^{-1}.

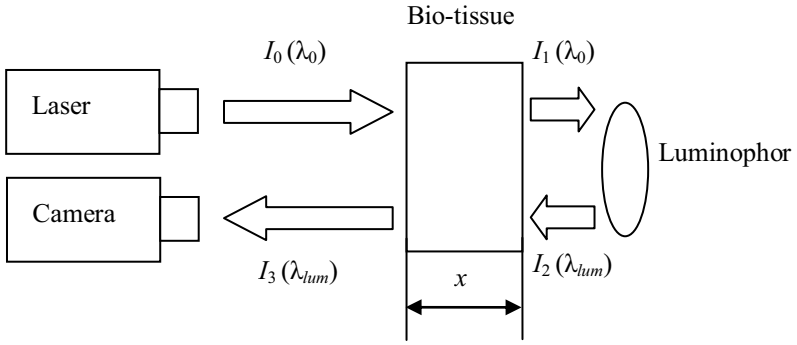

Fig. 1. Scheme of the light propagation in biological tissue with a luminophor

The dependences of the preparation concentration on the depth after different time intervals are presented in figure 2. All distributions have been normalized by the value of the preparation concentration on the surface for each distribution because some technical reasons forbad to produce a more general distribution normalization for several different samples.

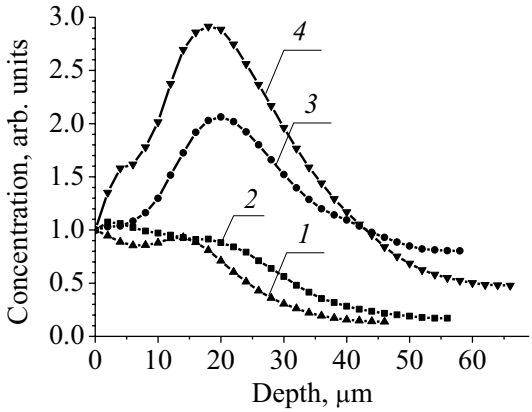

Fig. 2. The dependences of the luminophor concentration in skin on the depth after 1 min (1), 3 min (2), 5 min (3) and 10 min (4) after application of the preparation to the skin surface

We mentioned the presence of a preparation depot at a depth of 20 μm. This depth corresponds to the boundary between stratum corneum and the underlying layer of epidermis. In this depot the introduced preparation concentration can greatly exceed the preparation concentration on the skin surface in the course of time. This fact should be taken into account when modeling the process of the preparation penetration into the skin.

In our opinion, dye curcumin is well suited by means of luminescent mark to assess the laser-phoresis effectiveness in real time. Because curcumin is poorly soluble in water, it is advisable to use its oil and water-alcohol solutions with low content of alcohol including the curcuma extracts.

3. Conclusion

Presumably, the laser radiation can significantly accelerate the preparation penetration into the skin starting from the depot coordinate. On this basis, as well as available data about the increase of preparation concentration in the depth of biological tissue exposed to laser radiation [1], we consider it is advisable to conduct a further experiments to study the dynamics of the preparation penetration under the action of laser radiation. In these experiments the harmless-to-human dye named curcumin in its oil and water-alcohol solutions (in particular in solutions of curcuma extract) can be used.

References

[1] Ryzhevich A.A., Zheleznyakova T.A., Solonevich S.V. *Vvedenie preparatov v organism pod deistviem lazernogo izlucheniia. Eksperimental'naia baza, zakonomernosti, oblast' primeneniia i perspektivy razvitiia* [Introduction of medications in organism under laser radiation influence. Experimental base, regularities, range of application and prospect of development]. (Lambert Academic Publ., Saarbrücken, 2011). (in Russian).

[2] Lakowicz, Jo. R. *Principles of Fluorescence Spectroscopy*, 3rd edn. (Springer, Berlin, 2006).

[3] Tuchin, V.V. *Lazeri i volokonnaya optika v biomedicinskih issledovaniyah* [Lasers and fiber optics in biomedical investigations]. (Saratov, 1998). (in Russian).

Laser impact monitoring during photocoagulation using optoacoustic technique

Anton Lytkin[1], Andrey Larichev[1], Svetlana Shmeleva[1], Varvara Simonova[1], Vladimir Sipliviy[2], Andrey Bolshunov[2], Alesya Ardamakova[2]

[1]M.V.Lomonosov Moscow State University, Moscow, Russian Federation

[2]State Research Institute of Eye Diseases of the Russian Academy of Sciences, Moscow, Russian Federation

author's e-mail: aplytkin@gmail.com

Method aimed at temperature control during lasercoagulation is based on optoacoustic technique that includes experimental determination of laser absorption coefficient and following numerical calculations. Values for different series of chorioretinal samples *ex vivo* were obtained in range from 1300 to 12000 1/m. Three-dimentional model of chorioretinal thermal heating is developed.

1.Introduction

Laser technology is widespread phenomenon in ophthalmology. One of the most popular applications is lasercoagulation. However, there is no reliable rapid method for monitoring laser impact during operation until nowadays. The problem that appears during lasercoagulation is to avoid damage of the photoreceptor layer. One short pulse of scanning laser is able to produce an acoustic wave of pressure in the biological tissue that can be registered by an acoustic receiver. One way to use OA based on continuous pulsing is widely known [1,2]. Another way of using OA for remote laser impact control is performed in this work.

2.Experimental setup and methods

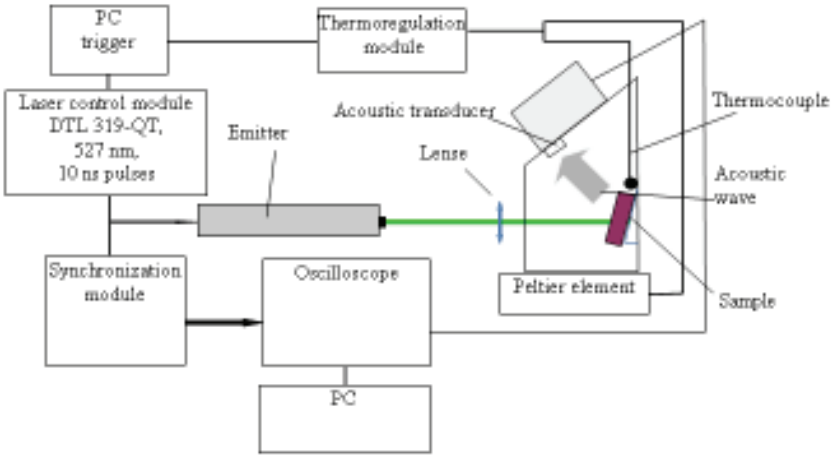

Fig.1. Experimental setup

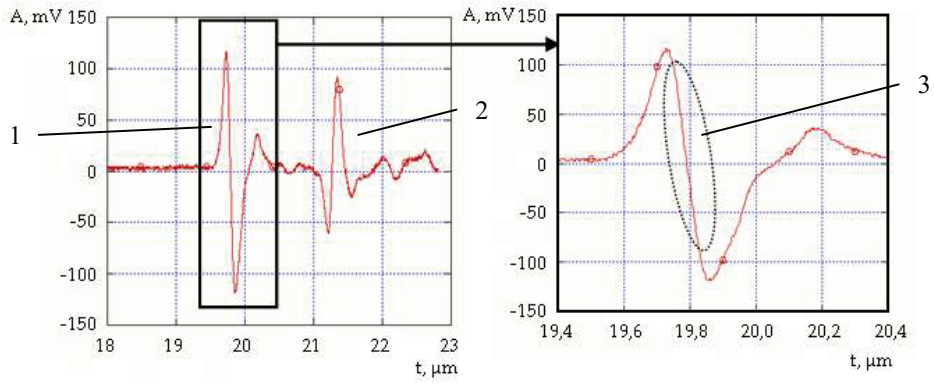

Fig.2. Typical acoustic wave obtained in experiment. 1- Main wave pulse contains information about absorption coefficient. 2 – reflected pulse is separated from main, it doesn't interfere. 3 - Part of the curve used to estimate absorption coefficient

Experimental setup is presented in **fig.1**. Main parts of this setup are: probe laser (DTL-319QT, wavelength 527 nm, pulse duration 10 ns) and cuvette. The cuvette had been constructed in special way for simulating eye structure. Sample

of biological tissue that is chorioretinal complex *ex vivo* is placed on the stand in cuvette, and then cuvette space is filled by saline solution to prevent tissue drying. Probe laser pulses applied to sample generate acoustic waves. Lens focuses laser beam on the sample. Typical signal that was obtained in experiment is displayed in **fig.2**. Absorption coefficient is determined by acoustic waveform that can be registered by transducer and viewed by oscilloscope. To simulate therapeutic laser heating thermoregulation module with peltier element was used.

3.Results

In the first method using the approximation allowed to estimate absorption coefficient of the sample tissues. Values for seven different series of experiments were obtained in range from 1300 to 12000 1/m. Difference of estimated value of absorption coefficient within one series is not more than 20%.The approximation equations is $f = A*exp(\alpha t)+B*exp(\beta t)$, where α is absorption coefficient. Retinal pigment epithelium (RPE) is a thin 6 μm narrowed layer that surrounded by vitreous body from one side and choroid from another. RPE is the only layer that able to absorb laser irradiation that propagates through tissues. Laser irradiation is gauss-shaped beam with 100 μm radius. Tissues that are far enough from beam don't suffer any heating, so border conditions are T = 0 for borders of the box $[0\times L_x; 0\times L_y; 0\times L_z]$ (here and below T means difference between native temperature T_0=37˚C and final temperature).Mathematical equations for this model are presented below:

$$\begin{cases} \frac{\partial T}{\partial t} = \chi \Delta T + F(x, y, z, t), \\ T|_{x,y,z=0} = 0 \\ T|_{x=Lx, y=Ly, z=Lz} = 0 \end{cases}$$

Where $$F = \frac{\alpha I_0}{\rho C} * \exp\left(\frac{-\alpha (z - z_c)}{\cos \gamma}\right) * \exp\left(\frac{-((x - x_c) - (z - z_c) tg\,\gamma)^2 \cos^2 \gamma - (y - y_c)^2}{2 r_0}\right) * \cos \gamma$$

F=F(x,y,z) determinates the geometry of system. γ is angle between beam and a normal to RPE layer, χ = 1,52*10-7 m2/s– coefficient of thermal conductivity, ρ=993 kg/m3 – density, C = 4180 J/kg K – heat capacity and I0 – intensity of the beam centre. (xc, yc, zc) – are coordinates of the lesion center. Example of simulation result predicted for preset parameters is shown in **Fig.3**.

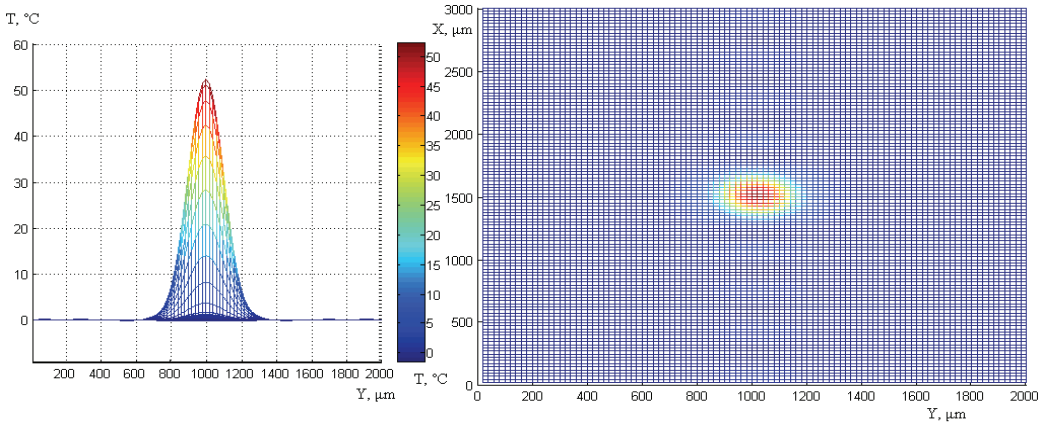

Fig.3. Results of numerical calculations for therapeutic laser impact with exposure time t = 100 μs, laser power N = 100 mW, tissue absorption coefficient is 90000 1/m.

4.Conclusion

Developed method uses two-step approach for determination of laser impact during laser photocoagulation. First step involves experimental determination of laser absorption coefficient in eye tissues. Experimental determination using OA technique was carried out for seven samples of human chorioretinal complex. Obtained values lie witih range from 1300 to 12000 1/m. Difference of estimated value of absorption coefficient within one series is not more than 20%. Second step requires absorption coefficient to be known and uses developed model to calculate therapeutic laser impact.

5.References

[1] Brinkmann R, Koizner S, Schlott K et al. "Real-time temperature determination during retinal photocoagulation on patients." *Journal of biomedical optics 2012;* 17(6):061219.

[2] Schlott K, Koinzer S, Ptaszynski L, Bever M, Baade A, Roider J, Birngruber R, Brinkmann R. "Automatic temperature controlled retinal photocoagulation." *Journal of Biomedical Optics 2012;* 17(6), 061223

Ablation treatment of dental tissue by 1060 nm radiation

S. Anufrick, A. Volodenkov, K. Znosko
Yanka Kupala State University of Grodno, 22, Ozheshko Street, 230023, Grodno, Belarus,
Fax: +375-172-108599, Ph.433346, E-mail: a.volodenkov@grsu.by

Abstract: The treatment of dental tissue is executed by 1060 nm radiation and dependence of value of specific energy of evaporation from density of peak power of laser radiation is determined. It is established, that threshold of ablation of dental enamel is 12 J/cm^2 and it is found that at density of energy more then 3 J/cm^2 the efficient removal of dental calcium takes place without ablation of dental enamel.

1. Experimental setupt.

Ablation influence of ultraviolet radiation on a surface of dental enamel and dental calcium was investigated. The maximal value of energy of generation of the «Lotis» (TII LS2147) made 0,2 J, thus duration of generation pulse on half-height was 15 nanoseconds.

For transportation of radiation of the e laser (1060 nanometers) the system on the basis of prism, mirrors and lenses has been used which optical circuit is described on fig. 1.

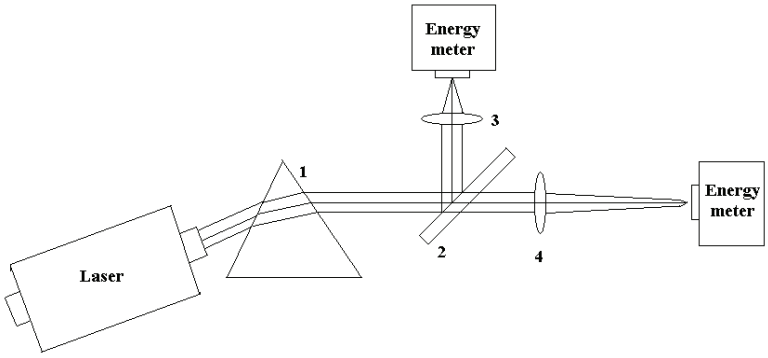

Fig.1. Optical schematic model of irradiation

Radiation of the laser went on a quartz prism 1, which was used for obtaining 1060 nm radiation The radiation reflected from a quartz substrate (2), went on focusing lens (3) and got on a measuring instrument of energy (ИМО-2Н) which was used for the control of energy of radiation. Radiation past through a quartz substrate (2) went on focusing lens (4) and further on irradiated object. Lenses (3, 4) had the antireflection covering for wave length 1060 nanometers. Calibration of measuring instrument of energy (ИМО-2Н), allowed to define energy falling on irradiated object, is executed. For this purpose on a place of irradiated object second device (ИМО-2Н) was put.

The focusing lens with a focal length of 235 mm has been used and radiation was focused in an oval spot with average diameter ~ 1mm. For reception of various values of energy of a pulse of radiation sets of diaphragms and adjustment of value charging voltage were used. Samples of dental tissue were irradiated with a series from 1000 pulses at use of frequency of following of pulses of 10 Hz. Depth of a crater was defined by means of an optical microscope.

2. Experimental results.

In fig. 2 dependence of depth of a crater in dental enamel (1) and dental calcium (2) from density of power after 1000 pulses is submitted.

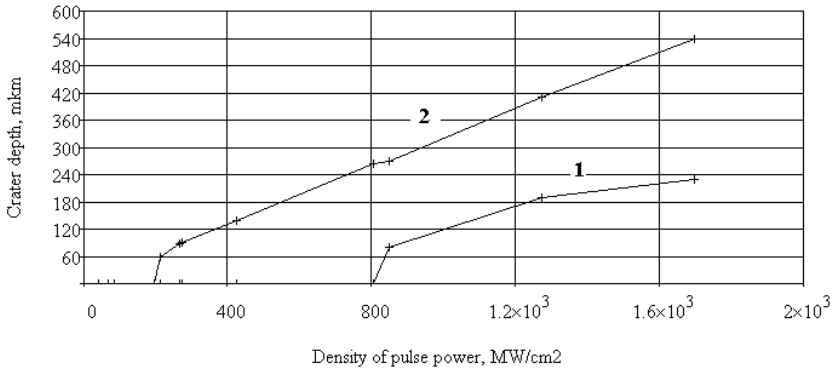

Fig. 2 Dependence of depth of a crater in dental enamel (1) and dental calcium (2) from density of power

From data, submitted in fig. 2, follows, that dependence (1) has threshold character and at density of energy smaller than 12 J/cm^2 (800 MW/cm^2) process of formation of craters in dental enamel is not observed. From data, submitted in fig. 2, follows, that dependence (2) has threshold character and at density of energy smaller than 3 J/cm^2 (200 MW/cm^2) process of formation of craters in dental calcium is not observed.

Then at density of energy more then 3 J/cm^2 (200 MW/cm^2) and less then 12 J/cm^2 (800 MW/cm^2) the efficient removal of dental calcium takes place without ablation of dental enamel.

In fig. 3 dependence of specific energy of evaporation of dental enamel from density of power is submitted.

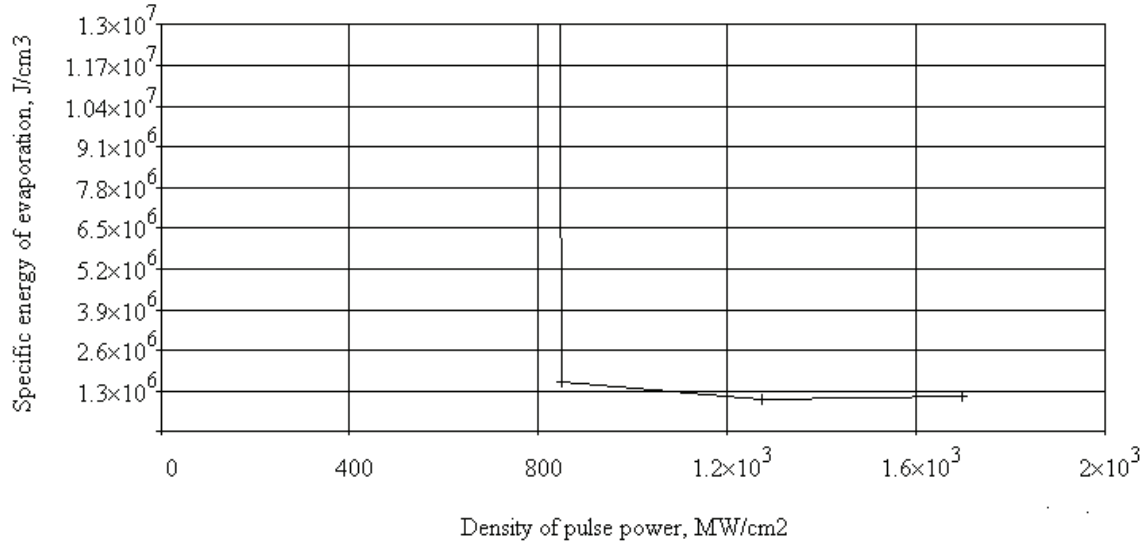

Fig. 3 Dependence of specific energy of evaporation of dental enamel from density of power

In fig. 4 dependence of specific energy of evaporation of dental calcium from density of power is submitted.

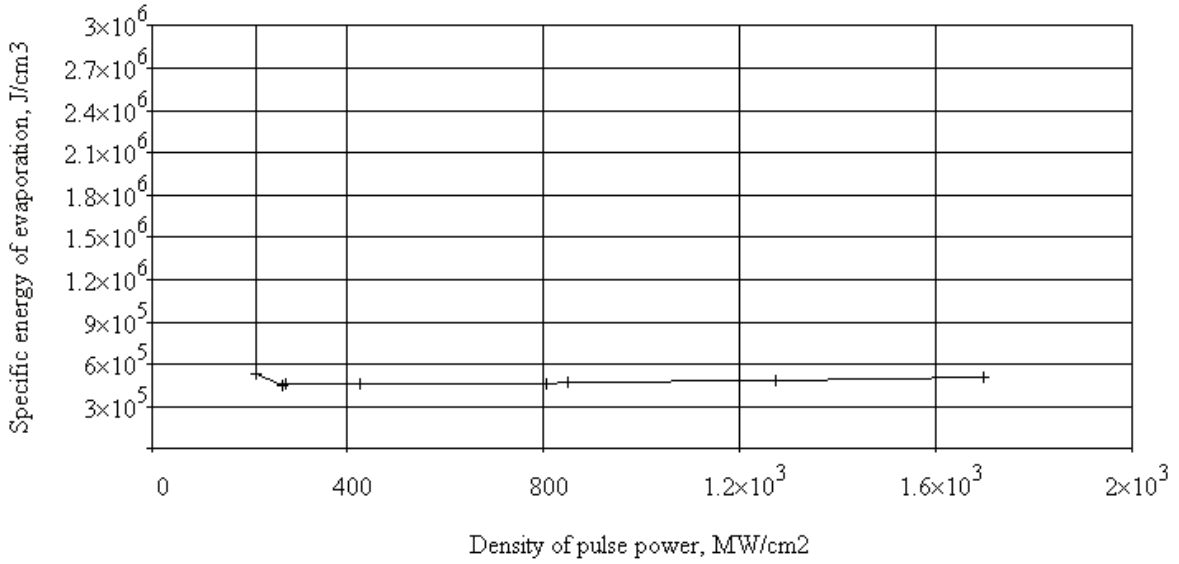

Fig. 4 Dependence of specific energy of evaporation of dental calcium from density of power

From data, submitted in fig. 3, follows, that specific energy of evaporation of dental enamel has minimum value ~ 1000 kJ/cm^3 at density of power ~ 1270 MW/cm^2.

From data, submitted in fig. 4, follows, that specific energy of evaporation of dental calcium has minimum value ~ 450 kJ/cm^3 at density of power ~ 400 MW/cm^2.

Ablation treatment of dental tissue by 530 nm radiation

S. Anufrick, A. Volodenkov, K. Znosko
Yanka Kupala State University of Grodno, 22, Ozheshko Street, 230023, Grodno, Belarus,
Fax: +375-172-108599, Ph.433346, E-mail: a.volodenkov@grsu.by

Abstract: The treatment of dental enamel is executed by 530 nm radiation and dependence of value of specific energy of evaporation from density of peak power of laser radiation is determined. It is established, that threshold of ablation of dental enamel is 4,1 J/cm^2 and it is found that at density of energy more then 1 J/cm^2 the efficient removal of dental calcium takes place without ablation of dental enamel.

1. Experimental setupt.

Ablation influence of ultraviolet radiation on a surface of dental enamel and dental calcium was investigated. The maximal value of energy of generation of the «Lotis» (TII LS2147) made 0,2 J, thus duration of generation pulse on half-height was 15 nanoseconds.

For transportation of radiation of the e laser (530nanometers) the system on the basis of prism, mirrors and lenses has been used which optical circuit is described on fig. 1.

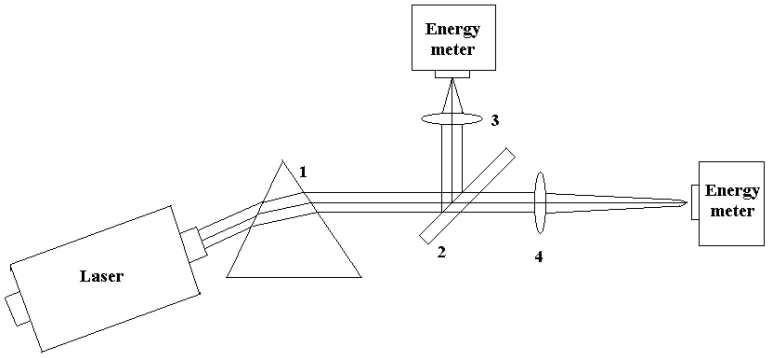

Fig.1. Optical schematic model of irradiation

Radiation of the laser went on a quartz prism 1, which was used for obtaining 530 nm radiation The radiation reflected from a quartz substrate (2), went on focusing lens (3) and got on a measuring instrument of energy (ИМО-2Н) which was used for the control of energy of radiation. Radiation past through a quartz substrate (2) went on focusing lens (4) and further on irradiated object. Lenses (3, 4) had the antireflection covering for wave length 530 nanometers. Calibration of measuring instrument of energy (ИМО-2Н), allowed to define energy falling on irradiated object, is executed. For this purpose on a place of irradiated object second device (ИМО-2Н) was put.

The focusing lens with a focal length of 235 mm has been used and radiation was focused in an oval spot with average diameter ~ 1mm. For reception of various values of energy of a pulse of radiation sets of diaphragms and adjustment of value charging voltage were used. Samples of dental tissue were irradiated with a series from 1000 pulses at use of frequency of following of pulses of 10 Hz. Depth of a crater was defined by means of an optical microscope.

2. Experimental results.

In fig. 2 dependence of depth of a crater in dental enamel (1) and dental calcium (2) from density of power after 1000 pulses is submitted.

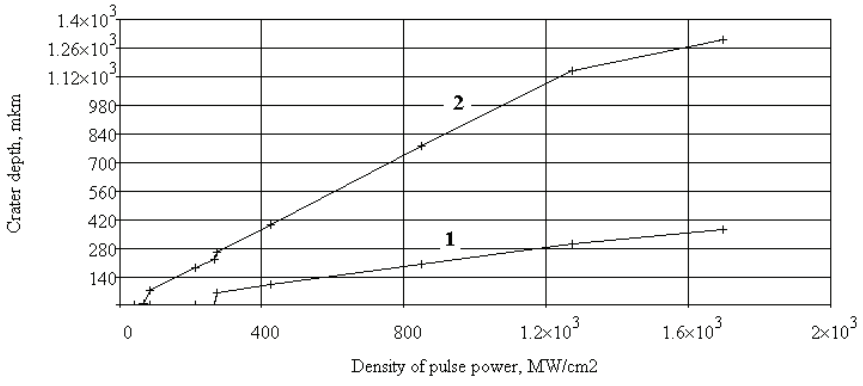

Fig. 2 Dependence of depth of a crater in dental enamel (1) and dental calcium (2) from density of power

From data, submitted in fig. 2, follows, that dependence (1) has threshold character and at density of energy smaller than 4 J/cm^2 (260 MW/cm^2) process of formation of craters in dental enamel is not observed. From data, submitted in fig. 2, follows, that dependence (2) has threshold character and at density of energy smaller than 1 J/cm^2 (65 MW/cm^2) process of formation of craters in dental calcium is not observed.

Then at density of energy more then 1 J/cm^2 (65 MW/cm^2) and less then 4 J/cm^2 (260 MW/cm^2) the efficient removal of dental calcium takes place without ablation of dental enamel.

In fig. 3 dependence of specific energy of evaporation of dental enamel from density of power is submitted.

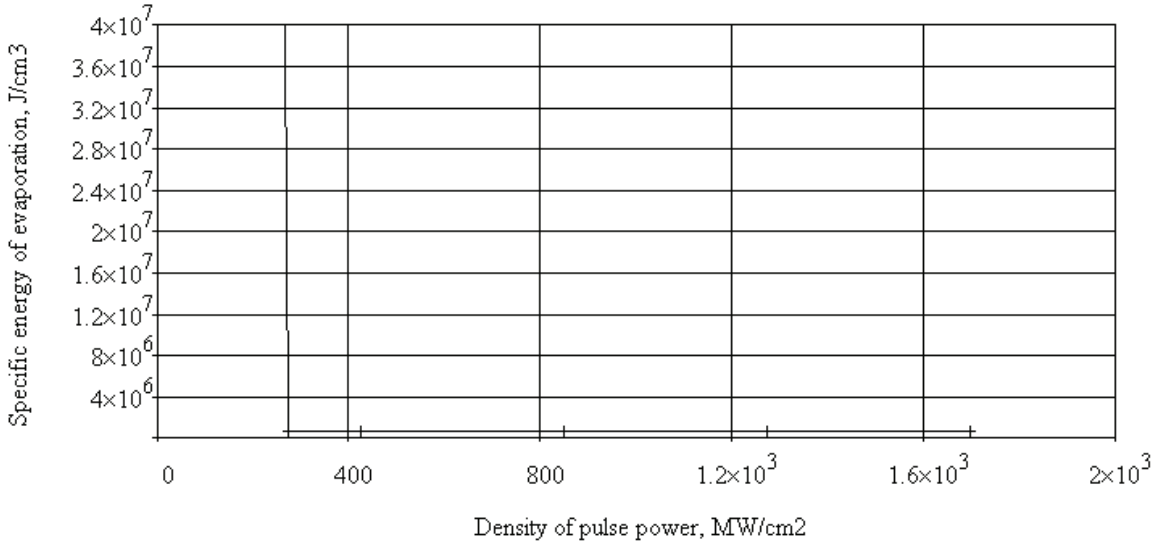

Fig. 3 Dependence of specific energy of evaporation of dental enamel from density of power

In fig. 4 dependence of specific energy of evaporation of dental calcium from density of power is submitted.

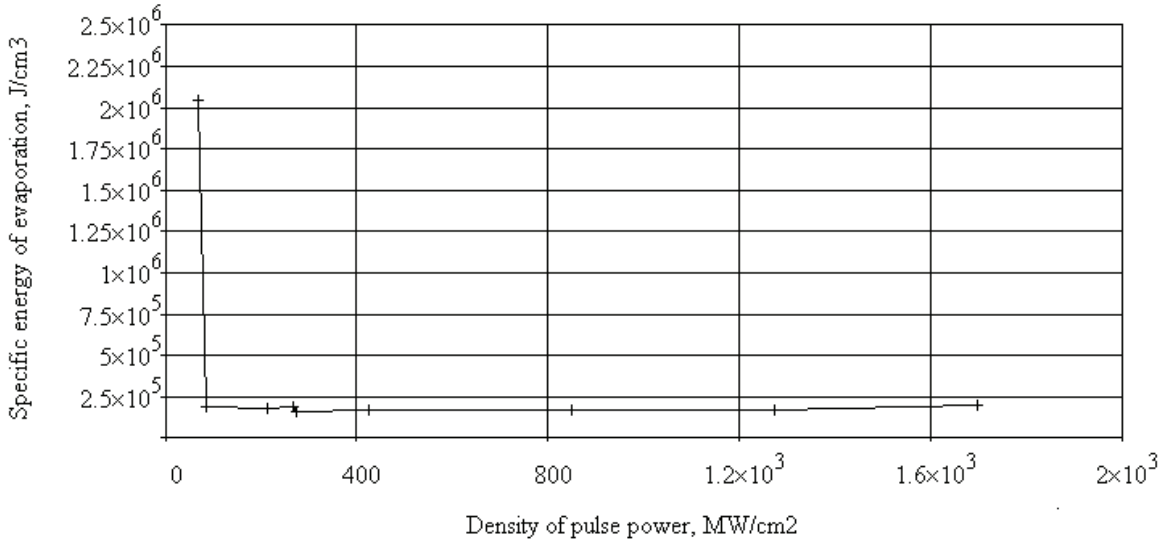

Fig. 4 Dependence of specific energy of evaporation of dental calcium from density of power

From data, submitted in fig. 3, follows, that specific energy of evaporation of dental enamel has minimum value ~ 630 kJ/cm^3 at density of power ~ 1200 MW/cm^2.

From data, submitted in fig. 4, follows, that specific energy of evaporation of dental calcium has minimum value ~ 160 kJ/cm^3 at density of power ~ 800 MW/cm^2.

The influence of various factors on the interaction mechanism of collagen and collagenase molecules in water solutions by dynamic light scattering

M.V. Lomonosov Moscow State University

I.A. Sergeeva, K.A. Anenkova, A.D. Maslennikova, A.V. Shlenskaya, G.P. Petrova

Enzyme based drugs are commonly used in medicine. Bacterial collagenase (for example from Clostridium histolyticum) is one of them. Collagenase main feature is its ability to break the peptide bonds in collagen.

Collagen is the key component of the animal extracellular matrix. Violation of the collagen catabolism leads to fibrosis of organs and tissues. Increasing of collagen degradation rate occurs in case of autoimmune diseases (rheumatoid arthritis and lupus) because of excess collagenase synthesis in the immune response.

Bacterial collagenases break down mutliple bonds in collagen triple helixeas as well as peptide bonds. Clostridium histolyticum collagenases G and H (ColG and ColH) can easily digest collagens, regardless of their types and sizes.

Bacterial collagenase from Closrtidium hostolyticum is extensively used as a clinical tool in the nonsurgical treatment of Dupuytren's disease, for enzymatic debridement, in eye's diseases treatment for accelerated resorption of catgut sutures.

Therefore, the main purpose is to study the real-time enzymatic biodegradation of collagen molecules to estimate degradation rate at different circumstances conditions?.

Optical methods, like dynamic light scattering (DLS), enable to investigate "collagen + collagenase" water solutions in conditions close to physiological. Variating the solution's parameters (pH, temperature, solvent type) and adding of collagenase activators/inhibitors enables to simulate different diseases in living organizms.

The main result of this work are:

- the main process of collagen biodegradation occurs within the first 30 minute;
- heating the water collagen solution with collagenase results in increased enzyme activity;
- adding Ca^{2+} ions in water solutions of collagen and collagenase lead to increasing biodegradation rate in 4 times, while addition of Zn^{2+} ions 2.2 times as compared with the pure water solutions;
- adding EDTA inhibitor in water solutions of collagenase and collagen causes a decrease of enzyme activity and slows down the rate of protein biodegradation the 1.3 times compared with the pure water solutions.

Reconnectable fiberscopes for long-term, subcellular-resolution *in vivo* deep-brain imaging

M.S. Pochechuev,[1] I.V. Fedotov,[1,2,3] O.I. Ivashkina,[1,3] M.A. Roshchina,[1,3] A.B. Fedotov,[1,2,3] K.V. Anokhin,[1] and A.M. Zheltikov[1,2,3,4]

[1] Kurchatov Institute National Research Center, pl. akad. Kurchatova 1, Moscow 123182, Russia
[2] Physics Department, International Laser Center, M.V. Lomonosov Moscow State University, Moscow 119992, Russia
[3] Russian Quantum Center, ul. Novaya 100, Skolkovo, Moscow Region, 143025 Russia
[4] Department of Physics and Astronomy, Texas A&M University, College Station, TX 77843, USA
Author e-mail address: zheltikov@physics.msu.ru

Abstract: Reconnectable bundles consisting of thousands of optical fibers are shown to enable high-quality image transmission, offering a platform for the creation of implantable fiberscopes for minimally invasive, long-term *in vivo* brain imaging with subcellular resolution.

Integration of advanced fiber imaging methods with optogenetic technologies [1 – 4] leads to revolutionary changes in neurosciences, helping confront long-standing challenges in brain research and providing unique tools to study, with an unprecedented spatial resolution and cell specificity, how complex space–time patterns of neural activity relate to higher brain functions. Bundles of optical fibers have been shown to enable imaging of neural structures in living animals [5], multicolor *in vivo* fluorescence [6] and Raman [7] brain imaging, as well as molecular neuroimaging of post-injury neural plasticity [8]. In combination with metal electrodes, bundles of optical fibers have been employed to demonstrate in vivo control of neural activity by means of photostimulation of light-sensitive protein channels in transgenic mice [9]. In a widely used fiber-optic interface for optogenetic work [10, 11], an optical fiber is inserted into a living brain through a guiding cannula right before the experiment. Such a fiber-optic interface has been a crucial milestone for the establishment of optogenetics as a method for the control of deep-brain neuron circuits and behavioral studies. However, as the optical method in brain research are advancing toward challenging goals of understanding the cell biology behind learning and memory, fiber-optic interfaces have to be adapted to the needs of long-term neuroimaging with subcellular resolution on deep-brain neuron circuits.

In this work, we demonstrate reconnectable bundles consisting of thousands of optical fibers, which enable, as our experiments show, high-quality image transmission, offering a platform for the creation of implantable fiberscopes for minimally invasive *in vivo* brain imaging. The concept of reconnectable fiberscopes demonstrated in this work extends the idea of reconnectable implantable single-fiber optical neurointerfaces [12 – 14] to the fiber-bundle imaging technology. Experiments on various lines of transgenic mice presented below in this paper verify the performance of this fiberscope as a powerful tool for a chronic, subcellular-resolution *in vivo* neuroimaging using genetically encoded calcium indicators, neuronal activity markers, as well as axon growth regulators and brain-specific protein drivers in deep regions of awake brain.

In vivo neuroimaging experiments with reconnectable fiberscopes were performed on Thy1-EGFP, Fos-EGFP, and GCaMP3 lines of transgenic mice. In these experiments, continuous-wave 473-nm diode-laser radiation is coupled into the individual fibers in the fiber bundle by a galvanometric optical scanner (Fig. 1). Laser radiation transmitted through the fiber bundle is used to induce the fluorescence response of enhanced green fluorescent protein (EGFP) in the brain of awake, freely behaving transgenic mice (Fig. 2). The same fiber bundle is used to collect the multicolor fluorescence response from biomarkers in a brain tissue and to transmit fluorescent images to the input end of the fiber bundle, which is placed in the focal plane of the confocal microscope (Fig. 1).

This work was supported by the Russian State Targeted Program ‘Research and Development in Priority Areas of Development of the Russian Scientific and Technological Complex for 2014–2020’ (Contract 14.607.21.0092 of November 21, 2014; unique identifier of applied research: RFMEFI60714X0092).

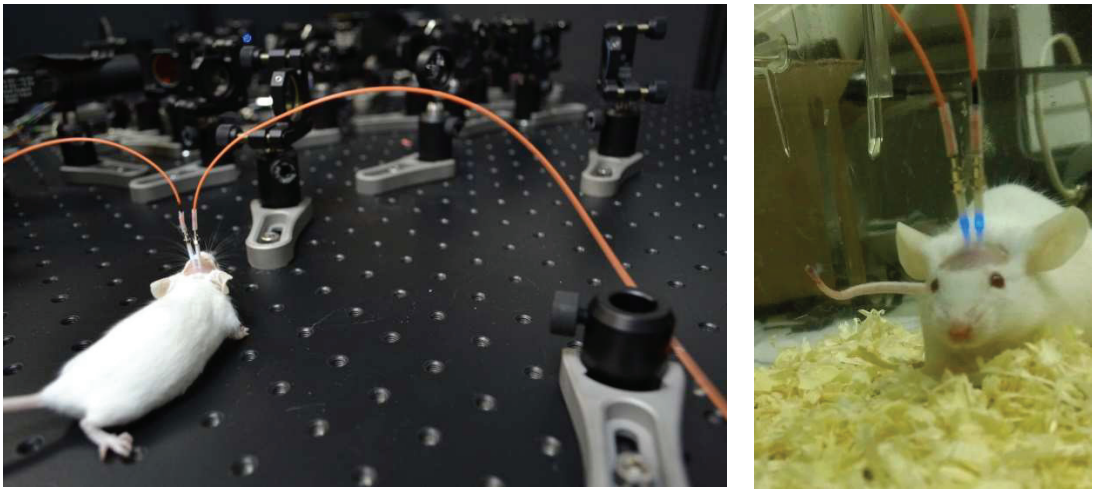

Fig. 1. Transgenic mice with implanted reconnectable fiberscopes.

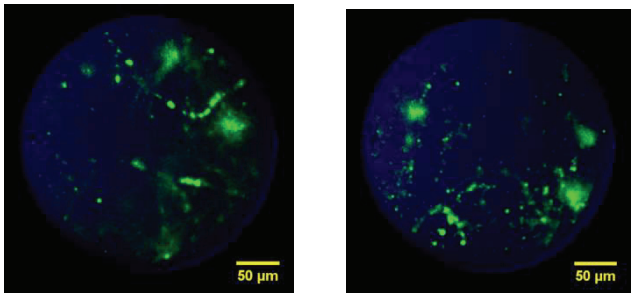

Fig. 2. Images of lower cortical layers in an awake Thy1-EGFP mouse taken with the reconnectable fiberscope.

References

[1] E.S. Boyden, F. Zhang, E. Bamberg, G. Nagel, and K. Deisseroth, "Millisecond-timescale, genetically targeted optical control of neural activity," Nature Neuroscience **8**, 1263–1268 (2005).

[2] I. Diester et al. “An optogenetic toolbox designed for primates,” Nature Neuroscience **14**, 387–397 (2011).

[3] K. Deisseroth, “Optogenetics,” Nature Methods **8**, 26–29 (2011)

[4] G. Miesenböck, "The optogenetic catechism," Science **326**, 395–399 (2009).

[5] P. Vincent et al. “Live imaging of neural structure and function by fibred fluorescence microscopy,” EMBO Rep. **7**, 1154–1161 (2006).

[6] L.V. Doronina-Amitonova, I.V. Fedotov, O. Efimova, M. Chernysheva, A.B. Fedotov, K.V. Anokhin, and A.M. Zheltikov, Appl. Phys. Lett. **101**, 233702 (2012).

[7] L.V. Doronina-Amitonova, I.V. Fedotov, O.I. Ivashkina, M.A. Zots, A.B. Fedotov, K.V. Anokhin, and A.M. Zheltikov, Appl. Phys. Lett. **101**, 113701 (2012).

[8] J. Yan et al. “Molecular Neuroimaging of Post-Injury Plasticity,” *Journal of Molecular Neuroscience* **54**, 6302014 (2014).

[9] Y. Hayashi et al. “Spatio-temporal control of neural activity *in vivo* using fluorescence microendoscopy,” Eur. J. Neurosci. **36**, 6 (2012).

[10] A.M. Aravanis, L.-P. Wang, F. Zhang, L.A. Meltzer, M.Z. Mogri, M.B. Schneider, and K. Deisseroth, “An optical neural interface: in vivo control of rodent motor cortex with integrated fiber-optic and optogenetic technology,” J. Neural Eng. **4**, S143–S156 (2007).

[11] A.R. Adamantidis, F. Zhang, A.M. Aravanis, K. Deisseroth, and L. de Lecea, “Neural substrates of awakening probed with optogenetic control of hypocretin neurons,” Nature **450**, 420 – 424 (2007).

[12] D.R. Sparta, A.M. Stamatakis, J.L. Phillips, N. Hovelsø, R. van Zessen, and G.D. Stuber, “Construction of implantable optical fibers for long-term optogenetic manipulation of neural circuits,” Nature Protocols **7**, 12 – 23 (2012).

[13] G.D. Stuber et al. “Excitatory transmission from the amygdale to nucleus accumbend facilitates reward seeking,” Nature **475**, 377 – 380 (2011).

[14] L. V. Doronina-Amitonova, I. V. Fedotov, O. I. Ivashkina, M. A. Zots, A. B. Fedotov, K. V. Anokhin, and A. M. Zheltikov, "Implantable fiber-optic interface for parallel multisite long-term optical dynamic brain interrogation in freely moving mice," Sci. Rep. **3**, 3265 (2013).

Detection of flavin fluorescence in lung adenocarcinoma cells by FLIM

Boruleva E.A.[1], Zherdeva V.V.[2], Savitsky A.P.[2]

[1] *National research nuclear university "MEPHI"*

[2] *Bach Institute of Biochemistry, Research Center of Biotechnology of the Russian Academy of Sciences*

e-mail: ipcoova@yandex.ru

Abstract: Changes of endogenous fluorescence can serve as an indicator of changes in biochemical status of the cells, which is to date, demonstrated for a number of endogenous fluorophores. Evaluated the conditions of endogenous fluorescence detection in tumor cells by the FLIM method for determining the flavin fluorescence.

1. Introduction

The aim of our work was to visualize the endogenous fluorescence in tumor cells by FLIM and determine the sources of flavin fluorescence.

2. Materials and methods

FLIM was performed on the time-resolved confocal fluorescence microscope MicroTime 200 (PicoQuant GmbH, Germany). The solid-state 473 nm laser was used for excitation (PicoQuant GmbH, Germany), 500 / 14-25 nm filter (Semrock, USA) was used for registration of fluorescence. The fluorescence spectra were registered using Andor chamber (PicoQuant GmbH, Germany). The images were processed using the PicoHarp and SymPhoTime software (PicoQuant GmbH, Germany).

3. Results

The lifetime distribution of autofluorophors in tumor cells was obtained. It has been shown that the signal was distributed unevenly, originated from the organelle morphed structure. Part of these organelles were colored by the specific mitochondria dye Mitotracker Orange (Thermo Scientific, USA).

Fluorescence decay curves were approximated well by double exponential model with an average lifetime of 2.3 ns. Presumably, it was corresponded to the lifetime of flavins.

4. Conclusions

The results can be applied in the studying of cell biochemistry in real time mode when the change level of endogenous fluorophores may be an indicator of some pathological processes.

Femtosecond laser surgery of mammalian embryo and oocytes.

Osychenko A.A.[1], Astafiev A.A. [1], Shakhov A.M. [1]Zalessky A.D.[1],A.A. Titov[1], , Nadtochenko V.A. [1,2,3]

[1] Semenov Institute of Chemical Physics, RAS, Russia, Moscow
[2] Institute of Problems of Chemical Physics, RAS, Russia, Chernogolovka
[3] MSU, Faculty of Chemistry, Russia, Moscow
e-mail: nadtochenko@gmail

Abstract: The work reports the study of the size and dynamics cavitation bubbles produced by focused femtosecond laser pulse when laser irradiation is focused at different components (organelles) in the mammalian oocyte.

Introduction. Femtosecond laser nanosurgery of cells and embryos is topical field of biophotonics. Nowadays mechanism of femtosecond laser irradiation absorption by embryo cells is not very clear. The most commonly used model object of laser absorption in cell is water, because cells contain more than 90% of water. But sufficient differences of chemical composition and properties between water and living cell confine application of this model.

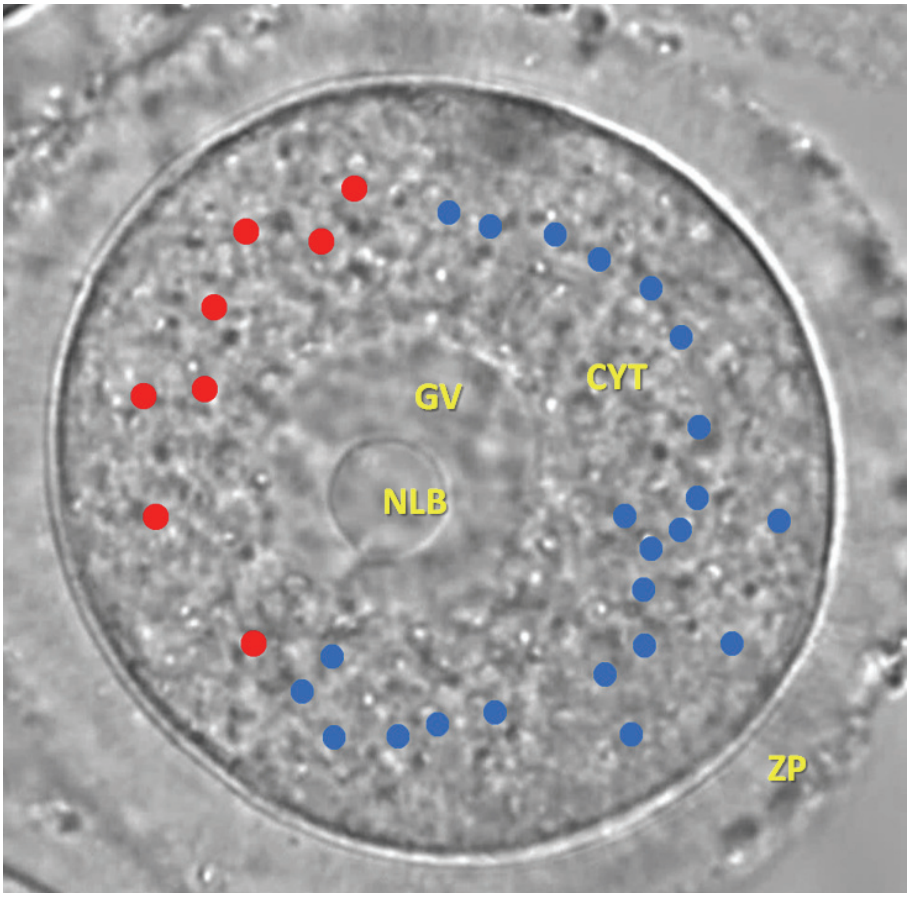

Figure 1. image of GV oocyte in the phosphate buffer droplet. NLB – nucleolus-like body; GV – nucleoplasm in the germinal vesicle; CYT – cytoplasm; ZP - zona pellucida. Red and blue spots were irradiated by fs laser pulse.

Fully-grown mammalian oocytes (or germinal vesicle, GV), rather than typical nucleoli, contain prominent but structurally homogenous in optical image bodies called “nucleolus-like bodies” (NLBs). Figure 1 shows the components: a) zona pellucida (ZP) shows the strong glycoprotein membrane surrounding the plasma membrane of mammalian oocytes, the layer that cover oocyte; b) cytoplasm (CYT) containing the cytosol, organelles, cytoskeleton, and various particles; c) germinal vesicle (GV) - shows the enlarged nucleus of an oocyte before it develops into an

ovum and d) NLB immersed in germinal vesicle.. NLBs accumulate a vast amount of material, but their biochemical composition and functions remain uncertain [1]. The goals of the present work are: 1) the study of the size and dynamics cavitation bubbles produced by focused femtosecond laser pulse when irradiation is focused at different components (organelles) in the cell; 2) the examination of the development of oocyte after laser pulse focused at different components (organelles) in the cell. We determined the probability to reach metaphase II (*MII*) stage of oocyte after laser surgery pulse directed to the particular organelles.

Experimental. Titanium-sapphire oscillator (Tsunami, Spectra-Physics) generated femtosecond pulses with wavelength of 790 nm, a repetition rate of 80 MHz and pulse energy close to 30 nJ. The Pockels cell (Avesta Project Ltd.) selected single pulses. Single pulses were amplified by Ti: sapphire oscillator (TiF-20, Avesta Project Ltd.) amplifier. The amplified pulse energy was 150 nJ. A laser attenuator consisting of a half-wave plate and a polarizing cube attenuated the pulse energy. The inverted optical microscope Olympus IX71 was used with a lens 40x 0.75NA (UPlanFLN, Olympus). The spot in the focal plane is characterized: the radius of the laser beam waist was $w0 = 0.61\lambda / N.A.$ = 0.64 microns, and Raleigh parameter Z_R=1.63 microns. The formation of the cavitation bubbles was monitored by the measurements of the intensity of the backscattered probe light from the bubbles. The wavelength of the probe light was 445 nm. Light intensity was measured by photomultiplier tube and LeCroy WaveSurfer 62Xs oscilloscope. The time resolution of the scattered light measurements was 5 ns. The Ethics committee approved the experimental protocols of the work carried out at Institute of Chemical Physics RAS. The GV oocytes were obtained from 4-8 week old C57Bl/6 mice.

Results and discussion. It was found that when NLB material was cut the probability of development of GV oocytes to MII stage is reduced by 3 to 7 times as compared with control measurements. It suggests the important role of the organization NLB material in the maturation of mouse oocytes. Laser shorts directed to NLB – nucleolus-like body, GV – nucleoplasm in the germinal vesicle or CYT – cytoplasm do not effect on the probability of GV oocyte to reach M II phase.

It was found, that the size and lifetime of the cavitation bubble are significantly different during laser action on various organelles. Moreover, the lifetime of the bubble is different for different areas inside the cytoplasm. For example, for shoots in the red dots it was 1.3 mks whereas in the blue dots it was 0.4 mks. It suggests meaningful heterogeneity of the cell. The lifetime of the bubble can provide the information about this heterogeneity

This work was supported by The Ministry of education and science of Russia, grant No. 14.604.21.0058 (unique identifier RFMEFI60414X0058).

References

[1] Alexander Gulin, Victor Nadtochenko, Artyom Astafiev,Valentina Pogorelova, Sami Rtimi, Alexander Pogorelov "Correlating microscopy techniques and ToF-SIMS analysis of fully grown mammalian oocytes" Analyst, **141**, 4121–4129, (2016)

UV VANADATE LASERS FOR MEDICINE APPLICATIONS

A.A. Sirotkin, G.P.Kuzmin
Prokhorov General Physics Institute of the Russian Academy of Sciences, Moscow, Russia
Advanced Energy Technologies LTD, Moscow, Russia
E-mail: kuzmin@kapella.gpi.ru

Abstract. We have demonstrated a low-cost, compact, high-efficiency passively Q-switched UV-VIS-IR laser for medicine systems based on the variable-cut Nd:$GdVO_4$ laser with Cr^{4+}:YAG saturable absorber crystal. The average power of visible and UV radiation up to 310 and 7 mW has been obtained in crystals PPLN and BBO, respectively.

We present UV laser sources for medicine application based on a novel methods control of spectral parameters in diode-pumped vanadate lasers.

Spectroscopic and lasing properties of Nd:YVO_4 , Nd:$GdVO_4$ and mixed Nd:$Y_xGd_{1-x}VO_4$, Nd:$Y_xSc_{1-x}VO_4$ crystals were investigated. We have investigate polarization and angular dependences of the luminescence intensity of Stark transitions in vanadate crystals. The frequency shift and redistribution of the luminescence intensity of Stark transitions are observed.

It is known, that too large emission cross-section of with a-cut π-polarized vanadate crystals is a shortcoming for Q-switched lasers, because it limits their energy-storage capacity, leading to smaller pulse energies. Usual methods to avoid this drawback are to use *c*-cut vanadat crystals [1,2] , mixed vanadates Nd:$Gd_xY_{1-x}VO_4$[3] or *a*-cut (σ-polarization) vanadat crystals [4,5].

However wavelengths of c-cut and a-cut σ-polarized vanadate crystals distinct from a-cut π-polarized emission. In addition c-cut vanadate crystals have nonpolarised radiation.

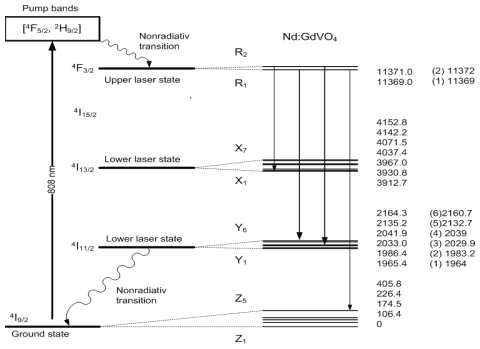

Fig.1 Energy levels diagram in Nd^{3+}:$GdVO_4$ vanadate crystals.

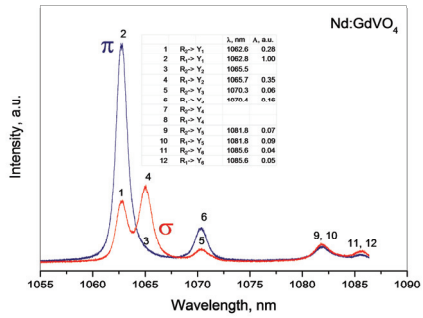

Fig.2 The luminescence spectra of Nd^{3+}:$GdVO_4$ (π- and σ-polarization)

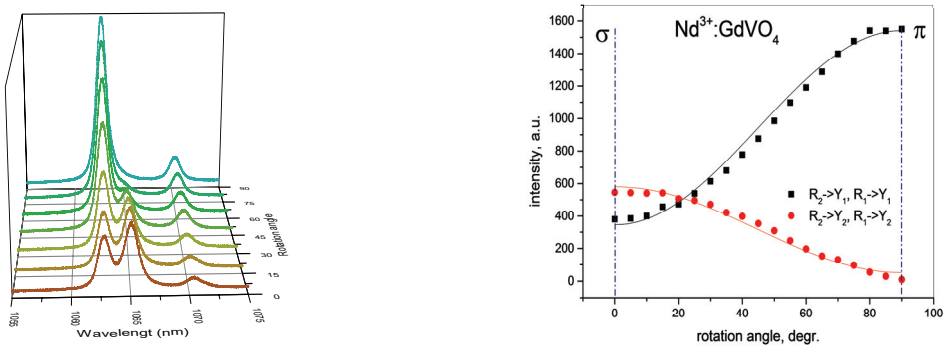

a. b.

Fig.3 The angular dependences of the luminescence intensity of Stark transitions in Nd:$GdVO_4$ crystals.

It is seen (fig.3) that the transition from σ-polarization (θ=0°, φ=0) to π -polarization (θ=90°, φ=0) the redistribution of radiation intensities for different Stark levels. The effective stimulated emission cross-section

value change in 5 times the variation in θ=0° to θ=90°. The minimum stimulated emission cross-section value is reached at the intersection of two curves (fig.3). On the right of this point will generate laser radiation with a wavelength of 1.063 μm and 1.065 μm on the left.

So, using angular dependences of the luminescence intensity of Stark transitions in vanadate crystals we can to create active media with different coefficients of gain and wavelengths.

Variable-cut Nd^{3+}:$GdVO_4$ (θ=25°, φ=0) crystal have stimulated emission cross-section value are comparable to one *c*-cut or *a*-cut (σ-polarization) vanadate crystals. It has the polarized radiation, Moreover wavelength of radiation coincide with a-cut π-polarized emission. It allows creating effective master oscillator-amplifier systems.

Laser operation under different angles of cut were investigated for Nd^{3+}:YVO_4 and Nd^{3+}:$GdVO_4$.

Variable-cut (θ=var, φ=0) vanadate crystals have the polarized radiation, and wavelengths of radiation coincide with a-cut π-polarized emission. It allows creating effective master oscillator-amplifier systems.

Cr^{4+}:YAG saturable absorber with initial transmission 65 % and 80 % oriented with their normal along the (111)-crystal axis, were used as the passive Q switch.

We have shown experimentally that the variable-cut (θ=25°, φ=0) Nd^{3+}:YVO_4 and Nd^{3+}:$GdVO_4$ laser could have good passively Q-switched performance, which gives the narrowest pulse of 2.5 ns with the highest peak power of 12 kW.

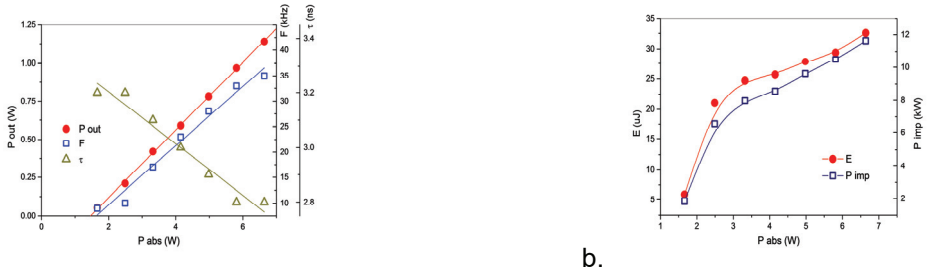

a. b.

Fig.4 a. The average output power, the pulse width and the pulse-repetition rate and b. The pulse energy and the peak power of *var*-cut (θ=25°, φ=0) Nd^{3+}:$GdVO_4$ passively Q-switched lasers vs absorbed pump power.

In addition the vanadate crystals have the polarized radiation. High peak power and beam quality of the IR lasers are required for efficient conversion of the radiation into visible or UV spectrum range by means of nonlinear crystals.

The average power of visible and UV radiation up to 310 and 7 mW has been obtained in the case of extracavity conversion of the laser radiation in crystals PPLN and BBO, respectively.

We have demonstrated a low-cost, compact, high-efficiency passively Q-switched UV-VIS-IR laser medicine systems based on the variable-cut Nd^{3+}:$GdVO_4$ laser with Cr^{4+}:YAG saturable absorber crystal.

References

[1] Y. F. Chen and Y. P. Lan , "Comparison between c-cut and a-cut Nd:YVO4 lasers passively Q-switched with a Cr4+:YAG saturable absorber", Appl. Phys. B 74, 415 (2002)

[2] J. Liu, J. M. Yang, and J. L. He, "Diode-pumped passively Q-switched c-cut Nd : GdVO 4 laser", Opt. Commun. 219, 317 (2003)

[3] J. Liu, Zh. Wang, X. Meng, Z. Shao, B. Ozygus, A. Ding, H. Weber , "Improvement of passive Q-switching performance reached with a new Nd-doped mixed vanadate crystal Nd : Gd 0.64 Y 0.36 VO 4", Opt. Lett. 28, 2330 (2003)

[4] A. Agnesi and S. Dell'acqua, "High-peak-power diode-pumped passively *Q*-switched Nd:YVO4 laser," Appl. Phys. B B76,351–354 (2003)

[5] A.A.Sirotkin, V. I.Vlasov, A. I.Zagumennyi, Yu. D.Zavartsev, S. A.Kutovoi, " Vanadate lasers with σ-polarised radiation", Quantum Electronics, 41 (7), 584 (2011)

Clinical application of the multiwavelength laser medical installation with antibacterial and therapeutic effect.

A.G.Kuzmina[4], K.K.Baranov[2,3], N.E.Gorbatova[2,3], V.P.Kurilov[4], G.P.Kuzmin[1,3], A.A.Sirotkin[1,3], O.V.Tikhonevich[1,3], S.A.Zolotov[2,3]

[1]Prokhorov General Physics Institute,Russian Academy of Scienses, Moscow, Russia
[2]Institute of Emergency Children's Surgery and Traumatology, Moscow, Russia
[3]Advanced Energy Technologies LTD, Moscow, Russia
[4] First Moscow State Medical University by I.M.Sechenov, Russia
E-mail: kuzmin@kapella.gpi.ru

Annotation Multiwavelength laser medical device "Livadia" is created on the basis of the laser on YVO4-Nd: YVO4 with subsequent conversion of the infrared radiation in the visible and ultraviolet regions of the spectrum . The radiation device is used with antibacterial and anti-inflammatory target for treatment a range of infectious and inflammatory diseases of external and intracavitary sites.

Multiwave laser medical device "Livadia" has been developed either for bactericidal or for therapeutic impact on the affected organism parts [1]. This device is on the diode pumped solid state laser and main wavelength radiation conversion 1064 nm into the second harmonic 532 nm and forth harmonic 266 nm. The average power UV radiation 5 mW.

By using an v*ariable*-cut YVO_4-Nd:YVO_4 crystal, we have shown experimentally that the best passively *Q*-switched performance obtained in our experiments is from the v*ariable*-cut laser, which gives the narrowest pulse of 1.5 ns with the highest peak power of 29 kW. In addition v*ariable*-cut vanadate crystals have the polarized radiation. High peak power and beam quality of the IR lasers are required for efficient conversion of the radiation into visible or UV spectrum range by means of nonlinear crystals.

The average power of visible and UV radiation up to 340 and 37 mW has been obtained in the case of extracavity conversion of the laser radiation in crystals PPLN and BBO, respectively. It has been shown that UV radiation on the wavelength 266 nm on bronchia mucosa with various inflammation types improves regenerative processes in bronchia tissues that comes to treatment deadline decrease[2].

Therapeutic effect of the device use is achieved by multiwave radiation function in UV, visible and IR wavelength ranges. There is the opportunity to use either separate wavelengths or their combinations that allows choosing the most optimal radiation regime for each disease. Combined radiation effect can be used for endocavernous treatment of destructive lung tuberculosis forms. The alternative region use is purulent-inflammatory soft tissue processes treatment. Combined radiation effect in soft tissues causes pathogenic microorganisms growth inhibition and simultaneous stimulation in reparative tissue processes. That is actually observed in gynecology, otolaryngology, therapy and especially in purulent surgery.

In order to combat wound infection and septic lesions of the soft tissues was applied by multiwavelength laser system "Livadia" and the reliable experimental data on its high efficiency

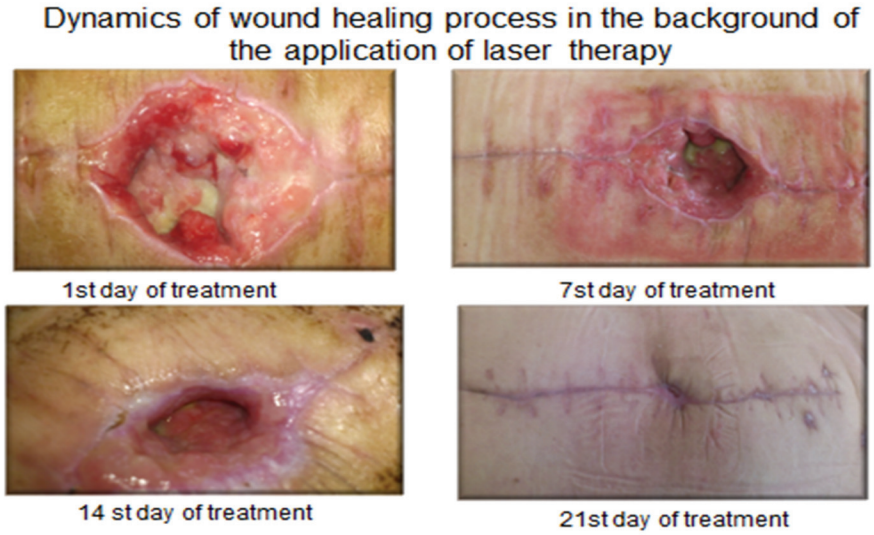

Patient P. 60 years. The diagnosis : postoperative ventral hernia. Factors that led to a high risk of postoperative complications : - obesity - chronic obstructive pulmonary disease , bronchial asthma- microcirculation disturbance , due to tissue hypoxia - The volume of transactions , a vast area of tissue trauma , suppuration of postoperative wounds .

Applications in otorhinolaryngology (otology)

In this paper, we proposed a method for the treatment of chronic middle purulent otitis. After the introduction of the optical fiber through the perforations of the tympanic membrane was carried out under the supervision of an endoscope processing structures of the middle ear laser irradiation. According to the research confirmed the positive clinical effect. In 25 patients included in the core group of the study, noted earlier relief of disease and lengthening the period of remission after the laser treatment in conjunction with standard treatment, in comparison with the nature of the disease in 15 control patients who used only conventional therapy.

Patient D. 15 years old . Diagnosis: Chronic middle purulent otitis , exacerbation . It uses the combined method of treatment , including conventional standard pharmacological therapy and course of treatment of the middle ear cavity laser by setting the " Livadia "

Perforation of the tympanic membrane

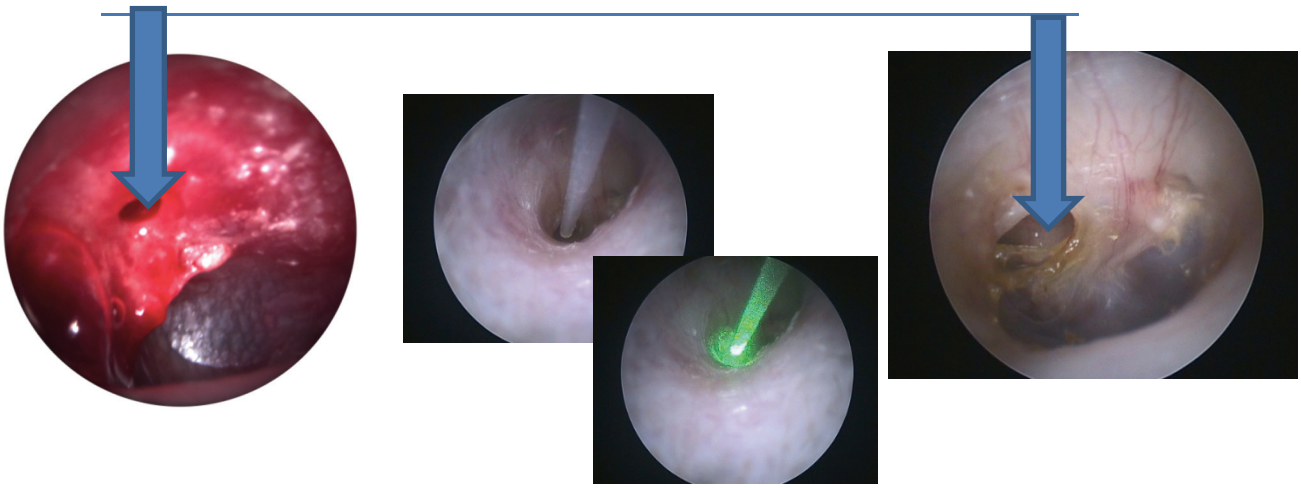

1 st day of treatment . There is hyperemia and infiltration of the tympanic membrane , a thick muco - purulent discharge .	The light guide is inserted under the endoscopic control via the external auditory canal and tympanic membrane perforation in the middle ear cavity . Exposure 10 min irradiation .	12th day of treatment. There is cessation of suppuration , and no inflammatory response .

1. G.P.Kuzmin , A.A.Sirotkin , Yu.L.Kalachev . Multiwave laser installation bactericidal and therapeutic effect in the treatment of infectious diseases . The patent for invention №2448746 from June 7, 2010

2. G.P.Kuzmin, A.G. Kuzmina, O.V.Lovacheva, A.A.Sirotkin. Multiwave Medical Device on the Diode Pumped Solid State Laser for the Microbe Nature Disease Treatment. Journal of Innovative Optical Health Sciences. 2012, Vol.5, No.2, 1250011, p.1-5.

Electrostatic interaction in biopolimer water solutions investigated by Laser light scattering.

K.V. Fedorova, G.P. Petrova.
Faculty of physics M. V. Lomonosov State University, Moscow, Russia
E-mail address: fedorova@physics.msu.ru

Abstract: In this paper we consider electrostatic interaction of lysozyme molecules in aqueous solution in the presence of the third component - the metallic ions. This paper deals with the most suitable methods for measurement of these parameters - laser light scattering.

In solution the surface of protein macromolecules is always charged and so the electrostatic interaction between the polar solvent and charged groups on the biopolymer surface is strong enough. It is of interest to consider three types of interaction: protein - protein, protein - metal ion, protein - solvent. All of these interactions can change as static parameters of macromolecules solution.

Metals play an important role in a human organism. Concentrations of metals, particularly, heavy metals, exceeding the maximum allowable level in the organism are dangerous for persons. But some of them containing in living organisms and implement some functions. At present, it is of topical interest to study molecular mechanisms of the effect of metal ions on biological fluids.

It was found that cluster formation depends on metal ion radius [1]. The nature of interaction protein macromolecules in case when the solution contains metal ions with a large ionic radius depends largely on dipole-dipole forces. Protein molecules may come extremely closely to one another to form a macromolecular complex - a dipole cluster.

The mass and radius of protein clusters forming in the solution increases by more than one order of magnitude as compared to the mass of a macromolecule and reaches its maximum near the isoelectric point of protein.

Interaction of these ions with a protein surface involves, as a rule, their hydrated shells. In cases where protein solutions contain small ions like sodium (the ion radius equals 0.87 A), dipole clusters are not formed, because sodium ions are located near the protein surface surrounded by water molecules and cannot bind directly with the negative charges on the protein.

In interacting with the protein surface directly, a metal ion with a large radius is bound more strongly to negatively charged groups on the protein and can form a Coulomb complex on a protein macromolecule with a common hydrated shell. In this case, the metal ions compensate completely for the local surface charge of the protein molecule.

The effective decrease of the protein surface charge that takes place as a result of strong binding of metal ions with a large radius and the macromolecule can lead to a situation where the main type of interaction between the protein molecules is a dipole–dipole attraction instead of Coulomb repulsion, because the proteins have abnormally high dipole moments (several hundred Debye uniques). So the protein molecules can go closely to each other and forming aggregates – dipole clusters

The energy of the ion and the water dipole molecule binding, determined by equation

Lysozyme it is found out practically in all organisms. At vertebrates contains mainly in tears, a saliva, a spleen, lungs, kidneys and leukocytes; in fabrics it is localized in lisosomes. At vertebrates lysozyme carries out functions of a nonspecific antibacterial barrier. The mechanism of action is caused by ability of enzyme to break

a cellular wall of bacteria and to cause them lisis (destruction). Lysozyme apply in medicine as antimicrobial agent (including as the additive in food stuffs for kids).

The nature of interaction of protein (lysozyme) macromolecules in case when the solution contains ions with a large ionic radius depends largely on dipole–dipole forces. When dipoles are spaced at no more than 30–50 Å, the energy of dipole-dipole interaction may exceed thermal energy kiloteslas by almostv100 times [3]. Protein molecules may come extremely closely to one another to form a macromolecular complex-a dipole cluster. The mass of protein clusters forming in the solution increases by more than one order of magnitude as compared to the mass of a macromolecule and reaches its maximum near the isoelectric point of protein. In our study has been received dependence of factor of interaction of molecules lysozyme in a water solution. According to Scatchard theory: the pH dependence of ***B*** has nonlinear character with a minimum in a point pH ~ 3, 5 and it testifies that the isoelectric point of lysozyme is near pI = 3, 5 [4].

Apparently, this feature is due to the small size of the molecule of lysozyme and its ability to greatly change the surface charge.

The work was supported by RFBR grant № 16-32-00847.

References

1. J. Edsall, H. Edelhoch, R. Lontie, and. P. Morrison, J. Am. Chem. Soc., **72**, p. 4641, (1950).
2. W.L. Hubbell, H.M. McConnell, J. Am. Chem. Soc., **93**, p. 314, (1971).
3. P. Debye. Light scattering in solutions, Journal Appl.Phys. 15, 338-349,(1944)
4. G. Petrova and all, Laser Physics, Vol. 19, No. 6, pp. 1308–1311 (2009).
5. G.P. Petrova, Yu.M. Petrusevich, D.I. Ten Quantum electronics, 32, №10, p. 1-5

Optical Coherence Tomography: Technology and Applications

James G. Fujimoto[1]

[1]Department of Electrical Engineering and Computer Science and Research Laboratory of Electronics, Massachusetts Institute of Technology, Cambridge, MA 02139, USA

Optical coherence tomography (OCT) uses photonics to enable micron-resolution 3D structural and functional imaging in tissues. It is a standard ophthalmic diagnostic and is being developed for many clinical applications. We review technology and applications.

Multiphoton Fluorescence Microscopy and Real Time Rendering for Rapid Evaluation of Surgical Cancer Specimens

Michael G. Giacomelli[1], Tadayuki Yoshitake[1], Lucas Cahill[1], Yury Sheykin[2], Hilde Vardeh[2], James Connolly[2], and James G. Fujimoto[1]

[1]Department of Electrical Engineering and Computer Science and Research Laboratory of Electronics, Massachusetts Institute of Technology, Cambridge, MA 02139, USA
[2]Department of Pathology, Beth Israel Deaconess Medical Center, Harvard Medical School, Boston, MA, USA

Surgical cancer specimens can be imaging by rapid staining and multiphoton fluorescence microscopy. GPU accelerated color re-mapping generates images similar to H&E histology. These methods promise to enable real time evaluation of surgical cancer margins.

Multicomponent diode laser gas analyzer for medical screening diagnostics: Qualitative and quantitative feature of biomarkers of human exhaled air at different functional states

A. Karabinenko[1], A. Bogomolova[1], S. Shastun[2] , A. Nadezhdenskii[3], Ya. Ponurovskii[3], M. Spiridonov[3], V. Zaslavskii[3]

[1] Pirogov Russian National Research Medical University (RNRMU), Ostrovitianov str. 1, 117997 Moscow, Russia. E-mail: karabinenkoa@mail.ru
[2] Peoples Friendship University of Russia., 117198 Moscow, Russia
[3] A.M. Prokhorov General Physics Institute, 38 Vavilov str.,119991 Moscow, Russia E-mail: ponur1960@yandex.ru

Screening tests are effective methods of assessing the functional state of the organism. The screening study in medicine is understood as a set of measures aimed at identifying the diseases in a large group of patients in the absence of pronounced symptoms. The main requirements for a screening test is its simplicity, noninvasiveness, and safety of the testing procedures, as well as high processing speed and the ability to detect diseases at an early stage.

An experimental prototype of multi-channel analyzer for non-invasive screening and biomedical research was developed on the basis of fiber coupled the near-IR range diode lasers. Device enables to measure $^{12}CO_2$, $^{13}CO_2$, CH_4, NH_3 and H_2S biomarkers of the exhaled air. Detection of CH4 was carried out in the wavelength range of 1.65 μm, ammonium NH_3 in the 1.51 μm and the $^{12}CO_2$, $^{13}CO_2$ and H_2S in the range 1.60 μm. Measuring the concentrations of the five molecules simultaneously were carried out in Herriot type multipass cell with full optical path length of 26 m and a volume of 2.5 liters. All measurements were made in real time. Fig. 1 presents photo multi-channel diode laser analyzer for non-invasive screening and biomedical research.

Clinical tests of the diode laser spectrometer were performed in the Moscow City Clinical Hospital No 12. The measurements were performed in 162 patients with various diseases in phase and remission at rest, during exercise, recovery and after meals. Identified biomarkers of exhaled air, allowing to assess the state of the cardiorespiratory function, gaseous Ingredients, reflecting the intensity of the digestive system and the degree of infestation B. Helicobacter pylori, the nature of the food regime. Identified deviations biomarkers of exhaled air levels have diagnostic and prognostic value during mass screening.

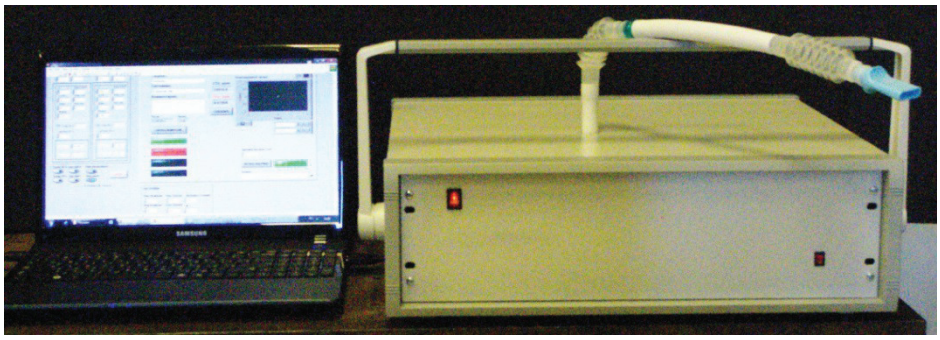

Fig.1 Photo multi-channel diode laser analyzer for non-invasive screening and biomedical research

References

1. *А. Какрабиненко и др., Тезисы I Всероссийской конференции с международным участием ««Химический анализ и медицина», Москва 2015, стр. 10.*